Micro-Scale Scratching by Soft Pad Asperities in Chemical-Mechanical Polishing

by

Sanha Kim

B.S., Mechanical Engineering
Seoul National University, 2008

M.S., Mechanical Engineering
Seoul National University, 2010

Submitted to the Department of Mechanical Engineering
in Partial Fulfillment of the Requirements for the Degree of

DOCTOR OF PHILOSOPHY IN MECHANICAL ENGINEERING

at the

MASSACHUSETTS INSTITUTE OF TECHNOLOGY

September 2013

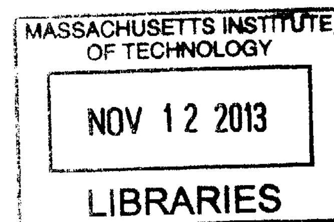
ARCHIVES
MASSACHUSETTS INSTITUTE OF TECHNOLOGY
NOV 12 2013
LIBRARIES

© 2013 Sanha Kim. All Rights Reserved.
The author hereby grants to MIT permission to reproduce
and to distribute publicly paper and electronic
copies of this thesis document in whole or in part
in any medium now known or hereafter created.

Signature of Author: ______________________
Department of Mechanical Engineering
August 16, 2013

Certified by: ______________________
Jung-Hoon Chun
Professor of Mechanical Engineering
Thesis Supervisor

Certified by: ______________________
Nannaji Saka
Research Affiliate, Department of Mechanical Engineering
Thesis Supervisor

Certified by: ______________________
David E. Hardt
Professor of Mechanical Engineering
Chairman, Department Committee on Graduate Students

Micro-Scale Scratching by Soft Pad Asperities in Chemical-Mechanical Polishing

by

Sanha Kim

Submitted to the Department of Mechanical Engineering
on August 16, 2013 in partial fulfillment of the requirements for the Degree of
Doctor of Philosophy in Mechanical Engineering

ABSTRACT

In the manufacture of integrated circuits (IC) and micro-electromechanical systems (MEMS), chemical-mechanical polishing (CMP) is widely used for providing local and global planarization. In the CMP process, polishing pads, typically made of polyurethanes, play a key role. Due to the random, rough surface of the pad, only the tall asperities contact the wafer and transmit the necessary down force and motion to the abrasive particles for material removal. As the applied pressure is concentrated under few asperities, however, the asperities themselves, even though softer, may generate unintended micro-scratches on relatively hard surfaces under certain conditions.

This thesis investigates the effects of topographical, mechanical, and tribological properties of the pad and of the wafer surfaces on pad scratching in CMP. The generation and probability of scratching by soft pad asperities on hard monolithic layers are modeled. At single-asperity sliding contact, the asperity contact pressure along with the interfacial friction that can induce surface layer yielding are first derived, for different asperity deformation modes: elastic, elastic but at the onset of yielding, elastic-plastic, and fully-plastic. Under multi-asperity sliding contact, the probability of scratching asperities is determined taking into account the asperity height variation of the rough pad surface. The models are further advanced for scratching of patterned Cu/dielectric layers. As a result, the conditions for and probability of scratching are presented in terms of the asperity-to-layer hardness ratio, friction coefficient, asperity modulus-hardness ratio and ratio of asperity radius to standard deviation of asperity heights. The scratching models are validated by performing sliding experiments using solid polymer pins and CMP pads. For scratch mitigation, especially, a novel, cost-effective asperity-flattening method is introduced to control the pad topography, i.e., to increase the ratio of asperity radius to standard deviation of asperity heights.

Finally, the role of asperities in material removal is studied based on contact mechanics and abrasive wear models. A new material removal rate model is developed in terms of pad surface properties, and polishing experiments are conducted on Cu to validate the theoretical prediction that the asperity-flattened pads not only reduce the pad scratching but also improve the material removal rate.

Thesis Supervisor: Jung-Hoon Chun
Title: Professor of Mechanical Engineering

Thesis Supervisor: Nannaji Saka
Title: Research Affiliate, Department of Mechanical Engineering

Acknowledgments

I would like to thank all the people who supported and guided me through my past three years at MIT. This thesis would not have been possible without their contributions.

First of all, my utmost gratitude goes to my thesis advisors, Professor Jung-Hoon Chun and Dr. Nannaji Saka, who gave me the opportunity to be a member of the CMP research group. Their guidance and advises throughout the research were invaluable not only to this thesis but also to my development as an engineer and as a researcher. I would like to specifically thank Prof. Chun for his continuous efforts to make me develop a broader view of things. Also, I particularly thank to Dr. Saka for spending an enormous amount of time with me to discuss every technical detail and to instruct me the appropriate research attitude for a better scholar. I will not forget what I have learned from them for the rest of my professional life. In addition, I wish to express my gratitude to Professor Duane Boning, my thesis committee member. His many valuable comments have significantly improved this thesis.

Second, I wish to thank the former members of the CMP research group, Thor Eusner and Michael Roberts, for their prior work on the research project and for all the discussion and help on managing the equipment in the Tribology lab.

Third, I thank all the staff members at MIT who have helped me to use the research facilities: Dr. Alan Schwartzman in the NanoLab, Patrick Boisvert, Libby Shaw and Tim McClure in the Center of Materials Science and Engineering, and Pierce Hayward in the Department of Mechanical Engineering. I thank the staff members at Graduate student office in Department of Mechanical Engineering: Leslie Regan, Joan Kravit and Una Sheehan. Also, I thank the staff members at Laboratory for Manufacturing and Productivity for their administrational help: David Rodriguera, Kierstin Wesolowski, Carissa Leal and Corey Hains.

I wish to acknowledge the financial support of the Samsung Electronics Corporation. Thanks are due Dr. Sung-Ho Shin, Dr. Ji-Chul Yang, Dr. Seoung-Man Lee and Dr. Joo-Chul Han for their valuable comments and providing the materials on this research. In addition, I would like to acknowledge Dr. Taewook Hwang at Saint-Gobain Abrasives for sharing the experimental work.

I also thank all my friends in the Korean Graduate Student Association – Mechanical Engineering, who have made my time in Boston less stressful.

Finally, I thank my parents, Jin Kim and Hyungrae Park, who always show their endless love on me and encourage me to try out my own life. I also want to thank my grandmother, my brother and his family, for their love and support. And most of all, I give my special thank to Jihyun Kim for her constant love.

Table of Contents

Title page 1
Abstract 3
Acknowledgements 5
Table of Contents 7
List of Figures 11
List of Tables 21

CHAPTER 1. INTRODUCTION **25**
- 1.1. Background 25
- 1.2. The process of CMP 32
- 1.3. Scratching mechanisms in CMP 35
- 1.4. Thesis organization 37
- References 39

CHAPTER 2. MODELING PAD SCRATCHING: EFFECTS OF MECHANICAL AND TRIBOLOGICAL PROPERTIES **43**
- 2.1. Introduction 43
- 2.2. Pad scratching models: single-asperity sliding contact 44
  - 2.2.1. Mean contact pressure under a single asperity 44
  - 2.2.2. Mean contact pressure at the onset of surface layer yielding 47
  - 2.2.3. Scratching criteria 50
  - 2.2.4. Scratch-regime maps 54
- 2.3. Pad scratching models: multi-asperity sliding contact 56
  - 2.3.1. Relative proportions of pad asperity deformation modes 57
  - 2.3.2. Proportion of scratching asperities in contact 61
- 2.4. Characterization of surface properties 64
- 2.5. Pad sliding experiments on monolithic surface layers 68
- 2.6. Summary 78
- Nomenclature 80
- References 82

CHAPTER 3. SCRATCHING OF PATTERNED CU/DIELECTRIC SURFACES BY PAD ASPERITIES **85**
3.1. Introduction 85
3.2. Theory of scratching of interconnects and dielectrics 87
3.2.1. Scratching of monolithic Cu and dielectric layers 88
3.2.2. Scratching of patterned Cu/dielectric layers 90
3.3. Sliding experiments on patterned Cu/dielectric layers 95
3.3.1. Solid polymer pins 95
3.3.2. Monolithic and patterned surface layers 100
3.3.3. Experimental apparatus and determination of friction coefficient 100
3.3.4. Results and discussion 104
3.4. Pad sliding experiments on patterned Cu/dielectric layers 108
3.5. Summary 116
Nomenclature 118
References 119

CHAPTER 4. MITIGATION OF PAD SCRATCHING BY TOPOGRAPHY CONTROL **121**
4.1. Introduction 121
4.2. The effect of pad topography on scratching 121
4.3. Pad topography control by asperity-flattening 123
4.3.1. Compression by a smooth, flat plate 126
4.3.2. Rolling/sliding by a smooth roller 130
4.4. Sliding experiments using asperity-flattened pads 130
4.5. Summary 138
Nomenclature 139
References 140

CHAPTER 5. THE ROLE OF PAD ASPERITIES IN MATERIAL REMOVAL **141**
5.1. Introduction 141
5.2. Material removal by single-asperity sliding contact 143
5.2.1. Particle-layer contact 145
5.2.2. Asperity-particle contact 149
5.2.3. Number of particles at single-asperity sliding contact 152
5.2.4. Material removal rate by single-asperity sliding contact 153

5.3. Material removal by multi-asperity sliding contact 156
5.3.1. Contact area ratio between pad and wafer 157
5.3.2. Relative proportions of asperities in "low-pressure" and in "high-pressure" contact 160
5.3.3. Overall material removal rate 165
5.4. Polishing experiments using asperity-flattened pads 168
5.5. Summary 172
Nomenclature 174
References 176

CHAPTER 6. CONCLUSION 179
6.1. Summary 179
6.2. Suggestions for future work 182

APPENDIX A. SURFACE TOPOGRAPHY OF CMP PADS 185

APPENDIX B. MECHANICAL PROPERTIES OF CMP PADS, SURFACE LAYERS, AND POLYMER PINS 197

APPENDIX C. ANALYTICAL DERIVATION OF MAXIMUM VON MISES STRESS IN AN ELASTIC HALF-SPACE UNDER FRICTIONAL CONTACT 209
C.1. Stress field in an elastic half-space 209
C.2. Estimation of maximum Von Mises stress 213
Nomenclature 221
References 222

APPENDIX D. EFFECTS OF GRIT SIZE AND SHAPE ON PAD TOPOGRAPHY IN DIAMOND CONDITIONING 223

APPENDIX E. METHODS OF FLATTENING PAD ASPERITIES 229

E.1. Compression by a smooth, flat metal plate 229

E.2. Rolling/sliding by a smooth metal roller 231

E.3. Sliding a smooth metal torus 237

APPENDIX F. PAD SLIDING EXPERIMENTS USING ASPERITY-FLATTENED PADS ON PATTERNED CU/DIELECTRIC LAYERS 241

APPENDIX G. POLISHING EXPERIMENTS USING ASPERITY-FLATTENED PADS ON CU SURFACE LAYERS 253

List of Figures

Figure 1.1.	The number of components per integrated circuit over time [Moore, 1965].	26
Figure 1.2.	The number of transistors per microprocessor chip versus time showing introduction of new enabling technologies [Cavin III *et al.*, 2012].	26
Figure 1.3.	A schematic cross-sectional view of a three-level metallization scheme. The concept can be extended to any number of levels in a multilevel scheme [Murarka, 1997].	27
Figure 1.4.	Cross-section of a device with 12 metal interconnect layers [IBM].	27
Figure 1.5.	Schematics of (a) interlevel dielectric (ILD) planarization and (b) shallow trench isolation processes.	29
Figure 1.6.	Schematics of (a) damascene and (b) dual-damascene processes.	30
Figure 1.7.	Ultraplanar aluminum mirror array fabricated by CMP: (a) Schematic of manufacturing process and (b) SEM image of Al mirror array [Ganguly and Krusius, 2004].	31
Figure 1.8.	Schematic of the CMP process.	33
Figure 1.9.	Low-*k* dielectric roadmap [ITRS 2012].	34
Figure 1.10.	Modulus and Hardness of low-*k* dielectric thin films [Volinsky and Gerberich, 2003].	34
Figure 1.11.	Three contact modes and scale of scratches in CMP.	36

Figure 2.1. Surface tractions under a single asperity sliding contact in different asperity deformation modes: elastic ($0 \leq \delta < \delta_y$), elastic but at the onset of asperity yielding ($\delta = \delta_y$), elastic-plastic ($\delta_y < \delta < \delta_{f\text{-}p}$) and fully-plastic ($\delta_{f\text{-}p} \leq \delta$). 45

Figure 2.2. Normalized mean asperity contact pressure at the onset of surface layer yielding under Hertzian and uniform pressure distribution. 51

Figure 2.3. Scratch regime maps for extreme cases of elastically and plastically deforming pad asperities: (a) elastic, but at the onset of yielding and (b) fully-plastic. 55

Figure 2.4. Deformation modes of exponentially distributed asperity heights. 58

Figure 2.5. Proportions of asperity deformation modes, elastic and plastic, according to plasticity index, ψ. 60

Figure 2.6. Proportion of asperities in contact that can scratch the surface layer, n_s/n_c, versus the scratching index, α_p, at different values of plasticity index, ψ. 65

Figure 2.7. Surface profiles of CMP pads: (a) pad A and (b) IC1000 pad. 66

Figure 2.8. Determined probability densities and the standard deviations of asperity heights: (a) pad A and (b) IC1000 pad. Solid lines are the probability density functions of an exponential distribution based on the determined standard deviations. 67

Figure 2.9. Probability density of log normalized nano-hardness for pad A and IC1000 pad. H_a* is the normalized asperity hardness and σ* is the standard deviation of the normalized asperity hardness: (a) pad A and (b) IC1000 pad. 70

Figure 2.10. Probability density of nano-hardness of Al and Cu surface layers: (a) Al layer and (b) Cu layer. 70

Figure 2.11. Reciprocating sliding apparatus. 71

Figure 2.12. (a) Scratch-regime map for pad A and (b) SEM images of the surface layers after the pad sliding experiments using pad A. 73

Figure 2.13. (a) Scratch-regime map for IC1000 pad and (b) SEM images of the surface layers after the pad sliding experiments using IC1000 pad. 74

Figure 2.14. Normalized number of scratches versus the scratching index, α_p. The points present average values and the bars the standard errors. 77

Figure 3.1. SEM images of patterned Cu/low-*k* surface layers after the pad sliding experiments: (a) using IC1000 pad and (b) using commercial pad A. 86

Figure 3.2. Schematic of contact between a random, rough pad and a smooth flat surface layer. 89

Figure 3.3. Modes of asperity contact and the surface tractions under each asperity deformation modes: (a) no contact ($z_a < d$), (b) elastic contact ($0 \leq \delta < \delta_y$), (c) elastic contact but at the onset of asperity yielding ($\delta = \delta_y$), (d) elastic-plastic contact ($\delta_y < \delta < \delta_{f\text{-}p}$), and (e) fully-plastic contact ($\delta_{f\text{-}p} \leq \delta$). 89

Figure 3.4. Scratch-regime map for a fully-plastically deformed asperity. 91

Figure 3.5. Two extreme cases of asperity contact on composite Cu/dielectric layers: (a) features wider than the contact diameter ($w_{cu} > 2a_c$ and $w_d > 2a_c$) and (b) features much narrower than the contact diameter ($w_{cu} << 2a_c$ and $w_d << 2a_c$). 92

Figure 3.6. Schematic of iso-strain compression of a composite layer. 94

Figure 3.7. Schematic of single-asperity sliding experiment. 96

Figure 3.8. Probability density of hardness for (a) PS and (b) PMMA pins. 99

Figure 3.9. Schematic of contact between the solid polymer pin, at the extreme cases of deformation, and the surface layer: (a) elastic, but at the onset of yielding and (b) fully-plastic. 99

Figure 3.10. Images of a PMMA pin (a) before and (b) after applying a normal load of 1N. 101

Figure 3.11. Probability density of hardness values of monolithic layers. 102

Figure 3.12. Scratch-regime map for PMMA pin and monolithic Cu, low-*k*, SiO_2 layers. The SEM images are the surfaces of the monolithic layers after the pin sliding experiments: (a) Scratch-regime map, (b) PMMA | Cu, (c) PMMA | Low-*k*, and (d) PMMA | SiO_2. 105

Figure 3.13. Scratch-regime map for PS pin and monolithic Cu, low-*k* layers. The SEM images are the surfaces of the monolithic layers after the pin sliding experiments: (a) Scratch-regime map, (b) PS | Cu, and (c) PS | Low-*k*. 106

Figure 3.14. Scratch-regime map for PMMA pin and monolithic Cu, SiO_2 layers. The SEM images are the surfaces of the patterned Cu/SiO_2 layers with wide lines (w_{Cu} > 1 μm and w_d > 1 μm) after the pin sliding experiments: (a) Scratch-regime map, (b) PMMA | Pattern S1, (c) PMMA | Pattern S2, and (d) PMMA | Pattern S3. 107

Figure 3.15. Scratch-regime map for PMMA, PS pins and monolithic Cu, low-*k* layers. The SEM images are the surfaces of the patterned Cu/low-*k* layers with wide lines (w_{Cu} > 1 μm and w_d > 1 μm) after the pin sliding experiments: (a) Scratch-regime map, (b) PMMA | Pattern K1, and (c) PS | Pattern K1. 109

Figure 3.16. Scratch-regime map for PMMA pin and composite Cu/low-k, Cu/SiO_2 layers. The SEM images are the surfaces of the patterned Cu/low-k and Cu/SiO_2 layers with narrow lines ($w_{Cu} < 1$ μm and $w_d < 1$ μm) after the pin sliding experiments: (a) Scratch-regime map, (b) PMMA | Pattern K2, (c) PMMA | Pattern K3, and (d) PMMA | Pattern S4. 111

Figure 3.17. Scratch-regime map for PS pin and composite Cu/low-k layers. The SEM images are the surfaces of the patterned Cu/low-k layers with narrow lines ($w_{Cu} < 1$ μm and $w_d < 1$ μm) after the pin sliding experiments: (a) Scratch-regime map, (b) PS | Pattern K2, and (c) PS | Pattern K3. 112

Figure 3.18. Scratch-regime map for the pads (IC1000 pad and pad A) and monolithic layers (Cu and low-k). The SEM images are the surfaces of the patterned Cu/low-k layers with relatively wide lines ($w_{Cu} = 4.5$ μm and $w_d = 1$ μm) after the pad sliding experiments: (a) Scratch-regime map, (b) IC1000 | Cu/low-k, and (c) pad A | Cu/low-k. 114

Figure 3.19. Scratch-regime map for the pads (IC1000 pad and pad A) and composite Cu/low-k layers. The SEM images are the surfaces of the patterned Cu/low-k layers with relatively narrow lines ($w_{Cu} = 0.05$ μm and $w_d = 0.05$ μm) after the pad sliding experiments: (a) Scratch-regime map, (b) IC1000 | Cu/low-k, and (c) pad A | Cu/low-k. 115

Figure 4.1. Proportion of plastically deformed asperities versus $1/\psi^2$. 124

Figure 4.2. SEM image of a new IC1000 pad. 124

Figure 4.3. Surface profile of a new IC1000 pad; $R_a = 23.5$ μm, $\sigma_z = 4.0$ μm. 125

Figure 4.4. Schematic of asperity-flattening process by compression. 127

Figure 4.5. Experimental system for asperity-flattening by compression: (a) photograph and (b) schematic. 128

Figure 4.6. Surface profiles of asperity-flattened IC1000 pads by compression: (a) compression at 25 °C; R_a = 39.5 μm, σ_z = 3.9 μm, and (b) compression at 185 °C; R_a = 173.4 μm, σ_z = 1.7 μm. 129

Figure 4.7. Schematic of asperity-flattening processes by rolling/sliding. 131

Figure 4.8. Photograph of experimental system for asperity-flattening by rolling/sliding. 131

Figure 4.9. Surface profiles of asperity-flattened IC1000 pads by rolling/sliding: (a) rolling at 25 °C; R_a = 57.8 μm, σ_z = 3.7 μm, (b) rolling at 185 °C; R_a = 106.9 μm, σ_z = 3.4 μm, and (c) sliding at 25 °C; R_a = 57.8 μm, σ_z = 3.3 μm. 132

Figure 4.10. Normalized number of scratches after pad sliding experiments versus $1/\psi^2$. The points represent the average values and the bars the standard error. 135

Figure 4.11. Photograph and schematic of a face-up polisher. 136

Figure 4.12. Material removal rate using new and asperity-flattened IC1000 pads. The asperities were flattened by sliding a roller over the pad. 136

Figure 4.13. Schematic of *in-situ* asperity-flattening CMP system. 137

Figure 5.1. Schematic of contact between a rough pad and smooth, flat surface: (a) microscopic view of the contact represented as multiple pad asperities in contact with the flat surface, and (b) nano-scale view of the contact that shows the nano-sized particles trapped under each asperity contact. 144

Figure 5.2. Schematic of scratching on surface layer by a hard abrasive particle. 146

Figure 5.3. Cross-section of the scratch generated by a spherical particle showing pile-up. 148

Figure 5.4. Formation of thin film on the surface layer by chemical reaction in CMP. 148

Figure 5.5. Development of asperity-particle contact under increased asperity contact pressure, p_a: (a) under low contact pressure ($p_a < p_c$), (b) under critical contact pressure ($p_a = p_c$), and (c) under high contact pressure ($p_a > p_c$). 150

Figure 5.6. Contact pressure and area at an asperity contact: (a) small approach of distant points ($\delta < \delta_c$) and (b) large approach of distant points ($\delta \geq \delta_c$). 155

Figure 5.7. Contact area ratio between a rough pad and a smooth, flat surface versus plasticity index, at p = 35 kPa and H_a = 290 MPa. 161

Figure 5.8. Relative proportions of asperities with "low-pressure" ($p_a < p_c$) and with "high-pressure" ($p_a \geq p_c$). 162

Figure 5.9. Estimated relative proportions of asperities in contact with "low-pressure" ($p_a < p_c$) and with "high-pressure" ($p_a \geq p_c$) versus plasticity index, at C_{vol} = 0.1 which corresponds to $C_c^{1/2}$ = 0.45. 163

Figure 5.10. Normalized height reduction rate of surface layer versus plasticity index, at ζ = 0.01, H_a = 293 MPa, H_l^* = 1.5 GPa, p_a = 35 kPa (5 psi), and C_{vol} = 0.1. 167

Figure 5.11. Experimental face-up CMP polishing tool. 169

Figure 5.12. Results of the Cu polishing experiments according to the plasticity index, ψ. Grey line is the estimated normalized thickness reduction rate of surface layer versus plasticity index, when ζ = 0.01, H_a = 293 MPa, H_l^* = 1.5 GPa, p_a = 35 kPa (5 psi), and C_{vol} = 0.1. 171

Figure A.1. Tencor P16 Profilometer. 186

Figure A.2. Surface profiles of (a) new, (b) broken-in, and (c) used Pad A. 187

Figure A.3. Surface profiles of (a) new, (b) broken-in, and (c) used IC1000 pads. 191

Figure B.1. Hysitron Triboindenter TI 900. 198

Figure C.1. Elastic half-space under normal and tangential tractions. 210

Figure C.2. Pressure distribution of fully-plastically deformed pad asperity under frictionless contact: (a) the pressure is uniform inside the contact area (discontinuous pressure distribution) and (b) the pressure is uniform except in an annulus at the edge where the pressure gradually decreases to zero (continuous pressure distribution). 214

Figure C.3. Normalized normal stresses, σ_x/p and σ_y/p, at the trailing edge as a function of normalized boundary width, where pressure decreases to zero, for different coefficients of friction and $\nu = 0.33$: (a) in the x-direction and (b) in the y-direction. 217

Figure C.4. Normalized maximum von Mises stress, σ_M / p, as a function of Poisson's ratio, ν.: (a) $\varepsilon / a = 0.1$ and (b) $\mu = 0.4$. 217

Figure C.5. Normalized maximum von Mises stress, σ_M / p, as a function of normalized boundary width, ε/a, for different coefficients of friction, μ. 219

Figure C.6. Normalized maximum von Mises stress, σ_M/p, as a function of the coefficient of friction, μ. The lines show the values for different normalized boundary widths, ε/a, and the X points indicate the results of finite element analysis [Eusner, 2010]. 219

Figure D.1. Surface profiles of the IC1000 pads after diamond conditioning: (a) pad D1, and (b) pad D4. 225

Figure D.2. Surface profiles of the IC1000 pads after diamond conditioning: (a) pad D5, and (b) pad D6. 226

Figure D.3. Height distribution of pad surfaces after diamond conditioning: (a) pad D1, (b) pad D4, (c) pad D5, and (d) pad D6. 227

Figure E.1. Asperity-flattening by compressing with a smooth, flat plate. 230

Figure E.2. Schematic of "asperity-flattening" using a smooth, flat plate that has the same radius as that of the pad. 232

Figure E.3. Schematic of "asperity-flattening" using a smooth, flat plate that has a smaller radius than that of the pad. 232

Figure E.4. Schematic of in-situ "asperity-flattening" in CMP using a smooth, flat disk. 233

Figure E.5. "Asperity-flattening" process by rolling/sliding using a smooth roller. 233

Figure E.6. Schematic of "asperity-flattening" using a smooth roller. 235

Figure E.7. Top view of the rigid metal rollers: (a) cylindrical roller and (b) cone-shaped roller. 235

Figure E.8. Top view of the combinations of short rollers: (a) cylindrical roller and (b) cone-shaped roller. 236

Figure E.9. Schematic of in-situ "asperity-flattening" using a smooth roller. 236

Figure E.10. Schematic of a diamond conditioner with a smooth, rigid torus attached at the circumference for in-situ asperity-flattening. 238

Figure E.11. Schematic of in-situ pad conditioning and asperity-flattening by a hybrid conditioner. 239

Figure F.1. Photograph and schematic of the face-up polisher. 242

Figure F.2. Patterned layers within the controlled area in each die. The shaded area is the "polished" region on the faced-up polisher. 243

Figure F.3. Images of patterned Cu/low-*k* layers after pad sliding experiments using a new IC1000 pad. 245

Figure F.4. Images of patterned Cu/low-*k* layers after pad sliding experiments using a new Pad A. 245

Figure F.5. Thirty-two sets of patterned layers within the "polished" region. 246

Figure F.6. Total number of scratched, patterned blocks after "polishing" experiments using new and "asperity-flattened" pads. 251

Figure G.1. Mass of the wafer with Cu surface layer before and after 2 min polishing on a face-up polisher. 254

List of Tables

Table 2.1. Statistical results of pad topography. 67

Table 2.2. Statistical results of mechanical properties. 69

Table 2.3. Estimated plasticity indices and relative proportions of asperity deformation modes of Pad A and IC1000. 71

Table 2.4. Scratching indices and results of sliding experiments between pads and surface layers. 75

Table 3.1. Statistical results of determined mechanical properties of polymer pins (LDPE, PP, PTFE, HDPE, PS, PC, and PMMA) and CMP pads (IC1000 and Pad A). 97

Table 3.2. Statistical results of determined mechanical properties of monolithic surface layers. 102

Table 3.3. Linewidths of tested patterned Cu/dielectric layers. 103

Table 3.4. Estimated effective hardness of Cu/dielectric composite. 110

Table 4.1. Topographical parameters and mechanical properties of an IC1000 CMP pad, and of a monolithic Cu layer. 125

Table 4.2. Asperity radius, standard deviation of asperity heights, their ratio, and the estimated plasticity indices of new and "broken-in" IC1000 pads (E_a / H_a = 7.6). 127

Table 4.3. Asperity radius, standard deviation of asperity heights, and their ratio of IC1000 pads (E_a / H_a = 7.6). Also listed are the number of scratches generated by the pads on a Cu layer in sliding experiments. 133

Table 5.1. Experimental conditions for Cu polishing experiments. 169

Table 5.2.	Asperity radius, standard deviation of asperity heights, and their ratio of IC1000 pad (E_a / H_a = 7.6). Also listed are the material removal rate (MRR) and the normalized MRR.	170
Table A.1.	Experimental conditions for pad topography characterization.	186
Table A.2.	Roughness parameters of new, broken-in and used Pad A. All measurements are in μm.	188
Table A.3.	Asperity height, radius and spacing of new, broken-in, and used Pad A.	189
Table A.4.	Roughness parameters of new, broken-in and used IC1000 pads. All measurements are in μm.	192
Table A.5.	Asperity height, radius, and spacing of new, broken-in, and used IC1000 pads.	193
Table A.6.	Roughness parameters of IC1000 pads before and after asperity flattening. All measurements are in μm.	195
Table A.7.	Asperity height, radius, and spacing of IC1000 pads after flattened by compression using a flat plate and rolling/sliding using a smooth roller.	196
Table B.1.	Experimental conditions for Young's modulus and hardness determination.	198
Table B.2.	Young's modulus and hardness of new, broken-in, and used Pad A.	199
Table B.3.	Young's modulus and hardness of new, broken-in, and used IC1000 pads.	201
Table B.4.	Young's modulus and hardness of Al and Cu layers.	203
Table B.5.	Young's modulus and hardness of low-k A, B, and C layers.	204
Table B.6.	Young's modulus and hardness of SiO_2, Si_3N_4 and TiN layers.	205

Table B.7.	Young's modulus and hardness of polymer pins (LDPE, PP, PTFE and HDPE).	206
Table B.8.	Young's modulus and hardness of polymer pins (PS, PC, and PMMA).	207
Table C.1.	Results of finite element analysis for normalized maximum shear stress, τ_{max} / p, and normalized maximum von Mises stress, σ_M / p [Eusner, 2010].	220
Table D.1.	Process conditions for pad conditioning.	224
Table D.2.	Properties of IC 1000 pads before and after conditioning using conditioners with different diamond shapes and sizes.	224
Table F.1.	Experimental conditions for "polishing" experiments on a face-up polisher.	242
Table F.2.	Linewidthes and pattern density of patterned Cu/low-*k* layers.	244
Table F.3.	Scratched patterned blocks after the "polishing" experiments using a new IC1000 pad.	247
Table F.4.	Scratched patterned blocks after the "polishing" experiments using an "asperity-flattened" IC1000 pad.	248
Table F.5.	Scratched patterned blocks after the "polishing" experiments using a new Pad A.	249
Table F.6.	Scratched patterned blocks after the "polishing" experiments using an "asperity-flattened" Pad A.	250
Table G.1.	Calculated thickness reduction rate of Cu layer after polishing experiments.	255

CHAPTER 1

INTRODUCTION

1.1. Background

An integrated circuit, commonly referred to as an IC, is a microscopic array of electronic circuits and components that have been fabricated in the surface of a semiconducting material, such as silicon. The impact of ICs on modern life can be found in all aspects from entertainment media, electronics and wireless equipment to aerospace communication and cutting-edge scientific applications.

In the late 1950s when the first IC chips were created, they were composed of only a few components [Wallmark, 1960; Murphy, 1964]. In 1965, Dr. Gordon E. Moore postulated that the number of components per chip will approximately double every year, Figure 1.1 [Moore, 1965]. Though the historic data, Figure 1.2, shows that the number has doubled roughly every two years, the trend has persisted for more than fifty years from then, and now the number of components in an IC chip is more than a billion [Mack, 2011; Cavin III *et al.*, 2012; ITRS 2012].

The challenge for the semiconductor manufacturing industry to continue the trend is not just increasing the number but also reducing the size of the features. In order to accomplish both, the products should have smaller devices and denser packing, as well as more levels of wiring and therefore more levels of photolithography. That is, continued shrinking of the devices demands multilevel interconnections (MLI) in which the metal interconnections are isolated by the insulating dielectric layers interconnected by the wiring in three-dimensions, Figure 1.3 [Murarka, 1997]. As more layers are built on the silicon surface, however, it was found that non-planarity can cause severe problems [Kuo, 1987]. To planarize the micro-featured surfaces, accordingly, several techniques were suggested between the late 1980s and early 1990s, such as pulsed laser [Tuckerman

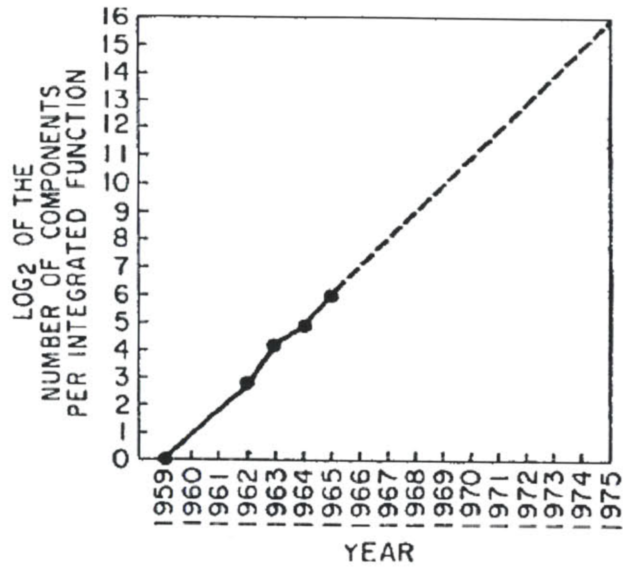

Figure 1.1. The number of components per integrated circuit over time [Moore, 1965].

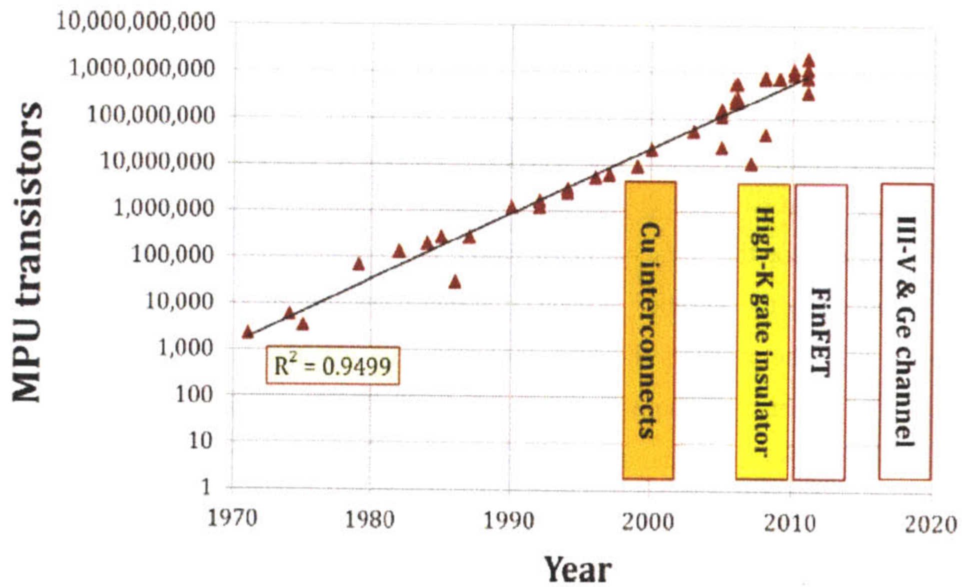

Figure 1.2. The number of transistors per microprocessor chip versus time showing introduction of new enabling technologies [Cavin III *et al.*, 2012].

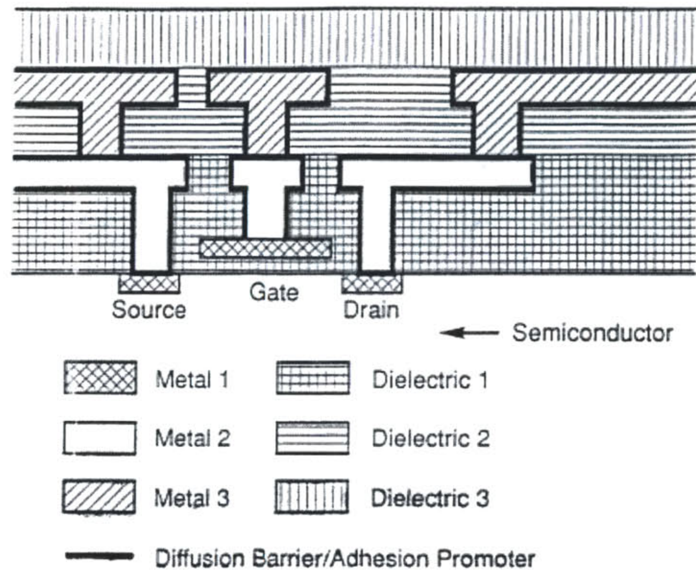

Figure 1.3. A schematic cross-sectional view of a three-level metallization scheme. The concept can be extended to any number of levels in a multilevel scheme [Murarka, 1997].

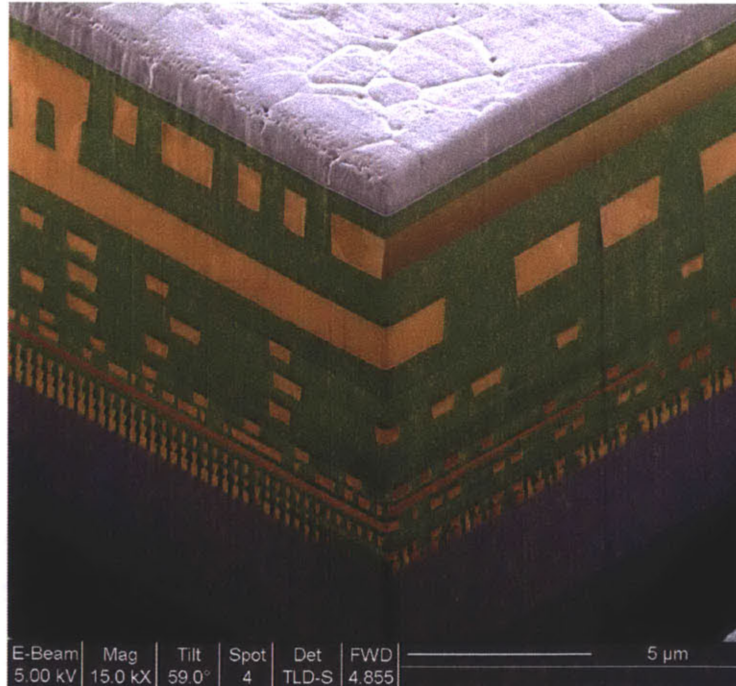

Figure 1.4. Cross-section of a device with 12 metal interconnect layers [IBM].

and Weisberg, 1986; Boeck *et al.*, 1990], selective electroless metal deposition [Wei *et al.*, 1988], resist etch-back [Somero, 1993], spin on glass [Bacchetta *et al.*, 1993], gap-filling [Bar-Ilan and Gutmann, 1995], and chemical-mechanical polishing (CMP). Among those, CMP has become the dominant planarization technology in semiconductor manufacturing, providing excellent local and global planarization on both metal interconnects and dielectrics [Davarik *et al.*, 1989; Malik and Hasan, 1995; Perry, 1998; Zantye *et al.*, 2004]. Current manufacturing technologies in the semiconductor industry along with CMP enable one to build more than a dozen interconnect levels above the device level, Figure 1.4.

CMP was originally developed from substrate manufacturing in the 1980s by IBM [Medel, 1967]. It was first used to planarize SiO_2 interlayer dielectrics (ILD), Figure 1.5a, reducing the surface roughness to submicron- or to nano-scale [Patrick, 1991]. The planarization process was further advanced to the device level by the development of shallow trench isolation (STI) technology [Nandakumar *et al.*, 1998], Figure 1.5b. While the ILD CMP comprises polishing only a single material, in STI CMP more than one material, such as SiO_2 and Si_3N_4, are concurrently polished. As the width of the metal interconnects continuously shrank to about 130 nm, Cu began to replace Al because of its significantly lower resistivity and its high immunity to electro-migration. Cu is difficult to be etched, however. Therefore, damascene technology was developed in Cu interconnect fabrication [Kaanta *et al.*, 1991; Wrschka *et al.*, 2000]. In the damascene process, copper is first deposited into ILD trenches by electrochemical deposition or electroplating, and the overburdened copper is removed by CMP, Figure 1.6. The Cu interconnects have now gained wide acceptance in the microelectronics industry [Gambino *et al.*, 2009].

In addition, many applications other than IC manufacturing, such as microelectromechanical systems (MEMS), require a precise planarization process, and CMP, therefore, is widely used in such fields [Sneigowski, 1996]. For instance, Ganguly and Krusius fabricated a high-planarity microdisplay mirror array using a concept of an encapsulation CMP, Figure 1.7 [Ganguly and Krusius, 2004], and Kourouklis *et al.* used CMP in high aspect ratio Su-8/permalloy structures [Kourouklis *et al.*, 2003]. CMP is also used for hard disk drive (HDD) manufacturing [Lei and Luo, 2004].

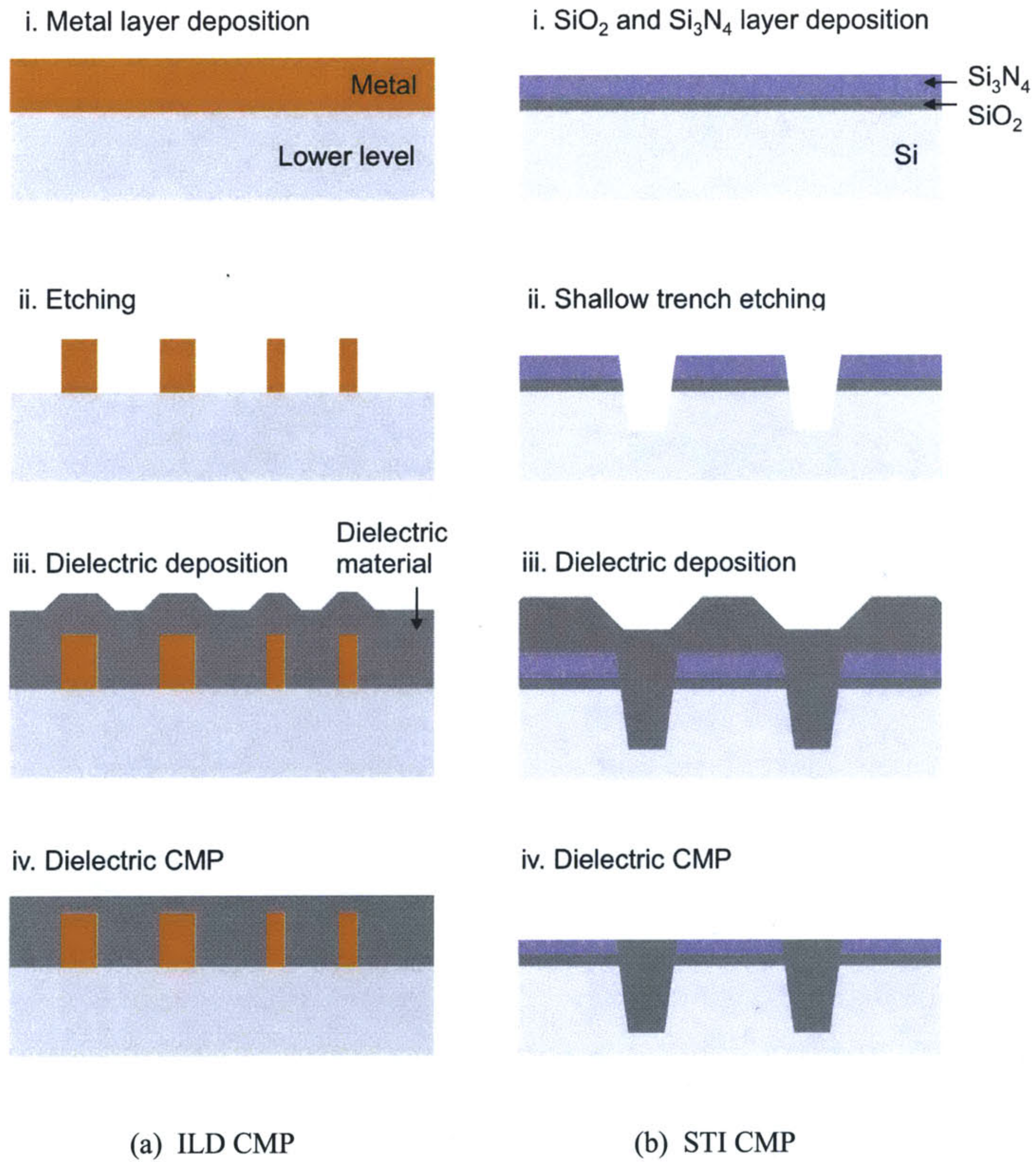

Figure 1.5. Schematics of interlevel dielectric (ILD) planarization and shallow trench isolation processes.

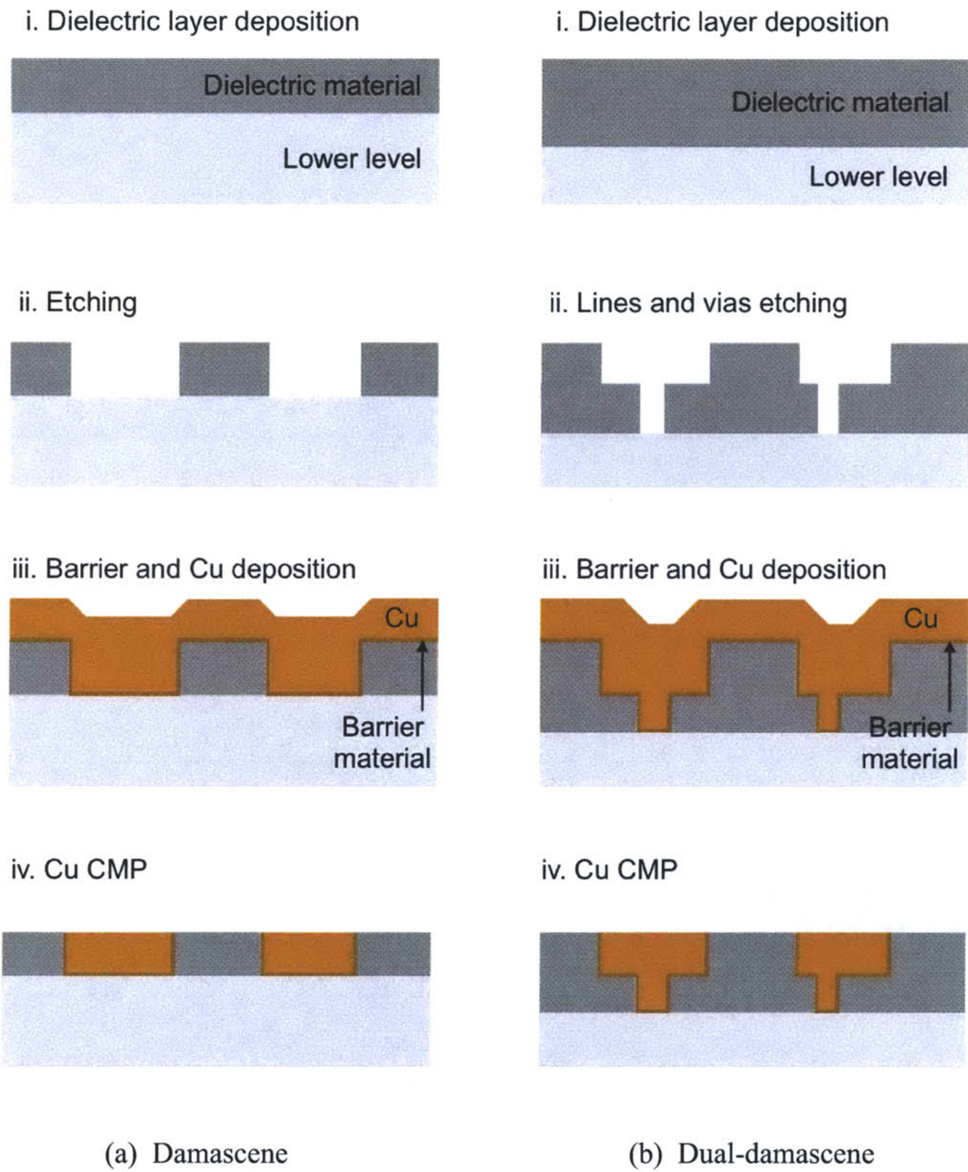

(a) Damascene (b) Dual-damascene

Figure 1.6. Schematics of damascene and dual-damascene processes.

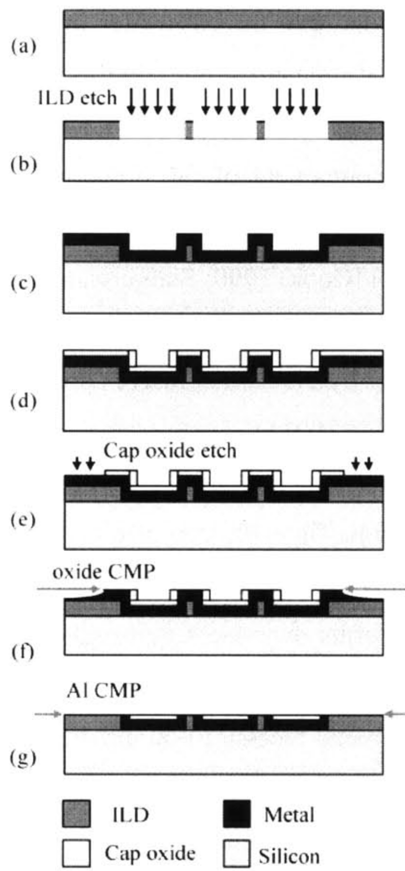

(a) Schematic of manufacturing process

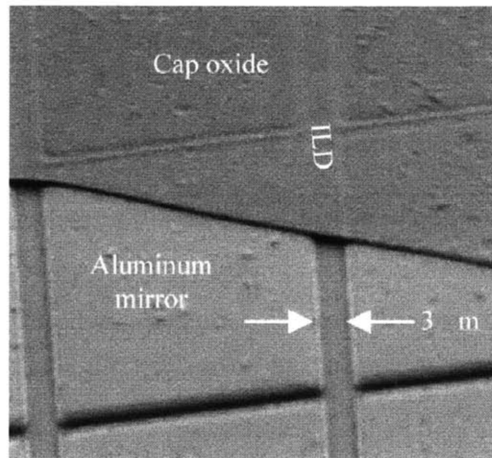

(b) SEM image of Al mirror array

Figure 1.7. Ultraplanar aluminum mirror array fabricated by CMP [Ganguly and Krusius, 2004].

1.2. The process of CMP

The CMP process is conducted, in general, by forcing a rotating wafer against a rotating polishing pad, at a selected load, Figure 1.8. Polishing slurry, which contains abrasive particles and chemicals, is continuously provided into the pad-wafer interface. Despite its apparent simplicity, the material removal, planarization, and polishing mechanisms in CMP are highly complex—basically due to the combined action of chemical and mechanical phenomena. The chemical component of the process is the reaction of the wafer surface with chemicals present in the slurry to form a softened surface layer for enhanced material removal rate (MRR) [Cook, 1990; Steigerwald *et al.*, 1995] and to prevent particle agglomeration [Biswas *et al.*, 2008]. The mechanical component of the process is the removal of the soft layer by the hard abrasives present in the slurry [Kaufman *et al.*, 1991; Liu *et al.*, 1996; Fu *et al.*, 2001].

In years past, the greatest challenges in CMP were polishing non-uniformity across the wafer and interconnect (Cu) dishing and dielectric erosion. The reduction of metal due to dishing results in increased line resistance. Dishing is mainly a problem for features with wide interconnect lines because the pad elastically deforms over the feature. Dielectric erosion is more widespread in features with a high area density of metal, compared with the dielectric, because of the increased pressure (due to metal recession) on the dielectric, and thus higher dielectric material removal rate [Park *et al.*, 2000; Lai *et al.*, 2002; Noh *et al.*, 2004]. In recent years, however, as the width of the Cu interconnects, or feature size, has shrunk to less than 60 nm, in part due to the high electrical conductivity and the high softening temperature of Cu, the traditional dielectric, SiO_2, is being replaced by the low-dielectric-constant (low-k) materials for faster signal propagation. The low-k dielectrics are both compliant and soft compared with SiO_2 and thus provide little protection against scratching of the wafer surface while being polished. As the demand for low dielectric constant, k, is expected to increase further, Figure 1.9 [ITRS, 2012], the dielectrics are becoming even more porous or soft, Figure 1.10 [Volinsky and Gerberich, 2003]. Therefore, micro- and nano-scale scratching of the planar and composite Cu/low-k surfaces has recently emerged as a dominant defect in CMP.

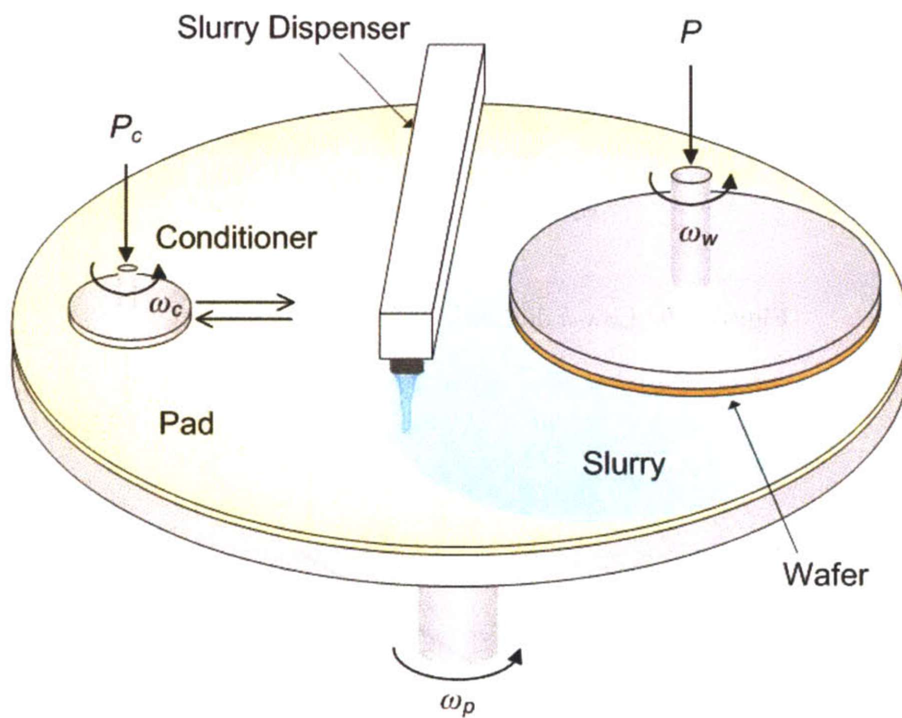

Figure 1.8. Schematic of the CMP process.

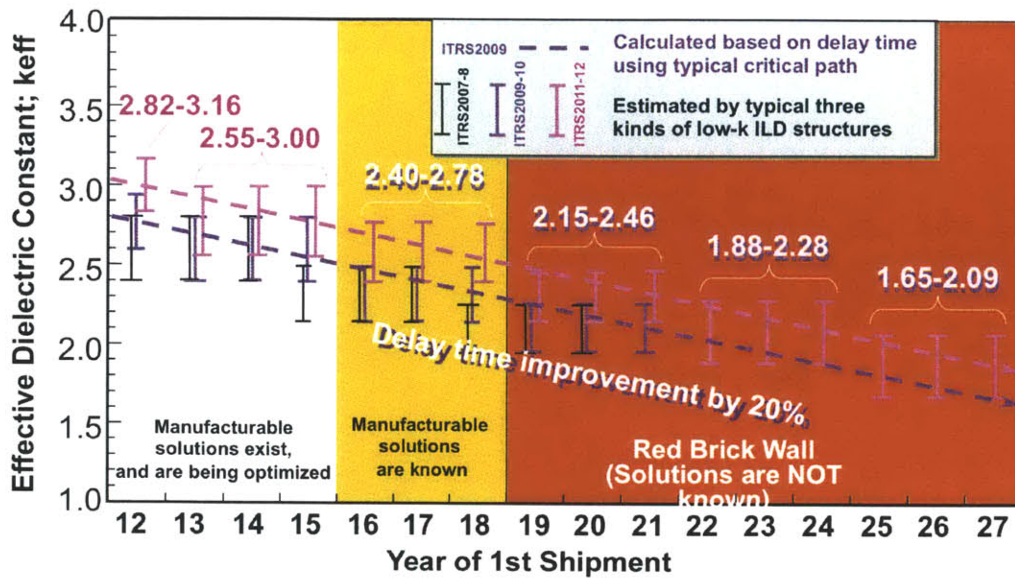

Figure 1.9. Low-*k* dielectric roadmap [ITRS 2012].

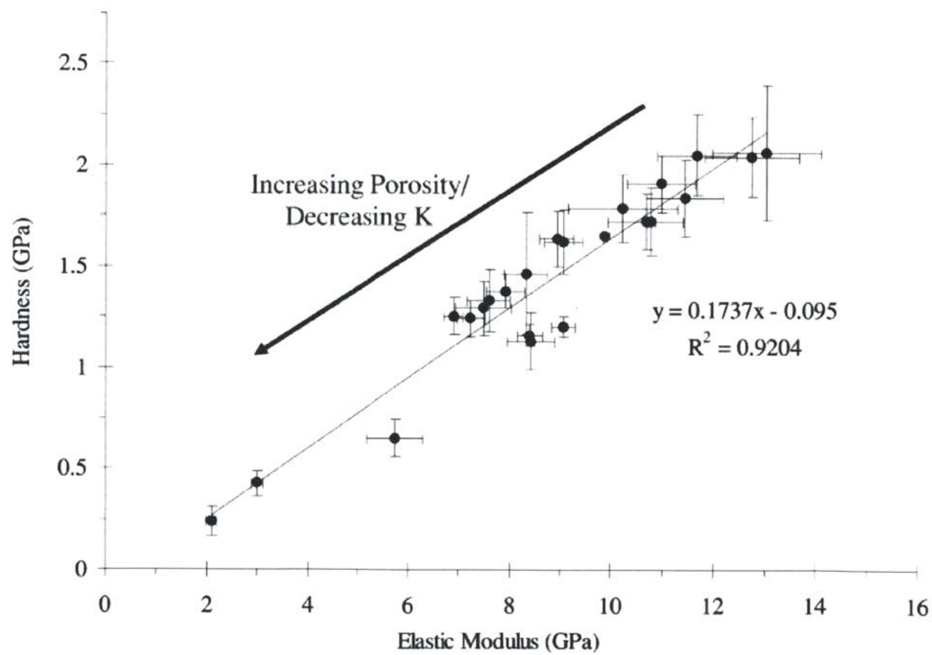

Figure 1.10. Modulus and hardness of low-*k* dielectric thin films [Volinsky and Gerberich, 2003].

1.3. Scratching mechanisms in CMP

Scratches generated by three different modes of contact in CMP are illustrated in Figure 1.11. CMP is carried out as the wafer moves over a polishing pad under applied pressure, while chemical slurry containing hard, abrasive particles is provided between the two surfaces. The fundamental mechanism of CMP is the accumulation of "fine scratches" continuously generated by the abrasive particles. The nano-sized particles, 50 – 300 nm in diameter, which are loaded by the pad asperities, may plow the surface layer which is softened by chemical reactions. Such scratches are preferred for polishing the top layer of the wafer at a few nanometer scale to result in smooth, flat surfaces.

During the polishing process, however, the small abrasives may agglomerate due to the fluctuations of slurry delivery and interparticle forces. The scratches generated by these agglomerated particles are surface defects, because the size of scratches increases by an order of magnitude compared with those created by the individual particles. The abnormally large, hard particles have been reported to be the primary sources of undesirable, defective scratching, which may cut the interconnection "wires" in IC chips and cause malfunctions in the microelectronic devices [Basim *et al.*, 2002; Chandra *et al.*, 2008; Saka *et al.*, 2008; Armini *et al.*, 2009; Eusner *et al.*, 2009; Choi *et al.*, 2009]. To minimize particle agglomeration, and thus mitigate such particle-induced scratching, particle interaction models as well as some practical methods, such as a magnetic-levitated centrifugal pump, have been developed and suggested [Chang *et al.*, 2009; Johnson and Boning, 2010].

Recently, it has been reported, however, scratches can be generated when the polymer pads are slid over the Cu layers without providing any abrasive particles between the two surfaces, which is the typical condition used in "abrasive-free CMP." [Balakumar *et al.*, 2005; Eusner *et al.*, 2011]. The experimental results show that not only the hard agglomerates but even the soft pad asperities themselves may also scratch the relatively hard surfaces. As the rough polymer pad is pressed against the relatively smooth, flat layer and slid over, under certain conditions the surface traction applied by the soft asperities can be large enough to initiate scratching [Eusner, 2010; Saka *et al.*, 2010].

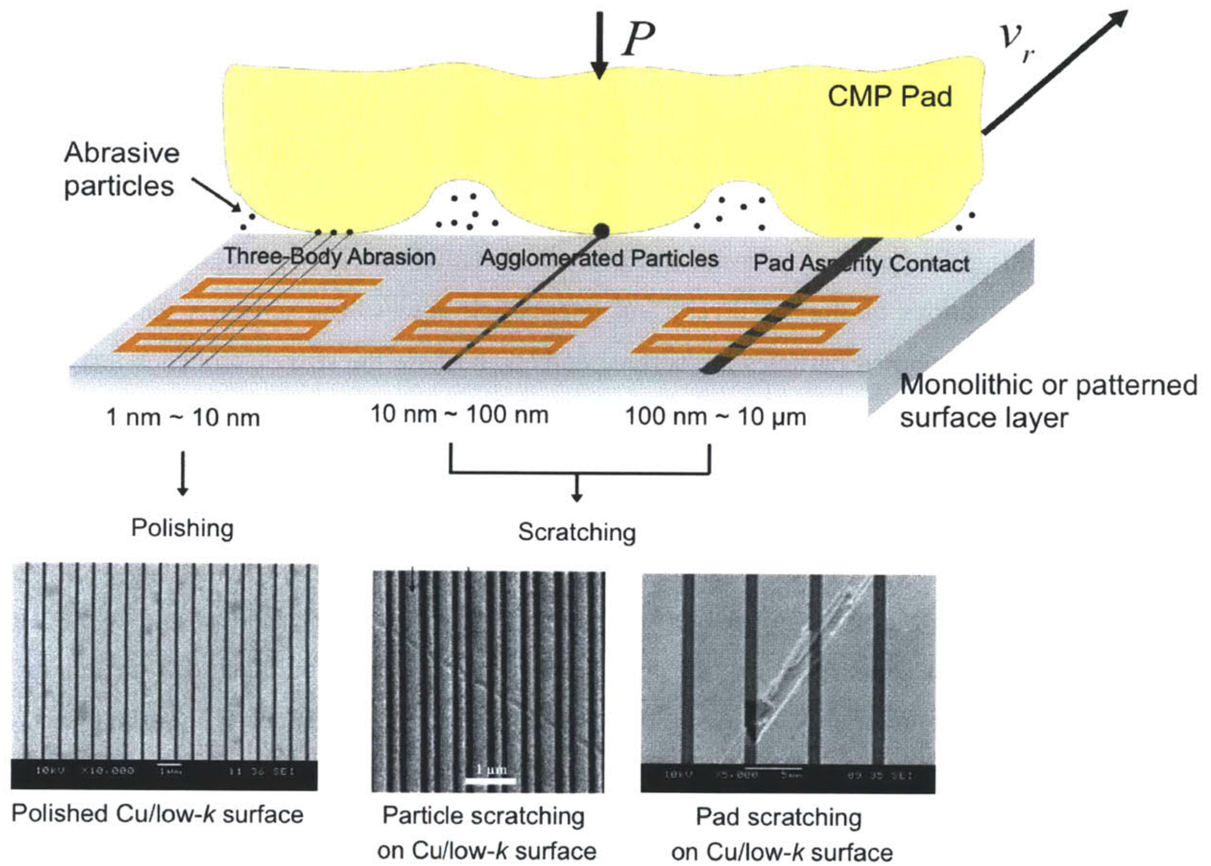

Figure 1.11. Three contact modes and scale of scratches in CMP.

Furthermore, since the size of the scratches generated by the asperities are the largest compared with those by the other two sources, pad scratching creates far more severe defects. Despite the potential of scratching by pad asperities, studies on pad scratching have not been widely reported in the literature.

1.4. Thesis organization

The overall goals of the thesis are to investigate the mechanisms and the statistical probability of scratching by soft pad asperities and to develop practical methods to mitigate scratching without deteriorating the material removal rate in CMP. In Chapter 1, background and organization of the thesis are described. Chapter 2 presents contact mechanics models of pad-induced scratching, and focuses on the effects of surface layer and pad asperity hardnesses and of interfacial friction on scratch generation. Scratch-regime maps are established to provide the criteria for whether the soft pad asperities can scratch the hard surface or not, and scratching indices are introduced to predict the probability of scratching asperities in contact. For experimental validations, two commercial CMP pads (IC1000 pad and Pad A) are slid over various thin films (Al, Cu, SiO_2, Si_3N_4, TiN and three low-*k* dielectrics) using deionized water as a "lubricant". In Chapter 3, scratching of Cu/dielectric line structures by the pad asperities are investigated. The scratching criteria and the scratch-regime maps constructed for monolithic layers are extended for patterned layers. Then sliding experiments are conducted on Cu/dielectric patterns of various linewidths using solid, polymer pins loaded to the fully-plastically deformed state. Specifically, the role of the width of Cu and dielectric lines, in comparison with the contact diameter, is examined. Chapter 4 studies the effect of pad topography on the number of scratching asperities. The key topographical parameter that promotes scratching is identified based on contact mechanics models by considering the random, rough surface of the pad. A novel, cost-effective process, asperity-flattening, is introduced to manipulate the identified parameters. Scratching mitigation by pad topography control is validated by experiments on the asperity-flattened pads. In Chapter 5, the role of pad asperities on material removal

is investigated. A new model for material removal rate is presented based on contact mechanics analysis between the asperity-particle and particle-layer under single-asperity sliding contact, and taking into account the statistical asperity height variation under multi-asperity contact. The model suggests that controlling the surface topography of the pad also improves the polishing rate. Cu polishing experiments using the asperity-flattened pads validates the theoretical predictions. Chapter 6 concludes the thesis and offers suggestions for future research.

References

Armini, S., Whelan, C.M., Moinpour, M. and Maex, K., 2009, "Copper CMP with composite polymer core-silica shell abrasives: a defectivity study," *J. Electrochem. Soc.*, vol. 156, no. 1, pp. H18-H26.

Bacchetta, M., Bacci, L., Iazzi, N., Liles, I. and Zanotti, L., 1993, "Spin on glass (SOG) – based planarization scheme compatible with a stacked via multilevel metal process," *Proc. SPIE Multilevel Interconnection*, vol. 2090, pp. 72-84.

Balakumar, S., Haque, T., Senthil Kumar, A., Rahman, M. and Kumar, R., 2005, "Wear phenomena in abrasive-free copper CMP process," vol. 152, no. 11, pp. G867-G874.

Bar-Ilan, A. H. and Gutmann, N., 1995, "A comparative study of sub-micro gap filling and planarization techniques," *Proc. SPIE Microelectronic Device and Multilevel Interconnection Technology*, vol. 2636, pp. 277-288.

Basim, G. B. and Moudgil, B. M., 2002, "Effect of soft agglomerates on CMP slurry performance," *J. Colloid and Interface Sci.*, vol. 256, pp. 137-142.

Biswas, R., Han, Y., Karra, P., Sherman, P. and Chandra, A., 2008, "Diffusion-limited agglomeration and defect generation during chemical mechanical planarization," *J. Electrochem. Soc.*, vol. 155, no. 8, pp. D534-D537.

Boeck, B. A., Fu, K. Y., Pintchovski, F. and Crain, N., 1990, "Evaluation of laser planarized second aluminum for semiconductor devices," *IEEE VLSI Multilevel Interconnection Conf.*, pp. 90-96, Santa Clara, CA.

Cavin III, R. K., Lugli, P. and Zhirnov, V. V., 2012, "Science and engineering beyond Moore's law," *Proc. of the IEEE*, vol. 100, pp. 1720-1749.

Chandra, A., Karra, P., Bastawros, A. F., Biswas, R., Sherman, P. J., Armini, S. and Lucca, D. A., 2008, "Prediction of scratch generation in chemical mechanical planarization," *Annals of the CIRP*, vol. 57, pp. 559-562.

Chang, F.-C., Tanawade, S. and Singh, R. K., 2009, "Effects of stress-induced particle agglomeration on defectivity during CMP of low-*k* dielectrics," *J. Electrochem. Soc.*, vol. 156, pp. H39-H42.

Choi, J. H. and Korach, C. S., 2009, "Nanoscale defect generation in CMP of low-*k*/copper interconnect patterns," *J. Electrochem. Soc.*, vol. 156, pp. H961-H970.

Cook, L. M., 1990, "Chemical process in glass polishing," *J. Non-Crystalline Solids*, vol. 120, pp. 152-171.

Davarik, B., Koburger, C. W., Schulz, R., Warnock, J. D., Furukawa, T., Jost, M., Taur, Y., Schwittek, W. G., DeBrosse, J. K., Kebaugh, M. L. and Mauer, J. L., 1989, "A new planarization technique, using a combination of RIE and chemical mechanical polish (CMP)," *IEEE Int. Electron Devices Meeting (IEDM)*, pp.61-64, Washington, DC.

Eusner, T., Saka, N., Chun, J.-H., Armini, S., Moinpour, M. and Fischer, P., 2009, "Controlling scratching in Cu chemical mechanical planarization," *J. Electrochem. Soc.*, vol. 156, no. 7, pp. H528-H534.

Eusner, T., 2010, "Multi-scale scratches in chemical-mechanical polishing," Ph.D. thesis, Department of Mechanical Engineering, MIT, Cambridge, MA.

Eusner, T., Saka, N. and Chun, J.-H., 2011, "Break-in a pad for scratch-free, Cu chemical-mechanical polishing," *J. Electrochem. Soc.*, vol. 158, no. 4, pp. H379-H389.

Fu, G., Chandra, A., Guha, S. and Subhash, G., 2001, "A plasticity-based model of material removal in chemical-mechanical polishing (CMP)," *IEEE Trans. Semicon. Manuf.*, vol. 14, no. 4, pp. 406-417.

Gambino, J., Chen, F. and He, J., 2009, "Copper interconnect technology for the 32 nm node and beyond," *IEEE Custom Integrated Circuits Conf. (CICC)*, pp. 141-148, San Jose, CA.

Ganguly, U. and Krusius, J. P., 2004, "Fabrication of ultraplanar aluminum mirror array by novel encapsulation CMP for microoptics and MEMS applications," *J. Electrochem. Soc.*, vol. 151, no. 11, pp. H232-H238.

International Technology roadmap for Semiconductors (ITRS), 2012.

Johnson, J. M. and Boning, D. S., 2010, "Slurry particle agglomeration model for chemical mechanical planarization (CMP)," *Mater. Res. Soc. Symp. Proc.*, vol. 1249, 1249-E04-03.

Kaanta, C. W., Bombardier, S. G., Cote, W. J., Hill, W. R., Kerszykowski, G., Landis, H. S., Poindexter, D. J., Pollard, C. W., Ross, G. H., Ryan, J. G., Wolff, S. and Cronin, J. E., 1991, "Dual Damascene: A ULSI wiring technology," *IEEE VLSI Multilevel Interconnection Conf.*, pp. 144-152, Santa Clara, CA.

Kaufman, F. B., Thompson, D. B., Broadie, R. E., Jaso, M. A., Guthrie, W. L., Pearson, D. J. and Small, M. B., 1991, "Chemical-mechanical polishing for fabricating patterned W metal features as chip interconnects," *J. Electrochem. Soc.*, vol. 138, no. 11, pp. 3460-3465.

Kourouklis, C., Kohlmeier, T. and Gatzen, H. H., 2003, "The application of chemical-mechanical polishing for planarizing a SU-8/permalloy combination used in MEMS devices," *Sensors and Actuators A*, vol. 106, pp. 263-266.

Kuo, Y., 1987, "Planarization of multilevel metallization processes: a critical review," *Proc. SPIE Adv. Process. of Semicond. Devices*, vol. 0797, pp. 49-60.

Lai, J.-Y., Saka, N. and Chun, J.-H., 2002 "Evolution of copper-oxide damascene structures in chemical mechanical polishing: II. Dishing and overpolishing," *J. Electrochem. Soc.*, vol. 149, pp. G41-G50.

Lei, H. and Luo, J., 2004, "CMP of hard disk substrate using a colloidal SiO_2 slurry: preliminary experimental investigation," *Wear*, vol. 257, pp. 461-470.

Liu, C.-W., Dai, B.-T., Tseng, W.-T. and Yeh, C.-F., 1996, "Modeling of the wear mechanism during chemical-mechanical polishing," *J. Electrochem. Soc.*, vol. 143, pp. 716-721.

Mack, B. A., 2011, "Fifty year of Moore's Law," *IEEE Trans. Semicond. Manuf.*, vol. 24, no. 2, pp. 202-207.

Malik, F. and Hasan, M., 1995, "Manufacturability of the CMP process," *Thin Solid Films*, vol. 270, pp. 612-615.

Medel, E., 1967, "Polishing of silicon," Solid State Technol., vol. 10, pp. 27-39.

Moore, G. E., 1965, "Cramming more components onto integrated circuits," *Electronics*, vol. 38, pp. 114-117.

Murarka, S. P., 1997, "Multilevel interconnections for ULSI and GSI era," *Mater. Sci. Eng.*, vol. R19, pp. 87-151.

Murphy, B. T., 1964, "Cost-size optima of monolithic integrated circuits," *Proc. of the IEEE*, vol. 52, no. 12, pp. 1537-1545.

Nandakumar, M., Chatterjee, A., Sridhar, S., Joyner, K., Rodder, M. and Chen, I.-C., 1998, "Shallow Trench Isolation for advanced ULSI CMOS technologies," *IEEE Int. Electron Devices Meeting (IEDM)*, pp. 133-136, San Francisco, CA.

Noh, K., Saka, N. and Chun, J.-H., 2004, "Effect of slurry selectivity on dielectric erosion and Cu dishing in copper chemical mechanical polishing", *Annals of the CIRP*, vol. 53, pp. 463-466.

Park, T., Tugbawa, T. and Boning, D., 2000, "Overview of methods for characterization of pattern dependencies in copper CMP," *Proc. CMP-MIC*, pp. 196-205, Santa Clara, CA.

Patrick, W. J., Guthrie, W. L., Standley, C. L. and Schiable, P. M., 1991, "Application of chemical mechanical polishing to the fabrication of VLSI circuit interconnections," *J. Electrochem. Soc.*, vol. 138, no. 6, pp. 1778-1784.

Perry, K. A., 1998, "Chemical mechanical polishing: the impact of a new technology on an industry," *Symp. VLSI Tech.*, pp. 2-5, Honolulu, HI.

Saka, N., Eusner, T. and Chun, J.-H., 2008, "Nano-scale scratching in chemical-mechanical polishing," *Annals of the CIRP*, vol. 57, pp. 341-344.

Saka, N., Eusner, T. and Chun, J.-H., 2010, "Scratching by pad asperities in chemical-mechanical polishing," *Annals of the CIRP*, vol. 59, pp. 329-332.

Sniegowski, J. J., 1996, "Chemical-mechanical polishing: enhancing the manufacturability of MEMS," *Proc. SPIE Micromachining Processes I*, vol. 2879, pp. 104-115.

Somero, B. M., 1993, "A modular in-situ integration scheme for deep submicron," *Proc. Int. VMIC*, pp 28-34.

Steigerwald, J. M., Murarka, S. P., Gutmann, R. J. and Duquette, D. J., 1995, "Chemical processes in the chemical mechanical polishing of copper," *Mater. Chem. Phys.*, vol. 41, pp. 217-228.

Tuckerman, D. B. and Weisberg, A. H., 1986, "Planarization of gold and aluminum thin films using a pulsed laser," *IEEE Electron Device Letters*, vol. 7, no. 1, pp. 1-4.

Volinsky, A. A. and Gerberich, W. W., 2003, "Nanoindentation techniques for assessing mechanical reliability at the nanoscale," *Microelectronic Eng.*, vol. 69, pp. 519-527.

Wallmark, J. T., 1960, "Design considerations for integrated electronic devices," *Proc. of the IRE*, vol. 48, no. 3, pp. 293-300.

Wei, C. S., Fraser, D. B., Wu, A. T., Paunovic, M. and Ting, C. H., 1988, "The use of selective electronless metal deposition for micro size contact fill," *IEEE Int. Electron Devices Meeting (IEDM)*, pp.446-449.

Wrschka, P., Hernandez, J., Oehrlein, G. S. and King, J., 2000, "Chemical mechanical planarization of copper damascene structures," *J. Electrochem. Soc.*, vol. 147, no. 2, pp. 706-712.

Zantye, P. B., Kumar, A. and Sikder, A. K., 2004, "Chemical mechanical planarization for micro electronics applications," *Mater. Sci. Eng. R.*, vol.45, pp. 89-220.

CHAPTER 2

MODELING PAD SCRATCHING: EFFECTS OF MECHANICAL AND TRIBOLOGICAL PROPERTIES

2.1. Introduction

In chemical-mechanical polishing, even the soft pad asperities may, under certain conditions, generate scratches on relatively hard surfaces. In this chapter, accordingly, contact mechanics models are presented to describe the scratching by soft pad asperities on the relatively hard surface layers. Based on the stress analysis under a single-asperity sliding contact, criteria for scratch initiation in different asperity deformation modes – elastic, elastic but at the onset of asperity yielding, elastic-plastic and fully-plastic – are first presented. In addition, scratch-regime maps for elastically and plastically deformed asperities, considering their extreme cases, are constructed in terms of the hardness ratio and the friction coefficient between the asperity and the surface layer. The pad scratching models are further advanced based on the assumption of exponentially distributed asperity heights. Proportion of scratching asperities in contact is estimated in terms of scratching indices, which characterize the effect of relative hardness and the interfacial friction on scratching. To validate the theoretical predictions, the nano-hardness of various thin films, such as Al, Cu, Si, SiO_2, TiN, and low-dielectric-constant (low-k) materials, are determined by nano-indentation. Then, pad sliding experiments are conducted on monolithic surface layers of these materials using two CMP pads, without any abrasive particles. Furthermore, the coefficient of friction between the pad asperities and the surface layers is concurrently measured during each sliding test. The scratches generated on the surface layers are examined and compared with the theoretical predictions based on the determined hardnesses and friction coefficients.

2.2. Pad scratching models: single-asperity sliding contact

As a single asperity is pressed against a smooth surface layer by a given asperity load, P_a, the asperity may experience four distinct deformation modes depending on the approach of distant points, δ [McCool, 1986; Zhao *et al.*, 2000]. When δ is small, the asperity deforms elastically. The onset of asperity yielding, the extremum of elastic deformation, may occur as δ reaches to the elastic limit, δ_y. Beyond the onset of yielding, the asperity deformation is composed of both elastic and plastic. Finally, fully-plastic deformation, the extremum of plasticity, occurs as δ exceeds a critical value of $\delta_{f\text{-}p}$. The contact pressure under the single asperity, accordingly, depends on δ, for given Young's modulus, E_a, hardness, H_a, and the radius, R_a, of the asperity. Moreover, as the asperity begins to slide over the surface layer, shear stresses will appear on the surface due to the interfacial friction. Assuming that the tangential traction is proportion to the normal pressure at every point inside the contact area, the tangential traction can also be determined by δ, if the coefficient of friction between the two surfaces is additionally given. Figure 2.1 shows the four possible types of surface tractions under an asperity sliding contact depending on δ.

The following assumptions are made in the scratching model for a single asperity contact to be further developed:

i. Both the asperity and layer materials are homogeneous and isotropic.
ii. Young's modulus of surface layer is much greater than that of the asperity ($E_l >> E_a$).
iii. Peak of the asperity is spherical and has a radius of R_a.
iv. The strains in both the pad asperity and the surface layer are small.

2.2.1. Mean contact pressure under a single asperity

For an elastic contact between an asperity and a smooth, flat elastic body, the Hertz solution can be used [Hertz, 1882]. The mean contact pressure under an elastically deformed asperity is given as

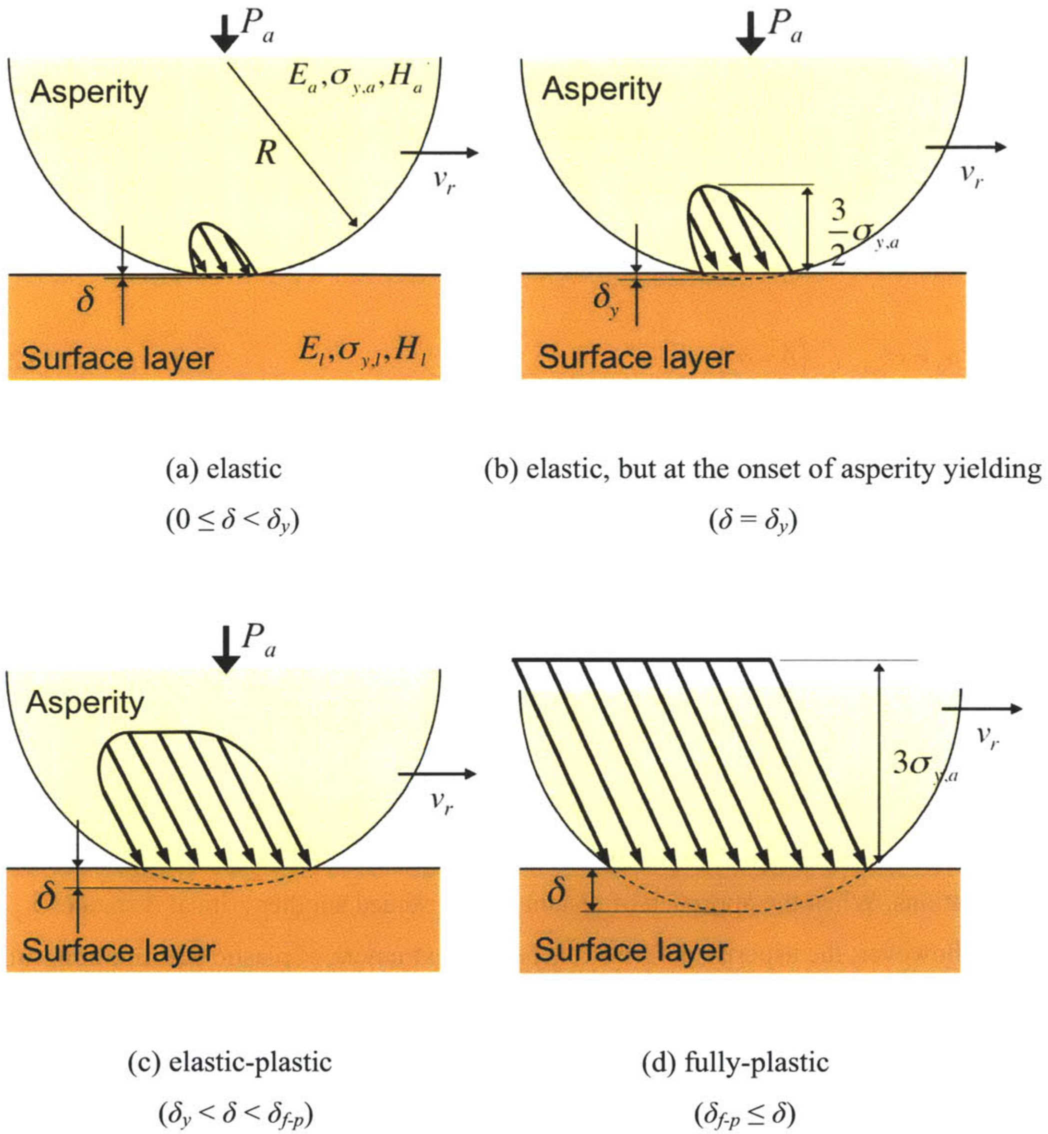

(a) elastic
($0 \leq \delta < \delta_y$)

(b) elastic, but at the onset of asperity yielding
($\delta = \delta_y$)

(c) elastic-plastic
($\delta_y < \delta < \delta_{f\text{-}p}$)

(d) fully-plastic
($\delta_{f\text{-}p} \leq \delta$)

Figure 2.1. Surface tractions under a single asperity sliding contact in different asperity deformation modes.

$$p_a = \frac{4}{3\pi} E_a \left(\frac{\delta}{R_a} \right)^{1/2} \quad , \quad \left(0 \le \delta < \delta_y \right) \tag{2.1}$$

The asperity deformation reaches its elastic limit when the maximum contact pressure, p_o, is about 1.5 times the yield stress of the asperity, $\sigma_{y,a}$ [Johnson, 1985]. The contact pressure distribution between two elastic bodies is Hertizan, and therefore, the mean pressure under elastically deformed asperity but at the onset of asperity yielding will be

$$p_a = \frac{2}{3} p_0 = \sigma_{y,a} \quad , \quad \left(\delta = \delta_y \right) \tag{2.2}$$

From Eqs. (2.1) and (2.2), the approach of distant points at the onset of asperity yielding, δ_y, can be given as

$$\delta_y = \frac{9\pi^2}{16} \left(\frac{\sigma_{y,a}}{E_a} \right)^2 R_a \tag{2.3}$$

Analysis of the pressure under an asperity contact beyond the elastic limit becomes quite complex, since the asperity deformation is composed of both elastic and plastic deformations. When the approach of distant points exceed another critical distance, $\delta_{f\text{-}p}$ (= $C_{f\text{-}p}\delta_y$), however, the asperity deforms reaches the extremum of plastic deformation, fully-plastic. The contact pressure under fully-plastically deformed asperity is then approximately uniform everywhere inside the contact, and the magnitude will be the hardness of the asperity, H_a, which is about three times its yield strength [Bhushan, 1996; Jayaweera *et al.*, 2003; Busby *et al.*, 2005]. The mean contact pressure under a fully-plastically deformed asperity, therefore, can be expressed as

$$p_a = H_a \cong 3\sigma_{y,a} \quad , \quad \left(\delta_{f\text{-}p} < \delta \right) \tag{2.4}$$

A number of attempts have been made to characterize the transitional regime from elastic to fully-plastic using mathematical functions and using finite element analysis [Ishigaki *et al.*, 1979; Yu and Blanchard, 1996; Chang *et al.*, 1987; Horng, 1998]. Zhao et al. suggested that the mean contact pressure can be represented by a logarithmic function based on the statistical analysis results of spherical indentations done by Francis [Francis, 1976; Zhao *et al.*, 2000]. Kogut and Etsion analyzed the problem by finite element methods and showed that the logarithmic function gives fairly close values than other theoretical models compared to their FEA results [Kogut and Etsion, 2002]. In logarithmic function formulation, the mean contact pressure under an elastic-plastically deformed asperity can be expressed as

$$p_a = \sigma_{y,a}\left[1 + 2\frac{\ln\left(\delta/\delta_y\right)}{\ln C_{f\text{-}p}}\right], \quad \left(\delta_y < \delta < \delta_{f\text{-}p}\right) \tag{2.5}$$

where $C_{f\text{-}p}$ is the factor approach of distant points at the onset of fully-plastic deformation, defined as $C_{f\text{-}p} = \delta_{f\text{-}p} / \delta_y$.

Based on the experimental results using a spherical indenter, Johnson revealed that the fully-plastically deformation is reached when the asperity load becomes 400 times greater than the yield load [Johnson, 1985]. From the elastic analysis, where the asperity load, P_a, is given as

$$P_a = \frac{4}{3} E_a R_a^{1/2} \delta^{3/2} \tag{2.6}$$

the approach of distant points at the onset of fully-plasticity is 54 times greater than that at the onset of asperity yielding; i.e. $C_{f\text{-}p}$ will be at least 54 [Zhao *et al.*, 2000].

2.2.2. Mean contact pressure at the onset of surface layer yielding

As an asperity is pressed against the surface layer and deforms elastically, the pressure distribution inside the contact area is known to be Hertzian. In addition, as the asperity

slides over, tangential traction is applied on the surface and its distribution will also be Hertzian. For frictionless or low frictional contact ($0 \leq \mu < 0.3$), the maximum shear stress, τ_{max}, in the surface layer under an Hertzian traction distribution locates below the surface and the normalized maximum shear stress is given by [Johnson, 1985; Eusner, 2010]:

$$\frac{\tau_{\max}}{p_a} = 0.46 \cong \frac{1}{2} \tag{2.7}$$

Using the Tresca yield criterion, the surface layer will yield if the maximum shear stress reaches half of the yield strength of the surface layer, $\sigma_{y,l}$. That is, the mean contact pressure at the onset of surface layer yielding, p_s, under elastically deformed asperity will be

$$p_s = \sigma_{y,l} \quad , \quad (0 \leq \mu < 0.3) \tag{2.8}$$

As the interfacial friction increases, however, the shear stress at the surface rapidly rises and the maximum shear stress locates no longer beneath the surface. It has been revealed by Hamilton and Goodman that when the coefficient of friction becomes greater than 0.3, the location of the maximum Von Mises stress moves to the surface [Hamilton and Goodman, 1966; Hamilton, 1983]. Based on the closed-form, analytic solution, the normalized maximum Von Mises stress, $\sigma_{M,max}$, in a elastic body under Hertizian traction distribution is given by

$$\frac{\sigma_{M,\max}}{p_a} = \left[\frac{9\pi^2}{256}\left(16 - 4\upsilon_l + 7\upsilon_l^2\right)\mu^2 + \frac{9\pi}{16}\left(1 - 2\upsilon_l\right)\left(2 - \upsilon_l\right)\mu + \frac{3}{4}\left(1 - 2\upsilon_l\right)^2\right]^{1/2} \tag{2.9}$$

Though Eq. (2.9) depends on the poisson's ratio of the surface layer, ν_l, the diffenece of the maximum Von Mises from $\nu_l = 0.1$ to 0.5, is not significant. Throughout this study, accordingly, Eq. (2.9) is simplified, when ν_l is 0.3, as

$$\frac{\sigma_{M,\max}}{p_a} = \left(5.35\mu^2 + 1.20\mu + 0.12\right)^{1/2} \tag{2.10}$$

Using the Von Mises yield criterion, the surface layer will yield if the maximum equivalent stress reaches to the yield stress of the surface layer. That is, the mean asperity contact pressure at the onset of surface layer yielding under elastically deformed asperity will be

$$p_s = \sigma_{y,l}\left(5.35\mu^2 + 1.20\mu + 0.12\right)^{-1/2} \quad , \quad \left(0.3 \le \mu\right) \tag{2.11}$$

As the asperity deforms fully-plastically, the traction distribution inside the contact becomes uniform. For frictionless or low frictional contact ($0 \le \mu < 0.05$), the maximum shear stress under uniform traction distribution in the surface layer locates below the surface and the normalized maximum shear stress can be given as [Love, 1929; Eusner, 2010]

$$\frac{\tau_{\max}}{p_a} = 0.325 \cong \frac{1}{3} \tag{2.12}$$

Using the Tresca yield criterion, the mean asperity contact pressure at the onset of surface layer yielding under fully-plastically deformed asperity will be

$$p_s = \frac{3}{2}\sigma_{y,l} \quad , \quad \left(0 \le \mu < 0.05\right) \tag{2.13}$$

When the coefficient of friction becomes greater than 0.05, however, Eusner revealed using finite element analysis that the location of the maximum Von Mises stress under uniform pressure distribution moves to the surface [Eusner, 2010]. Based on second-order polynomial regression of the FEA results, the magnitude of the normalized maximum von Mises stress in high friction is given by

$$\frac{\sigma_{M,\max}}{p_a} = \left(7.76\mu^2 + 0.76\mu + 0.41\right)^{1/2} \tag{2.14}$$

Therefore, using the Von Mises criterion, the mean contact pressure at the onset of surface layer yielding under fully-plastically deformed asperity will be

$$p_s = \sigma_{y,l}\left(7.76\mu^2 + 0.76\mu + 0.41\right)^{-1/2} \quad , \quad \left(0.05 \le \mu\right) \tag{2.15}$$

The normalized mean contact pressures at the onset of surface layer yielding under Hertzian and uniform traction distributions are plotted in Figure 2.2, according to the friction coefficient. For both cases, the layer yields beneath the surface when friction coefficient is low, and therefore, the effect of interfacial friction on layer yielding is neglegible. However, as the friction coefficient increases, the layer yields at the surface, and therefore, friction becomes significant.

The analysis of the stress field in the surface layer under the elastic-plastically deformed asperity is more complicated than those under elastically and fully-plastically deformed asperities, since the pressure distribution inside the contact continuously changes as δ increases, from Hertzian to uniform. It should be noted that, however, at high frictional contact ($\mu \geq 0.3$), difference in the magnitude between these two extreme cases is small, less than fifteen percent. The normalized mean contact pressure at the onset of surface layer yielding under elastic-plastically deformed asperity, accordingly, can be approximated assuming the pressure distribution to be either Hertzian or uniform.

2.2.3. Scratching criteria

Scratching on the surface layer may initiate by the onset of yielding. Therefore, an asperity in sliding contact will scratch the surface layer only if the mean contact pressure, p_a, exceeds a critical limit, p_s, mean contact pressure at the onset of surface layer yielding.

First, under an elastically deformed asperity ($0 \leq \delta < \delta_y$), from Eqs. (2.1), (2.8) and (2.11), the scratch criteria can be given as

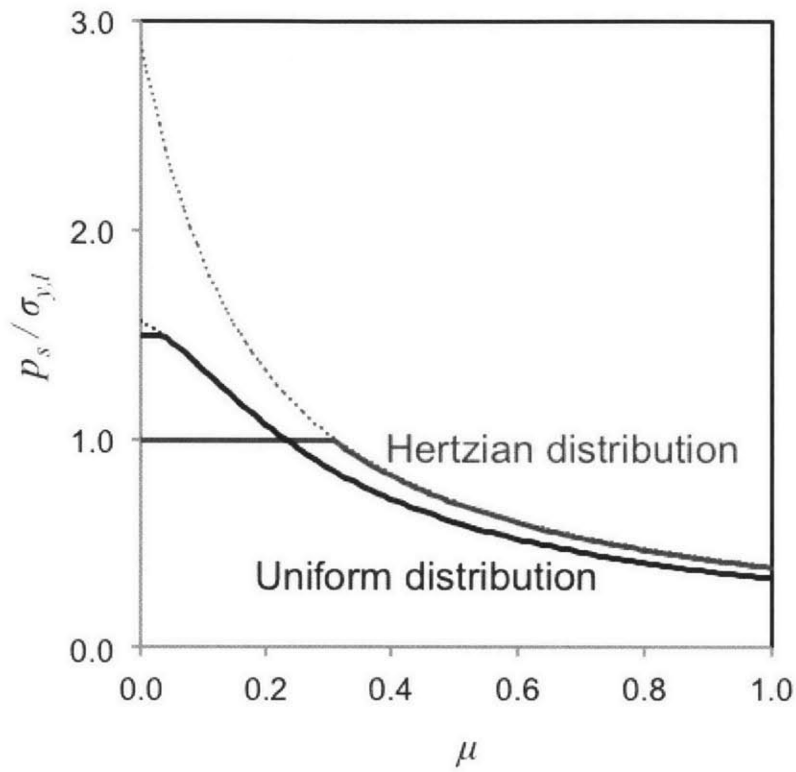

Figure 2.2. Normalized mean asperity contact pressure at the onset of surface layer yielding under Hertzian and uniform pressure distribution.

$$\delta \geq \frac{9\pi^2}{16}\frac{\sigma_{y,l}^2}{E_a^2}R_a \quad , \quad (0 \leq \mu < 0.3) \tag{2.16-a}$$

$$\delta \geq \frac{9\pi^2}{16}\frac{\sigma_{y,l}^2}{E_a^2}R_a\left(5.35\mu^2 + 1.20\mu + 0.12\right) \quad , \quad (0.3 \leq \mu) \tag{2.16-b}$$

Equation (2.16) indicates that an elastically deformed asperity can scratch the layer if the approach of distant points, δ, is greater than a certain limit determined by the modulus and radius of the asperity, the yield strength of the surface layer, and the friction coefficient. The scratching criteria can be simply rewritten as

$$\delta \geq \delta_{s,e} \tag{2.17}$$

where $\delta_{s,e}$ is approach of distant points at the onset of surface layer yielding under an elastically deformed asperity in sliding contact, defined from Eq. (2.16) as

$$\delta_{s,e} = \begin{cases} \dfrac{9\pi^2}{16}\dfrac{\sigma_{y,l}^2}{E_a^2}R_a & , \quad (0 \leq \mu < 0.3) \\ \dfrac{9\pi^2}{16}\dfrac{\sigma_{y,l}^2}{E_a^2}R_a\left(5.35\mu^2 + 1.20\mu + 0.12\right) & , \quad (0.3 \leq \mu) \end{cases} \tag{2.18}$$

In the extreme of elastic asperity deformation, i.e., under an elastically deformed asperity but at the onset of asperity yielding ($\delta = \delta_y$), from Eqs. (2.2), (2.8) and (2.11), the scratch criteria can be given as

$$1 \geq \frac{\sigma_{y,l}}{\sigma_{y,a}} \quad , \quad (0 \leq \mu < 0.3) \tag{2.19-a}$$

$$1 \geq \frac{\sigma_{y,l}}{\sigma_{y,a}}\left(5.35\mu^2 + 1.20\mu + 0.12\right)^{-1/2} \quad , \quad (0.3 \leq \mu) \tag{2.19-b}$$

At this extreme case of elastic contact, the condition whether the asperity can scratch the surface only depends on both yield strengths of asperity and surface layer, and the friction coefficient.

Under elastic-plastically deformed asperity ($\delta_y < \delta < \delta_{f\text{-}p}$), assuming that the contact pressure distribution is uniform and the magnitude equals to the mean contact pressure given as Eq. (2.5), from Eqs. (2.9) and (2.12), the scratch criteria can be given as

$$\delta \geq \delta_y \exp\left\{2\left[\frac{3}{2}\frac{\sigma_{y,l}}{\sigma_{y,a}} - 1\right]\right\} \ , \quad (0 \leq \mu < 0.05) \tag{2.20-a}$$

$$\delta \geq \delta_y \exp\left\{2\left[\frac{\sigma_{y,l}}{\sigma_{y,a}}\left(7.76\mu^2 + 0.76\mu + 0.41\right)^{-1/2} - 1\right]\right\} \ , \quad (0.05 \leq \mu) \tag{2.20-b}$$

where the approach of distant points at the onset of asperity yielding, δ_y, is given in Eq. (2.3). An elastic-plastically deformed asperity, accordingly, can scratch the layer if the approach of distant point, δ, is greater than a certain limit determined by the modulus, yield strength and radius of the asperity, the yield strength of the surface layer, and the friction coefficient. The scratching criteria can be again rewritten as

$$\delta \geq \delta_{s,p} \tag{2.21}$$

where $\delta_{s,p}$ is approach of distant points at the onset of surface layer yielding under an elastic-plastically deformed asperity in sliding contact, defined from Eq. (2.21) as

$$\delta_{s,p} = \begin{cases} \delta_y \exp\left\{2\left[\frac{3}{2}\frac{\sigma_{y,l}}{\sigma_{y,a}} - 1\right]\right\} & , \quad (0 \leq \mu < 0.05) \\ \delta_y \exp\left\{2\left[\frac{\sigma_{y,l}}{\sigma_{y,a}}\left(7.76\mu^2 + 0.76\mu + 0.41\right)^{-1/2} - 1\right]\right\} & , \quad (0.05 \leq \mu) \end{cases} \tag{2.22}$$

Finally, in the extreme of plastic asperity deformation, i.e., under fully-plastically deformed asperity ($\delta_{f\text{-}p} \leq \delta$), from Eqs. (2.4), (2.9) and (2.12), the scratch criteria can be given as

$$1 \geq \frac{1}{2}\frac{\sigma_{y,l}}{\sigma_{y,a}} \quad , \quad (0 \leq \mu < 0.05) \tag{2.23-a}$$

$$1 \geq \frac{1}{3}\frac{\sigma_{y,l}}{\sigma_{y,a}}\left(7.76\mu^2 + 0.76\mu + 0.41\right)^{-1/2} \quad , \quad (0.05 \leq \mu) \tag{2.23-b}$$

At this extreme case of plastic contact, similar to that of elastic contact, the condition whether the asperity can scratch the surface only depends on both yield strengths of asperity and surface layer, and the friction coefficient.

2.2.4. Scratch-regime maps

It is important to notice that the scratching criteria for the extreme cases of elastic and plastic deformations only depend on the mechanical properties and the interfacial friction. That is, both criteria are independent of geometrical parameters of the asperities. As the material hardness is about the three times its hardness, the scratching criteria for elastically deformed asperities can be expressed from Eq. (2.19) as a function of asperity-to-layer hardness ratio and the coefficient of friction as

$$\frac{H_a}{H_l} \geq 1 \quad , \quad (0 \leq \mu < 0.3) \tag{2.24-a}$$

$$\frac{H_a}{H_l} \geq \left(5.35\mu^2 + 1.20\mu + 0.12\right)^{-1/2} \quad , \quad (0.3 \leq \mu) \tag{2.24-b}$$

Accordingly, a scratch-regime map can be constructed with the ratio of pad hardness to layer hardness and with the coefficient of friction as coordinates, Figure 2.3a [Eusner, 2010; Saka *et al.*, 2010]. The map primarily provides that whether an asperity in sliding contact can scratch the surface layer at the state of elastic deformation. If pad-to-layer

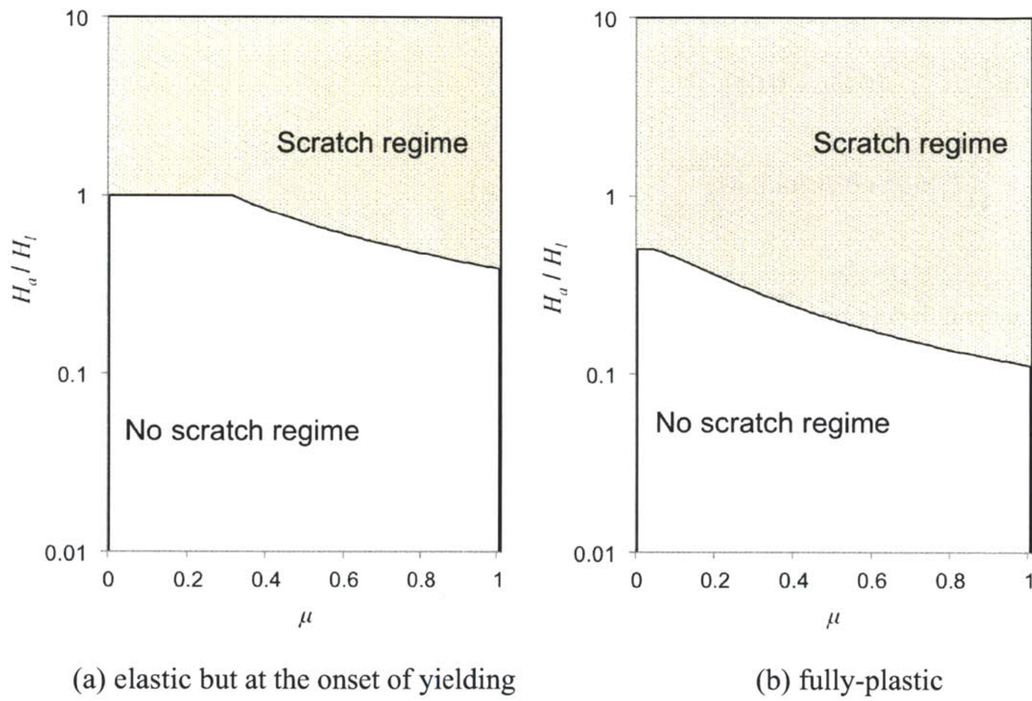

(a) elastic but at the onset of yielding

(b) fully-plastic

Figure 2.3. Scratch-regime maps for extreme cases of elastically and plastically deformed pad asperities.

hardness and friction coefficient fall in 'scratch regime,' an elastically deformed asperity but at the onset of yielding will scratch the surface layer whereas an elastically deformed asperity may scratch the surface for those additionally satisfies Eq. (2.17). However, an elastically deformed asperity, even at the onset of asperity yielding, cannot scratch the surface layer, if the conditions fall in 'no-scratch regime.'

Similarly, the scratching criteria for plastically deformed asperities can be expressed from Eq. (2.23) as

$$\frac{H_a}{H_l} \geq \frac{1}{2} \quad , \quad (0 \leq \mu < 0.05) \tag{2.25-a}$$

$$\frac{H_a}{H_l} \geq \frac{1}{3}\left(7.76\mu^2 + 0.76\mu + 0.41\right)^{-1/2} \quad , \quad (0.05 \leq \mu) \tag{2.25-b}$$

and a scratch-regime map can be constructed as Figure 2.3b. If pad-to-layer hardness and friction coefficient fall in 'scratch regime,' a fully-plastically deformed asperity will scratch the surface layer whereas an elastic-plastically deformed asperity may scratch the surface for those additionally satisfies Eq. (2.21). However, a plastically deformed asperity, even at the fully-plastic deformation mode, cannot scratch the surface layer, if the conditions fall in 'no-scratch regime.'

2.3. Pad scratching models: multi-asperity sliding contact

Typically, the roughness of the pad surface is much higher than that of the surface layer being polished. Therefore, the contact between the two surfaces can be regard as contact between multi-asperities of a pad surface and a smooth flat surface [Greenwood and Williamson, 1966]. The following assumptions are made in the scratching model for multi-asperities to be further developed:

1. All asperities are homogeneous and isotropic.
2. All asperity peaks are spherical and have identical radius, R_a.

3. Asperities are so far apart that the interactions among asperity contacts can be neglected.
4. Asperity heights, z_a, are exponentially distributed.

Generally, asperity heights of CMP pads are normally or exponentially distributed [Sorooshian *et al.*, 2005; Fan, 2012; Vasilev *et al.*, 2013]. Though normal distribution may possibly give a better description of the topography, the exponential distribution has analytical advantages and gives similar results [Johnson, 1985; Vlassak, 2004].

2.3.1. Relative proportions of the pad asperity deformation modes

The probability density function of exponentially distributed asperity heights, $\phi(z_a)$, can be written as

$$\phi(z_a) = \frac{1}{\sigma_z}\exp\left(-\frac{z_a}{\sigma_z}\right) \tag{2.26}$$

where σ_z is the standard deviation of asperity heights.

As n asperities per unit area are pressed against the smooth, flat surface layer, only the asperities that are taller than the separation distance, d, will be in contact, as shown in Figure 2.4. Therefore, the number of asperities in contact per unit area, n_c, will be

$$n_c = n\int_d^\infty \phi(z_a)dz_a = n\exp\left(-\frac{d}{\sigma_z}\right) \tag{2.27}$$

Figure 2.4 shows the proportion of each asperity deformation mode depending on the approach of distant points, δ, which equals to $(z_a - d)$. Of the asperities in contact, the relatively small asperities, that have approach of distant points less than δ_y, determined by Eq. (2.3), will deform elastically, whereas the tall asperities, that have approach of distant points greater than δ_y, will deform plastically (i.e., elastic-plastic and/or fully plastic).

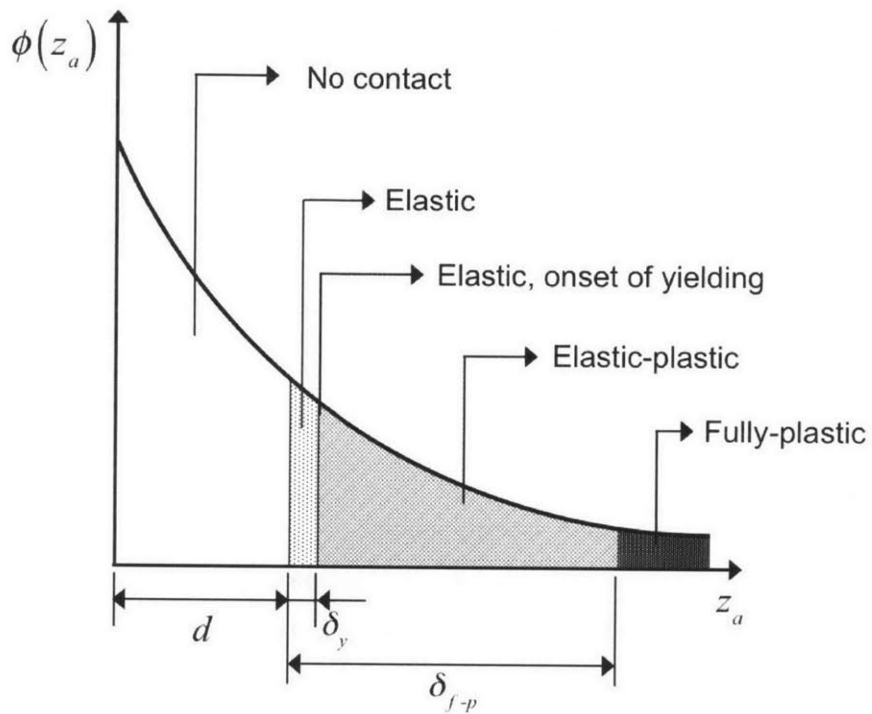

Figure 2.4. Deformation modes of exponentially distributed asperity heights.

Thus, the number of elastically and plastically deformed asperities per unit area, n_e and n_p, respectively, can be expressed as

$$n_e = n\int_d^{d+\delta_y} \phi(z_a)\,dz_a = n\exp\left(-\frac{d}{\sigma_z}\right)\left\{1-\exp\left(-\frac{\delta_y}{\sigma_z}\right)\right\} \tag{2.28-a}$$

$$n_p = n\int_{d+\delta_y}^{\infty} \phi(z_a)\,dz_a = n\exp\left(-\frac{d}{\sigma_z}\right)\exp\left(-\frac{\delta_y}{\sigma_z}\right) \tag{2.28-b}$$

Therefore, the proportion of elastically and plastically deformed asperities in contact can be given by

$$\frac{n_e}{n_c} = 1-\exp\left(-\frac{1}{\psi^2}\right) \tag{2.29-a}$$

$$\frac{n_p}{n_c} = \exp\left(-\frac{1}{\psi^2}\right) \tag{2.29-b}$$

where ψ is the plasticity index, which is defined as

$$\psi \equiv \left(\frac{\sigma_z}{\delta_y}\right)^{1/2} = \frac{4}{\pi}\frac{E_a}{H_a}\left(\frac{\sigma_z}{R_a}\right)^{1/2} \tag{2.30}$$

Thus, the relative proportions of elastic and plastic deformation of pad asperities depend solely on the plasticity index, which is determined by the ratio of asperity hardness to asperity modulus, H_a / E_a, and the ratio of asperity radius to the standard deviation of asperity heights R_a / σ_z. Based on Eq. (2.29), the probability of pad asperity deformation modes can be estimated once the plasticity index of the pad surface is known. As shown in Figure 2.5, approximately, unity of plasticity index is the transition from elastic-dominant contact to plastic-dominant contact. If the plasticity index of the pad surface is much less than unity, it may be assumed that most asperities in contact deform elastically. Then, Eq. (2.24) and Figure 2.3a should be considered as criteria for pad

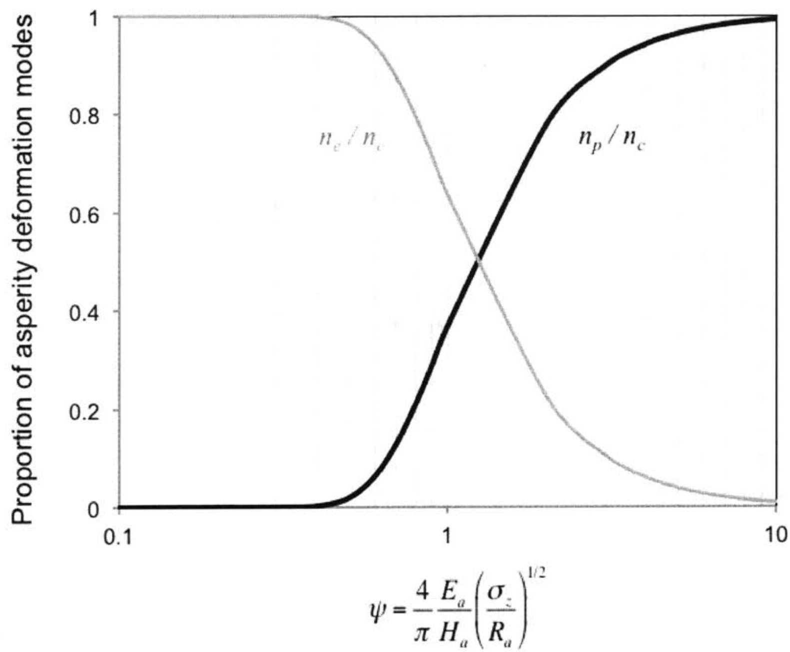

Figure 2.5. Proportions of asperity deformation modes, elastic and plastic, according to plasticity index, ψ.

scratching. On the other hand, if the plasticity index of the pad surface is greater than unity, a considerable number of asperities in contact will deform plastically, and therefore, Eq. (2.25) and Figure 2.3b should be the scratching criteria.

2.3.2. Proportion of scratching asperities in contact

Though the scratch-regime maps provide the criteria for given pad-to-layer hardness ratio and friction coefficient, they can only indicate whether the pad may scratch the surface layer or not. For a quantitative analysis of pad scratching, the models can be further advanced by estimating the relative proportion of asperities that can scratch the layer among those in contact.

When multiple asperities slide over the layer it is the approach of distant points, δ (= $z_a - d$), which determines the mean pressure, p_a, under each asperity in contact. The surface layer will yield only if p_a is greater than p_s, which is developed in Section 2.2.2. That is, only the asperities that deform greater than the approach of distant points at the onset of surface layer yielding, δ_s, which corresponds to p_s and developed in Section 2.2.3, can scratch the surface layer. Therefore, the number of scratches per unit area, n_s, can be estimated from

$$n_s = n\int_{d+\delta_s}^{\infty} \phi(z_a)\,dz_a = n\exp\left(-\frac{d}{\sigma_z}\right)\exp\left(-\frac{\delta_s}{\sigma_z}\right) \qquad (2.31)$$

Then, from Eq. (2.27) and (2.31), the relative proportion of asperities that can scratch the layer among those in contact, n_s/n_c, can be obtained by

$$\frac{n_s}{n_c} = \exp\left(-\frac{\delta_s}{\sigma_z}\right) \qquad (2.32)$$

Determination of δ_s varies depending on where the relative hardness and interfacial friction fall in the scratch-regime maps. First, if the pad-to-layer hardness ratio and the friction coefficient fall in the 'scratch regime' of Figure 2.3a, i.e. if the conditions satisfy

Eq. (2.24), then the asperities will scratch the surface layer which additionally satisfy Eq. (2.17). As multiple asperities are in sliding contact, accordingly, the proportion of scratching asperities in contact can be obtained from Eqs. (2.18) and (2.32) as

$$\frac{n_s}{n_c} = \begin{cases} \exp\left(-\frac{9\pi^2}{16}\frac{\sigma_{y,l}^2}{E_a^2}\frac{R_a}{\sigma_z}\right) & , \quad (0 \le \mu < 0.3) \\ \exp\left(-\frac{9\pi^2}{16}\frac{\sigma_{y,l}^2}{E_a^2}\frac{R_a}{\sigma_z}\left(5.35\mu^2 + 1.20\mu + 0.12\right)\right) & , \quad (0.3 \le \mu) \end{cases} \tag{2.33}$$

Second, if the pad-to-layer hardness and the friction coefficient fall in 'no scratch regime' of Figure 2.3a but fall in 'scratch-regime' of Figure 2.3b, i.e., if the conditions not satisfy Eq. (2.24) but satisfy Eq. (2.25), then asperities will scratch the surface layer which additionally satisfy Eq. (2.21). Therefore, from Eqs. (2.22) and (2.32),

$$\frac{n_s}{n_c} = \begin{cases} \exp\left(-\frac{\delta_y}{\sigma_z}\exp\left\{2\left[\frac{3}{2}\frac{\sigma_{y,l}}{\sigma_{y,a}} - 1\right]\right\}\right) & , \quad (0 \le \mu < 0.05) \\ \exp\left(-\frac{\delta_y}{\sigma_z}\exp\left\{2\left[\frac{\sigma_{y,l}}{\sigma_{y,a}}\left(7.76\mu^2 + 0.76\mu + 0.41\right)^{-1/2} - 1\right]\right\}\right) & , \quad (0.05 \le \mu) \end{cases} \tag{2.34}$$

Finally, if the pad-to-layer hardness ratio and the friction coefficient fall in 'no scratch regime' of Figure 2.3b, i.e., if the conditions do not satisfy Eq. (2.25), then any asperities in contact cannot scratch the surface and therefore,

$$\frac{n_s}{n_c} = 0 \tag{2.35}$$

To simplify the equations from Eq. (2.33) to Eq. (2.35), scratching indices for elastically and plastically deformed asperities, α_e and α_p respectively, can be introduced as

$$\alpha_e \equiv \begin{cases} \dfrac{H_a}{H_l} & , \quad (0 \le \mu < 0.3) \\ \dfrac{H_a}{H_l}\left(5.35\mu^2 + 1.20\mu + 0.12\right)^{1/2} & , \quad (0.3 \le \mu) \end{cases} \tag{2.36}$$

$$\alpha_p \equiv \begin{cases} \dfrac{2}{3}\dfrac{H_a}{H_l} & , \quad (0 \le \mu < 0.05) \\ \dfrac{H_a}{H_l}\left(7.76\mu^2 + 0.76\mu + 0.41\right)^{1/2} & , \quad (0.05 \le \mu) \end{cases} \tag{2.37}$$

Then, the scratching criteria for the extreme cases of elastically and plastically deformed asperities, Eqs. (2.24) and Eqs. (2.25) respectively, can be expressed as

$$\alpha_e \ge 1 \tag{2.38}$$

$$\alpha_p \ge \frac{1}{3} \tag{2.39}$$

Consequently, the proportion of scratching asperities in sliding contact can be summarized, from Eqs. (2.23) to (2.39), as

$$\frac{n_s}{n_c} = \begin{cases} \exp\left\{-\dfrac{1}{\psi^2\alpha_e^2}\right\} & , \quad (\alpha_e \ge 1) \\ \exp\left\{-\dfrac{1}{\psi^2}\exp\left[2\left(\dfrac{1}{\alpha_p}-1\right)\right]\right\} & , \quad \left(\alpha_e < 1 \text{ and } \alpha_p \ge \dfrac{1}{3}\right) \\ 0 & , \quad \left(\alpha_p < \dfrac{1}{3}\right) \end{cases} \tag{2.40}$$

Equation (2.40) indicates that the relative proportion of the asperities that can scratch the surface layer depends on the scratching index, α_e or α_p, and the plasticity index, ψ.

The scratching indices characterize the effects of relative hardnesses and interfacial friction between the pad asperities and the surface layer on the number of scratches. If $\alpha_e \geq 1$, the larger the α_e value is the more elastically deformed asperities can scratch the surface layer. If $\alpha_e < 1$ and $\alpha_p \geq 1/3$, none of the elastically deformed asperities can scratch the surface. However, plastically deformed asperities may scratch surface and the number of scratch may increase as the α_p value increases. If $\alpha_p < 1/3$, none of the asperities will scratch. For different values of plasticity index, Figure 2.6 shows the proportion of scratching asperities in contact according to the scratching index. Typically, the pad-to-layer hardness ratios of CMP pads and the surface layers are between 0.01 and 0.5, and the friction coefficients are between 0.4 and 0.6. Therefore, the α_e value in a general CMP system is less than one, and thus the elastically deformed asperities cannot scratch the surface layers: i.e., the plastically deformed asperities are the primary cause of pad scratching. Moreover, typical pad surfaces have plasticity index of more than one. Therefore, it can be predicted that soft pad asperities can scratch the relatively hard surfaces when α_p is greater than 0.33, and the number of scratches will abruptly increase as α_p increases beyond as shown in Figure 2.6.

2.4. Characterization of surface properties

The surface profiles of a commercial pad, Pad A, and a standard pad, IC1000, manufactured by Dow Chemical Co., were measured by a Tencor P16 profilometer, Figure 2.7. Length of 5 mm was scanned at 200 Hz of sampling rate by a stylus tip of 20 μm in diameter applying 20 μN of normal load and 50 μm/s of scanning speed. Table 2.1 shows the statistics of the determined topographical parameters, heights and radii of the asperities within the scanned length. In addition, the probability densities of the asperity heights are shown in Figure 2.8. It shows that the asperity height distributions for both pads can be well expressed by probability density functions of an exponential distribution based on the standard deviation of asperity heights.

To determine the mechanical properties, Young's modulus and hardness, of the pad asperities and of the thin film layers, a Hysitron TriboIndenter, model TI900, was used.

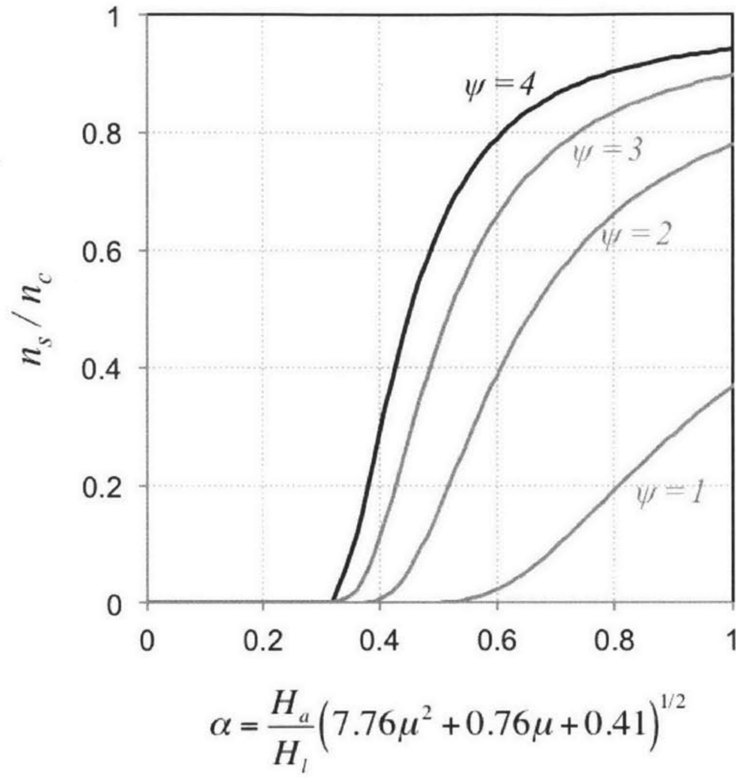

Figure 2.6. Proportion of asperities in contact that can scratch the surface layer, n_s / n_c, versus the scratching index, α_p, at different values of plasticity index, ψ.

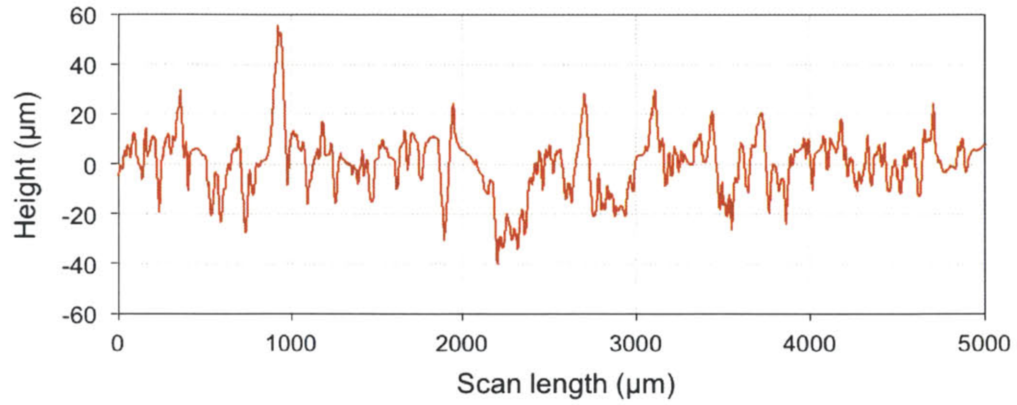

(a) Pad A

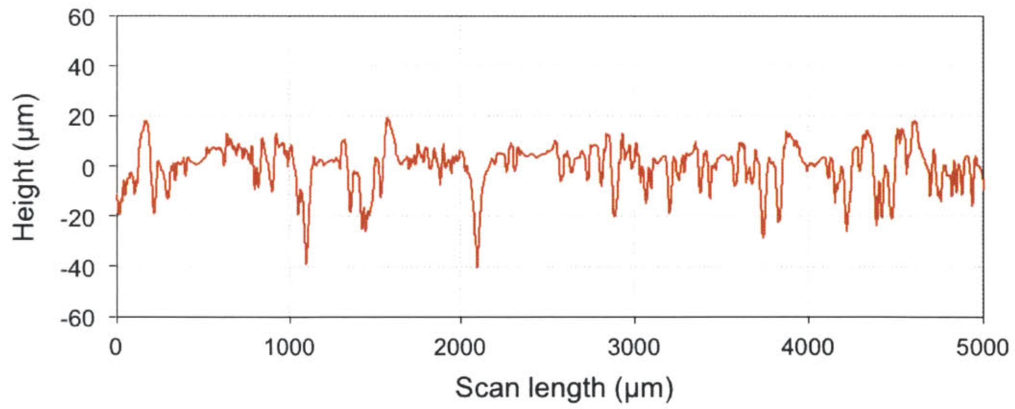

(b) IC1000 pad

Figure 2.7. Surface profiles of CMP pads.

Table 2.1. Statistical results of pad topography.

Pad	Parameters	Avg. (μm)	Std. Dev. (μm)	C.V.*
Pad A	Asperity height, z_a	11.8	10.5	0.89
	Asperity radius, R_a	26.1	9.6	0.37
IC1000	Asperity height, z_a	6.7	4.4	0.66
	Asperity radius, R_a	23.9	9.8	0.41

* Coefficient of Variation (C.V.) = Std. Dev. / Avg.

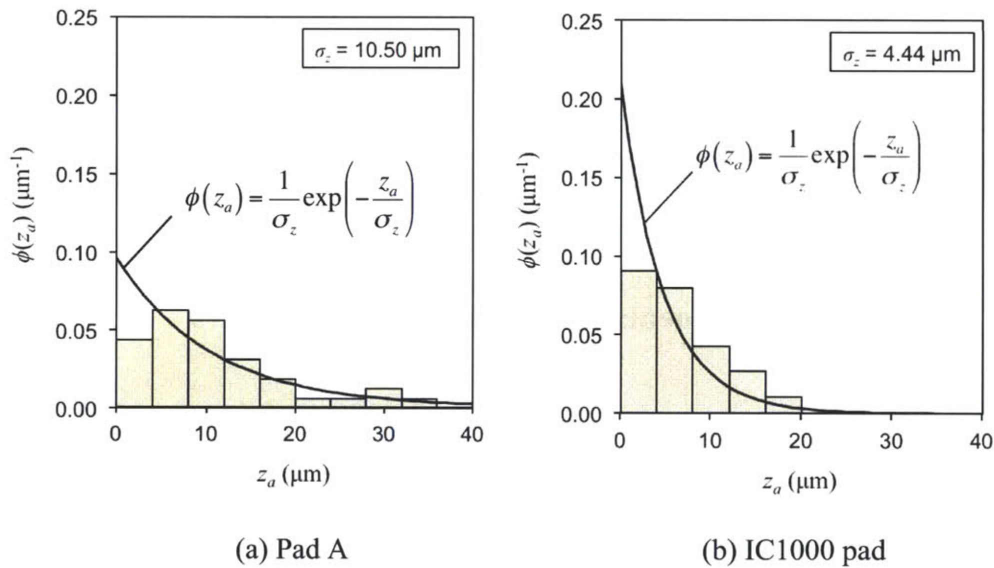

(a) Pad A

(b) IC1000 pad

Figure 2.8. Determined probability densities and the standard deviations of asperity heights. Solid lines are the probability density functions of an exponential distribution based on the determined standard deviations.

Eight different monolithic layers, Al, Cu, SiO_2, Si_3N_4, TiN and three low-k dielectrics, of 1 μm thickness coated on silicon wafers, were tested. Over 100 indentations on the pad and 49 indentations on each monolithic surface layer were made. In all cases, a Berkovich indenter was used and the depth of indentation was 90 nm.

Table 2.2 shows the statistics of the determined nano-hardnesses and nano-moduli. Comparing the average values, the hardnesses of all surface layers are much greater than those of the pad asperities. It may be noted that, however, the variation of pad properties are considerably large, probably due to their porosity. It was experimentally shown that the Young's modulus and hardness of CMP pads are log normally distributed [Eusner *et al.*, 2011]. Figure 2.9 shows the probability density of the normalized logarithm of asperity hardness for both Pad A and IC1000. The data were normalized with the average value of asperity hardness. Moreover, the variations of local Al and Cu properties are also relatively large compared to those of other layer properties. The hardnesses of surface layers are normally distributed as shown in Figure 2.10.

Based on the determined topographical and mechanical properties of pad asperities, plasticity indices of Pad A and IC1000 pad are calculated from Eq. (2.30) as 3.5 and 4.2, respectively. The probability of asperity deformation modes then can be readily estimated using Eq. (2.29). As listed in Table 2.3, when the both pads are compressed on the surface layer, most of the pad asperities, more than 90 %, will deform plastically.

2.5. Pad sliding experiments on monolithic surface layers

Figure 2.11 shows the reciprocating sliding apparatus used for the pad sliding experiments. Circular disks, 20 mm in diameter, of polishing pads were pressed at a normal load of 2 N, which corresponds to an average pressure of 7 kPa, and were slid over the wafers at 7 mm/s. All sliding tests were conducted in deionized water, and the number of cycles of each experiment was 15. The coefficient of friction between the two surfaces was determined by the strain gage measuring the tangential forces during each sliding. After each experiment, the scratches on the surface layer of the wafer were characterized by optical and scanning electron microscopes.

Table 2.2. Statistical results of mechanical properties.

Material	Hardness			Young's modulus		
	Avg. (MPa)	Std. Dev. (MPa)	C.V.	Avg. (GPa)	Std. Dev. (GPa)	C.V.
Pad A	32	15	0.59	0.14	0.12	0.81
IC1000	290	220	0.76	2.21	1.59	0.72
Al	970	160	0.17	88.7	13.6	0.15
Low-*k* A	1,360	21	0.01	7.74	0.06	0.01
Cu	1,560	260	0.17	126.5	12.5	0.10
Low-*k* B	1,800	78	0.04	23.1	0.78	0.03
Low-*k* C	2,470	51	0.02	25.8	0.43	0.02
SiO_2	8,000	110	0.01	69.8	0.73	0.01
Si_3N_4	9,780	160	0.02	123.2	2.79	0.02
TiN	15,400	150	0.01	172.2	1.53	0.01

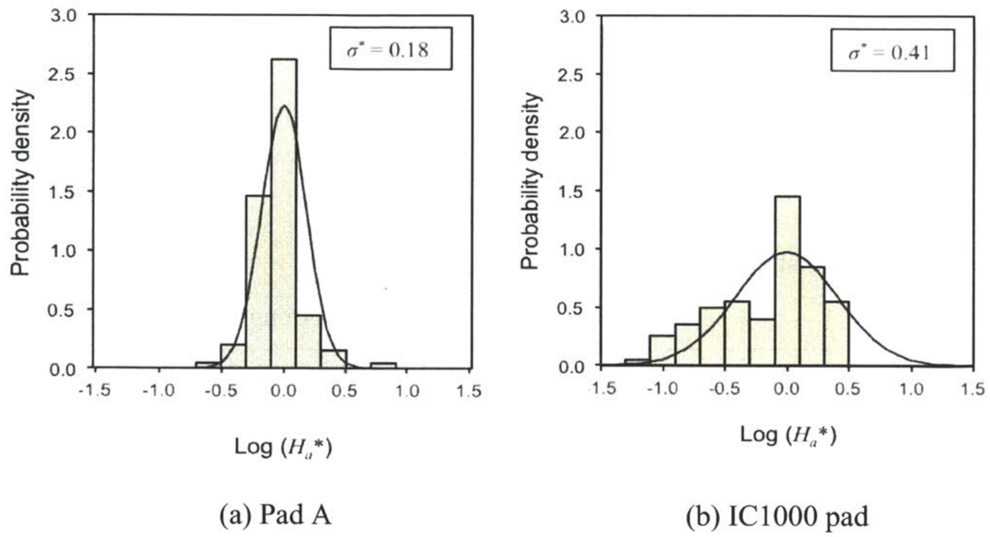

(a) Pad A (b) IC1000 pad

Figure 2.9. Probability density of log normalized nano-hardness for Pad A and IC1000 pad. H_a* is the normalized asperity hardness and σ* is the standard deviation of the normalized asperity hardness.

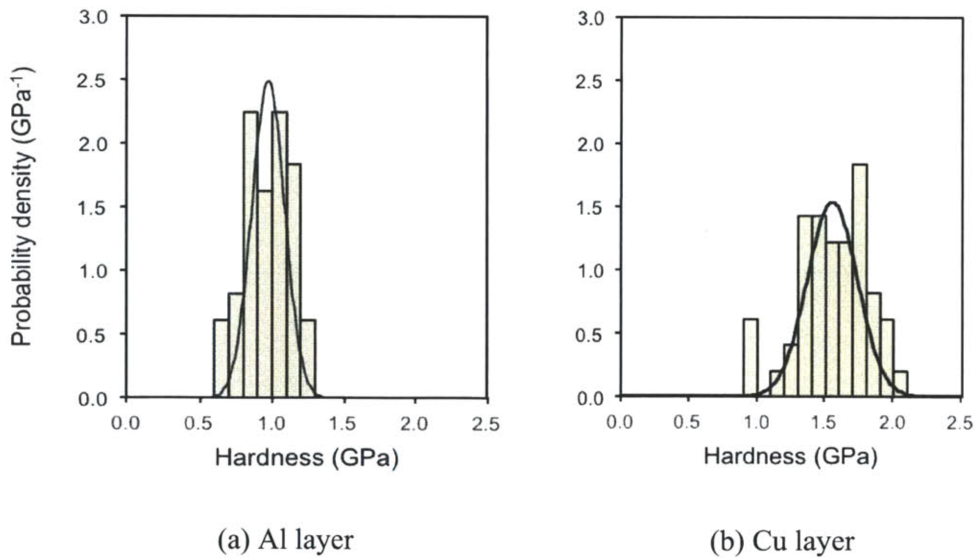

(a) Al layer (b) Cu layer

Figure 2.10. Probability density of nano-hardness of Al and Cu surface layers.

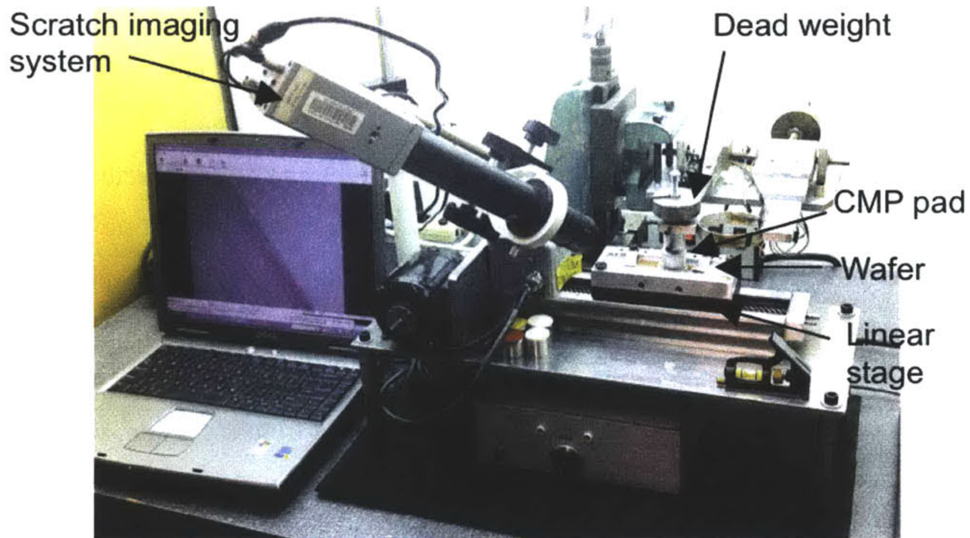

Figure 2.11. Reciprocating sliding apparatus.

Table 2.3. Estimated plasticity indices and relative proportions of asperity deformation modes of Pad A and IC1000.

Pad	E_a (MPa)	H_a (MPa)	σ_z (μm)	R_a (μm)	ψ	n_e / n_c	n_p / n_c
Pad A	140	32	10.5	26.1	3.5	0.08	0.92
IC1000	2210	290	4.4	23.9	4.2	0.06	0.94

As listed in Table 2.3, when the pad is pressed against the thin film layers, most of the pad asperities deform plastically. Therefore, the pad will scratch the wafer surface if the scratching criteria for plastically deformed asperities, Eq. (2.25), is satisfied. That is, the pad will scratch when the relative hardness and the friction coefficient fall on the scratch regime in the scratch-regime map, Figure 2.3b.

The scratch-regime map for plastically deformed asperities can be constructed for Pad A and IC1000 as Figures 2.12a and 2.13a respectively, considering the extreme hardness values: the maximum hardness of pad asperities and the minimum hardness of the surface layers. The reason for considering the extreme values is that scratching may occur when the hardest pad asperity rides over the softest point of the surface layer. The minimum hardnesses of surface layers, $H_{l,min}$, were statistically estimated from $H_{l,avg} - 3\sigma$, where the average and the standard deviation are listed in Table II. Although, the maximum hardnesses of pad asperities may similarly estimated from $\text{Log}(H_{a,max}{}^*) = \text{Log}(H_{a,avg}{}^* + 3\sigma^*)$, the statistically estimated maximum value for the IC1000 pad was 19 GPa, which is unrealistic for a polyurethane-based polymer. Instead, measured maximum values, $H_{a,max}$ = 162 MPa for Pad A and $H_{a,max}$ = 915 MPa for IC1000 pad were used for the scratching criteria.

Comparing the experimental results, as shown in Figures 2.12b, Pad A scratches the Al and Cu layer since the extreme hardness ratio and the friction coefficient fall on the 'scratch regime' of the map. The pad cannot scratch the other surface layers, three low-*k* dielectrics, SiO_2, Si_3N_4 and TiN, because even the extreme conditions between Pad A and the other layers fall on the 'no scratch regime'. Similarly, Figure 2.13b, IC1000 pad can only scratch Al, Cu and three low-*k* dielectrics since their extreme conditions fall on the 'scratch regime', but cannot scratch SiO_2, Si_3N_4 and TiN. It should be noted due to the greater variation of local hardness, Cu layers can be more vulnerable to scratching than the low-*k* layers even though the average hardness and the friction between the pad is smaller.

For further quantitative analysis of pad scratching, the numbers of scratches generated on the surface layers were examined by optical and scanning electron microscopes. In Table 2.4, the scratching indices, α_e and α_p, between the CMP pads and the surface layers are calculated, from Eqs. (2.36), (2.37) and using the determined hardnesses and friction

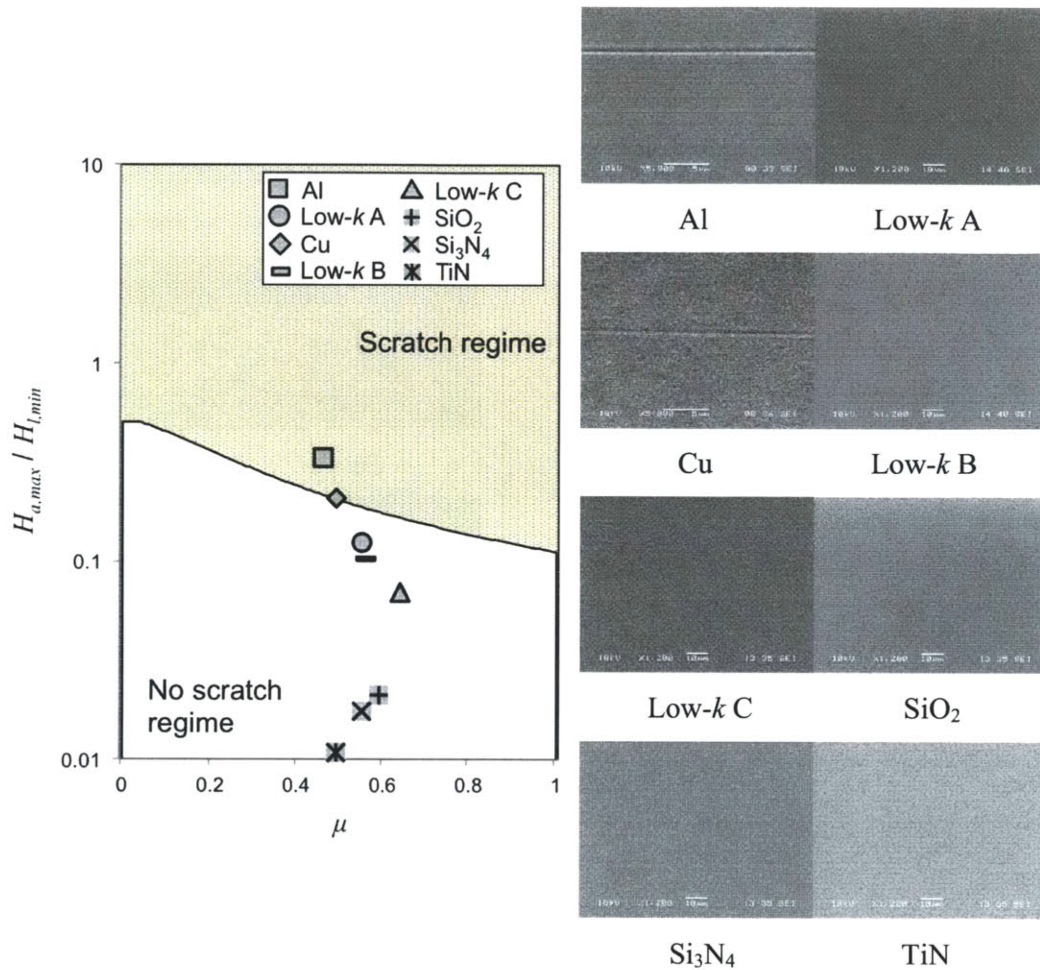

(a) Scratch-regime map (b) SEM images

Figure 2.12. Scratch-regime map for Pad A and SEM images of the surface layers after the pad sliding experiments using Pad A.

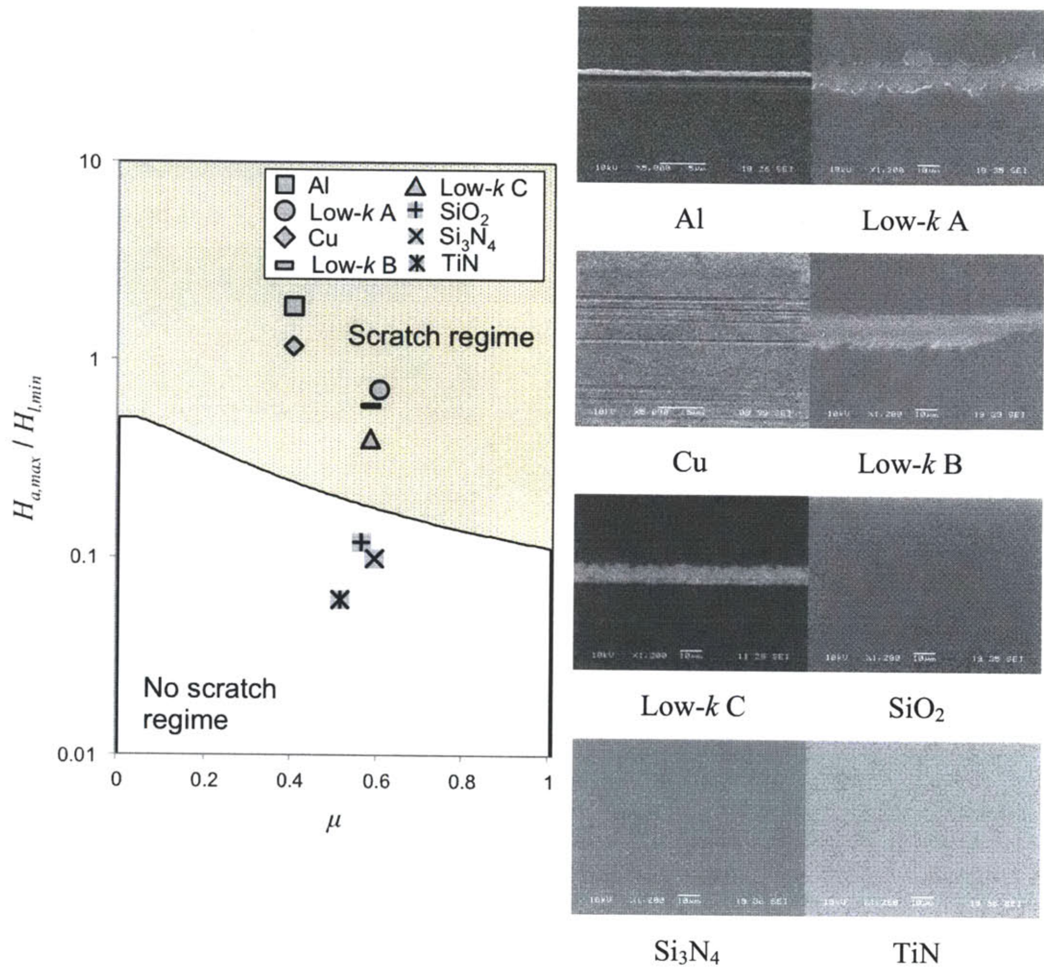

(a) Scratch-regime map (b) SEM images

Figure 2.13. Scratch-regime map for IC1000 pad and SEM images of the surface layers after the pad sliding experiments using IC1000 pad.

Table 2.4. Scratching indices and results of sliding experiments between pads and surface layers.

Pad	Surface layer	$H_a/H_{l,min}$	μ	α_e	α_f	# of scratches
Pad A	Al	0.065	0.46	0.09	0.1	4
	Low-*k* A	0.025	0.55	0.06	0.04	0
	Cu	0.041	0.49	0.04	0.07	1
	Low-*k* B	0.021	0.57	0.03	0.04	0
	Low-*k* C	0.014	0.64	0.02	0.03	0
	SiO_2	0.004	0.59	0.007	0.008	0
	Si_3N_4	0.003	0.55	0.005	0.006	0
	TiN	0.002	0.49	0.003	0.003	0
IC1000	Al	0.60	0.40	0.72	0.83	45
	Low-*k* A	0.23	0.60	0.45	0.43	9
	Cu	0.38	0.40	0.38	0.53	22
	Low-*k* B	0.19	0.58	0.30	0.35	3
	Low-*k* C	0.13	0.58	0.20	0.24	2
	SiO_2	0.038	0.40	0.06	0.07	0
	Si_3N_4	0.031	0.40	0.05	0.06	0
	TiN	0.019	0.40	0.03	0.04	0

coefficients. For α_e and α_p calculation, the average asperity hardness and the minimum surface layer hardness are used. Because, as the multi-asperities in contact slide over, a scratch may initiate as each asperity encounters the softest points of the layer. In all cases, the α_e values are less than one, which again suggests that, from Eq. (2.38), only the plastically deformed asperities may scratch the surface layer. In addition, α_p values between Pad A and the surface layers are much less than those between pad B and the surface layers primarily due to the low hardness of Pad A. The number of scratches generated on the surface layers by Pad A and IC1000 pad are listed in the last column of Table 2.4 and are also plotted in Figure 2.14 according to α_p. The number of scratches is few when α_p is less than 0.33, but the number of scratches increases as α_p exceeds 0.33, which validates the theoretical predictions, Eq. (2.40) and Figure 2.6.

To mitigate scratching by the pad asperities on the surface layers, both the theoretical models and the experimental results show that the scratching index, α_p, should be reduced, i.e., either the ratio of pad asperity hardness to surface layer hardness, H_a / H_l, or the coefficient of friction between the pad asperity and the surface layer, μ, need to be reduced. Practically, in CMP of low hardness materials such as Al and Cu, softer polishing pads and lubricants should be used to have α_p preferably less than 0.33. Furthermore, the scratch-regime map suggests that the scratches by pad asperities can be eliminated if the hardness ratio and the friction coefficient fall into the 'no scratch regime' of the map. More importantly, however, not only the average values, but also the variation of the local hardnesses of pad asperities should be carefully controlled so that even the extreme values satisfy such criteria. In addition, the theoretical model, Eq. (2.40), also suggests that the pad-induced scratching can be mitigated by reducing the plasticity index, ψ, of the pad surface, i.e., by decreasing either the modulus-to-hardness ratio of pad asperities, E_a / H_a, or the ratio of standard deviation of asperity height to asperity radius, σ_z / R_a, which will be discussed in Chapter 4.

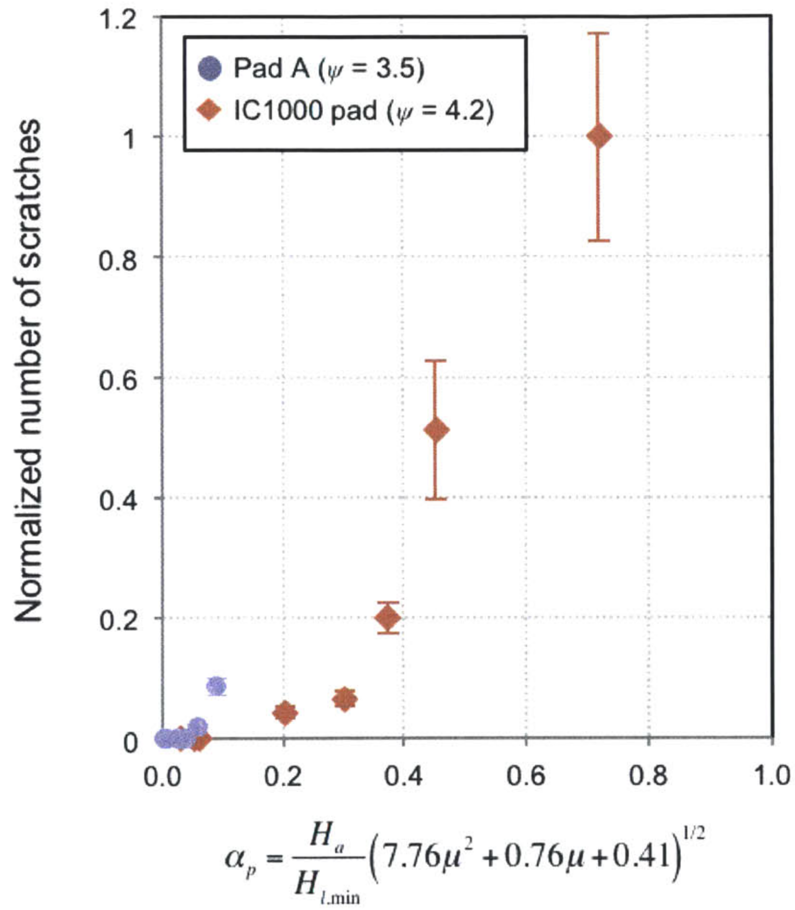

Figure 2.14. Normalized number of scratches versus the scratching index, α_p. The points present average values and the bars the standard errors.

2.6. Summary

In this chapter, scratching by soft pad asperities on relatively hard surfaces in chemical-mechanical polishing was investigated.

(1) Based on the mechanics of sliding frictional contacts, scratching criteria were developed and scratch-regime maps were constructed for two different types of pad asperity deformation modes, elastic and plastic, considering their extremes cases of modes, at the onset of asperity yielding and fully-plastic. In both cases, scratching conditions were determined by the ratio of pad asperity hardness to surface layer hardness and the coefficient of friction.

(2) As multi-asperities are in contact, the relative proportions of each asperity deformation modes, elastic and plastic, were found to depend on plasticity index of the pad surface, which is determined by the ratio of hardness to modulus of the pad asperities, and by the ratio of asperity radius to the standard deviation of asperity height. Typical CMP pads have plasticity index of greater than one, and thus most asperities deform plastically. Therefore, scratch criteria and scratch-regime map for plastically deformed asperities must be considered whether the pad asperities can scratch the hard surface or not.

(3) For a quantitative analysis of pad scratching, scratching indices were introduced in terms of pad-to-layer hardness ratio and friction coefficient. The proportion of scratching asperities in contact can be estimated from the scratching index between the pad asperities and the surface layer, and the plasticity index of the pad surface.

(4) The nano-indentation results showed that CMP pads as well as Cu and Al layers have large variation in local hardnesses compared with other layers, such as low-*k* dielectrics, SiO_2, Si_3N_4 and TiN. For scratch-regime maps, accordingly, the extreme hardness values should be considered.

(5) A reciprocating sliding apparatus was used for friction measurements as well as scratch experiments. The theoretical models and the experimental results have shown that the number of scratches rises as the scratch index increases beyond 0.33. Only few scratches were found when the scratch index is less than 0.33. The pad

scratching can only be eliminated, if the maximum asperity hardness satisfies the scratching criteria.

The present work, consequently, suggests that to reduce or even eliminate pad scratching, the scratching index, which incorporates the relative hardness and interfacial friction between pad asperities and the surface layer, should be reduced to preferably less than 0.33. Furthermore, to eliminate the pad scratching, the local hardnesses of asperities and surface layers should be tightly controlled.

Nomenclature

$C_{f\text{-}p}$	$= \delta_{f\text{-}p} / \delta_y$
d	distance between the centerline of pad surface and surface layer [m]
E_a	Young's modulus of asperity [N m^{-2}]
E_l	Young's modulus of surface layer [N m^{-2}]
H_a	hardness of asperity [N m^{-2}]
H_a^*	normalized hardness of asperity
H_l	hardness of surface layer [N m^{-2}]
n	number of asperities per unit area [m^{-2}]
n_c	number of asperities in contact per unit area [m^{-2}]
n_e	number of elastically deformed asperities per unit area [m^{-2}]
n_p	number of plastically deformed asperities per unit area [m^{-2}]
n_s	number of scratching asperities per unit area [m^{-2}]
P_a	asperity load [N]
p_a	mean asperity contact pressure [N m^{-2}]
p_o	maximum asperity contact pressure [N m^{-2}]
p_s	mean asperity contact pressure at the onset of surface layer yielding [N m^{-2}]
R_a	asperity radius [m]
v_r	relative velocity [m s^{-1}]
z_a	asperity height [m]
α_e	scratching index for elastically deformed asperity
α_p	scratching index for plastically deformed asperity
δ	approach of distant points [m]
$\delta_{f\text{-}p}$	approach of distant points at the onset of fully-plastic asperity deformation [m]
δ_s	approach of distant points at the onset of surface layer yielding [m]
$\delta_{s,e}$	approach of distant points at the onset of surface layer yielding under an elastically deformed asperity in sliding contact [m]
$\delta_{s,p}$	approach of distant points at the onset of surface layer yielding under a plastically deformed asperity in sliding contact [m]

δ_y	approach of distant points at the onset of asperity yielding [m]
μ	coefficient of friction
ν_l	Poisson's ratio of surface layer
$\sigma_{M,max}$	maximum Von Mises stress [N m^{-2}]
$\sigma_{y,a}$	yield strength of asperity [N m^{-2}]
$\sigma_{y,l}$	yield strength of surface layer [N m^{-2}]
σ_z	standard deviation of asperity heights [m]
τ_{max}	maximum shear stress [N m^{-2}]
ψ	plasticity index
$\phi(z_a)$	probability density of asperity heights

References

Bhushan, B., 1996, "Contact mechanics of rough surfaces in Tribology: Single asperity contact," *Appl. Mech. Rev.*, vol. 49, pp. 275-298.

Busby, J. T., Hash, M. C. and Was, G. S., 2005, "The relationship between hardness and yield stress in irradiated austenitic and ferritic steels," *J. Nuclear Mater.*, vol. 336, pp. 267-278.

Chang, W. R., Etsion, I. and Bogy, D. B., 1987, "An elastic-plastic model for the contact of rough surfaces," *ASME J. Tribol.*, vol. 109, pp. 257-263.

Eusner, T., 2010, "Multi-scale scratches in chemical-mechanical polishing," Ph.D. Thesis, Department of Mechanical Engineering, MIT, Cambridge, MA.

Eusner, T., Saka,, N. and Chun, J.-H., 2011, "Breaking-in a pad for scratch-free, Cu chemical-mechanical polishing," *J. Electrochem. Soc.*, vol. 158, no. 4, pp. H379-H389.

Fan, W., 2012, "Advanced modeling of planarization processes for integrated circuit fabrication," Ph.D. Thesis, Department of Electrical Engineering and Computer Science, MIT, Cambridge, MA.

Francis, H. A., 1976, "Phenomenological analysis of plastic spherical indentation," *ASME J. Eng. Mater. Technol.*, vol. 98, no. 3, pp. 272-281.

Greenwood, J. A. and Williamson, J. B. P., 1966, "Contact of nominally flat surfaces," *Proc. Royal Soc. London A*, vol. 295, pp. 300-319.

Hamilton, G. M. and Goodman, L. E., 1966, "The stress field created by a sliding circular contact," *J. Appl. Mech.*, vol. 88, pp. 371-376.

Hamilton, G. M., 1983, "Explicit equations for the stresses beneath a sliding spherical contact," *Proc. Instn. Mech. Eng.*, vol. 197, pp. 53-59.

Hertz, H., 1882, "Über die berührung fester elastischer köper (On the contact of elastic solieds)," *J. Reine und Angewandte Mathematik*, vol. 92, pp. 156-171.

Horng, H. H., 1998, "An elliptic elastic-plastic asperity microcontact model for rough surfaces," *ASME J. Tribol.*, vol. 120, pp. 82-88.

Ishigaki, H., Kawaguchi, I. and Mizuta, S., 1979, "A simple estimation of the elastic-plastic deformation of contacting asperities," *Wear*, vol. 54, pp. 157-164.

Jayaweera, N. B., Downes, J. R., Frogley, M. D., Hopkinson, M., Bushby, A. J., Kidd, P., Kelly, A. and Dunstan, D. J., 2003, "The onset of plasticity in nanoscale contact loading," *Proc. Roy. Soc. London A*, vol. 459, pp. 2049-2068.

Johnson, K. L., 1885, *Contact Mechanics*, Cambridge University Press, Cambridge, UK.

Kogut, L. and Etsion, I., 2002, "Elastic-plastic contact analysis of a sphere and a rigid flat," *ASME J. Appl. Mech.*, vol. 69, pp. 657-662.

Love, A. E. H., 1929, "Stress produced in a semi-infinite solid by pressure on part of the boundary," *Phil. Trans. Royal Soc. A*, vol. 228, pp. 377- 420.

McCool J. I., 1986, "Comparison of models for the contact of rough surfaces," *Wear*, vol. 107, pp. 37-60.

Saka, N., Eusner, T. and Chun, J.-H., 2010, "Scratching by pad asperities in chemical-mechanical polishing," *Annals of the CIRP*, vol. 59, pp. 329-332.

Sorooshian, J., Borucki, L., Stein, D., Timon, R., Hetherington, D. and Philipossian, A., 2005, "Revisiting the removal rate model for oxide CMP," *ASME J. Tribol.*, vol. 127, pp. 639-651.

Vasilev, B., Bott, S., Rzehak, R., Liske, R. and Bartha, J. W., 2013, "A method for characterizing the pad surface texture and modeling its impact on the planarization in CMP," *Microelectronic Eng.*, vol. 104, pp. 48-57.

Vlassak, J. J., 2004, "A model for chemical-mechanical polishing of a material surface based on contact mechanics," *J. Mech. Phys. Solids*, vol. 52, pp. 847-873.

Yu, W. and Blanchard, J. P., 1996, "An elastic-plastic indentation model and its solutions," *J. Mater. Res.*, vol. 11, no. 9, pp. 2358-2367.

Zhao, Y., Maietta, D. M. and Chang, L., 2000, "An asperity microcontact model incorporating the transition from elastic deformation to fully plastic flow," *ASME J. Tribol.*, vol. 122, pp. 86-93.

CHAPTER 3

SCRATCHING OF PATTERNED CU/DIELECTIC SURFACES BY PAD ASPERITIES

3.1. Introduction

In chemical-mechanical polishing (CMP), as the rough polymer pad slides over patterned structures of metal interconnects and dielectrics the pad asperities themselves, though soft, may scratch the relatively hard layers. In Chapter 2, it was revealed that the conditions for scratching by pad asperities on monolithic surface layers strongly depend on the relative hardnesses and the interfacial friction between the pad asperities and the surface layer. This chapter studies conditions for scratching patterned Cu/dielectric surfaces.

Figure 3.1 shows the example images of scratches produced on patterned Cu/low-*k* surfaces by pad asperities. A standard CMP pad, IC1000 manufactured by the Dow Chemical Co., and a commercial pad, Pad A, were slid over the wafers with patterned Cu/low-*k* layers on the surface, which have various pattern linewidths from 0.05 to 9 μm. The applied nominal pressure was 7 kPa (= 1 psi) and the linear velocity was 0.75 m/s. In all sliding experiments, only deionized water was provided into the interface, i.e., without any abrasive particles. As can be seen in Figure 3.1a, scratches with widths of a few hundred nanometers or of even greater than a micrometer were found on some patterned surfaces on both Cu and low-*k* lines regardless of the linewidths after sliding the IC1000 pad. Scratches were also found on the patterns after sliding the Pad A, which is determined to be much softer than the IC1000 pad; however, only the wide Cu lines were scratched whereas the wide low-*k* lines were not, Figure 3.1b. More interestingly, no scratches were found on patterns with relatively narrow Cu and low-*k* lines by Pad A. The results of the pad sliding experiments suggest that not only the hardness and friction

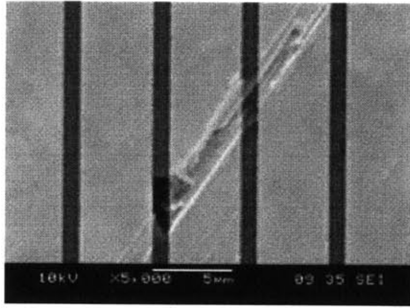

Cu linewidth: 4.5 μm

Low-*k* linewidth: 1.0 μm

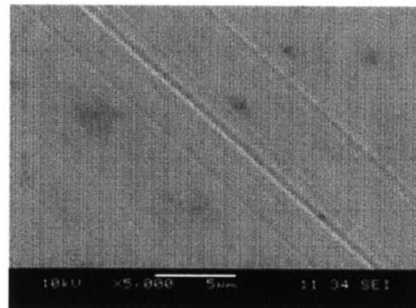

Cu linewidth: 0.05 μm

Low-*k* linewidth: 0.05 μm

(a) using IC1000 pad

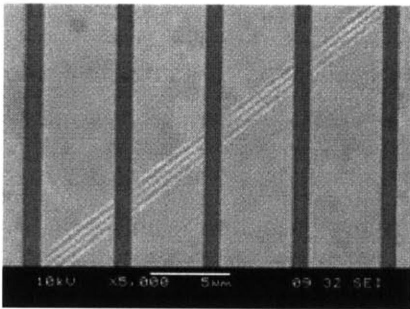

Cu linewidth: 4.5 μm

Low-*k* linewidth: 1.0 μm

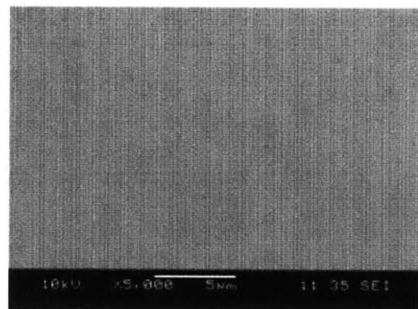

Cu linewidth: 0.05 μm

Low-*k* linewidth: 0.05 μm

(b) using Pad A

Figure 3.1. SEM images of patterned Cu/low-*k* surface layers after the pad sliding experiments.

but also the geometrical factors of the patterned surface, such as the linewidths of metal interconnects and dielectrics, may affect scratching conditions.

In this chapter, accordingly, scratching by pad asperities on patterned Cu/dielectric layers is investigated by contact mechanics models and by experiments using solid, polymer pins. Specifically, the effects of pattern geometry are additionally considered beyond the previous pad scratching models developed in terms of the mechanical properties of the pad and layer materials, and of the interfacial friction between the surfaces. The results of sliding experiments using solid polymer pins on patterned layers of various linewidths qualitatively validate the theoretical predictions. Finally, scratching conditions of patterned Cu/dielectric layers by the pad asperities are elucidated by comparing the developed contact mechanics models and the pad sliding experimental results.

3.2. Theory of scratching of interconnects and dielectrics

Typical CMP pads are relatively very rough compared with the surfaces being polished. The asperity height distribution of typical CMP pads which have a random, rough surface is known to be normal or exponential [Sorooshian *et al.*, 2005; Fan, 2012; Vasilev *et al.*, 2013]. As the rough polishing pad is pressed against a smooth, flat layer at nominal pressures, p, between 7 and 35 kPa (1 - 5 psi), the real area of contact is about a percent or less than the nominal area of contact, Figure 3.2 [Greenwood and Williamson, 1966; Elmufdi and Muldowney, 2006; Gray *et al.*, 2007]. That is, the relatively small asperities, which have asperity height, z_a, less than the separation distance, d, ($z_a < d$) do not contact the surface layer, and only the tall asperities ($z_a \geq d$) will be in contact with the flat surface, Figure 3.3a. The contact pressure, therefore, is concentrated under the asperities in contact, which will be much greater than the applied nominal pressure. Moreover, of those asperities in contact, the contact pressure may become even higher under a few tallest asperities that deform the greatest.

Figure 3.3b-e shows the different deformation modes of asperities in contact and the surface tractions applied by each asperity contact, according to their approach of distant

points, δ (= $z_a - d$). When the approach of distant points is smaller than the elastic limit, δ_y, then the asperity will deform elastically, Figure 3.3b. The contact pressure under such elastically deformed asperities is relatively small. The maximum contact pressure that can be achieved under elastically deformed asperities is about 1.5 times the yield strength of the asperity, $\sigma_{y,a}$, Figure 3.3c [Johnson, 1985]. Beyond the elastic limit, the asperity deforms elastic-plastically, Figure 3d. The contact pressure keeps increasing as the approach of distant points increases until the onset of the plastic limit, at the fully-plastic deformation point, $\delta_{f\text{-}p}$, applies [McCool, 1986; Zhao *et al.*, 2000]. The contact pressure under a fully-plastically deformed asperity will be uniform within the contact area. The magnitude is the asperity hardness, H_a, which is the maximum value that can be applied by the pad, Figure 3.3e. In Chapter 2, for typical pads that have exponentially distributed asperity heights, about 90 percent of the pad asperities in contact are estimated to deform plastically. Therefore, between the pad-layer contact, some pad asperities exist that deform fully-plastically, where the contact pressure is maximized. The hardness of pad asperities is in general about 10 to 1,000 MPa. That is, the maximum contact pressure that can be applied by the few tall asperities, which reaches to the fully-plastic deformation, can be 1,000 to even 100,000 times greater than the applied nominal pressure. Furthermore, as the asperities slide over the surface layer, not only the normal pressure but also the tangential traction due to the interfacial friction will be additionally applied on the surface. Such extreme conditions of pad asperity sliding contact with interfacial friction on the flat surface layer enable even the soft pad asperities to scratch the relatively hard surfaces.

3.2.1. Scratching of monolithic Cu and dielectric layers

When an asperity of hardness, H_a, slides over a monolithic layer of hardness, H_l, in the fully-plastically deformed mode, the criteria for scratching is given, from (2.21), as

$$\frac{H_a}{H_l} > \frac{1}{2} \quad , \quad (0 \le \mu \le 0.05) \tag{3.1a}$$

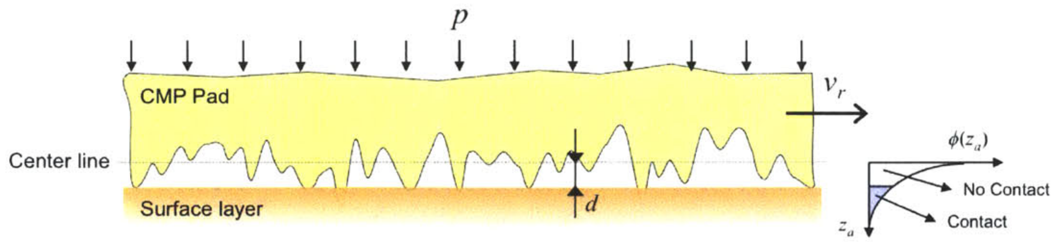

Figure 3.2. Schematic of contact between a random, rough pad and a smooth flat surface layer.

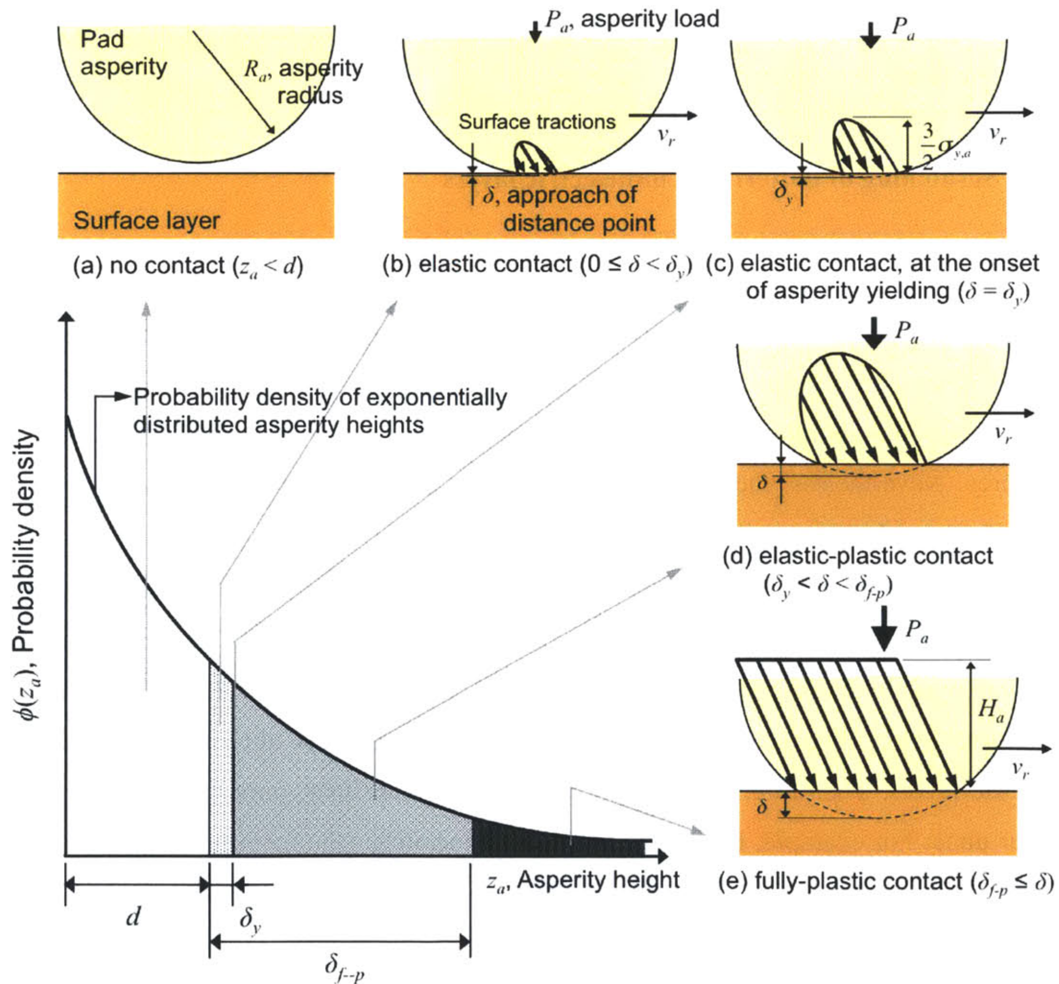

Figure 3.3. Modes of asperity contact and the surface tractions under each asperity deformation modes.

$$\frac{H_a}{H_l} > \frac{1}{3}\left(7.76\mu^2 + 0.76\mu + 0.41\right)^{-1/2} \quad , \quad \left(0.05 \le \mu\right) \tag{3.1b}$$

where μ is the coefficient of friction between the pad asperity and the layer.

These criteria explicitly suggest that the ratio of pad hardness to layer hardness and the interfacial friction primarily determine whether the fully-plastically deformed pad asperity will scratch the layer or not. Based on Eqs. (3.1a) and (3.1b), a scratch-regime map for monolithic layers can be constructed as in Figure 2.3b, which is replotted in linear scale for the y-axis in Figure 3.4. If the ratio of asperity-to-layer hardness and the coefficient of friction fall in the 'scratch regime,' the fully-plastically deformed asperity will scratch the layer. On the other hand, if the properties fall in the 'no scratch regime,' the layer cannot be scratched.

3.3.2. Scratching of patterned Cu/dielectric layers

Cu CMP is most commonly used for planarizing (or polishing) Cu interconnects in modern microelectronic devices. The top layer of the wafer being polished in general consists of parallel Cu and dielectric "line" structures. The scratch criteria and scratch-regime map of monolithic layers, therefore, may not be appropriate for such patterned structures. Nevertheless, the criteria can be further advanced considering two extreme cases of contact between a single pad asperity and the "line" structures.

Figure 3.5a shows an extreme case where both the Cu and dielectric linewidths, w_{Cu} and w_d, are greater than the contact diameter, $2a_c$. In this first extreme case, an asperity will slide over the lines serially and the stress field in the Cu and the dielectric lines under the asperity contact would be the same, respectively, as those for monolithic Cu or dielectric layers. Therefore, the asperity may scratch both lines, only the softer line, or neither none. For example, if a single pad asperity scratches the monolithic Cu layer but not the monolithic dielectric layer, then the pad asperity, as it slides over the patterns, will scratch only the Cu lines but not the dielectric lines.

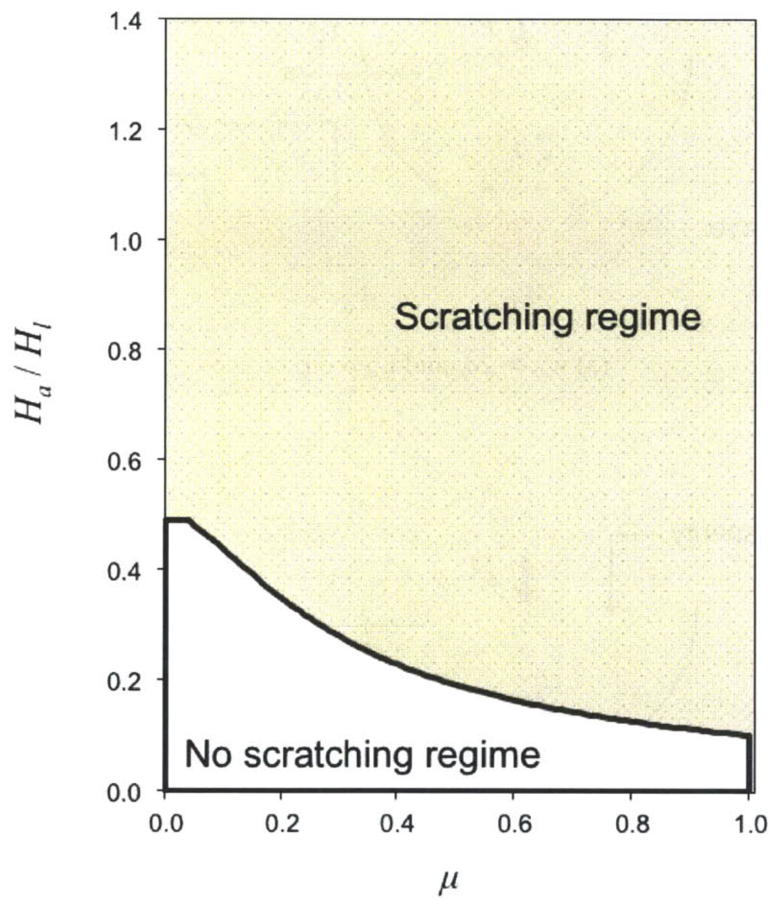

Figure 3.4. Scratch-regime map for a fully-plastically deformed asperity.

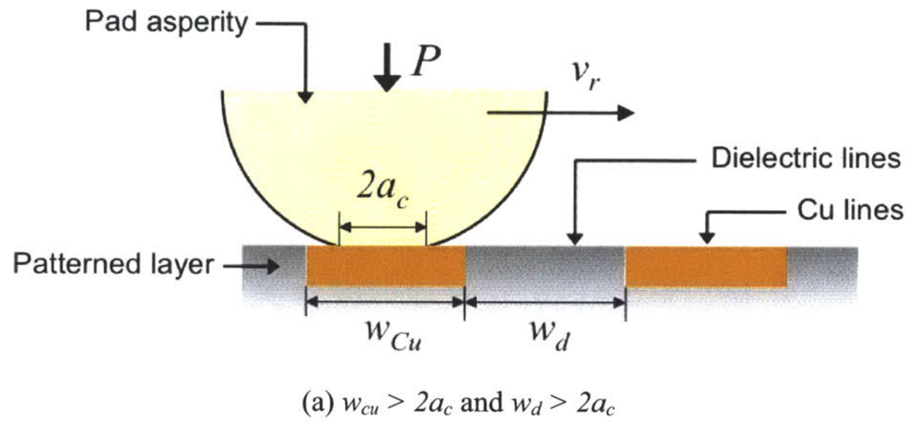

(a) $w_{cu} > 2a_c$ and $w_d > 2a_c$

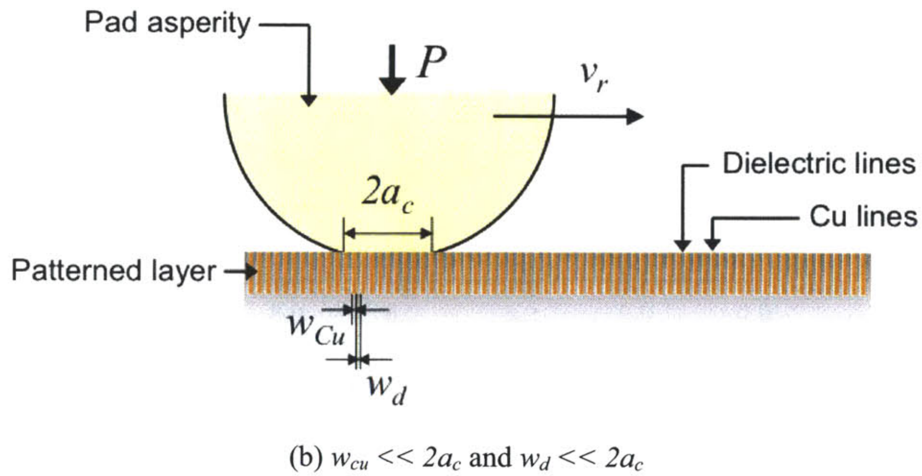

(b) $w_{cu} << 2a_c$ and $w_d << 2a_c$

Figure 3.5. Two extreme cases of asperity contact on composite Cu/dielectric layers: (a) features wider than the contact diameter, and (b) features much narrower than the contact diameter.

Figure 3.5b shows the other extreme case where both lines are much narrower than the asperity contact diameter. In this second extreme case, a single asperity will compress a great number of lines simultaneously. Then the medium of line structures can be assumed to be a composite, which behaves as a homogeneous material with effective mechanical properties as determined by the properties of the two materials and the pattern geometry.

Measurement of the effective mechanical properties, such as Young's modulus and hardness, of thin patterned layers by the current indentation techniques, however, is problematic. But the effective properties can be readily estimated from the geometrical parameters of the structures and the mechanical properties of the monolithic layers. The rule-of-mixtures (ROM) is commonly used to estimate the effective hardness of a composite [Weihs *et al.*, 1993; Liou *et al.*, 1995; Kim, 2000]. Figure 3.6 is a schematic of the iso-strain compression model. When the composite is compressed parallel to the layers, an iso-strain condition exists (i.e., the strain in the direction of loading in each lamina is the same), and the volume fraction and hardness of each material determine the plastic deformation resistance of the composite. The effective hardness of the surface layer, $H_{l,eff}$, is approximately given by:

$$H_{l,eff} = f_{Cu} \cdot H_{Cu} + f_d \cdot H_d \tag{3.2a}$$

where f_{Cu} and f_d are the volume fractions of Cu and dielectric lines. For parallel line structures, the effective hardness of the composite layer may be estimated by:

$$H_{l,eff} = \frac{w_{Cu}}{\lambda} \cdot H_{Cu} + \frac{w_d}{\lambda} \cdot H_d \tag{3.2b}$$

where λ is the pitch of the pattern; $\lambda = w_{Cu} + w_d$. Therefore, for the narrow-lined structures, the scratch criteria may be modified as:

$$\frac{H_a}{H_{l,eff}} > \frac{1}{2} \quad , \quad (0 \le \mu \le 0.05) \tag{3.3a}$$

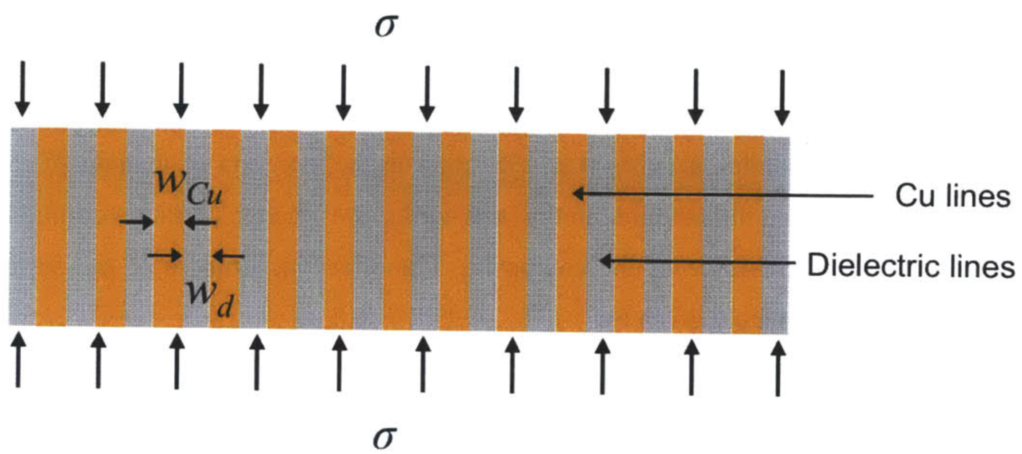

Figure 3.6. Schematic of iso-strain compression of a composite layer.

$$\frac{H_a}{H_{l,eff}} > \frac{1}{3}\left(7.76\mu^2 + 0.76 + 0.41\right)^{-1/2} \quad , \quad (\mu \geq 0.05) \tag{3.3b}$$

If Eq. (3.3a) or (3.3b) is satisfied, a fully-plastically deformed asperity may scratch both the Cu and dielectric lines; otherwise the asperity can scratch neither Cu nor the dielectric lines.

3.3. Sliding experiments on patterned Cu/dielectric layers

To validate the theoretical predictions of scratching on patterned structures, single-asperity sliding experiments using solid polymer pins have been designed as shown in Figure 3.7. The pin sliding experiments have several advantages compared with the pad sliding experiments. First, the location and trajectory of the asperity contact can be tracked and controlled. Second, the normal load on the single asperity can be varied so that the deformation mode of the tip of the pin can be manipulated to be elastic, elastic-plastic, or fully-plastic. Finally, the contact radius at a given load can be readily estimated and easily measured.

3.3.1. Solid polymer pins

In order to represent a single pad asperity, the solid pin should be selected to have similar hardness as that of the pad asperity. The Young's modulus and hardness of various polymer pins were determined by a Hysitron Triboindenter, model TI900. Using a Berkovich indenter, 25 indentations were made on various polymer pins and their statistical values are compared with those of an IC1000 pad and a Pad A, as Table 3.1. The depth of indentation was 90 nm. A Polystyrene (PS) pin can be selected since the average hardness and Young's modulus are closest to those of the IC1000 pad.

It is important to note, however, that all the measured values of the pins and of the pads have large variation in modulus and hardness. The CMP pads especially have the

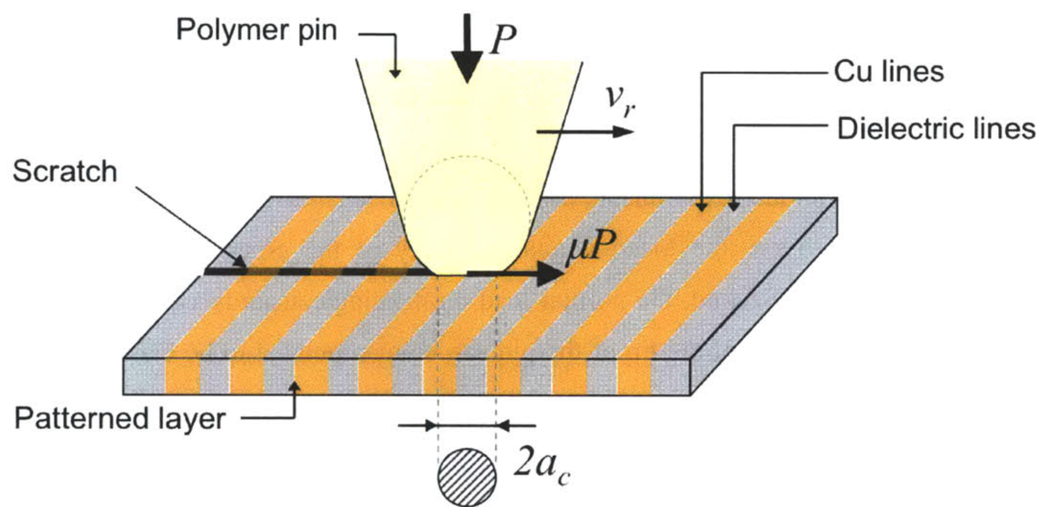

Figure 3.7. Schematic of single-asperity sliding experiment.

Table 3.1. Statistical results of determined mechanical properties of polymer pins (LDPE, PP, PTFE, HDPE, PS, PC, and PMMA) and CMP pads (pad A and IC1000).

Material	Hardness			Young's modulus		
	Avg. (MPa)	Std. Dev. (MPa)	C.V.*	Avg. (MPa)	Std. Dev. (MPa)	C.V.
Pad A	32	15	0.59	143	122	0.81
LDPE**	170	76	0.45	739	269	0.36
PP**	183	102	0.56	1976	983	0.50
PTFE**	184	80	0.43	1214	502	0.41
HDPE**	189	125	0.66	1967	1103	0.56
PS**	266	117	0.44	3367	1185	0.35
IC1000	293	220	0.75	2212	1591	0.72
PC**	323	151	0.47	4293	1531	0.43
PMMA**	389	196	0.50	5234	1614	0.31

* Coefficient of variation (C.V.) = Average / Standard deviation.

** LDPE : Low-density polyethylene
PP : Polypropylene
PTFE : Polytetrafluoroethylene
HDPE : High-density polyethylene
PS : Polystyrene
PC : Polycarbonate
PMMA : Polymethyl methacrylate

greater variation possibly due to the porosity. Therefore, not only the average value but also the extreme values of hardness should be considered in scratching problems, since scratching may occur by the hardest point of the material. As shown in Figure 3.8, the local hardnesses of polymer pins are approximately normally distributed. Estimation of maximum hardness of the pin, from $H_{avg}+3\sigma$, where the σ is the standard deviation of the local hardness, gives the maximum hardness of the PS pin to be about 617 MPa, which is much less than the measured maximum hardness of pad asperity hardness, 915 MPa. Therefore, the Polymethyl methacrylate (PMMA) pin also selected, as its maximum hardness can be estimated as 977 MPa, which is close to that of the pad asperity.

For a single asperity to deform fully-plastically, the normal load applied on the polymer pin should be significantly greater than the yield load. Figure 3.9 shows both extreme cases of contact: elastic at the onset of pin yielding and fully-plastic. The normal load at the onset of pin yielding, P_y, can be given as [Johnson, 1985]

$$P_y = \frac{\pi^3}{48}\frac{H_p^3}{E_p^2}R_p^2 \tag{3.4}$$

where E_p and H_p, respectively, are the Young's modulus and hardness of the polymer pin and R_p is the radius of the pin tip. If the pin is compressed with a normal load smaller than P_y, it will deform elastically and the pressure distribution in the contact will be Hertzian. As the load far exceeds P_y, the pin will deform fully-plastically and the pressure distribution in the contact region will be uniform, and its value will be the hardness of the pin. Thus the contact radius, a_c, for fully-plastic deformation of the tip of the pin can be estimated by

$$a_c = \sqrt{\frac{P}{\pi H_p}} \quad , \quad (P >> P_y) \tag{3.5}$$

Johnson experimentally revealed that the deformation reaches the fully-plastic case when the normal load is about 400 times greater than the yield load [Johnson, 1985]. The radius of the pin tip used in the experiments is 40 ± 10 μm. Using Eq. (3.4) and the

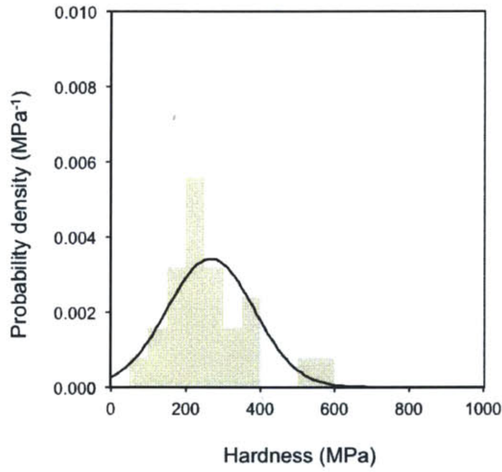

(a) PS

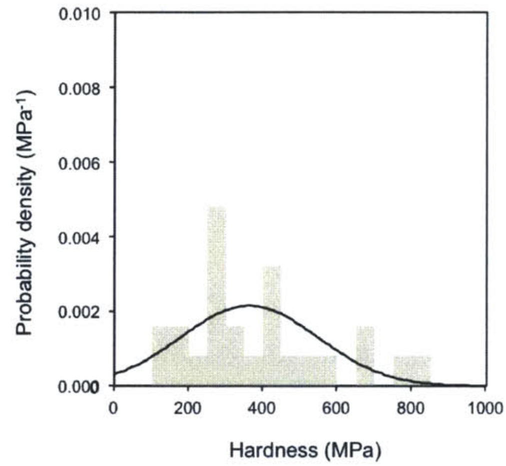

(b) PMMA

Figure 3.8. Probability density of hardness for PS and PMMA pins.

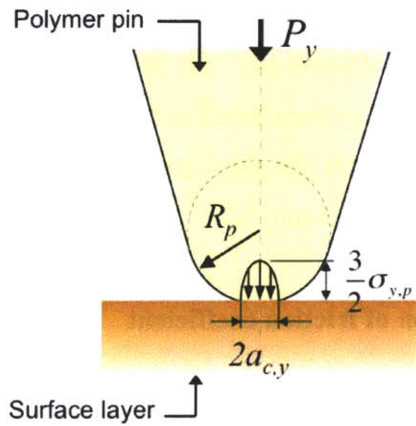

(a) elastic,
but at the onset of yielding

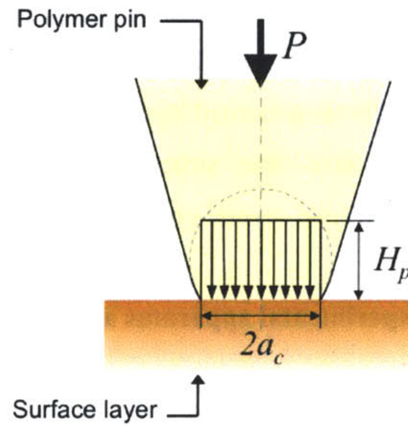

(b) fully-plastic

Figure 3.9. Schematic of contact between the solid polymer pin, at the exremum cases of deformation, and the surface layer.

determined hardnesses, The yield loads for both PS and PMMA pins can be estimated to be about 25 mN. Accordingly, in all sliding experiments 1 N was applied to the pin, which is about 400 times the yield load. Then, from Eq. (3.5), the contact radius can be estimated to be 30 μm. Figure 3.10 shows the image of the PMMA pin tip before and after loading against a flat coating under a normal load of 1 N. As can be seen, the spherical pin tip was permanently deformed upon the application of 1 N load, and the radius of the flattened area was about 35 μm.

3.3.2. Monolithic and patterned surface layers

Three monolithic layers, Cu, low-*k*, and SiO_2, of about 1 μm thickness on Si substrate, were tested in the experiments. The Young's modulus and hardness of the monolithic layers were determined by nano-indentation, Table 3.2, using the same experimental conditions as those used for polymer pins. Interestingly, while the properties of dielectric materials, low-*k* and SiO_2, have very small variation, those of the Cu layer shows relatively large variation. Since scratching will occur in the layer surface at the softest point, extreme values, particularly the minimum hardness of the layer, are important in scratching problems. The probability densities of local hardnesses are normally distributed, Figure 3.11, and therefore, the minimum hardness of surface layers can be estimated from $H_{avg} - 3\sigma$; 0.77 GPa for Cu, 2.32 GPa for low-*k* and 7.68 GPa for SiO_2.

Two different patterned layers, Cu/low-*k* and Cu/SiO_2, were tested in the experiments. All patterns have "line" structures. While all patterns have the same area density of 0.5, the linewidth span several orders of magnitude as listed in Table 3.3.

3.3.3. Experimental apparatus and determination of friction coefficient

The sliding experiments were conducted on a reciprocating friction apparatus, using solid polymer pins instead of pads in Figure 2.11. The polymer pin was loaded against the wafer by a deadweight, and the wafer was reciprocated by a linear stage at a speed of 7 mm/s. As the pin is slid over the top layer of the wafer, a strain gage bridge measured the frictional force. The friction coefficient between the two surfaces was determined

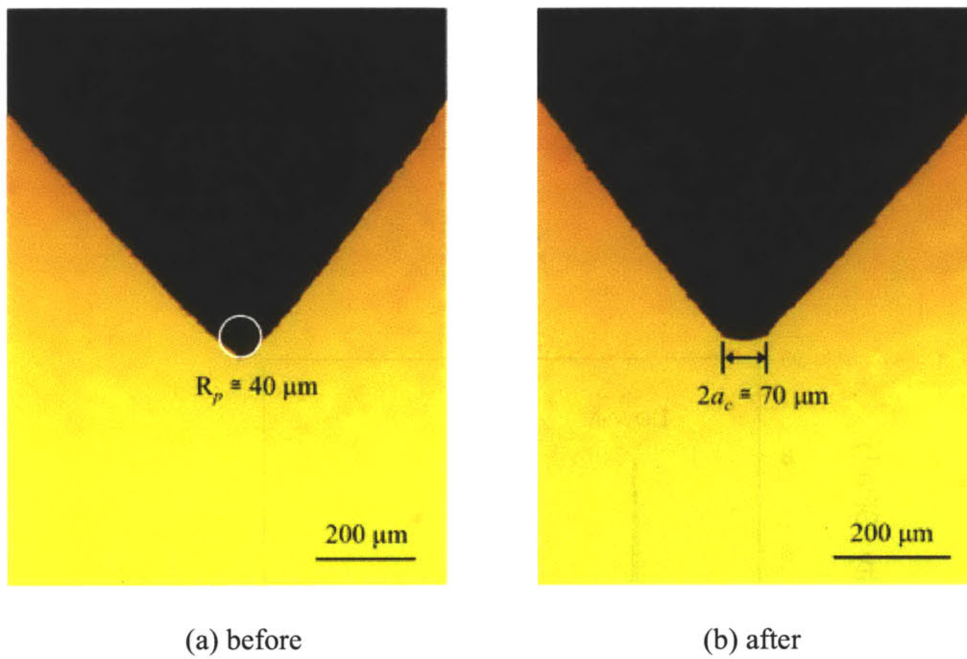

(a) before (b) after

Figure 3.10. Images of a PMMA pin before and after applying a normal load of 1N.

Table 3.2. Statistical results of determined mechanical properties of monolithic surface layers.

Material	Hardness Avg. (GPa)	Hardness Std. Dev. (GPa)	Hardness C.V.	Young's modulus Avg. (GPa)	Young's modulus Std. Dev. (GPa)	Young's modulus C.V.
Cu	1.56	0.26	0.17	126.50	12.51	0.10
Low-*k*	2.47	0.05	0.02	26.38	0.45	0.02
SiO_2	8.00	0.11	0.01	76.10	0.80	0.01

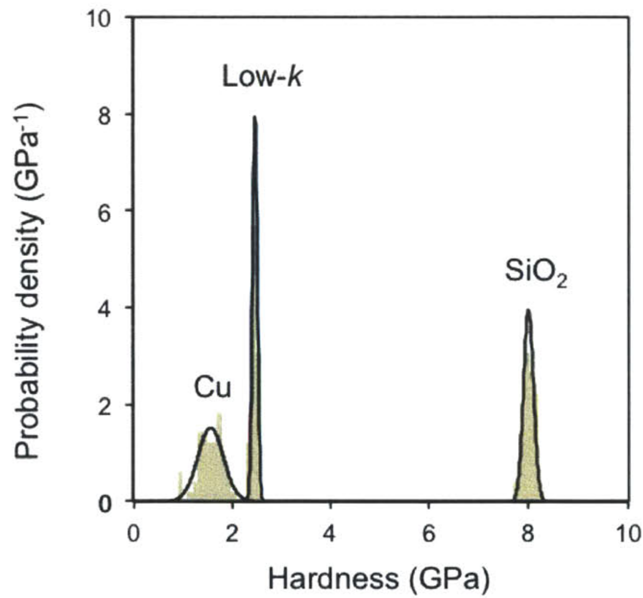

Figure 3.11. Probability density of hardness values of monolithic layers.

Table 3.3. Linewidths of tested patterned Cu/dielectric layers.

Pattern	Subdie	Cu linewidth (μm)	Dielectric linewidth (μm)
Cu/SiO_2	S1	100	100
	S2	25	25
	S3	2	2
	S4	0.5	0.5
Cu/Low-*k*	K1	4.5	4.5
	K2	0.35	0.35
	K3	0.05	0.05

as the ratio of the frictional force to the applied normal load. The solid polymer pins, PS and PMMA, were slid over the monolithic Cu, low-*k*, and SiO_2 layers, and over patterned Cu/low-*k* and Cu/SiO_2 layers. Deionized water was used as a "lubricant" in the sliding tests.

3.3.4. Results and discussion

For monolithic Cu, low-*k* and SiO_2 layers, as the fully-plastically deformed PMMA and PS pins slide over, scratching will occur only if Eq. (3.1a) or (3.1b) is satisfied, i.e., only if the pin-to-layer hardness ratio and the friction coefficient fall in the 'scratching regime' of the scratch-regime map, Figure 3.4. According to the scratch-regime map constructed for the PMMA pin and monolithic layers based on the determined hardness values and friction coefficient, Figure 3.12a, Cu and low-*k* fall in the 'scratching regime' whereas SiO_2 falls in the 'no-scratching regime.' Results of the sliding experiment, Figure 3.12b-d, indeed show that the PMMA pin scratches Cu and low-*k* but not SiO_2. Similarly, the scratch-regime map constructed for a PS pin and monolithic layers, Figure 3.13a, and the experimental results, Figure 3.13b and c, show that the PS pin scratches Cu but not the low-*k* layer.

In light of the above results, scratching of patterned Cu/dielectric layers that have relatively wide lines can be readily predicted. Pattern S1, for example, has Cu and SiO_2 linewidths of 100 μm, which are greater than the contact diameter of the PMMA pin, about 70 μm. It is expected, therefore, that the PMMA pin will scratch only Cu lines but not the SiO_2 lines, Figure 3.14a. The experimental results, Figure 3.14b, indeed show that scratches were generated on the Cu lines but not on the SiO_2 lines. It may be noted, additionally, that as the Cu and SiO_2 linewidths become smaller than the contact diameter, of 25 μm and 2 μm, the PMMA pin still scratched only the Cu lines but not the SiO_2 lines, Figure 3.14c and d. That is, the experimental results of patterns with linewidths larger than about a micrometer follow the scratch criteria of wide lines. The pin may scratch both the Cu and dielectric wide lines only if it can scratch each material individually. In the case of patterned Cu/low-*k*, for example, the PMMA pin scratched the Cu and low-*k* lines, of a patterned surface with 4.5 μm linewidths, Figure 3.15a and b,

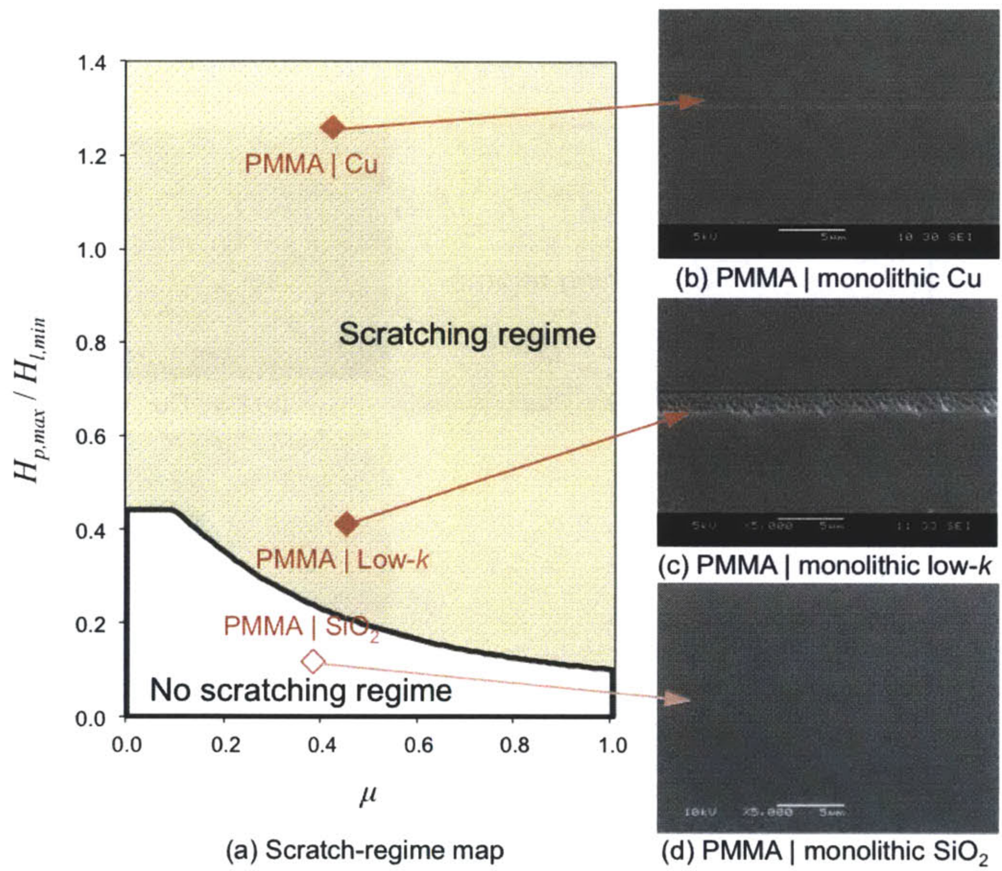

Figure 3.12. Scratch-regime map for PMMA pin and monolithic Cu, low-*k*, SiO_2 layers. The SEM images are the surfaces of the monolithic layers after the pin sliding experiments.

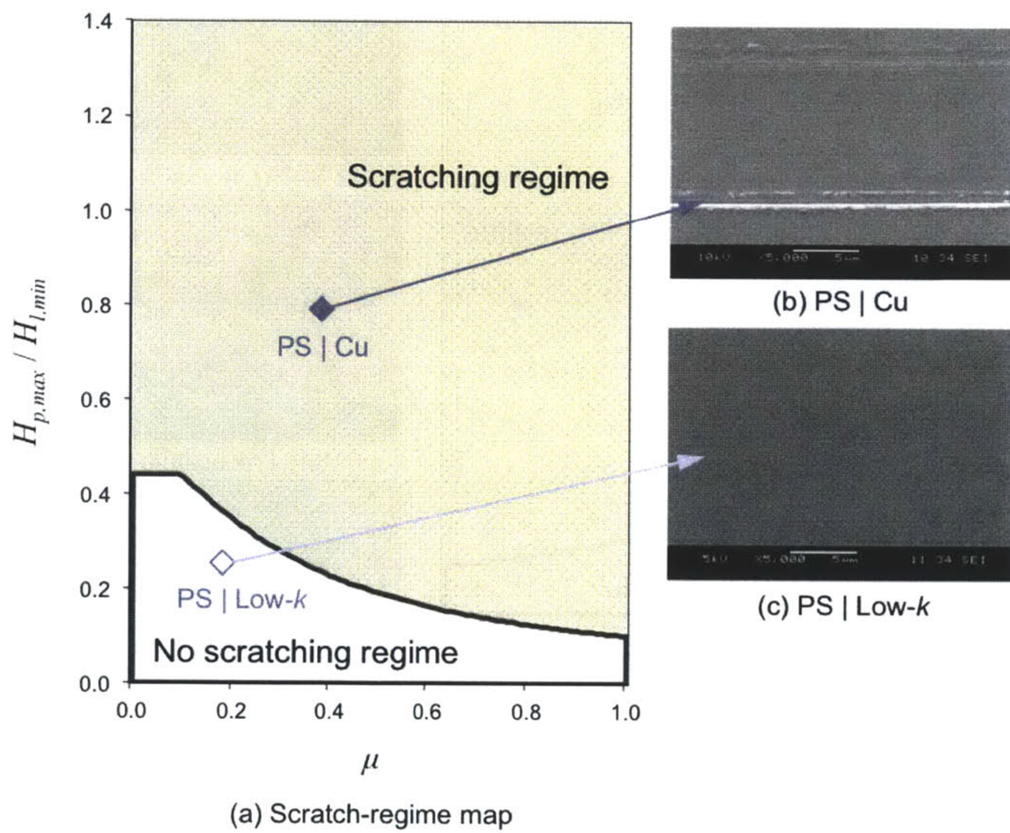

(a) Scratch-regime map

Figure 3.13. Scratch-regime map for PS pin and monolithic Cu, low-*k* layers. The SEM images are the surfaces of the monolithic layers after the pin sliding experiments.

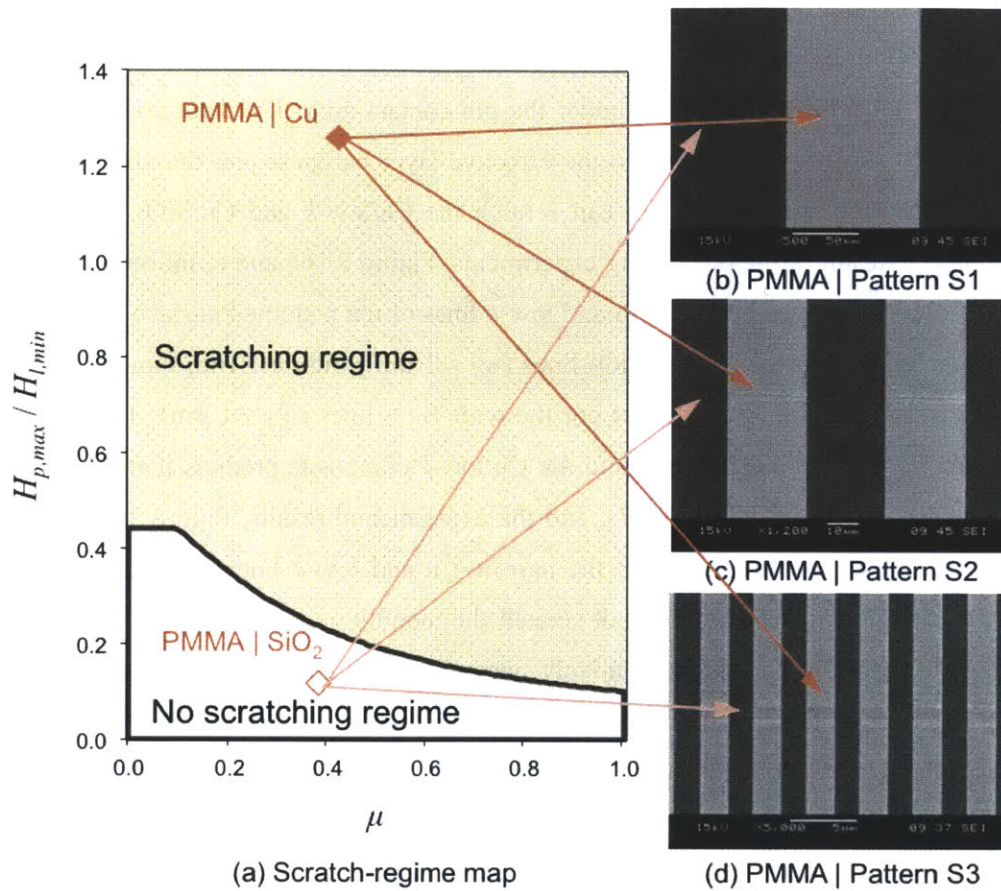

Figure 3.14. Scratch-regime map for PMMA pin and monolithic Cu, SiO_2 layers. The SEM images are the surfaces of the patterned Cu/SiO_2 layers with wide lines ($w_{Cu} > 1$ μm and $w_d > 1$ μm) after the pin sliding experiments.

the PMMA pin can scratch both monolithic layers. The PS pin, however, scratches only the Cu lines but not the low-k lines, Figure 3.15a and c, since the PS pin does not scratch the monolithic low-k layer.

By contrast, patterns that have Cu and dielectric lines much narrower than the asperity contact diameter may behave as a composite layer, whose effective hardness is estimated by Eq. (3.2b), Table 3.4. Pattern K3, for example, has Cu and low-k linewidths of 0.05 μm, about 150 times smaller than the contact diameter of the PMMA pin. That is, about 150 Cu and dielectric lines will be under the pin contact area. The scratch-regime map based on the ratio of pin hardness to the effective layer hardness and the coefficient of friction shows that the PMMA pin can scratch the Cu/low-k and Cu/SiO_2 composite, Figure 3.16a. Result of the pin sliding experiments, Figure 3.16b and c, indeed show that the PMMA pin scratches both the Cu and low-k lines of the patterned surface. Moreover, the pin scratches even the narrow SiO_2 lines ($w_d < 1$ μm), Figure 3.16d, though it could not scratch the monolithic SiO_2 layer nor the wide SiO_2 lines ($w_d > 1$ μm). The scratch-regime map constructed for PS pin and the Cu/low-k composite predicts that the PS pin may scratch the surface, Figure 3.17a, and the experimental results, Figure 3.17b and c, validates that the pin scratches both the narrow Cu and low-k lines. The results again show that the PS pin, which could not scratch the monolithic low-k layer or wide low-k lines ($w_d > 1$ μm), does scratch relatively narrow low-k lines ($w_d < 1$ μm). Thus, the scratch behavior of patterns with linewidths smaller than a micrometer is different from those with larger linewidths.

3.4. Pad sliding experiments on patterned Cu/dielectric layers

As seen previously in Figure 3.1, the IC1000 pads scratches both the Cu and low-k lines regardless of the pattern linewidths, whereas Pad A scratches only the relatively wide Cu lines. Similar to the results of the pin sliding experiments, the scratching results by pad asperities can be explained by the advanced scratching models. That is, as some of the asperities in contact reach to the extreme case of asperity deformation, fully-plastic, and slide over the patterned Cu/dielectric layers, such asperities will scratch the patterned

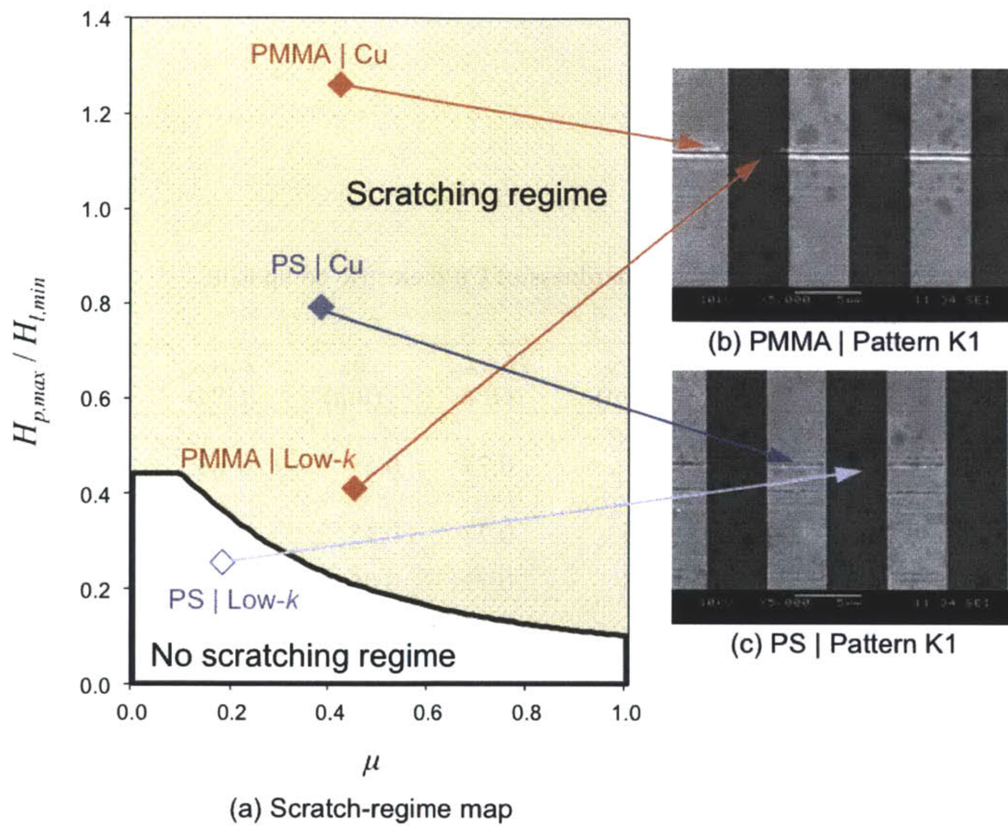

Figure 3.15. Scratch-regime map for PMMA, PS pins and monolithic Cu, low-*k* layers. The SEM images are the surfaces of the patterned Cu/low-*k* layers with wide lines ($w_{Cu} > 1$ μm and $w_d > 1$ μm) after the pin sliding experiments.

Table 3.4. Estimated effective hardness of Cu/dielectric composite.

Pattern	Subdie	w_{Cu} (μm)	$H_{Cu,min}$ (GPa)	w_d (μm)	$H_{d,min}$ (GPa)	$H_{l,eff}$ (GPa)
Cu/SiO_2	S4	0.5	0.77	0.5	7.68	4.22
Cu/low-*k*	K2	0.35	0.77	0.35	2.33	1.55
	K3	0.05	0.77	0.05	2.33	1.55

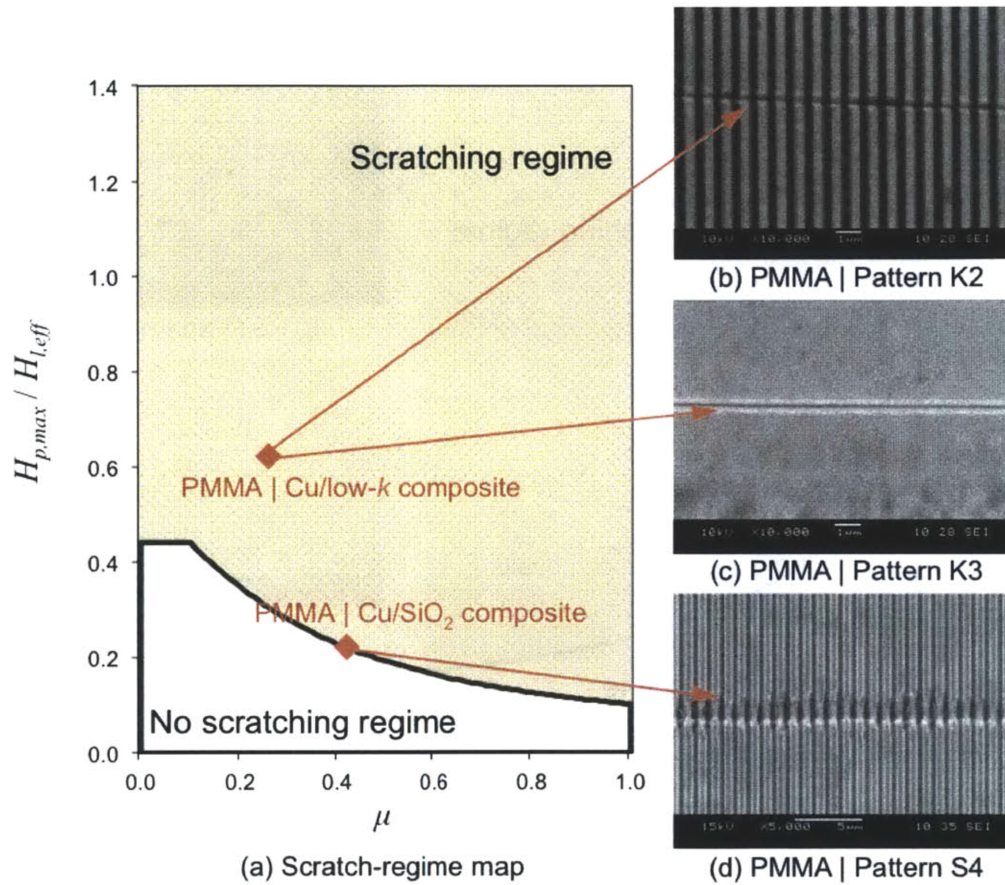

Figure 3.16. Scratch-regime map for PMMA pin and composite Cu/low-*k*, Cu/SiO_2 layers. The SEM images are the surfaces of the patterned Cu/low-*k* and Cu/SiO_2 layers with narrow lines ($w_{Cu} < 1$ μm and $w_d < 1$ μm) after the pin sliding experiments.

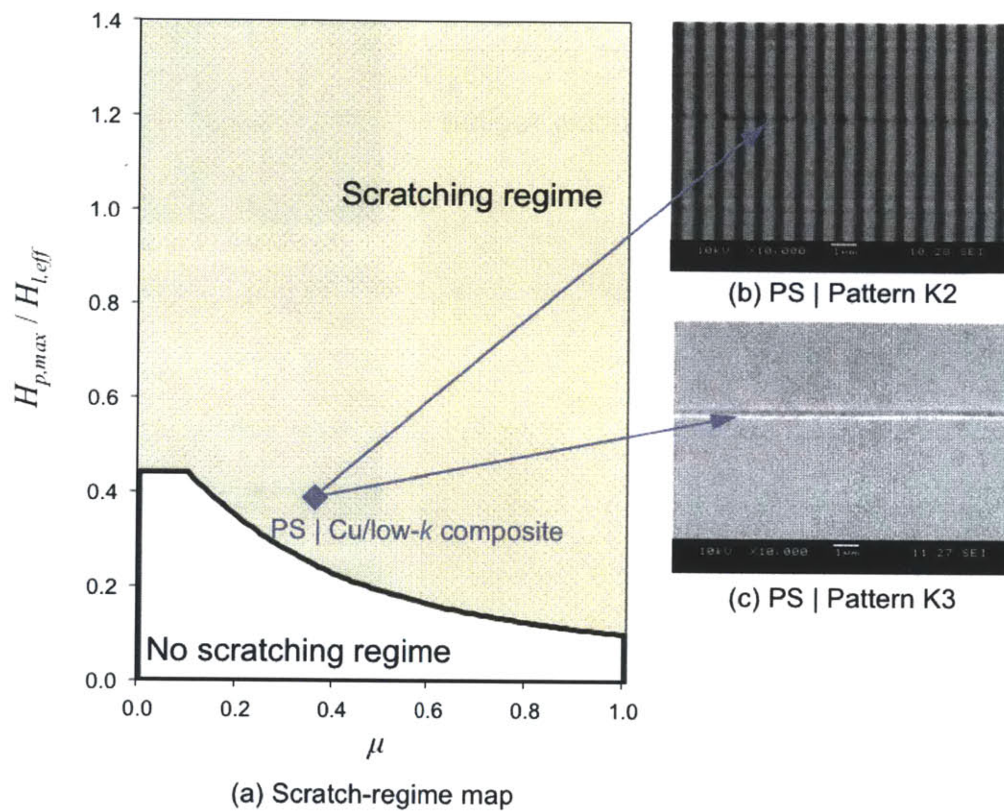

Figure 3.17. Scratch-regime map for PS pin and composite Cu/low-k layers. The SEM images are the surfaces of the patterned Cu/low-k layers with narrow lines ($w_{Cu} < 1$ μm and $w_d < 1$ μm) after the pin sliding experiments.

lines only if the scratching criteria are satisfied. The scratching criteria depend on the relative hardness ratio and the coefficient of friction between the pad asperity and surface layer materials, and depend on the relative size of the line structures of the patterns.

The pad asperity hardness, H_a, was determined by nano-indentation, Table 3.1. The variation of asperity hardness, however, was significantly large, and furthermore, the distribution is known to be not normal, rather to be close to log normal [Eusner *et al.*, 2011]. For determination of the maximum asperity hardness, $H_{a,max}$. accordingly, 100 indentations were conducted on each pad. The measured maximum hardness, 915 MPa for IC1000 and 162 MPa of Pad A, were considered in the theoretical predictions. The friction coefficients between the pad asperities and surface layers were determined on the sliding friction apparatus using a circular pad disk of 20 mm in diameter.

Figure 3.18a shows the scratch-regime map constructed for the pads and the monolithic layers. The relative hardness and interfacial friction between an IC 1000 pad and a Cu layer, and between an IC1000 pad and a low-*k* layer, both fall in the 'scratching regime' of the map, which indicates that the pad can scratch both layers. Therefore, the pad is expected to scratch the relatively wide Cu and low-*k* lines of the patterned surface, Figure 3.18b. In contrast, the relative hardness and interfacial friction between Pad A and Cu layer fall in the 'scratching regime,' whereas those between Pad A and low-*k* layer fall in the 'no-scratching regime' of the map. Accordingly, Pad A can only scratch the wide Cu lines but not the low-*k* dielectric, Figure 3.18c.

Figure 3.19a shows the scratch-regime map constructed for the pads and the composite Cu/low-*k* layers, which have same area density of Cu and low-*k* lines. The conditions between the IC1000 pad and the composite layer fall in the 'scratching regime,' and thus, the pad scratches the relatively narrow Cu and dielectric lines, Figure 3.19b. However, as the conditions between the Pad A and the composite layer fall in the 'no-scratching regime,' Pad A does not scratch any narrow lines, Figure 3.19c.

In light of the sliding experimental results using both the polymer pins and CMP pads, the scratch-regime map for monolithic Cu and dielectric layers can be used to predict the pad scratching on patterned Cu/dielectric layers with relatively wide lines ($w_{Cu} > 1$ μm and $w_d > 1$ μm), whereas the map for the composite layers can be used to predict those with relatively narrow lines ($w_{Cu} < 1$ μm and $w_d < 1$ μm). To eliminate scratching

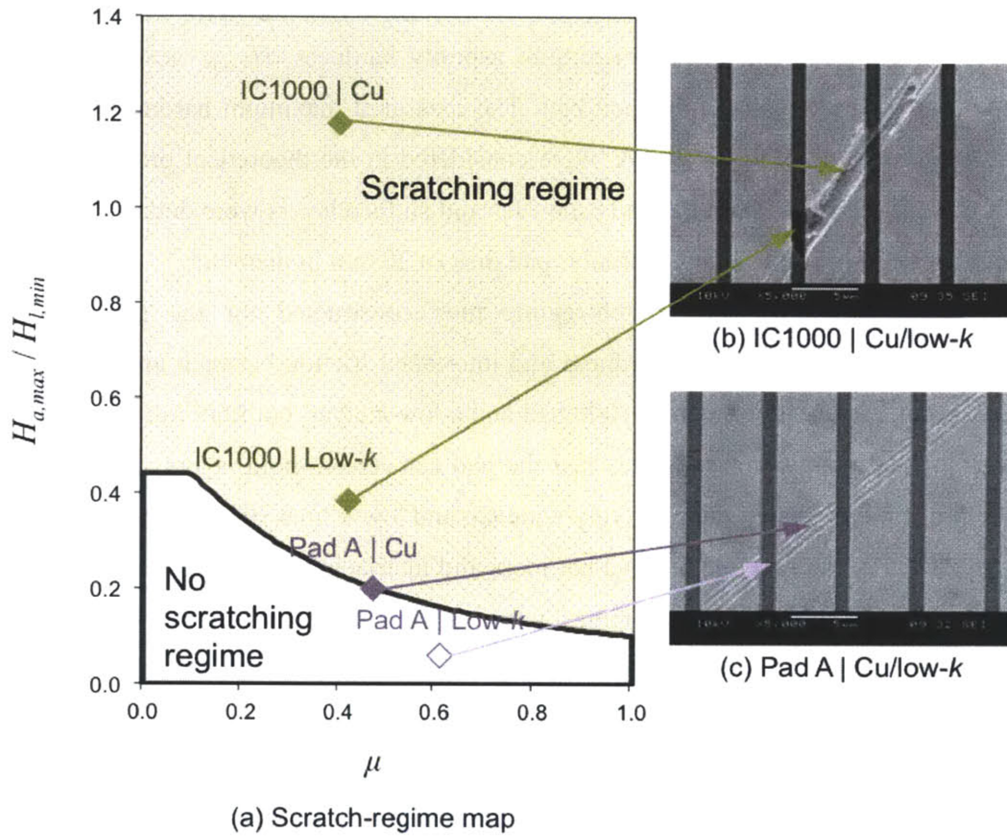

Figure 3.18. Scratch-regime map for the pads (IC1000 pad and Pad A) and monolithic layers (Cu and low-*k*), applicable to wide Cu and low-*k* lines. The SEM images are the surfaces of the patterned Cu/low-*k* layers with relatively wide lines (w_{Cu} = 4.5 μm and w_d = 1 μm) after the pad sliding experiments.

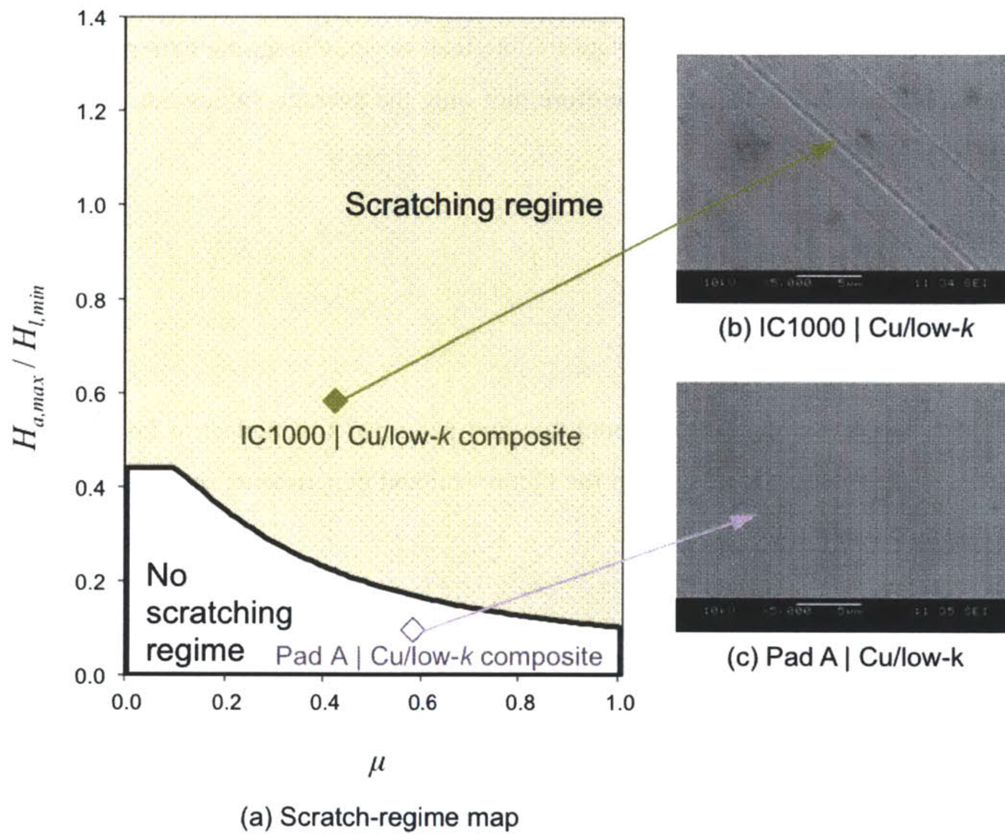

Figure 3.19. Scratch-regime map for the pads (IC1000 pad and pad A) and composite Cu/low-*k* layers. The SEM images are the surfaces of the patterned Cu/low-*k* layers with relatively narrow lines (w_{Cu} = 0.05 μm and w_d = 0.05 μm) after the pad sliding experiments.

by the pads, therefore, all of the relative hardness ratio and the surface friction between the pad and both monolithic and composite layers should fall in the 'no-scratching regime' of the maps. It is apparent that both the hardness ratio and the friction coefficient between the pad and various surface layers are important. However, if the hardness of the pad asperities can be controlled to be a tenth of the softer monolithic Cu or dielectric layer hardness, the pad will scratch neither the wide nor the narrow lines structures even at high frictional contact. It is important to note that, in scratching, the extreme hardness values should be considered, and therefore, not only the average values but the extreme values must be controlled.

3.5. Summary

In this chapter, scratching of monolithic and patterned Cu/ dielectric layers by soft asperities was investigated. Based on the theoretical and experimental investigations, the following conclusions can be drawn:

(1) When fully-plastically deformed pad asperities slide over the wafer, the ratio of pad-to-layer hardness and the coefficient of friction primarily determine whether the asperities scratch the relatively hard layers. For the lamellar Cu/dielectric line structures, the scratch criteria depend, additionally, on the relative widths of patterned lines compared with the contact diameter.

(2) If the Cu and dielectric lines are wider than the contact diameter, $w_{Cu} > 2a_c$ and $w_d > 2a_c$, scratching of each line is independent of the other, i.e., whether an individual line gets scratched or not depends solely on its hardness and the interfacial friction with respect to the asperity. Results of sliding experiments on patterns with linewidths greater than a micrometer indeed confirm that polymer pins scratch the Cu lines but not the dielectric lines, in accordance with the scratch criteria.

(3) If the Cu and dielectric lines are much narrower than the contact diameter, $w_{Cu} << 2a_c$ and $w_d << 2a_c$, however, the patterned layer behaves as a composite structure with an "effective hardness" determined by the pattern density and the hardness of

Cu and dielectric following the rule-of-mixtures. Therefore, Cu lines and even low-*k* and SiO_2 lines can be scratched if the ratio of pad hardness to effective hardness and the coefficient of friction satisfy the scratch criteria. Results of sliding experiments, on patterns with linewidths smaller than a micrometer, again show that polymer pins scratch both the Cu and dielectric lines since the scratch criteria based on the effective hardness are satisfied. It must be emphasized that the polymer pins scratched the narrow dielectric lines even though they could not scratch the wide dielectric lines or monolithic layers.

(4) The advanced pad scratching model well explains the scratching results after sliding the two different CMP pads on the patterned Cu/low-*k* layers. To minimize pad scratching in CMP, therefore, softer polishing pads and/or low friction slurries must be used. Scratching of patterned structures by pad asperities can be mitigated if the hardness of the polishing pad is about a tenth of the softest material in the structure.

Nomenclature

a_c	contact radius [m]
$a_{c,y}$	contact radius, at the onset of yielding [m]
d	separation distance between the centerline of pad surface and surface layer [m]
f_{Cu}	volume fraction of Cu lines
f_d	volume fraction of dielectric lines
E_p	Young's modulus of solid pin [N m^{-2}]
H_a	hardness of asperity [N m^{-2}]
H_{Cu}	hardness of monolithic Cu layer [N m^{-2}]
H_d	hardness of monolithic dielectric layer [N m^{-2}]
H_l	hardness of surface layer [N m^{-2}]
$H_{l,eff}$	effective hardness of composite layer [N m^{-2}]
H_p	hardness of solid pin [N m^{-2}]
P	normal load [N]
P_y	normal load at the onset of yielding [N]
p	nominal pressure [N m^{-2}]
R_a	radius of asperity [m]
R_p	radius of pin tip [m]
v_r	relative velocity [m s^{-1}]
w_{Cu}	width of Cu lines [m]
w_d	width of dielectric lines [m]
z_a	asperity height [m]
δ	approach of distant points [m]
$\delta_{f\text{-}p}$	approach of distant points at the onset of fully-plastic asperity deformation [m]
δ_y	approach of distant points at the onset of asperity yielding [m]
λ	pitch of the patterned lines ($= w_{Cu} + w_d$) [m]
μ	coefficient of friction
$\sigma_{y,a}$	yield strength of asperity [N m^{-2}]
$\sigma_{y,p}$	yield strength of pin [N m^{-2}]

References

Elmufdi, C. L. and Muldowney, G. P., 2006, "A novel optical technique to measure pad-wafer contact area in chemical mechanical planarization," *Mater. Res. Soc. Symp. Proc.*, vol. 914, 0914-F12-06 (6pp).

Eusner, T., Saka,, N. and Chun, J.-H., 2011, "Breaking-in a pad for scratch-free, Cu chemical-mechanical polishing," *J. Electrochem. Soc.*, vol. 158, no. 4, pp. H379-H389.

Fan, W., 2012, "Advanced modeling of planarization processes for integrated circuit fabrication," Ph.D. Thesis, Department of Electrical Engineering and Computer Science, MIT, Cambridge, MA.

Gray, C., Rogers, C., Manno, V. P., White, R., Moinpour, M. and Anjur, S., 2007, "Determining pad-wafer contact using dual cmmission laser induced fluorescence," *Mater. Res. Soc. Symp. Proc.*, vol. 991, 0991-C01-04 (12pp).

Greenwood, J. A. and Williamson, J. B. P., 1966, "Contact of nominally flat surfaces," *Proc. Royal Soc. London A*, vol. 295, pp. 300-319.

Johnson, K. L., 1885, *Contact Mechanics*, Cambridge University Press, Cambridge, UK.

Kim, H. S., 2000, "On the rule of mixtures for the hardness of particle reinforced composites," *Mater. Sci. Eng. A*, vol. 289, pp. 30-33.

Liou, J. W., Chen, L. H. and Lui, T. S., 1995, "The concept of effective hardness in the abrasion of coarse two-phase materials with hard second-phase particles," *J. Mater. Sci.*, vol. 30, pp. 258-262.

McCool, J. I., 1986, "Comparison of models for the contact of rough surfaces," *Wear*, vol. 107, pp. 37-60.

Sorooshian, J., Borucki, L., Stein, D., Timon, R., Hetherington, D. and Philipossian, A., 2005, "Revisiting the removal rate model for oxide CMP," *ASME J. Tribol.*, vol. 127, pp. 639-651.

Vasilev, B., Bott, S., Rzehak, R., Liske, R. and Bartha, J. W., 2013, "A method for characterizing the pad surface texture and modeling its impact on the planarization in CMP," *Microelectronic Eng.*, vol. 104, pp. 48-57.

Weihs, T. P., Barbee, T. W. and Wall, M. A., 1993, "Using the rule of mixtures to examine the hardness of Cu/Cu-Zr multilayers," *Mater. Res. Soc. Symp. Proc.*, vol. 308, pp. 753-758.

Zhao, Y., Maietta, D. M. and Chang, L., 2000, "An asperity microcontact model incorporating the transition from elastic deformation to fully plastic flow," *ASME J. Tribol.*, vol. 122, pp. 86-93.

CHAPTER 4

MITIGATION OF PAD SCRATCHING BY TOPOGRAPHY CONTROL

4.1. Introduction

In Chapters 2 and 3, it was shown that the pad, even though soft, can scratch the relatively hard top layers being polished when the hardness ratio and the interfacial friction between the pad asperities and the surface layer satisfy certain conditions. In order to reduce the pad-induced scratching, therefore, using softer polishing pads or adding lubricants in the slurry can be suggested. However, it was additionally shown in Chapter 2 that the pad topography also affects the pad scratching. In this chapter, accordingly, pad scratching models are presented in terms of the topographical and the mechanical properties of pad asperities. The key topographical parameters that promote pad scratching are identified. Based on the contact mechanics models, control of the topographical parameters of the polishing pads is suggested and found to be an effective method of scratch mitigation. Results of sliding experiments validate the theoretical prediction that scratching by the CMP pads can be mitigated by modifying their topography. It is observed, additionally, that material removal rate is enhanced by topography modification. Some contents in this chapter appear as published in Kim, S., Saka, N., Chun, J.-H. and Shin, S.-H., 2013, "Modeling and mitigation of pad scratching in chemical-mechanical polishing," *Annals of the CIRP*, vol. 62, pp. 307-310.

4.2. The effect of pad topography on scratching

At the typical polishing pressures employed in CMP, about 7 - 35 kPa (1 - 5 psi), the real contact area is one percent or less of the nominal contact area [Greenwood and

Williamson, 1966; Elmufdi and Muldowney, 2006; Gray *et al.*, 2007]. Thus, only the tallest asperities of the pad surface contact the layer being polished, and hence the geometry and the mechanical properties of these asperities play a dominant role in pad scratching. When n asperities per unit area contact the smooth, flat surface layer, the number of asperities in contact per unit area, n_c, is given in Eq. (2.27) and is

$$n_c = n\int_d^\infty \phi(z_a)\,dz_a = n\exp\left(-\frac{d}{\sigma_z}\right) \tag{4.1}$$

where d is the separation distance between pad and layer surfaces, z_a is the asperity height and σ_z is the standard deviation of asperity heights. As discussed in the previous chapters, scratching is primarily by the plastically deformed asperities in the contact, if the relative hardness and the interfacial friction satisfy the scratch criteria for the fully-plastic case. That is, a pad asperity can scratch the surface layer if the combination of hardness ratio and the friction coefficient falls in the "scratch regime" of the map, given in Figure 2.3b. For the IC1000 pad and a Cu layer, and a friction coefficient (between the two surfaces in water) of 0.4, elastically deformed asperities of the IC1000 pad do not scratch the Cu layer, whereas plastically deformed asperities will. The number of plastically deformed asperities, therefore, essentially determines the number of scratches.

In order for an asperity to deform plastically, the approach of distant point, δ (= $z_a - d$), should be greater than the elastic limit, δ_y, which is given as [Johnson, 1985]

$$\delta_y = \frac{\pi^2}{16}\left(\frac{H_a}{E_a}\right)^2 R_a \tag{4.2}$$

where H_a and E_a are the hardness and Young's modulus of pad asperities and R_a is the asperity radius. The proportion of plastic asperities among those in contact, n_p / n_c, accordingly, is given in Eq. (2.29-b) and is

$$\frac{n_p}{n_c} = \exp\left(-\frac{1}{\psi^2}\right) = \exp\left(-\frac{\pi^2}{16}\frac{H_a^2}{E_a^2}\frac{R_a}{\sigma_z}\right) \tag{4.3}$$

where ψ is the plasticity index defined as [Greenwood and Williamson, 1966]

$$\psi \equiv \left(\frac{\sigma_z}{\delta_y}\right)^{1/2} = \frac{4}{\pi}\frac{E_a}{H_a}\left(\frac{\sigma_z}{R_a}\right)^{1/2} \tag{4.4}$$

The probability of asperities to deform plastically solely depends on the plasticity index, ψ, Figure 4.1. Because pad scratching is mainly due to the plastically deformed asperities, scratching can be mitigated, from Eq. (4.3), by decreasing the value of ψ, i.e., by increasing H_a/E_a and R_a/σ_z. While H_a/E_a is the stronger parameter, in general H_a and E_a are proportional to each other for various polymers and thus cannot be varied independently. Therefore, the most effective means of scratch mitigation seems to be by increasing the value of R_a/σ_z, i.e., by modifying pad topography.

4.3. Pad topography control by asperity-flattening

Surfaces of the CMP pads are porous, Figure 4.2, and relatively rough, Figure 4.3. The average pore size is about 50 μm and the average roughness is about 5 μm. The surface profile of a new IC1000 CMP pad manufactured by the Dow Chemical Co. is shown in Figures 4.3. Such topographical parameters, as the asperity height, z_a, and radius, R_a were determined by a Tencor P16 stylus profilometer. The topographical data is listed in Appendix A and is summarized in Table 4.1. Additionally, the Young's modulus and hardness, determined by a Hysitron TI900 nano-indenter, are also listed in Appendix B and summarized in Table 4.1.

To facilitate slurry flow and eliminate hydroplaning during CMP, the pad roughness is maintained by an *in situ* diamond conditioner [Borucki, 2002; McGrath and Davis, 2004]. Although the only means that can control the surface topography of the pad is diamond conditioning, it rather decreases R_a/σ_z, as discussed in Appendix D.

In order to reduce scratching in CMP, the semiconductor manufacturing industry has been adopting a method called "breaking-in" process. Before polishing wafers with a new

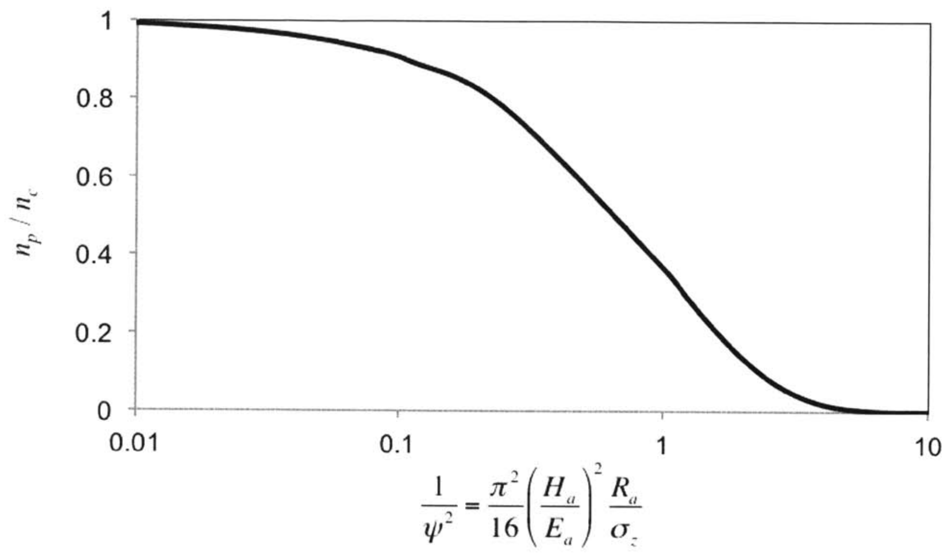

Figure 4.1. Proportion of plastically deformed asperities versus $1/\psi^2$.

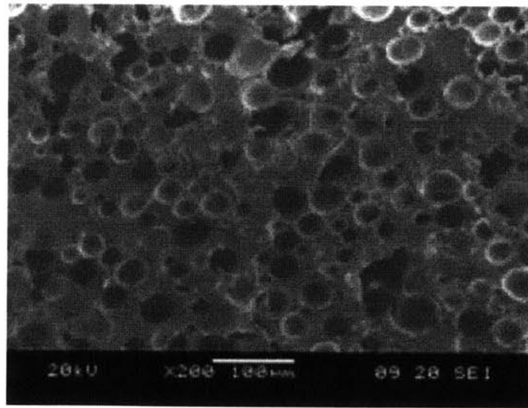

Figure 4.2. SEM image of a new IC1000 pad.

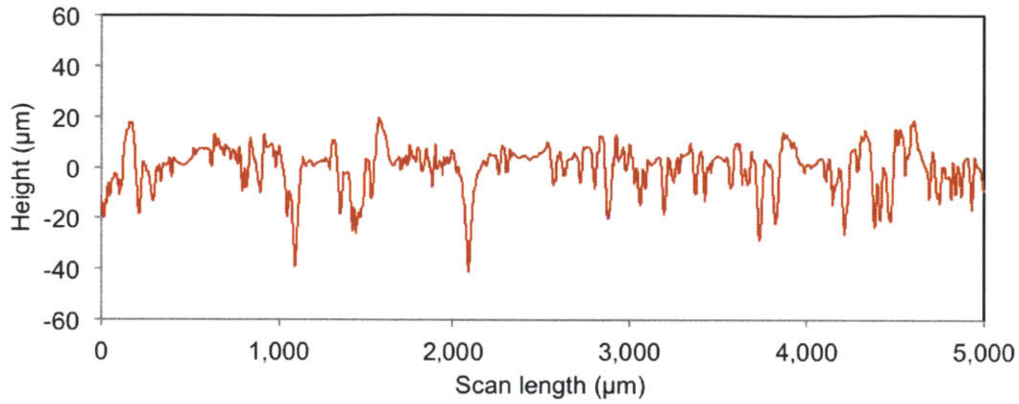

Figure 4.3. Surface profile of a new IC1000 pad; R_a = 23.5 μm, σ_z = 4.0 μm.

Table 4.1. Topographical parameters and mechanical properties of an IC1000 CMP pad, and of a monolithic Cu layer.

Material	Property	Avg.	Std.Dev.	C.V.*
CMP Pad	z_a (μm)	5.2	4.0	0.76
	R_a (μm)	23.5	10.7	0.46
	λ_a (μm)	102.4	70.1	0.69
	E_a (GPa)	2.2	1.5	0.67
	H_a (MPa)	290	220	0.76
Cu	E_l (GPa)	126.5	12.5	0.10
	H_l (MPa)	1,560	260	0.17

* Coefficient of Variation (C.V.) = Std. Dev./ Avg.

pad, the industry generally "breaks-in" the pad by polishing about 50 Cu-coated wafers while continuously roughening the pad surface using a diamond conditioner. About one to four hours are required for each new pad before its use. Moreover, it was experimentally determined that as more Cu wafers are used, and thus more "break-in" process time is allowed, scratching could be decreased [Luo *et al.*, 1998; Eusner *et al.*, 2011]. Therefore, time and costly consumables, such as wafers and slurry, are wasted more for less scratching. The major reason why the industry accepts this inefficient process is the lack of understanding of the mechanics and mechanisms of scratching. As shown in Table 4.2, typical "breaking-in" process used in the semiconductor industry may happen to increase the R_a / σ_z, so that the "broken-in" pad can reduce scratching. However, since the process is not optimized for increasing R_a / σ_z, it is inefficiently operated. Accordingly, novel processes, "asperity-flattening," are introduced for controlling the pad topography cost-effectively.

4.3.1. Compression by a smooth, flat plate

The simplest way of increasing the value of R_a / σ_z is by pressing, at high pressure, the pad asperities against a flat metal plate as shown in Figure 4.4. If the pressure is sufficiently high, the radius of the tall asperities will be increased and the height variation reduced, due to flattening, thus increasing the value of R_a / σ_z. Furthermore, by increasing the temperature of the metal plate, asperity-flattening can be accelerated. It should be noted, however, that the radii of the compressed asperities do not remain infinite and the height cannot be uniform since each flattened asperities springs back by elastic recovery [Kadin *et al.*, 2006; Jamari and Schipper, 2007].

For experiments, asperities of circular disks, 20 mm in diameter, of the IC1000 pad were flattened by pressing the specimens against a flat stainless steel plate, Figure 4.5. In flattening by a plate, a normal load of 400 N was applied, or an average pressure of 300 kPa. The hold time was 60 s. In elevated-temperature processing, the plate was heated to 185 °C before flattening. Figures 4.6a and b show the surface profiles of the asperity-flattened pads measured by the stylus profilometer.

Table 4.2. Asperity radius, standard deviation of asperity heights, their ratio, and the estimated plasticity indices of new and "broken-in" IC1000 pads ($E_a / H_a = 7.6$).

Parameter	New pad	"Broken-in" pad
R_a (μm)	23.5	53.8
σ_z (μm)	4.4	3.2
R_a / σ_z	5.3	16.8
ψ	4.0	2.4

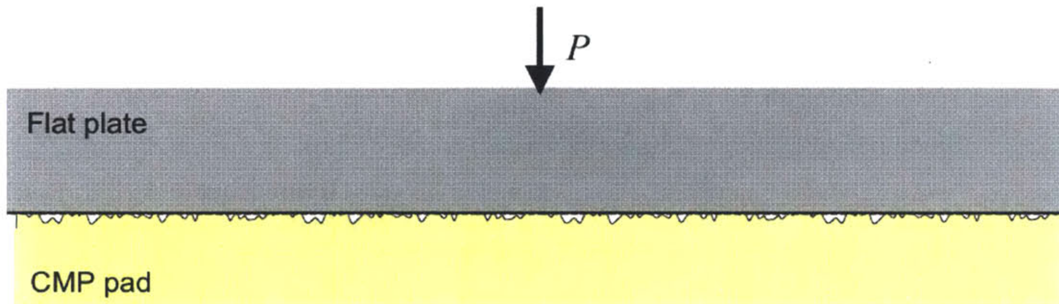

Figure 4.4. Schematic of asperity-flattening process by compression.

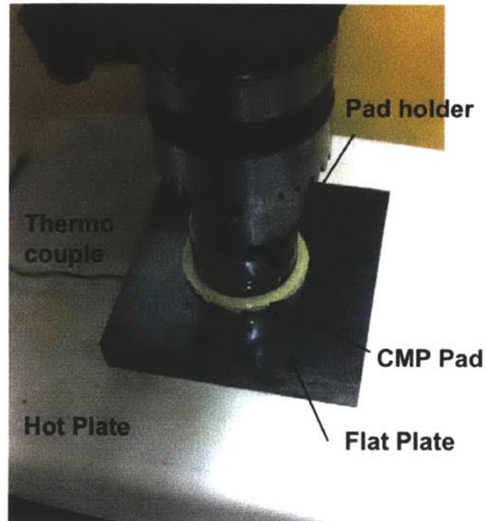

(a) photograph

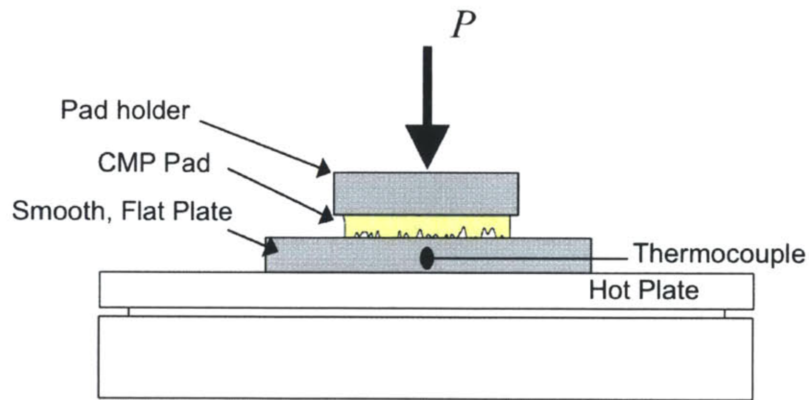

(b) schematic

Figure 4.5. Experimental system for asperity-flattening by compression.

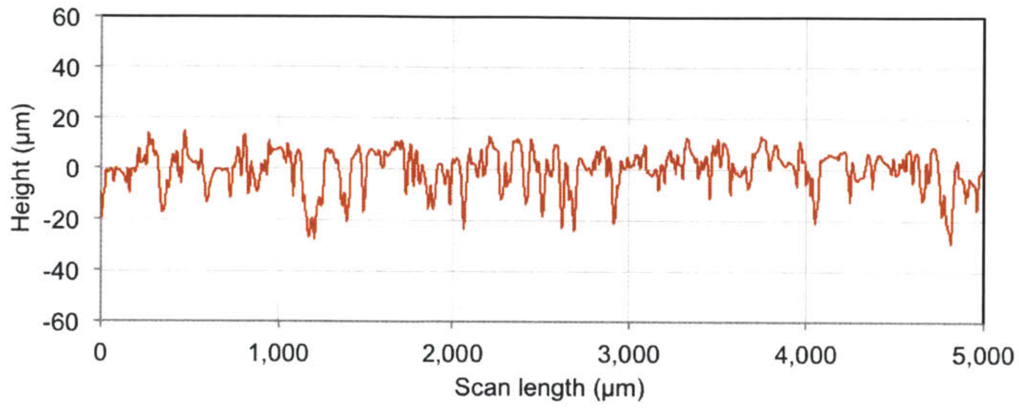

(a) compression at 25 °C; R_a = 39.5 μm, σ_z = 3.9 μm

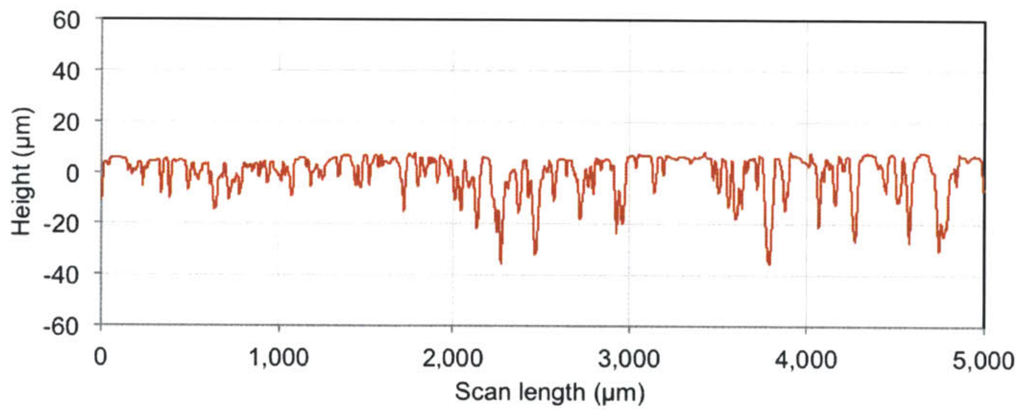

(b) compression at 185 °C; R_a = 173.4 μm, σ_z = 1.7 μm

Figure 4.6. Surface profiles of asperity-flattened IC1000 pads by compression.

4.3.2. Rolling/sliding by a smooth roller

Alternatively, the asperities can also be flattened by rolling or sliding a metal, or ceramic, roller over the pad surface at high enough load, Figure 4.7. If the radius of the roller is much greater than the asperity radius and the asperity spacing, subsurface deformation of the pad would be negligible, and only the pad asperities will deform and flatten [Rajendrakumar and Biswas, 1997]. A roller is preferred to a flat plate because it requires much less normal load to initiate plastic flow.

Asperities of circular disks, 20 mm in diameter, of the IC1000 pad were also flattened by rolling or sliding a stainless steel roller over the specimens, Figure 4.8. In flattening the asperities by rolling and sliding, a normal load of 1 kN/m was applied on the roller, or an average pressure of 2.3 MPa [Lo, 1969]. The sliding velocity was 5 mm/s. The surface profiles are shown in Figures 4.9a, b, and c.

4.4. Sliding experiments using asperity-flattened pads

Subsequent to asperity-flattening, scratching experiments were conducted on a reciprocating friction apparatus, Figure 2.11, using a new CMP pad and five differently asperity-flattened pads. The circular pad disks were slid over a 1 μm thick Cu layer. The normal load applied to the specimen was 2 N, which corresponds to an average pressure of 7 kPa (1 psi). The sliding velocity was 7 mm/s. Four experiments were conducted with each fresh pad, using deionized water as "lubricant." The scratches on the Cu layer were characterized by optical and scanning electron microscopes.

Table 4.3 lists the R_a and σ_z values of an IC1000 pad before and after asperity flattening under different process conditions. Not surprisingly, the increments in the R_a/σ_z values of asperity-flattened pads using a roller are greater than those of the pad flattened by a flat plate—due to the higher average pressure in rolling. Moreover, the pad flattened by sliding the roller has greater R_a/σ_z value than that of the pad flattened by just pure rolling, due to interfacial friction. Therefore, asperity flattening could be made

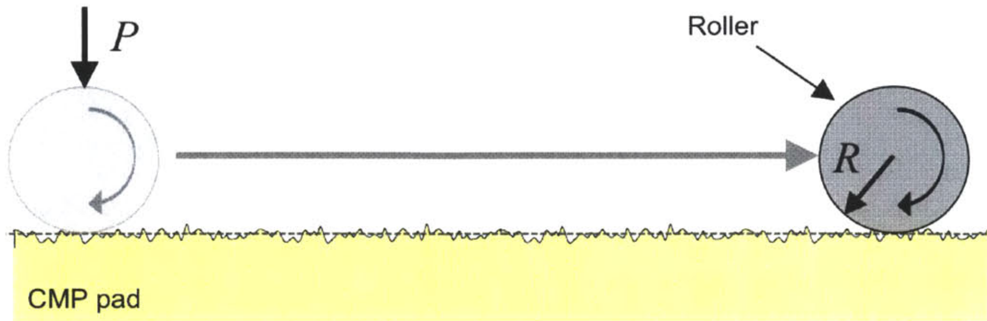

Figure 4.7. Schematic of asperity-flattening processes by rolling/sliding.

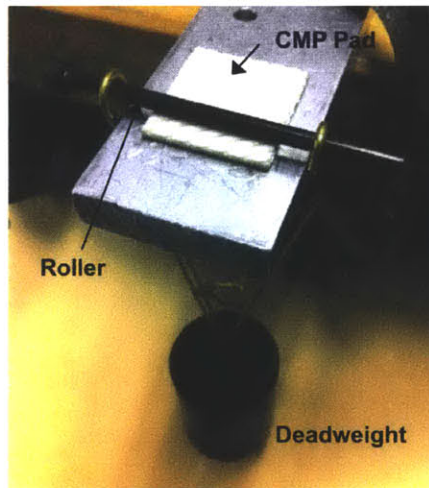

Figure 4.8. Photograph of experimental system for asperity-flattening by rolling/sliding.

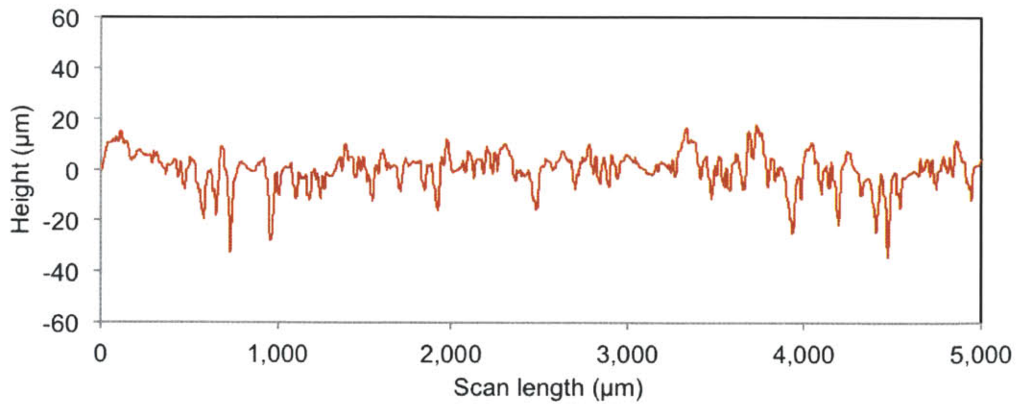

(a) rolling at 25 °C; R_a = 57.8 µm, σ_z = 3.7 µm

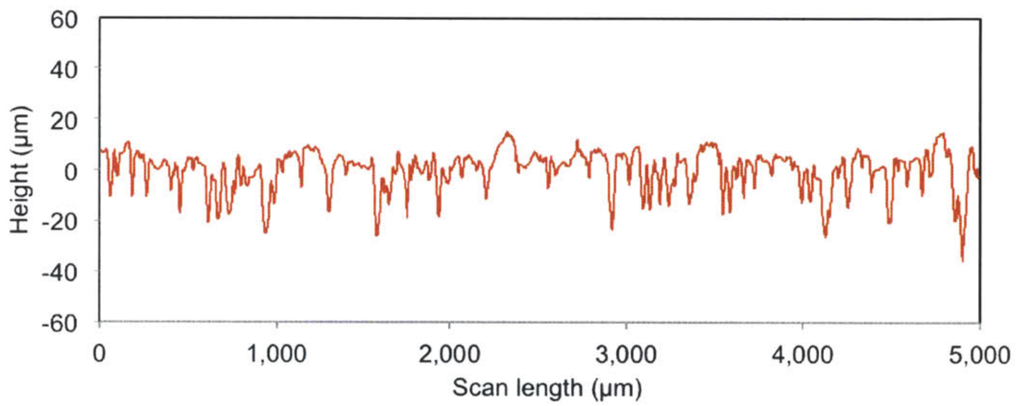

(b) rolling at 185 °C; R_a = 106.9 µm, σ_z = 3.4 µm

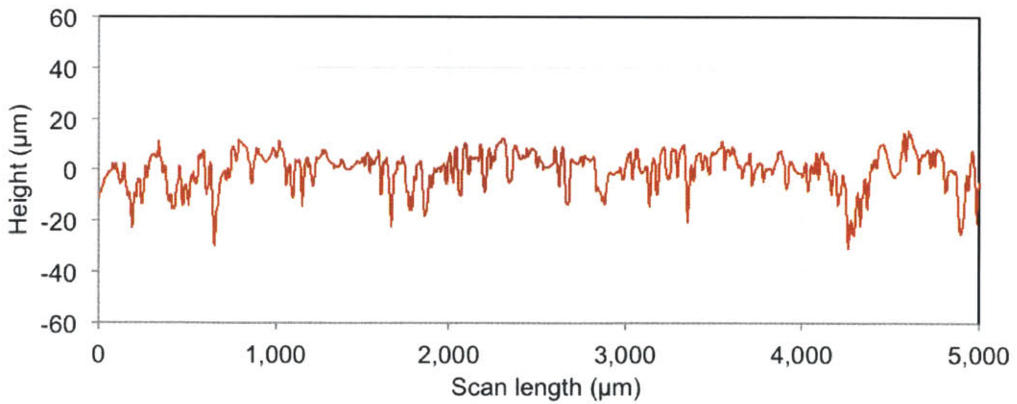

(c) sliding at 25 °C; R_a = 57.8 µm, σ_z = 3.3 µm

Figure 4.9. Surface profiles of asperity-flattened IC1000 pads by rolling/sliding.

Table 4.3. Asperity radius, standard deviation of asperity heights, their ratio, and the estimated plasticity indices of IC1000 pads (E_a / H_a = 7.6). Also listed are the number of scratches generated by the pads on a Cu layer in sliding experiments.

Parameter	New pad	Flattened pad				
		Compression		Rolling		Sliding
		300 kPa		2,300 kPa		
		25 °C	185 °C	25 °C	185 °C	25 °C
R_a (μm)	23.5	39.5	174.7	57.4	106.2	72.7
σ_z (μm)	4.4	3.9	1.7	3.7	3.4	3.3
R_a / σ_z	5.3	10.1	102.8	15.5	31.2	22.0
ψ	4.0	3.0	1.0	2.4	1.7	2.0
# of scratches	23	11	10	5	5	1

more effective by imposing sliding motion. However, it should be noted that sliding at high contact pressures may result in heavy wear of both the pad and the roller.

The results of the scratch experiments show, Figure 4.10, that the number of scratches indeed decreases as the R_a/σ_z value increases. While the R_a/σ_z value can be further increased by raising the process temperature and increasing the duration of loading, surprisingly scratch reduction with pads flattened at high temperatures was found to be less than that using the pads with asperities flattened at room temperature. In addition, scratching tests were also conducted on patterned Cu/dielectric layers using new and slide-flattened pads, as presented in Appendix F. The results again show that the asperity-flattened pads generate fewer scratches than do the new pads.

Additionally, Cu polishing experiments were conducted on a face-up polisher to determine the material removal rates of asperity-flattened pads, Figure 4.11. Two different sets of experimental conditions were used. In the first set, a slurry is used comprising 5 vol.% of Al_2O_3 abrasives of average size 300 nm, at a pressure of 13 kPa (2 psi) and a velocity of 0.87 m/s. In the second set a commercial slurry (HS-BT815, Hitachi Chemical Co.) was used; the pressure was 7 kPa (1 psi) and velocity was 0.66 m/s.

The results of polishing experiments are shown in Figure 4.12. Material removal rates were higher with pads flattened by sliding rollers. It seems, then, that an added benefit of flattening the asperities is that the contact area and hence the material removal rate will be increased. As asperities are flattened to have more elastic contacts, the real area of contact for a given nominal pressure will be increased compared with that of the new pads. Therefore, the material removal rate with flattened pads is expected to be greater than that with new pads.

It is apparent from Figure 4.12 that the material removal rate can be increased and the propensity for scratching decreased by controlling the topography of the CMP pads, i.e., by flattening the asperities. One way of controlling pad topography is by casting the pads in a mold with a micro-dimpled surface [Lee *et al.*, 2005]. Then, the height, radius and spacing of the asperities, too, can be independently controlled. Unfortunately, however, since the pads used in CMP are rather large, 0.7 m in diameter, manufacture of large molds with high-precision surfaces may not be possible. Furthermore, since pad topography continuously changes during CMP, due both to conditioning and wear,

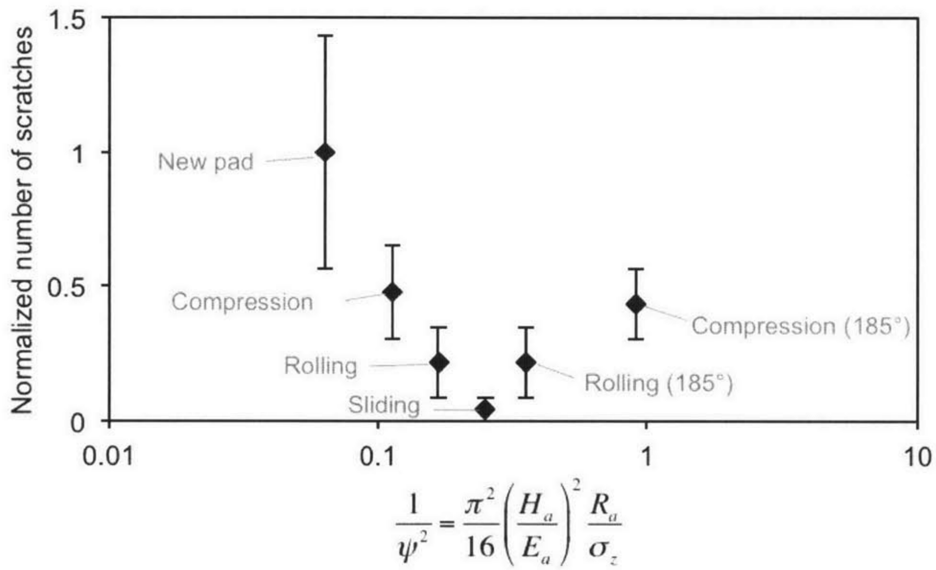

Figure 4.10. Normalized number of scratches after pad sliding experiments versus $1/\psi^2$. The points represent the average values and the bars the standard error.

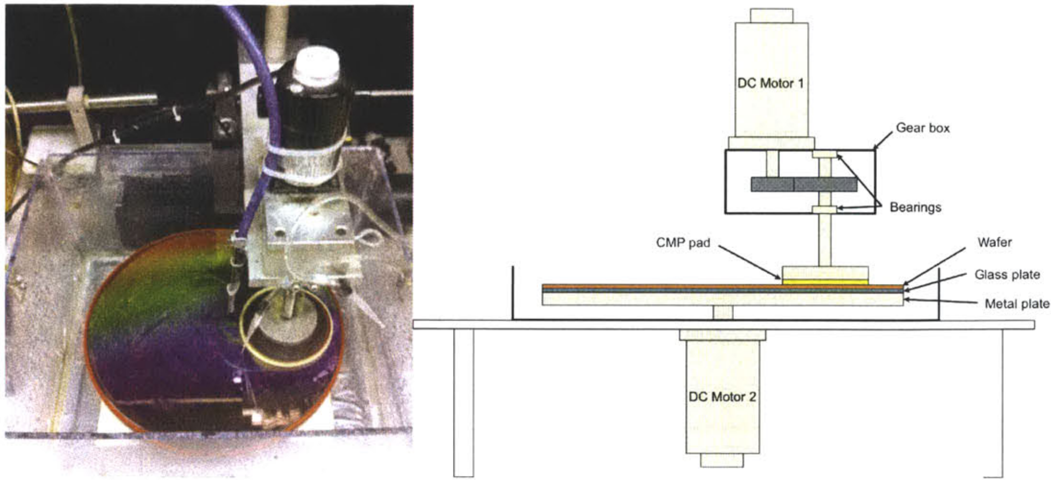

Figure 4.11. Photograph and schematic of face-up polisher.

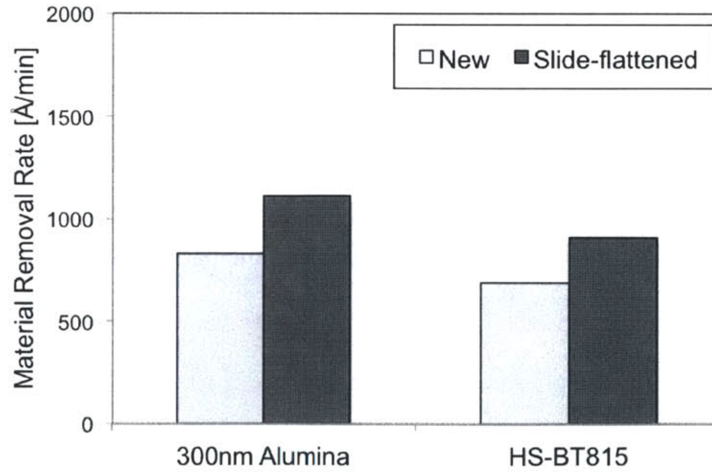

Figure 4.12. Material removal rate using new and asperity-flattened IC1000 pads. The asperities were flattened by sliding a roller over the pad.

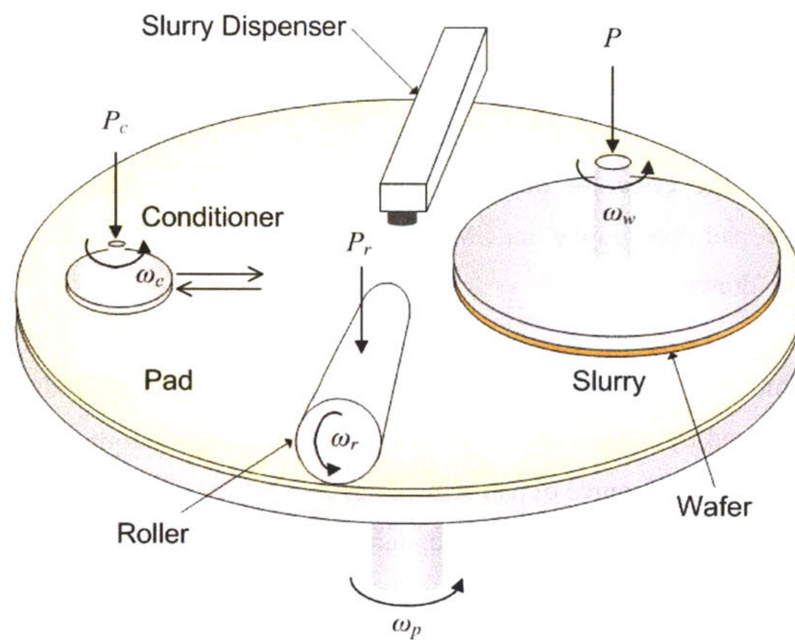

Figure 4.13. Schematic of *in-situ* asperity-flattening CMP system.

mitigation of pad scratching by molding the pads with optimal initial geometry may not eliminate scratching. Only novel methods of maintaining high R_a / σ_z value during polishing, such as *in situ* asperity flattening are expected to mitigate scratching. For instance, by implementing a smooth roller between the diamond conditioner and the wafer being polished in a general CMP system, Figure 4.13, pad asperities can be continuously flattened before they contact the wafer surface. Several practical methods for implementation of "asperity-flattening" in current CMP systems are suggested in Appendix E [Saka *et al.*, 2013].

4.5. Summary

In this work, the effect of pad topography on scratching and its mitigation by controlling the pad topography in CMP have been investigated, and the following conclusions are drawn.

(1) Contact mechanics models predict that the number of scratches produced in CMP can be reduced by decreasing the proportion of plastically deformed asperities, for they are the primary source of pad scratching.

(2) The ratio of asperity radius to the standard deviation of asperity heights, R_a/σ_z, is identified as the key parameter that determines the proportion of asperities in plastic contact.

(3) A novel, cost-effective process for pad topography control, asperity-flattening, is introduced. Compression by a smooth, flat plate or by rolling/sliding using a smooth roller can increase R_a/σ_z of the pad.

(4) Scratching experiments have shown that pad scratching is mitigated by flattening the asperities.

(5) Polishing experiments have shown that material removal rate also increases by flattening the pad asperities.

Nomenclature

d	separation distance between the centerline of pad surface and surface layer [m]
E_a	Young's modulus of pad asperity [N m^{-2}]
H_a	hardness of asperity [N m^{-2}]
n	number of asperities per unit area [m^{-2}]
n_c	number of asperities in contact per unit area [m^{-2}]
n_p	number of plastically deformed asperities per unit area [m^{-2}]
P	normal load applied for compression or rolling/sliding [N]
R	roller radius [m]
R_a	asperity radius [m]
z_a	asperity height [m]
δ	approach of distant points [m]
δ_y	approach of distant points at the onset of asperity yielding [m]
μ	coefficient of friction
σ_z	standard deviation of asperity heights [m]
ψ	plasticity index
$\phi(z_a)$	probability density of asperity heights

References

Borucki, L. J., 2002, "Polishing pad surface characterization in chemical-mechanical polishing," *J. Eng. Math.,* vol. 43, pp. 105-114.

Elmufdi, C. L. and Muldowney, G. P., 2006, "A novel optical technique to measure pad-wafer contact area in chemical mechanical planarization," *Mater. Res. Soc. Symp. Proc.*, vol. 914, 0914-F12-06 (6pp).

Eusner, T., Saka, N. and J.-H. Chun, 2011, "Breaking-In a pad for scratch-free, Cu chemical-mechanical polishing," *J. Electrochem. Soc.*, vol. 158, no. 4, pp.H379-H389.

Gray, C., Rogers, C., Manno, V. P., White, R. Moinpour, M. and Anjur, S., 2007, "Determining pad-wafer contact using dual emmission laser induced fluorescence," *Mater. Res. Soc. Symp. Proc.*, vol. 991, 0991-C01-04 (12pp).

Greenwood, J. A. and Williamson, J. B. P., 1966, "Contact of nominally flat surfaces," *Proc. Royal Soc. London A*, vol. 295, pp. 300-319.

Jamari, J. and Schipper, D. J., 2007, "Plastic deformation and contact area of an elasti-plastic contact of ellipsoid bodies after unloading," *Tribo. Int.*, vol. 40, pp. 1311-1318.

Johnson, K. L., *Contact Mechanics*, Cambridge University Press, Cambridge, UK, 1985.

Kadin, Y., Kligerman, Y. and Etsion, I., 2006, "Unloading an elastic-plastic contact of rough surfaces," *J. Mech. Phys. Solids*, vol. 54, pp. 2652-2674.

Lee, S., Kim, H., and Dornfeld, D., 2005, "Development of a CMP pad with controlled micro features for improved performance," *IEEE Inter. Symp. Semiconductor Manuf. (ISSM)*, pp. 173-176.

Lo, C. C., 1969, "Elastic contact of rough cylinders," *Int. J. Mech. Sci.*, vol. 11, pp. 105-115.

Luo, Q., Ramarajan, S. and Babu, S. V., 1998, "Modification of the preston equation for the chemical-mechanical polishing of copper," *Thin Solid Films*, vol. 335, pp. 160-167.

McGrath, J. and Davis, C., 2004, "Polishing pad surface characterization in chemical mechanical planarisation," *J. Mater. Process. Tech.,* vol. 153-154, pp. 666-673.

Rajendrakumar, P. K. and Biswas, S. K., 1997, "Deformation due to contact between a two-dimensional rough surface and a smooth cylinder," *Tribo. Letters*, vol. 3, pp. 297-301.

Saka, N., Chun, J.-H., Kim, S. and Shin, S.-H., 2013, "Scratch reduction by pad topography control in chemical-mechanical polishing," *US Provisional Patent*, Application number: 61/758,449.

CHAPTER 5

THE ROLE OF PAD APSERITIES IN MATERIAL REMOVAL

5.1. Introduction

Asperities of the polishing pads play a key role in CMP, as they transmit the necessary down force and motion to the particles. In Chapter 4, the results of polishing experiments have shown that polishing by asperity-flattened pads is faster than that by new pads. Asperity-flattening is used to increase the asperity radius and to reduce the asperity height variation, i.e., to decrease the plasticity index. The experimental results indeed indicate that the material removal rate can be increased by decreasing the plasticity index of the pad surface. The statement, however, might appear to be opposing other experimental observations.

New CMP pads have an average roughness of five micrometers. As polishing proceeds, the roughness is decreased due to the plastic deformation and wear of pad [Borucki, 2002; McGrath and Davis, 2004], which consequently results in lower plasticity index. Published experimental works show that polishing rate decays without re-roughening the surface [Borucki *et al.*, 2004; Park *et al.*, 2007; Lee *et al.*, 2010]. In industrial CMP systems, therefore, diamond conditioners are used to roughen the pad surface and regenerate the tall asperities continuously throughout the pad lifetime. The reduction in polishing rate may be due to the hydroplaning between the pad-wafer contact. That is, as smooth surfaces slide each other at high relative velocity, a layer of slurry builds between the contact which results in less real contact area [Thakurta *et al.*, 2000; Lai, 2001; Shi and Ring, 2010]. In addition, the polishing rate may drop because the slurry flow can be choked as the pad roughness reduces, and thereby the abrasives cannot be effectively delivered to every asperity contact point [Hooper *et al.*, 2002]. To eliminate hydroplaning and facilitate slurry flow, therefore the pad roughness should be

maintained to about five micrometers.

It should be noted, however, that although less surface roughness of the pad may result in less plasticity index between the pad-wafer contact, less plasticity index do not necessarily requires low surface roughness. A pad surface can have a low plasticity index and high average roughness simultaneously by having large average radii and large average heights with small height variation of asperities. Flattening the tall asperities by compression or rolling/sliding, accordingly, can achieve higher polishing rate by decreasing the plasticity index without much decrease in average roughness.

Despite the importance of the plasticity index on material removal, to the best of our knowledge, none of the previous studies attempt to take the parameter into account in material removal rate models. The first material removal rate model in CMP was presented by Preston [Preston, 1927]. It was empirically found that the thickness reduction rate, dh / dt, is directly proportional to the product of the applied nominal pressure, p, and the relative velocity, v_r, as

$$\frac{dh}{dt} = k_p p v_r \tag{5.1}$$

where k_p is a constant known as the Preston constant. Although the above relation has been validated by numerous experiments, the effect of other process variables, such as the topographical and mechanical properties of pad asperities, are not explicit and are contained in k_p.

To elucidate the material removal mechanism and explain the role of the other input parameters, a number of contact mechanics models were further developed in recent decades. Luo and Dornfeld suggested an abrasion model based on the assumptions that the sizes of abrasive particles are normally distributed whereas the pad asperity heights are uniform [Luo and Dornfeld, 2001]. It is well known, however, that typical random, rough pad surfaces have normal or exponential distribution of asperity heights with a few micrometers of standard deviation [Sorooshian *et al.*, 2005; Vasilev *et al.*, 2013]; hence, the effect of pad surface roughness is unaccounted for in the Luo-Dornfeld model. The model was further advanced considering the rough pad surface using the elastic contact

model was further advanced considering the rough pad surface using the elastic contact model formulated by Greenwood and Williamson [Greenwood and Williamson, 1966; Zhao and Chang, 2002; Qin *et al.*, 2004; Xie, 2007; Bozkaya and Müftü, 2009; Fan, 2012; Lee *et al.*, 2013]. Nevertheless, it has already been shown in previous chapters that the plasticity indices of commercial pads are estimated to be about four, and the pad-wafer contact can be assumed to be elastic only if the plasticity index is much less than one. These models, consequently, are developed assuming a contact with very low plasticity index which is not the case of typical pad-wafer contact in CMP.

This chapter, accordingly, is focused on the role of pad asperities in material removal in CMP. The rough pad surface is represented by multiple asperities which have an exponentially distributed heights, and each asperity in contact is considered to be in different modes of deformation according to its height: elastic, elastic-plastic, and fully-plastic. An equation for material removal rate is derived based on contact mechanics, in terms of the topographical and mechanical properties of the pad asperities together with the applied nominal pressure, relative velocity, particle concentration, and hardness of the surface layer. The model reveals the correlation between pad surface topography and the polishing rate, and thereby elucidates the key parameter of CMP pads for the polishing rate improvement. Cu polishing experiments, using the "asperity-flattened" pads reported in Chapter 4 to control the pad topography, validate the theoretical predictions.

5.2. Material removal by single-asperity sliding contact

The pad-wafer contact can be regarded microscopically as contact between multiple pad asperities and a smooth, flat surface, and only the asperities that have height, z_a, greater than the separation distance, d, will be in contact, Figure 5.1a. Since the moduli of the thin layers on the wafer surface are much greater than of the polymer pads ($E_l >> E_a$), the asperities in contact will be compressed and deform, whereas the elastic deformation of the surface layer is relatively negligible. Each single asperity in contact transfers loads to the abrasive particles that are trapped within its contact area, A_a, Figure 5.1b, which allows the particles to plow the wafer surface. It is assumed that the particles are

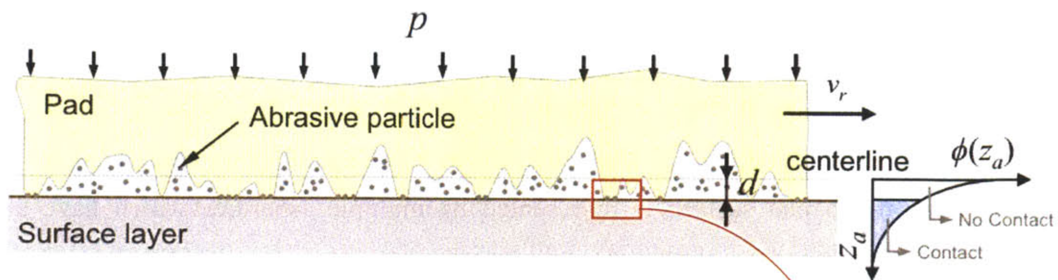

(a) multi-asperity sliding contact

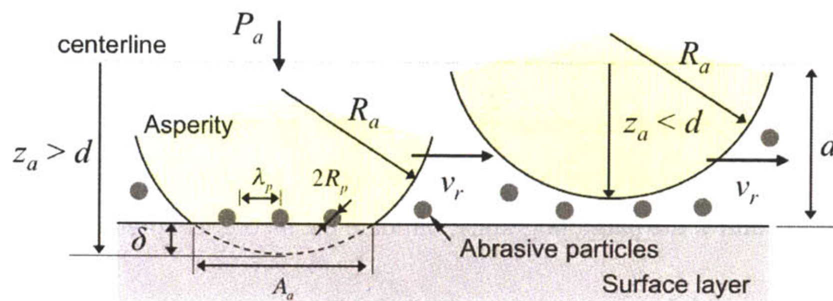

(b) single-asperity sliding contact

Figure 5.1. Schematic of contact between a rough pad and smooth, flat surface: (a) microscopic view of the contact represented as multiple pad asperities in sliding contact with the flat surface, and (b) nano-scale view of the contact that shows the nano-sized particles trapped under each single asperity in sliding contact.

spherical and have identical radius, R_p, which is much smaller than the radius of pad asperities ($R_p << R_a$). In addition, it is further assumed that the contact pressure, p_a, and the particle spacing, λ_p, are uniform within the asperity contact area, and thus the particle loads under a single asperity contact will also be uniform. The volumetric material removal rate by a single asperity, $dV_{r,a} / dt$, therefore, can be determined by the number of particles under the asperity, given as A_a / λ_p^2, and by the volumetric removal rate per single particle, $dV_{r,p} / dt$, as

$$\frac{dV_{r,a}}{dt} = \frac{A_a}{\lambda_p^2} \frac{dV_{r,p}}{dt} \tag{5.2}$$

In this section, first, the relation between removal rate per particle and the asperity contact pressure is explored. Then the removal rate under a single asperity, which has radius, R_a, Young's modulus, E_a, hardness, H_a, is derived as a function of approach of distance points, δ.

5.2.1. Particle-layer contact

Since the hardness of abrasive particles, H_p, is much greater than that of the surface layer, H_l ($H_p >> H_l$), the contact between the abrasive particle and the surface layer can be considered to be indentation of a flat surface by a rigid indenter, Figure 5.2. As the particle plows the smooth surface layer, by upper-bound analysis [Saka *et al.*, 2008], the pressure at the particle-layer contact will be equal to the layer hardness. Therefore, the normal load on a single particle, P_p, will be

$$P_p = \frac{1}{2} H_l \pi a_l^2 \tag{5.3}$$

For spherical particle scratching, the depth, δ_l, and the semi-width, a_l, of the particle scratch, if $\delta_l << R_p$, are related by

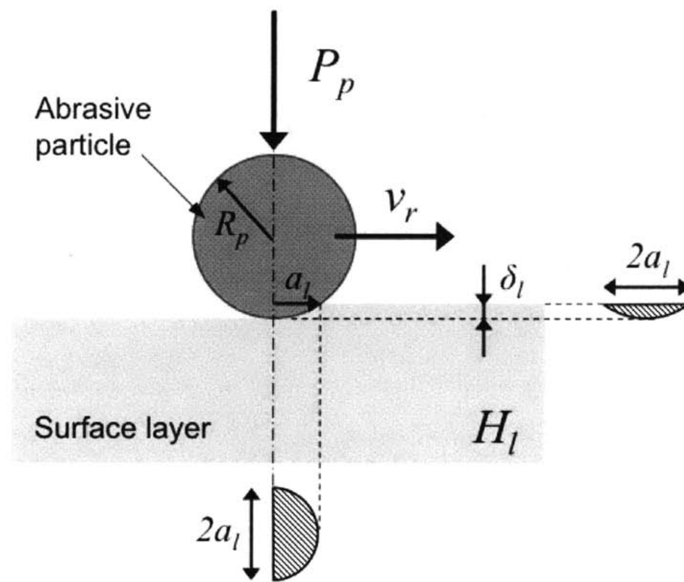

Figure 5.2. Schematic of scratching on surface layer by a hard abrasive particle.

$$\delta_l = \frac{1}{2}\frac{a_l^2}{R_p} \tag{5.4}$$

As the particle scratches the smooth surface, the amount of material displaced will be equal to A_l ($\approx a_l\delta_l$), Figure 5.3. However, of this material an amount equal to A_p is retained upon the surface as pile-up material [Buttery and Archard, 1970]. Therefore, the volumetric material removal rate by a single particle scratching, for given particle load and relative velocity, can be expressed as

$$\frac{dV_{r,p}}{dt} = \left(A_l - A_p\right)v_r = \zeta a_l \delta_l v_r = \frac{\sqrt{2}\zeta}{R_p}\left(\frac{P_p}{\pi H_l}\right)^{3/2} v_r \tag{5.5}$$

where ζ is the fraction of the material detached from the particle scratching, defined as

$$\zeta = \frac{A_l - A_p}{A_l} = 1 - \frac{A_p}{A_l} \tag{5.6}$$

Equation (5.5) is valid for scratching a homogeneous surface layer without any chemical reaction involved. In general, however, reactions between the chemical components, C, inside the slurry and workpiece material, M, produce a thin film, MC, on the top of the surface layer, Figure 5.4 [Paul, 2001]. In Cu-CMP, for example, hydrogen peroxide is typically used as an oxidant which produces a thin copper oxide layer. The oxidized film can exist in different states, CuO, Cu_2O, Cu(OH) and $Cu(OH)_2$ species, depending on the peroxide concentration [Hernandez *et al.*, 2001; Paul *et al.*, 2005]. Then, the reaction film is mechanically abraded by the hard particles. The film is expected to be softer than the surface layer material to enhance the material removal rate, but it may be similar or even harder depending on oxidant concentration and pH of the slurry [Ihnfeldt and Talbot, 2008]. Although the film may also be dissolved into the slurry by some additional etchants, the dissolution rate is generally slow compared with the rate of the film formation [Paul, 2001; Denardis *et al.*, 2010]. Accordingly, in this

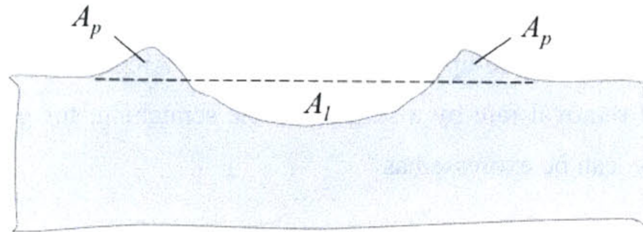

Figure 5.3. Cross-section of the scratch generated by a spherical particle showing pile-up.

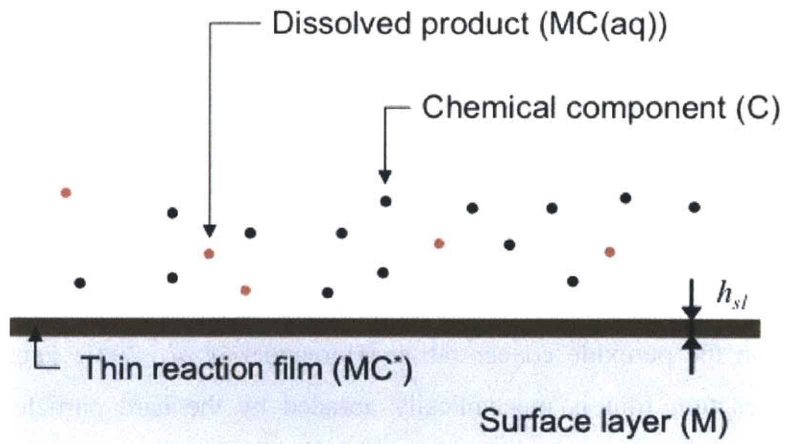

Figure 5.4. Formation of thin film on the surface layer by chemical reaction in CMP.

work, it is assumed that material removal is primarily due to mechanical abrasion.

As the particle indents, the hardness of the surface layer will alter depending on the hardness and the thickness of the thin reaction film as:

$$H_l^* = f\left(H_l, H_f, h_f\right) \tag{5.7}$$

where the influences of chemical reactions are reflected in the effective hardness value of the surface layer, H_l^*, which remains as an empirical parameter.

The volumetric material removal rate by a single particle scratching, given as Eq. (5.5), then, can be rewritten as

$$\frac{dV_{r,p}}{dt} = \frac{\sqrt{2}\zeta}{R_p}\left(\frac{P_p}{\pi H_l^*}\right)^{3/2} v_r \tag{5.8}$$

5.2.2. Asperity-particle contact

Equation (5.8) shows that the volumetric material removal rate by a hard abrasive strongly depends on the load applied on the particle. The particle loads in CMP are applied by the pad asperities in contact, Figure 1. Hence, the asperity contact pressure strongly determines the loads on the particles. Figure 5.5 shows the development of asperity-particle contact as the contact pressure increases. Since the hardness of abrasive particles is much greater than that of the pad asperities, H_a ($H_p >> H_a$), and since $R_p << R_a$, the contact between the pad asperity and the particle can be again considered to be an indentation of a flat asperity by a rigid indenter. Under the asperity that has relatively low contact pressure, p_a, the asperity load will be supported solely by the particles, Figure 5.5a; i.e., in nano-scopic view of the contact, the asperity may not directly contact the surface layer. The asperity load, P_a, therefore, is determined by the particle load and the number of particles under the asperity as

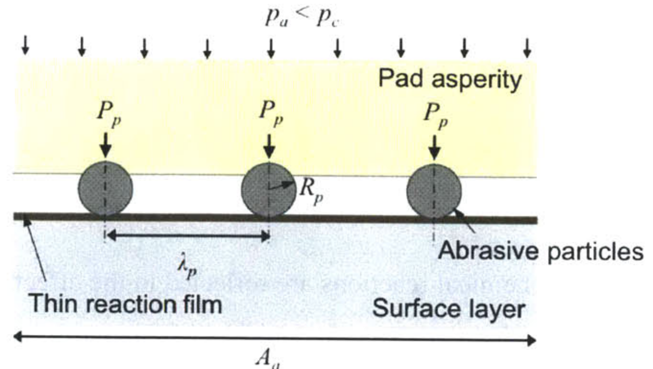

(a) under low contact pressure ($p_a < p_c$)

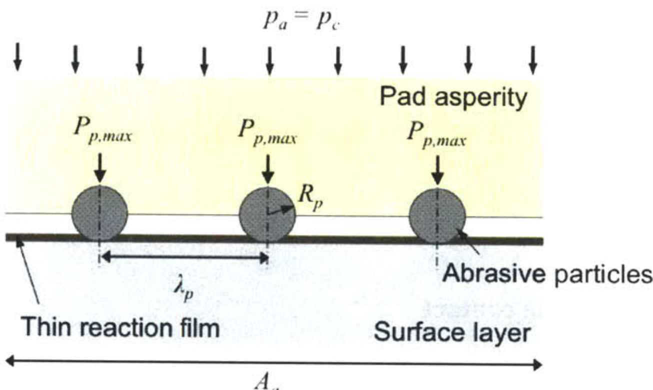

(b) under critical contact pressure ($p_a = p_c$)

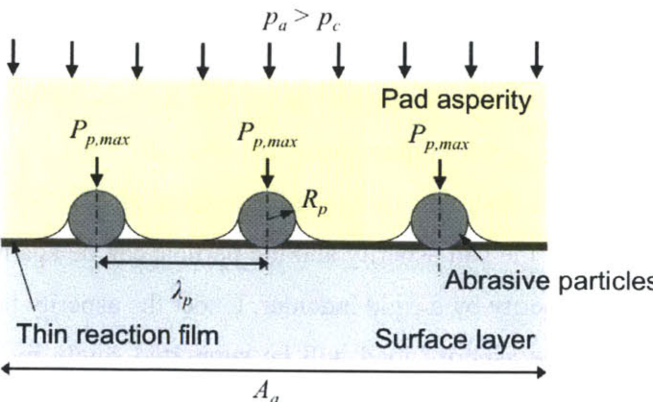

(c) under high contact pressure ($p_a > p_c$)

Figure 5.5. Development of asperity-particle contact under increased asperity contact pressure.

$$P_a = p_a A_a = P_p \frac{A_a}{\lambda_p^2} \tag{5.9}$$

which gives the relation between particle load and the asperity contact pressure as

$$P_p = p_a \lambda_p^2 \tag{5.10}$$

For low pressure contact, accordingly, the particle loads are proportional to the asperity contact pressure. By upper-bound analysis of spherical indentation [Saka *et al.*, 2008], however, the normal load that can be applied on the particle by the soft asperity has a maximum limit, Figure 5.5b, which is given as

$$P_{p,\max} = H_a \pi R_p^2 \tag{5.11}$$

The loads applied on the particles under the asperity will reach this maximum value when the particle load, given in Eq. (5.10), equals to the maximum load, given in Eq. (5.11). The asperity contact pressure when the loads applied on the particles become the maximum is defined as the "critical asperity contact pressure," p_c, which can be derived as

$$p_c = \pi H_a \frac{R_p^2}{\lambda_p^2} \tag{5.12}$$

Once the asperity contact pressure becomes greater than p_c, the asperity load cannot be supported solely by the particles. To support the excess load, asperity will directly contact the surface layer, Figure 5.5c. After the particle loads are maximized, accordingly, they are constant even though the asperity contact pressure is increased further, as

$$P_p = P_{p,\max} = H_a \pi R_p^2 \tag{5.13}$$

That is, the particles loads are maximum and thus independent of the asperity contact pressure as Eq. (5.13) if $p_a \geq p_c$, whereas the loads are proportional to the asperity contact pressure as Eq. (5.10) if $p_a < p_c$.

5.2.3. Number of particles at single-asperity sliding contact

Assuming that the spatial distribution of particles in the slurry is uniform, with n_p particles per unit volume, the number of particles per unit area trapped at an asperity contact, $1/\lambda_p^2$, can be estimated as [Qin *et al.*, 2004]

$$\frac{1}{\lambda_p^2} \approx 2R_p n_p \tag{5.14}$$

and the volumetric particle concentration, C_{vol}, is expressed as

$$C_{vol} = V_p n_p = \frac{4}{3}\pi R_p^3 n_p \tag{5.15}$$

The relation between the particle spacing and the volumetric concentration, from Eqs. (5.14) and (5.15), then will be

$$\pi \frac{R_p^2}{\lambda_p^2} = \frac{3}{2} C_{vol} \tag{5.16}$$

Then, the critical asperity contact pressure, p_c, Eq. (5.12), can be expressed by a function of asperity hardness and the particle concentration as

$$p_c = \frac{3}{2} H_a C_{vol} \tag{5.17}$$

5.2.4. Material removal rate by single-asperity sliding contact

When a single asperity is pressed against a smooth flat surface, the asperity may experience three distinct deformation modes as the approach of distant points, δ, increases: elastic ($0 \le \delta \le \delta_y$), elastic-plastic ($\delta_y \le \delta \le \delta_{f\text{-}p}$), and full-plastic ($\delta_{f\text{-}p} \le \delta$). For a homogeneous material with Young's modulus, E_a, yield strength, $\sigma_{y,a}$, and hardness, H_a, the contact pressure and area of an asperity with radius R_a are determined by δ as [Zhao *et al.*, 2000]:

$$p_a(\delta) = \begin{cases} \dfrac{4}{3\pi} E_a \left(\dfrac{\delta}{R_a}\right)^{1/2} & , \quad (0 \le \delta \le \delta_y) \\ \sigma_{y,a}\left[1 + \dfrac{1}{2}\ln(\delta/\delta_y)\right] & , \quad (\delta_y \le \delta \le \delta_{f\text{-}p}) \\ H_a & , \quad (\delta_{f\text{-}p} \le \delta) \end{cases} \tag{5.18}$$

$$A_a(\delta) = \begin{cases} \pi R_a \delta & , \quad (0 \le \delta \le \delta_y) \\ \pi R_a \delta \left[1 + 3\left(\dfrac{\delta/\delta_y - 1}{53}\right)^2 - 2\left(\dfrac{\delta/\delta_y - 1}{53}\right)^3\right] & , \quad (\delta_y \le \delta \le \delta_{f\text{-}p}) \\ 2\pi R_a \delta & , \quad (\delta_{f\text{-}p} \le \delta) \end{cases} \tag{5.19}$$

where δ_y is approach of distant points at the onset of asperity yielding, which can be estimated from [Johnson, 1985]

$$\delta_y = \frac{9\pi^2}{16}\frac{\sigma_y^2}{E_a^2} R_a \cong \frac{\pi^2}{16}\frac{H_a^2}{E_a^2} R_a \tag{5.20}$$

and $\delta_{f\text{-}p}$ is approach of distant points at the onset of fully-plastic asperity deformation which is assumed to be $\delta_{f\text{-}p} = 54\delta_y$ [Johnson, 1985; Zhao *et al.*, 2000].

Therefore, "critical approach of distant points," δ_c, when the asperity contact pressure becomes p_c, can be determined from Eqs. (5.17) and (5.18) as

$$\delta_c = \begin{cases} \delta_y \left(\frac{9}{2} C_{vol} \right)^2 & , \left(C_{vol} < \frac{2}{9} \right) \\ \delta_y \exp\left[2\left(\frac{9}{2} C_{vol} - 1 \right) \right] & , \left(C_{vol} \geq \frac{2}{9} \right) \end{cases} \tag{5.21}$$

When the approach of distant points is relatively small, less than δ_c, the contact pressure is not high enough so that the load applied on each particle does not reach the maximum load. Under an asperity sliding contact with small approach of distant points ($\delta < \delta_c$), Figure 5.6a, the volumetric removal rate per particle, from Eqs. (5.8), (5.10) and (5.16), is

$$\frac{dV_{r,p}}{dt} = \frac{4\zeta}{3\sqrt{3}} \left[\frac{p_a(\delta)}{H_l^*} \right]^{3/2} C_{vol}^{-3/2} R_p^2 v_r \quad , \quad (\delta < \delta_c) \tag{5.22a}$$

which indicates that the removal rate depends on asperity contact pressure.

Only when the approach of distant points is greater than δ_c, are the particle loads maximized. Under an asperity sliding contact with large approach of distant points ($\delta \geq \delta_c$), Figure 5.6b, the volumetric removal rate per particle, from Eqs. (5.8), (5.13) and (5.16), is given by

$$\frac{dV_{r,p}}{dt} = \sqrt{2}\zeta \left[\frac{H_a}{H_l^*} \right]^{3/2} R_p^2 v_r \quad , \quad (\delta \geq \delta_c) \tag{5.22b}$$

which shows that the removal rate is independent of asperity contact pressure.

The volumetric material removal rate by single-asperity sliding contact can be obtained from Eqs. (5.2), (5.16), and (5.22a,b), as

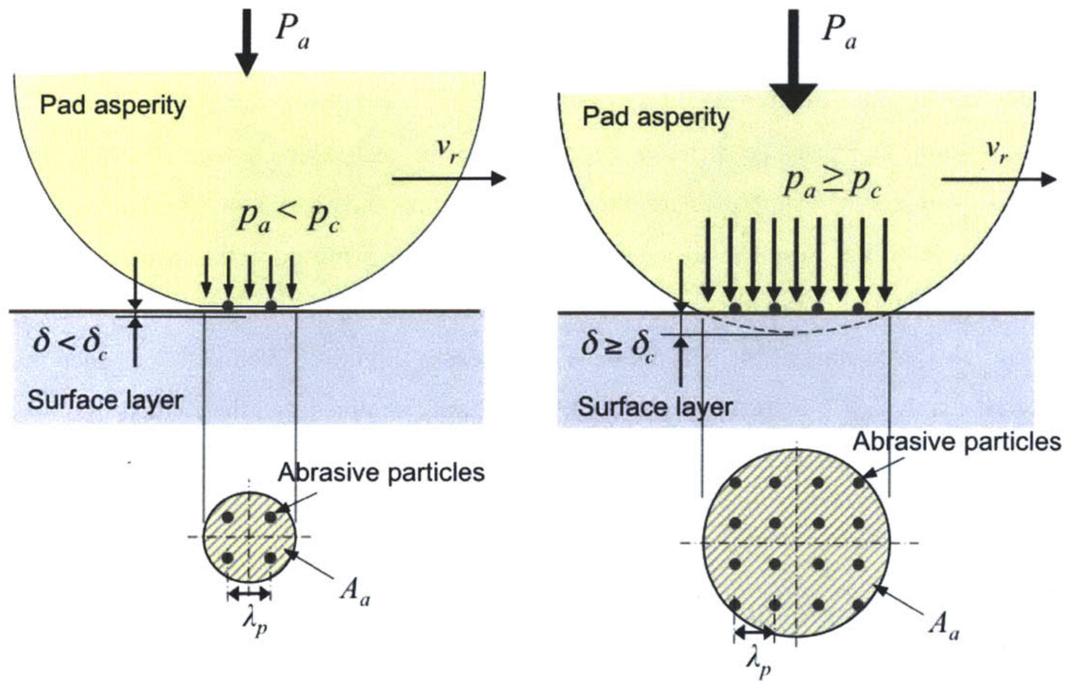

(a) small approach of distant points ($\delta < \delta_c$) (b) large approach of distant points ($\delta \geq \delta_c$)

Figure 5.6. Contact pressure and area at an asperity contact: (a) At small approach of distant points ($\delta < \delta_c$), the asperity contact pressure is less than the critical limit ($p_a < p_c$) and (b) at large approach of distant points ($\delta \geq \delta_c$), the asperity contact pressure is greater than the critical limit ($p_a \geq p_c$).

$$\frac{dV_{r,a}}{dt} = \begin{cases} \frac{2\zeta}{\sqrt{3}\pi}\left[\frac{p_a(\delta)}{H_l^*}\right]^{3/2} A_a(\delta)C_{vol}^{-1/2}v_r \ , & (\delta < \delta_c) \\ \frac{3\zeta}{\sqrt{2}\pi}\left(\frac{H_a}{H_l^*}\right)^{3/2} A_a(\delta)C_{vol}v_r \ , & (\delta \geq \delta_c) \end{cases} \tag{5.23}$$

Equation (5.23) shows that material removal rate per single asperity will be increased by increasing the approach of distant points, δ, by increasing the relative velocity, v_r, or by decreasing the effective hardness of the layer, H_l^*. However, the effect of particle concentration, C_{vol}, may be different depending on the pad-layer contact. If $\delta < \delta_c$, the asperity load is solely supported by the particles, Figures 5.5a and 5.6a. Therefore, more particle density may result in distribution of the load on many particles, which reduces the overall material removal rate. If $\delta \geq \delta_c$, the asperity can apply the maximum loads on the particles even though the particle density increases, Figures 5.5c and 5.6b; hence the material removal will increase as C_{vol} increases. It may be noted that the critical limit, δ_c, also depends on the C_{vol}, i.e., higher particle concentration has greater δ_c.

5.3. Material removal under multi-asperity sliding contact

The probability density of asperity heights, $\phi(z_a)$, of the rough pad surfaces which have standard deviation, σ_z, can be expressed by an exponential distribution function as

$$\phi(z_a) = \frac{1}{\sigma_z}\exp\left(-\frac{z_a}{\sigma_z}\right) \tag{5.24}$$

As the pad surface with n asperities per unit area is pressed against the flat layer to a separation distance, d, only the asperities that have heights, z_a, greater than d, will be in contact, Figure 5.1a. The number of asperities in contact, n_c, accordingly, is given by

$$n_c = n\int_d^\infty \phi(z_a)\,dz_a = n\exp\left(-\frac{d}{\sigma_z}\right) \tag{5.25}$$

Each asperity in contact is compressed by the approach of distant points, δ, which is equal to $z_a - d$, Figure 5.1b. Assuming all the peaks of the asperities are taken to be spherical with an identical radius, R_a, the contact pressure and area under the asperities are determined by z_a, at a selected distance d. Both pressure and area under the contact vary due to asperity height variation; therefore, the removal rate by an asperity in contact will be different depending on z_a.

Then the overall thickness reduction rate of the surface being polished, dh/dt, by n asperities in sliding contact per unit area can be obtained from the summation of volumetric material removal rate by individual asperities in sliding contact, as

$$\begin{aligned} \frac{dh}{dt} &= n\int_d^\infty \frac{dV_{r,a}}{dt}\phi(z_a)\,dz_a \\ &= n\int_d^{d+\delta_c} \frac{dV_{r,a}}{dt}\phi(z_a)\,dz_a + n\int_{d+\delta_c}^\infty \frac{dV_{r,a}}{dt}\phi(z_a)\,dz_a \end{aligned} \tag{5.26}$$

where the volumetric material removal rate by single asperities are given as Eq. (5.23).

In this section, the real contact area between the rough pad and the smooth, flat layer is first studied. Second, the relative proportions of asperities in sliding contact that have "low-pressure" ($p_a < p_c$) and "high-pressure" ($p_a \geq p_c$) are investigated. Finally, the overall material removal rate are presented in terms of the topographical and mechanical properties of the pad asperities: R_a, σ_z, E_a, H_a, and other input parameters, p, v_r, H_l^*, and C_{vol}. The role of the asperity properties on the overall material removal rate is discussed, based on the correlations among the real contact area, the proportions of "low-pressure" and "high-pressure" asperities in contact, and the polishing rate.

5.3.1. Contact area ratio between pad and wafer

The ratio of real contact area to nominal contact area, A_r / A_n, between the pad and

layer surfaces, is the summation of individual asperity contacts as

$$\frac{A_r}{A_n} = n\int_d^\infty A_a \phi(z_a)\, dz_a \tag{5.27}$$

For a selected separation distance, d, from Eqs. (5.19) and (5.24), and introducing $\xi = (z_a - d) / \sigma_z$, the contact area ratio will be

$$\frac{A_r}{A_n} = \pi R_a \sigma_z n \exp\left(-\frac{d}{\sigma_z}\right) f_A(\psi) \tag{5.28}$$

where f_A is a function of ψ as

$$\begin{aligned} f_A(\psi) &= \int_0^{1/\psi^2} \xi \exp(-\xi)\, d\xi \\ &+ \int_{1/\psi^2}^{54/\psi^2} \left[1 + 3\left(\frac{\psi^2\xi - 1}{53}\right)^2 - 2\left(\frac{\psi^2\xi - 1}{53}\right)^3\right] \xi \exp(-\xi)\, d\xi \\ &+ 2\int_{54/\psi^2}^{\infty} \xi \exp(-\xi)\, d\xi \end{aligned} \tag{5.29}$$

and ψ is the plasticity index, defined as

$$\psi \equiv \left(\frac{\sigma_z}{\delta_y}\right)^{1/2} = \frac{4}{\pi}\frac{E_a}{H_a}\left(\frac{\sigma_z}{R_a}\right)^{1/2} \tag{5.30}$$

Similarly, from Eqs. (5.18), (5.19), and (5.24), the relation between the nominal pressure, p, and the separation distance, d, can be estimated as

$$p = n\int_d^\infty p_a A_a \phi(z_a)\, dz_a = \pi H_a R_a \sigma_z n \exp\left(-\frac{d}{\sigma_z}\right) f_p(\psi) \tag{5.31}$$

where f_p is a function of ψ as

$$f_P(\psi) = \frac{\psi}{3}\int_0^{1/\psi^2} \xi^{3/2}\exp(-\xi)\,d\xi$$
$$+\int_{1/\psi^2}^{54/\psi^2} \frac{1}{3}\left[1+\frac{1}{2}\ln\psi^2\xi\right]$$
$$\times\left[1+3\left(\frac{\psi^2\xi-1}{53}\right)^2-2\left(\frac{\psi^2\xi-1}{53}\right)^3\right]\xi\exp(-\xi)\,d\xi \tag{5.32}$$
$$+2\int_{54/\psi^2}^{\infty}\xi\exp(-\xi)\,d\xi$$

From Eqs. (5.28) and (5.32), the contact area ratio for a given nominal pressure, p, can be given as

$$\frac{A_r}{A_n} = \frac{p}{H_a}\frac{f_A(\psi)}{f_P(\psi)} \tag{5.33}$$

which indicates that the contact area ratio depends on the plasticity index, ψ, in addition to the normalized nominal pressure, p/H_a.

The plasticity index was first introduced by Greenwood and Williamson combining topographical and mechanical properties of the surfaces [Greenwood and Williamson, 1966]. This dimensionless parameter characterizes the relative proportion of plastically deformed asperities in contact: higher plasticity index indicates more proportion of plastic asperity contact. Only when the index is much less than unity, can all asperities be assumed to deform elastically. If $\psi << 1$, Eq. (5.33) simplifies to

$$\frac{A_r}{A_n} = \sqrt{\pi}\frac{p}{E_a}\left(\frac{R_a}{\sigma_z}\right)^{1/2} \tag{5.34}$$

which is the Greenwood and Williamson model. For such elasticity-dominant contact Young's modulus of asperities governs the mechanical behavior of asperity deformation. On the other hand, if $\psi >> 1$, the equation simplifies to

$$\frac{A_r}{A_n} = \frac{p}{H_a} \tag{5.35}$$

which is the case of fully-plastic deformation. For such plasticity-dominant contact, the real contact area is determined by the asperity hardness and the applied load. If ψ is near unity, which is the case of typical CMP pads, however, the asperity contacts comprise both elastically and plastically deformed asperities. Figure 5.7 shows the contact area ratio versus ψ. As ψ decreases, i.e., as the relatively proportion of plastically deformed asperities decreases, the contact area between the pad and wafer increases.

In addition, it is apparent that softer pads will have larger contact area than harder pads for the same p and ψ. Though ψ also depends on the asperity hardness, H_a, in general E_a and H_a are proportional to each other for various polymers and thus ψ of polymeric surfaces cannot be significantly changed by the asperity modulus or by the hardness.

5.3.2. Relative proportions of asperities in "low-pressure" and in "high-pressure" contact

As shown in Eq. (5.23), the effect of contact pressure on material removal rate strongly depends on whether the asperity pressure is greater or less than p_c, Eq. (5.17). As the n asperities are compressed, relatively small asperities that deform less than the critical limit, δ_c, have "low-pressure," i.e., less than p_c, Figure 5.8. The number of asperities per unit area that have "low-pressure," n_{c,low_p}, is

$$n_{c,low_p} = n\int_{d}^{d+\delta_c} \phi(z_a)\,dz_a = n\exp\left(-\frac{d}{\sigma_z}\right)\left\{1-\exp\left(-\frac{\delta_c}{\sigma_z}\right)\right\} \tag{5.36a}$$

On the other hand, the tall asperities that deform greater than δ_c, have "high-pressure," i.e., greater than p_c. The number of asperities per unit area that have "high-pressure," $n_{c,high_p}$, is

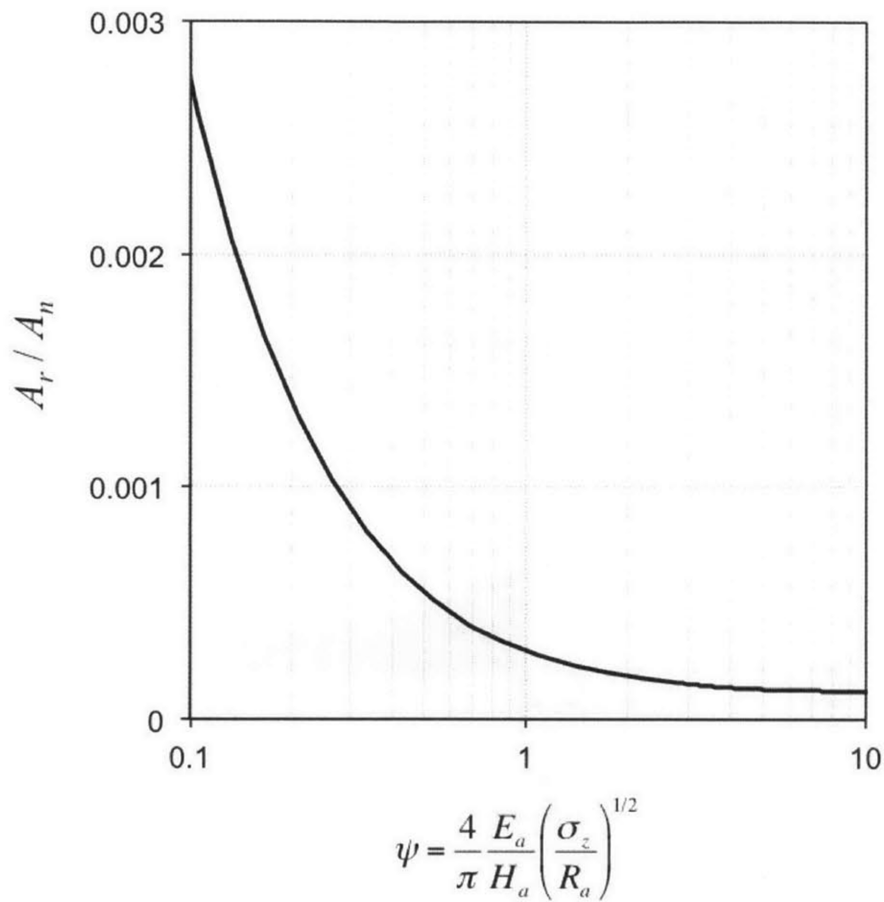

Figure 5.7. Contact area ratio between a rough pad and a smooth, flat surface versus plasticity index, at p = 35 kPa and H_a = 290 MPa.

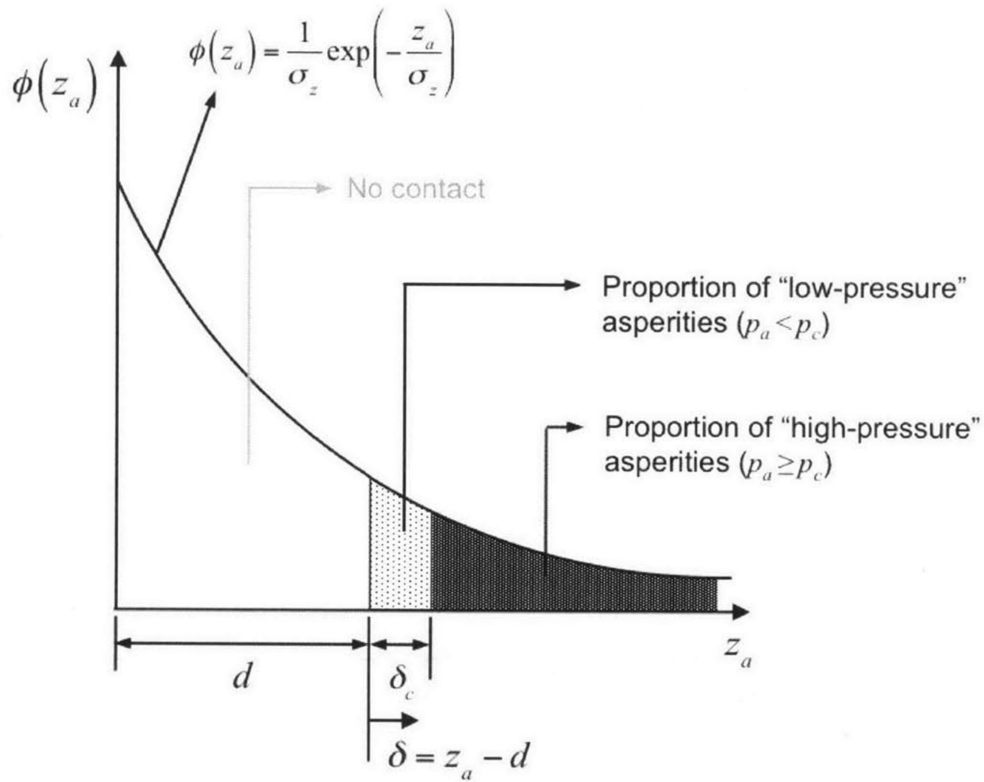

Figure 5.8. Relative proportions of asperities with "low-pressure" ($p_a < p_c$) and with "high-pressure" ($p_a \geq p_c$).

$$n_{c,high_p} = n\int_{d+\delta_c}^{\infty} \phi(z_a)dz_a = n\exp\left(-\frac{d}{\sigma_z}\right)\exp\left(-\frac{\delta_c}{\sigma_z}\right) \tag{5.36b}$$

From (5.21) and (5.25), the relative proportion of asperities for each asperity-particle contact case is given by

$$\frac{n_{c,low_p}}{n_c} = 1 - \exp\left(-\frac{C_c}{\psi^2}\right) \tag{5.37a}$$

$$\frac{n_{c,high_p}}{n_c} = \exp\left(-\frac{C_c}{\psi^2}\right) \tag{5.37b}$$

where C_c is a coefficient determined by the particle concentration, C_{vol}, as

$$C_c \equiv \frac{\delta_c}{\delta_y} = \begin{cases} \left(\frac{9}{2}C_{vol}\right)^2 & , \left(C_{vol} < \frac{2}{9}\right) \\ \exp\left[2\left(\frac{9}{2}C_{vol} - 1\right)\right] & , \left(C_{vol} \geq \frac{2}{9}\right) \end{cases} \tag{5.38}$$

Accordingly, the relative proportions of "low-pressure" and "high-pressure" asperities depends on C_{vol}. The greater C_{vol} is, less number of asperities will have contact pressure greater than p_c, because p_c increases as C_{vol} increases, Eq. (5.17). In addition to C_{vol}, the relative proportions are determined by the plasticity index, ψ. Figure 5.9 shows the relative proportions of asperities with low and high contact pressure versus ψ, at C_{vol} = 0.1. The pad-layer contact is dominated by the "high-pressure" asperities at high ψ, whereas the contact is dominated by "low-pressure" asperities at low ψ. Asperities in both high and low pressure cases will have a similar number of contacts when

$$\psi \approx C_c^{1/2} \tag{5.39}$$

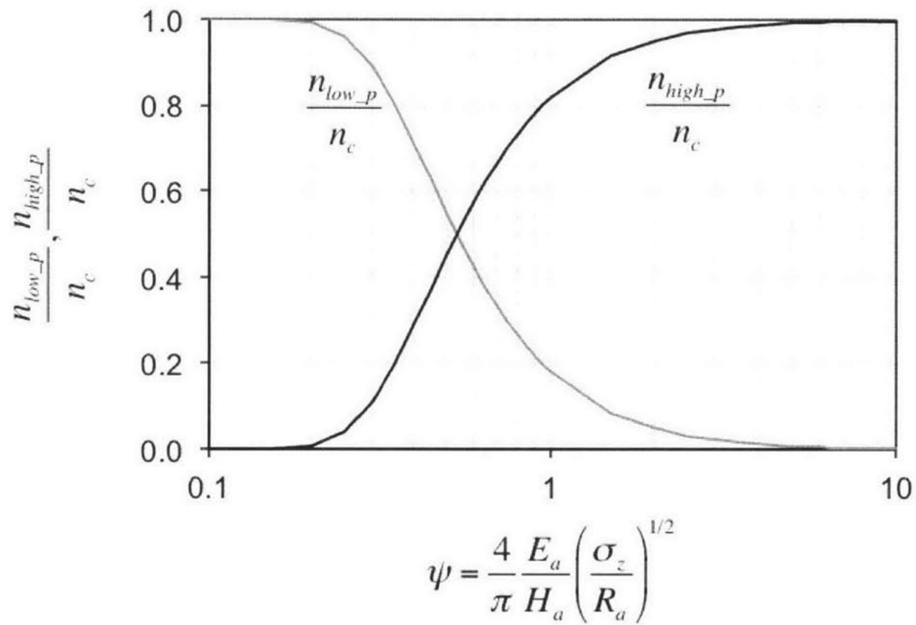

Figure 5.9. Estimated relative proportions of asperities in contact with "low-pressure" ($p_a < p_c$) and with "high-pressure" ($p_a \geq p_c$) versus plasticity index, at $C_{vol} = 0.1$ which corresponds to $C_c^{1/2} = 0.45$.

As shown in Figure 5.9, if $\psi << C_c^{1/2}$, contact pressure at all asperities can be assumed to be in "low-pressure" contact, i.e., less than p_c. If $\psi >> C_c^{1/2}$, on the other hand, contact pressure at all asperities can be assumed to be in "high-pressure" contact, i.e., greater than p_c.

5.3.3. Overall material removal rate

The thickness reduction rate of the surface layer, dh/dt, can be obtained from Eqs. (5.18), (5.19), (5.23), (5.24) and (5.26), by

$$\frac{dh}{dt} = \zeta \left(\frac{H_a}{H_l^*} \right)^{3/2} R_a \sigma_z v_r n \exp\left(-\frac{d}{\sigma_z} \right) f_{MRR}(\psi, C_{vol}) \tag{5.40}$$

where f_{MRR} is a function of ψ and C_{vol} as

$$\begin{aligned} f_{MRR}(\psi, C_{vol}) = & \frac{2C_{vol}^{-1/2}}{\sqrt{3}} \int_0^{(9C_{vol}/2\psi)^2} \left(\frac{\psi}{3\pi} \right)^{3/2} \xi^{7/4} \exp(-\xi) d\xi \\ & + \frac{3C_{vol}}{\sqrt{2}} \int_{(9C_{vol}/2\psi)^2}^{1/\psi^2} \xi \exp(-\xi) d\xi \\ & + \frac{3C_{vol}}{\sqrt{2}} \int_{1/\psi^2}^{54/\psi^2} \left[1 - 2\left(\frac{\psi^2 \xi - 1}{53} \right)^3 + 3\left(\frac{\psi^2 \xi - 1}{53} \right)^2 \right] \xi \exp(-\xi) d\xi \\ & + 3\sqrt{2} C_{vol} \int_{54/\psi^2}^{\infty} \xi \exp(-\xi) d\xi \end{aligned} \tag{5.41}$$

Equation (5.40) can be expressed as a function of given nominal pressure, p, using (5.31), as

$$\frac{dh}{dt} = \frac{\zeta}{\pi} \left(\frac{H_a}{H_l^{*3}} \right)^{1/2} p v_r \frac{f_{MRR}(\psi, C_{vol})}{f_P(\psi)} \tag{5.42}$$

Equation (5.42) indeed shows that the material removal rate is proportional to the

nominal pressure and the relative velocity, which is in agreement with the Preston's equation given as Eq. (5.1). The Preston constant, k_p, therefore, is determined to be

$$k_p = \frac{\zeta}{\pi}\left(\frac{H_a}{H_l^{*3}}\right)^{1/2} \frac{f_{MRR}(\psi, C_{vol})}{f_P(\psi)} \tag{5.43}$$

It is not a surprise that the effective hardness of the surface layer with a thin reaction film, H_l^*, affects the polishing rate. The harder the surface material is, other conditions being the same, the less the polishing rate will be. The chemicals may improve the material removal rate by decreasing H_l^* by forming a thin reaction film on the top.

Equation (5.42) indicates that softer pads may give less polishing rate than harder pads. Even though softer pads have more real contact area at the same given pressure, the harder asperities can apply greater loads to the particles. This statement, however, is only valid when the pads have similar plasticity index, ψ, which also influence the removal rate. That is, mechanical properties of pad asperities, not only the hardness, H_a, but the hardness-to-modulus ratio, H_a / E_a, are important on material removal. As discussed in Chapter 4, H_a and E_a of polymeric materials are typically proportional to each other, and hence cannot be varied much. Therefore, plasticity index of polymeric surface is mostly determined by the ratio of asperity radius to the standard deviation of heights, R_a / σ_a.

The normalized height reduction rate, from (5.42), is plotted versus ψ in Figure 5.10, when $\zeta = 0.01$, $H_a = 293$ MPa, $H_l^* = 1.5$ GPa, $p_a = 35$ kPa (5 psi), and $C_{vol} = 0.1$. Typical new pads have plasticity index of approximately 3 to 4. As ψ decreases by decrease in E_a / H_a and/or R_a / σ_z, the removal rate initially increases. This is mainly due to the increase in real contact area, Figure 5.7. At relatively high ψ, $\psi >> C_c^{1/2}$, most of the asperities in contact have high enough pressure, greater than the critical limit, p_c, that can apply the maximum particle loads, Figure 5.9. That is, the removal rates under the asperities are independent of asperity contact pressure, and hence the removal rate is approximately proportional to the contact area. As ψ become less than $C_c^{1/2}$, however, the contact pressure under each asperity decreases and the number of asperities that have less pressure than p_c may start to dominate the contact. The overall removal rate will then decrease though the contact area increases.

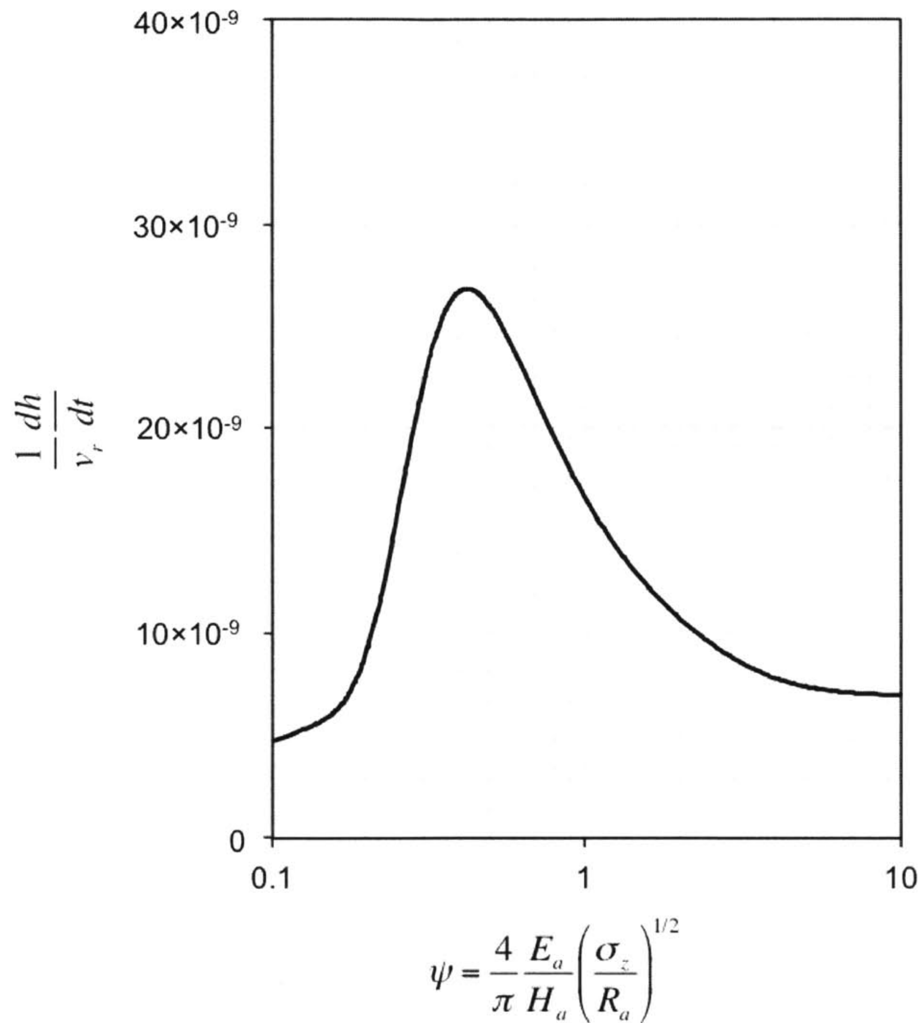

Figure 5.10. Normalized thickness reduction rate of surface layer, $dh / v_r dt$ versus plasticity index, ψ, at $\zeta = 0.01$, $H_a = 293$ MPa, $H_l^* = 1.5$ GPa, $p_a = 35$ kPa (5 psi), and $C_{vol} = 0.1$.

The overall material removal rate derived in Eq. (5.42) is based on the assumption that the surface layer is removed predominantly by the hard abrasives, even though the pad asperities themselves may also scratch the surface layer as discussed in the previous chapters. The surface layer is being "polished," due to the "fine scratches," by the abrasives under every pad asperity in sliding contact, whereas the surface layer is "scratched" in larger scale by few asperities themselves that only satisfy the scratching criteria. The amount of material removed by the pad asperities, accordingly, can be assumed to be negligible compared with that by the abrasives. The probability of pad scratching in CMP where slurry is provided between the pad-wafer contact might be even less than that where only deionized water is provided. That is, scratching by the soft pad asperities is a critical problem due to the massive width and depth of the scratch, but contribution on the material removal is minor due to its less probability. In other words, the assumption that the surface layer material is removed solely by the abrasives is only justified when the probability of pad scratching is not significant.

The friction coefficient between the pad asperities and the surface layer, accordingly, do not affect the overall material removal rate as shown in Eq. (5.42) based on the assumption above. Therefore, it is expected that pad scratching will decrease and that polishing rate will remain the same if the friction coefficient can be reduced by providing lubricants into the interface. However, usage of lubricants should be carefully managed, since the lubricant should only reduce the friction between pad asperities and the surface layer. If the friction between asperity-particle or particle-layer contact also decreases, the volumetric material removal rate by each particle may decrease and thus the overall material removal rate may eventually decrease.

5.4. Polishing experiments using asperity-flattened pads

In order to validate the theoretical predictions, Cu polishing experiments were conducted on a face-up polishing apparatus, Figure 5.11, using a new IC1000 pad and five differently asperity-flattened pads. The experimental processes and conditions for asperity-flattening are the same as explained in Section 4.3. Circular disks, 30 mm in

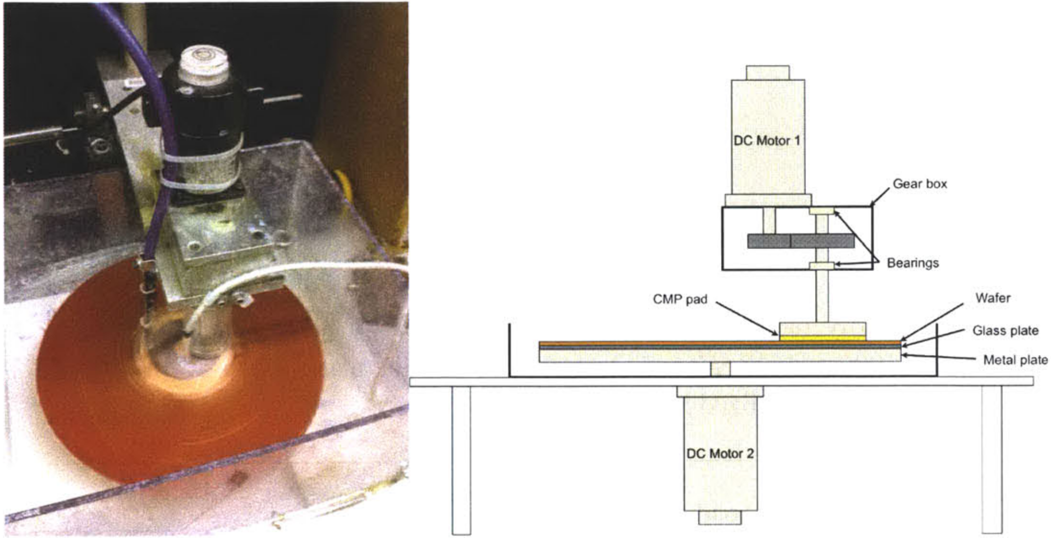

Figure 5.11. Experimental face-up CMP polishing tool.

Table 5.1. Experimental conditions for Cu polishing experiments.

Parameter	Value
diameter of CMP pad	30 mm
normal load	24 N
nominal pressure	35 kPa (= 5psi)
center-to-center distance	30 mm
rotational speed	150 rpm
relative velocity	0.5 m/s
polishing time	2 min
particle (Al_2O_3) radius	150 nm
volumetric particle concentration	10 vol%
H_2O_2 concentration	3 vol%
slurry flow rate	200 ml/min

Table 5.2. Asperity radius, standard deviation of asperity heights, and their ratio of IC1000 pad ($E_a / H_a = 7.6$). Also listed are the material removal rate (MRR) and the normalized MRR.

Parameter	New pad	Pad flattened by				
		Compression		Rolling		Sliding
		300 kPa		2,300 kPa		
		25 °C	185 °C	25 °C	185 °C	25 °C
R_a (μm)	23.5	39.5	173.4	57.8	106.9	72.3
σ_z (μm)	4.0	3.8	2.0	3.6	3.2	3.0
R_a / σ_z	5.9	10.6	85.8	16.0	33.5	23.8
ψ	4.0	3.0	1.0	2.4	1.7	2.0
dh / dt (nm / min)	264	309	345	329	438	364
$\frac{1}{v_r}\frac{dh}{dt}$ ($\times 10^9$)	8.8	10.3	11.5	11.0	14.6	12.1

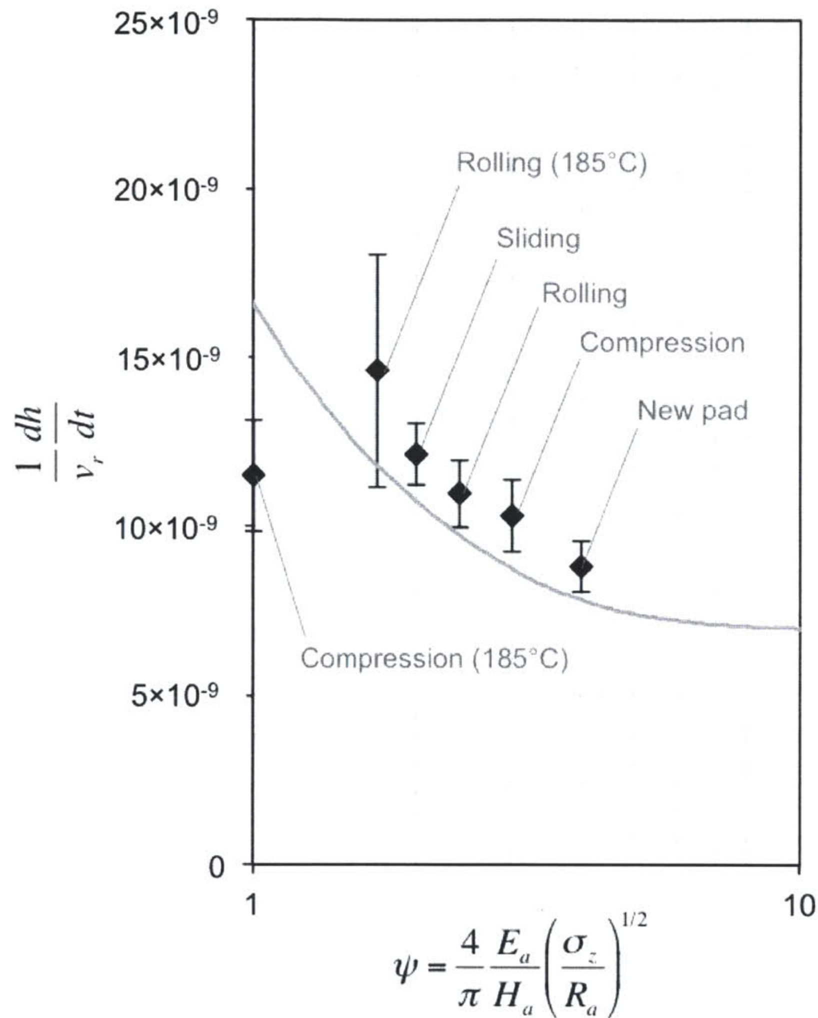

Figure 5.12. Results of the Cu polishing experiments according to the plasticity index, ψ. Grey line is the estimated normalized thickness reduction rate of surface layer versus plasticity index, when $\zeta = 0.01$, $H_a = 293$ MPa, $H_l^* = 1.5$ GPa, $p_a = 35$ kPa (5 psi), and $C_{vol} = 0.1$.

diameter, of polishing pads were pressed at 24 N, which corresponds to a nominal pressure of 35 kPa (= 5 psi), against a wafer with Cu layer at the top. The center-to-center distance between pad and wafer was 30 mm, and both were rotated at 150 rpm, which corresponds to a relative velocity of 0.5 m/s. A slurry comprising 10 vol.% of Al_2O_3 abrasives of average diameter 300 nm and 3 vol. % of H_2O_2 was provided at a flow rate of 200 ml / min. Wafers were polished for 2 minutes each and the polishing rates were determined by measuring the weight loss after polishing. In the calculations, the mass density of Cu layer is assumed to be 9 g/cm^3, Appendix G. The experimental conditions are summarized in Table 5.1. The topographical properties, R_a and σ_z, their ratio, and the plasticity indices of the new and asperity-flattened IC1000 pad are listed in Table 5.2. The asperity modulus-to-hardness ratio of 7.6, Table 4.1, was used to estimate the plasticity indices.

As the plasticity index can be decreased by asperity-flattening from 4.1 to 1, more than 80 percent of the asperities in all cases are expected to have greater pressure than the critical limit, Figure 5.9; hence the polishing rate will increase by increased real area of contact. Therefore, as the plasticity index decreases, it is expected that the material removal rate by asperity-flattened pads will be greater than that by the new pad. The height reduction rate of three polishing experiments per pad are calculated and listed in Appendix G, and the average removal rate for each pad is listed in Table 5.2. The results of the Cu polishing experiments indeed show that, Figure 5.12, the polishing rate increases as the plasticity index decreases.

5.5. Summary

In this chapter, the effects of topographical and mechanical properties of pad asperities on material removal have been investigated.

(1) An equation for material removal rate by hard abrasives under a single-asperity sliding contact has been derived based on contact mechanics and abrasive wear models. The model reveals that the removal rate per asperity strongly depends on the

asperity contact pressure and area, as higher pressure can transfer greater load on each abrasive and as larger area can have more particles involved. Since pads are softer than the surface being polished and much softer than the abrasive, the load that can be applied by the asperity on an abrasive particle is limited, determined by its hardness and by the particle geometry. Once the asperity contact pressure is greater than the critical limit the removal rate by single-asperity sliding contact becomes independent of the asperity contact pressure.

(2) Material removal rate by multi-asperity sliding contact has been modeled, taking into account the effects of asperity height variation of rough pad surfaces. The plasticity index, ψ, which characterizes the topographical and mechanical properties of rough surfaces being in contact, was identified as an important variable in material removal. The model reveals that at high plasticity index, the removal rate is relatively low due to the small real contact area. As the plasticity index decreases, the removal rate initially increases due to the increase in real contact area. As the plasticity index further decreases less than about five times the particle concentration, however, the removal rate will decrease due to the decreased proportion of asperities in "high-pressure" contact.

(3) New IC1000 pads were asperity-flattened to decrease the plasticity index from four to one. As most of the asperities in contact are expected to have pressure greater than the critical limit, the model predicts that the polishing rate should increase as the plasticity index decreases and the real contact area increases. The results of polishing experiments on Cu using asperity-flattened pads indeed showed that the material removal rate increases as the ratio of asperity radius to the standard deviation of heights, R_a / σ_z, increases, i.e., as the plasticity index, ψ, decreases.

Nomenclature

A_a asperity contact area [m^2]

A_l cross-sectional area of particle scratching [m^2]

A_n nominal contact area between pad and wafer [m^2]

A_p cross-sectional area of retained material on the surface after particle scratching as piled-up [m^2]

A_r real contact area between pad and wafer [m^2]

a_l semi-contact width of particle scratching [m]

C_{vol} volume concentration of particles in slurry

d separation distance [m]

k_p Preston constant [$m^2 N^{-1}$]

E_a Young's modulus of pad asperity [$N m^{-2}$]

E_l Young's modulus of surface layer [$N m^{-2}$]

H_a hardness of pad asperity [$N m^{-2}$]

H_f hardness of thin reaction film [$N m^{-2}$]

H_l hardness of surface layer [$N m^{-2}$]

H_l^* effective hardness of surface layer with thin reaction layer at the top [$N m^{-2}$]

h_f thickness of thin reaction film [m]

h thickness of surface layer removed [m]

N_p number of particles per unit volume [m^{-3}]

n total number of asperities per unit area [m^{-2}]

n_c number of asperities in contact per unit area [m^{-2}]

P_a normal load on an asperity [N]

P_p normal load on a particle [N]

p nominal pressure [$N m^{-2}$]

p_a mean asperity contact pressure [$N m^{-2}$]

R_a radius of asperity [m]

R_p radius of particle [m]

t process time [s]

V_p volume of particle [m^3]

$V_{r,a}$ volume of surface layer removed by single-asperity [m^3]

$V_{r,p}$ volume of surface layer removed by single-particle [m^3]

v_r relative velocity between pad and wafer [$m\ s^{-1}$]

z_a asperity height [m]

δ approach of distant points [m]

δ_c critical approach of distant points [m]

$\delta_{f\text{-}p}$ approach of distant points at the onset of fully-plastic asperity deformation [m]

δ_y approach of distant points at the onset of asperity yielding [m]

δ_l depth of the particle scratching [m]

ζ fraction of material detached from particle scratching

λ_p particle spacing [m]

ξ $= (z_a - d) / \sigma_z$

σ_z standard deviation of asperity heights [m]

$\sigma_{y,a}$ yield strength of asperity [$N\ m^{-2}$]

$\phi(z_a)$ probability density of asperity height

References

Borucki, L. J., 2002, "Polishing pad surface characterization in chemical-mechanical polishing," *J. Eng. Math.*, vol. 43, pp. 105-114.

Borucki, L. J., Witelski, T., Please, C., Kramer, P. R. and Schwendeman, D., 2004, "A theory of pad conditioning for chemical-mechanical polishing," *J. Eng. Math.*, vol. 50, pp. 1-24.

Bozkaya, D. and Müftü, S., 2009, "A material removal model for CMP based on the contact mechanics of pad, abrasives, and wafer," *J. Electrochem. Soc.*, vol. 156, no. 12, pp. H890-H902.

Buttery, T. C. and Archard, J. F., 1970, "Grinding and abrasive wear," *Proc. Inst. Mech. Eng.*, vol. 185, pp. 537-551.

DeNardis, D., Rosales-Yeomans, D., Borucki, L. and Philipossian, A., 2010, "A three-step copper chemical mechanical planarization model including the dissolution effects of a commercial slurry," *Thin Solid Films*, vol. 518, pp. 3910-3916.

Fan, W., 2012, "Advanced modeling of planarization processes for integrated circuit fabrication," Ph.D. Thesis, Department of Electrical Engineering and Computer Science, MIT, Cambridge, MA.

Greenwood, J. A. and Williamson, J. B. P., 1966, "Contact of nominally flat surfaces," *Proc. Roy. Soc. Lond. A*, vol. 295, pp. 300-319.

Hooper, B. J., Byrne, G. and Galligan S., 2002, "Pad conditioning in chemical mechanical polishing," *J. Mater. Process. Tech.*, vol. 123, pp. 107-113.

Hernandez, J., Wrschka, P. and Oehrlein, G. S., 2001, "Surface chemistry studies of Copper chemical mechanical planarization," *J. Electrochem. Soc.*, vol. 148, no.7, pp. G389-G397.

Ihnfeldt, R. and Talbot, J. B., 2008, "Effect of CMP slurry chemistry on Copper nanohardness," *J. Electrochem. Soc.*, vol. 155, no. 6, pp. H412-H420.

Johnson, K. L., *Contact Mechanics*, Cambridge, UK: Cambridge Press, 1985.

Lai, J.-Y., 2001, "Mechanics, mechanisms, and modeling of the chemical mechanical polishing process," Ph.D. Thesis, Department of Mechanical Engineering, MIT, Cambridge, MA.

Lee, H., Zhuang, Y., Sugiyama, M., Seike, Y., Takaoka, M., Miyachi, K., Nishiguchi, T., Kojima, H. and Philipossian, A., 2010, "Pad flattening ratio, coefficient of friction

and removal rate analysis during silicon dioxide chemical mechanical planarization," *Thin Solid Films,* vol. 518, pp. 1994-2000.

Lee, H. S., Jeong, H. D. and Dornfeld, D. A., 2013, "Semi-empirical material removal rate distribution model for SiO_2 chemical mechanical polishing (CMP) processes," *Prec. Eng.,* vol. 37, pp. 483-490.

Luo, J. and Dornfeld, D. A., 2001, "Material removal mechanism in chemical mechanical polishing: theory and modeling," *IEEE Trans. Semicon. Manuf.,* vol. 14, no. 2, pp. 112-133.

McGrath, J. and Davis, C., 2004, "Polishing pad surface characterization in chemical mechanical planarisation," *J. Mater. Process. Tech.,* vol. 153-154, pp. 666-673.

Park, K. H., Kim, H. J., Chang, O. M. and Jeong, H. D., 2007, "Effects of pad properties on material removal in chemical mechanical polishing," *J. Mat. Process. Tech.,* vol. 187-188, pp. 73-76.

Paul, E., 2001, "A model of chemical mechanical polishing," *J. Electrochem. Soc.*, vol. 148, no. 6, pp. G355-G358.

Paul, E., Kaufman, F., Brusic, V., Zhang, J., Sun, F. and Vacassy, R., 2005, "A model of copper CMP," *J. Electrochem. Soc.*, vol. 152, no. 4, pp. G322-G328.

Preston, F. W., 1927, "The theory and design of plate glass polishing machines," *J. Soc. Glass Tech.,* vol. 11, pp. 214-256.

Qin, K., Moudgil, B. and Park, C.-W., 2004, "A chemical mechanical polishing model incorporating both the chemical and mechanical effects," *Thin Solid Films,* vol. 446, pp. 277-286.

Saka, N., Eusner, T. and Chun, J.-H., 2008, "Nano-scale scratching in chemical-mechanical polishing," *Annals of the CIRP*, vol. 57, pp. 341-344.

Sorooshian, J., Borucki, L., Stein, D., Timon, R., Hetherington, D. and Philipossian, A., 2005, "Revisiting the removal rate model for oxide CMP," *ASME J. Tribo.,* vol. 127, pp. 639-651.

Shi, H. and Ring, T. A., 2010, "CMP pad wear and polish-decay modeled by asperity population balance with fluid effect," *Microelectronic Eng.*, vol. 87, pp. 2368-2375.

Thakurta, D. G., Borst, C. L., Schwendeman, D. W., Gutmann, R. J. and Gill, W. N., 2000, "Pad porosity, compressibility and slurry delivery effects in chemical-mechanical planarization: modeling and experiments," *Thin Solid Films*, vol. 366, pp. 181-190.

Vasilev, B., Bott, S., Rzehak, R., Liske, R. and Bartha, J. W., 2013, "A method for characterizing thc pad surfacc texture and modeling its impact on the planarization in CMP," *Microelectronic Eng.,* vol. 104, pp. 48-57.

Xie, X., 2007, "Physical understanding and modeling of chemical mechanical planarization in dielectric materials," Ph.D. Thesis, Department of Physics, MIT, Cambridge, MA.

Zhao, Y., Maietta, D. M. and Chang, L., 2000, "An asperity microcontact model incorporating the transition from elastic deformation to fully plastic flow," *ASME J. Trib.*, vol. 122, no. 1, pp. 86-93.

Zhao, Y. and Chang, L., 2002, "A micro-contact and wear model for chemical-mechanical polishing of silicon wafers," *Wear*, vol. 252, pp. 220-226.

CHAPTER 6

CONCLUSION

6.1. Summary

In this thesis, generation and mitigation of micro-scale scratching by soft pad asperities on both monolithic and patterned surfaces in CMP were investigated. Based on contact mechanics, analytical models were presented to examine the effects of topographical, mechanical and tribological properties on pad scratching, and to elucidate the key parameters for scratch mitigation. A novel, cost-effective method for controlling the pad topography, asperity-flattening, is developed and used to experimentally validate the scratch mitigation. Furthermore, a new material removal rate model considering the asperity height variation of the rough pad surfaces, which reveals that the asperity-flattened pads can also improve the polishing rate, is developed.

In Chapter 2, contact mechanics models of pad-induced scratching were presented, and the effects of mechanical and tribological properties were studied. Under single-asperity sliding contact, the critical limit of the asperity contact pressure, along with the interfacial friction, that can initiate the surface layer yielding was first explored, for each mode of asperity deformation: elastic, elastic but at the onset of yielding, elastic-plastic and fully-plastic. For the extreme cases, elastic but at the onset of yielding and fully-plastic, scratch-regime maps were established to provide the criteria to identify whether the soft asperities can scratch the hard surface or not. Under multi-asperity sliding contact, the probability of asperities that exceed the scratch criteria were derived in terms of the scratching index, which is determined by the relative hardnesses and the friction coefficient between the asperities and surface layer, and the plasticity index, which is determined by the modulus-to-hardness ratio and the radius-to-standard deviation of heights of the asperities. For experimental validations, two CMP pads (Pad A and IC1000) were slid over various thin films (Al, Cu, SiO_2, Si_3N_4, TiN and three low-*k*

dielectrics) using deionized water as a lubricant. Both the theoretical models, based on the hardnesses determined by nano-indentation and the friction coefficients determined by sliding friction apparatus, and the experimental results of the pad sliding experiments showed that the number of scratches rises as the scratching index increases beyond 0.33. Furthermore, it was found that Al and Cu layers are more vulnerable to pad scratching due to the large variation of local hardness. Compared with the scratching results, the scratch-regime maps using the extreme hardness values of pad asperities and surface layer provided good criteria for pad scratching. Consequently, it was suggested that the scratching index should be reduced to mitigate scratching and that the local hardnesses of asperities and layers should be tightly controlled to further eliminate scratching.

In Chapter 3, scratching of Cu/dielectric line structures by soft asperities was investigated. First the scratching criteria and the scratch-regime maps previously constructed for monolithic layers were advanced for the patterned layers. Compared with the contact diameter under a single-asperity, if the Cu and dielectric lines are wider, the scratching criteria and the scratch-regime maps for each line were expected to be the same as those for the monolithic layers. Therefore, the asperity may scratch Cu and/or dielectric lines individually, or neither. On the other hand, if the linewidths are much narrower than the contact diameter, the patterned layer is expected to behave as a composite structure with as an "effective hardness," which can be estimated by the rule-of-mixtures (ROM). The asperity, accordingly, may scratch both Cu and dielectric lines, or neither. Then sliding experiments were conducted on patterned Cu/dielectric layers of various linewidths using solid polymer pins, loaded into the fully-plastically deformed state. Results of sliding experiments on patterns with linewidths greater than a micrometer indeed confirmed that polymer pins scratch the Cu lines but not the dielectric lines, in accordance with the scratch criteria for monolithic layers. Experimental results on patterns with linewidths less than a micrometer again showed that polymer pins scratch both Cu and dielectric lines, in accordance with the scratch criteria for composite structures.

In Chapter 4, mitigation of scratching by controlling the pad topography was examined. Contact mechanics models predicted that pad scratching can be reduced by decreasing the number of plastically deformed asperities, for they are the primary source.

Considering the asperity height variation of rough pad surfaces, accordingly, the models specified the ratio of asperity radius to the standard deviation of asperity heights as a key parameter that determines the proportion of asperities in plastic contact. Asperity-flattening, either by compression using a smooth, flat plate or by rolling/sliding using a smooth roller, was introduced to control the identified parameter. In the scratching experiments, fewer scratches were found by asperity-flattened pads compared with those generated by new pads. In addition, polishing rates by asperity-flattened pads were higher than that of the new pad.

Chapter 5 explored the role of pad asperities in material removal. First, the material removal by hard abrasives under a single-asperity sliding contact was investigated. Based on contact mechanics and abrasive wear models between particle-layer and between asperity-particle contacts, the polishing rate per single-asperity was derived in terms of the asperity contact pressure and area. The model revealed that the removal rate under single-asperity sliding contact strongly depends on the asperity contact pressure and area at relatively low pressure. However, the removal rate per asperity becomes independent of asperity contact pressure once the contact pressure exceeds a critical limit, which is determined by the asperity hardness and the particle concentration. Then, the material removal by multi-asperity sliding contact was studied. The effects of topographical and mechanical properties of pad asperities on contact area ratio, and on relative proportions of "high-pressure" asperities that have greater pressure than the critical limit, were elucidated. For both the contact area ratio and the relative proportion of "high-pressure" asperities, the plasticity index was identified as a key parameter. It was shown theoretically and experimentally that the asperity-flattened pads with reduced plasticity index to about unity, improve the polishing rate compared to that of new pads. The improvement is mainly due to the increase in real contact area between the pad and the wafer. However, the model also indicates that the polishing rate will eventually decrease as the real contact area increases further, much less than unity, due to the decrease in proportion of asperities in "high-pressure" contact.

6.2. Suggestions for future work

Based on the analytical and experimental results presented in this thesis, future research on the CMP process may be directed toward the following areas.

Optimization of pad topography and its maintenance – In Chapters 4 and 5, pad topography control, by enhancing the R_a / σ_z, was suggested as an effective way to mitigate scratching and simultaneously improve the material removal rate. A greater challenge in pad topography control, however, is the maintenance of the enhanced R_a/σ_z value through the pad life. During the polishing of the wafers, the pad asperities are worn out by the hard abrasives in the slurry, which may further increase the R_a / σ_z. As discussed in Chapter 5, the material removal rate eventually decreases as R_a/σ_z increases beyond a certain point by reduced pressure under asperity contacts. In addition, pad wear may result in the choking of the slurry flow from the edge to the center of the wafer and may promote hydroplaning. Therefore, in a CMP system, diamond conditioners are used to "cut" the pad surface in order to maintain certain roughness. That is, if the pad roughness is too low, most of the asperities do not have enough pressure to press the hard abrasives to polish, whereas if the pad roughness is too high, the contact pressure under some asperities become high enough to generate large scratches themselves on the relatively hard surfaces. Therefore, optimization of pad topography as well as its preservation should be studied and practical methods need to be developed to promote polishing and to eliminate scratching in CMP.

Pad wear rates and improvement of pad life – For optimization of manufacturing processes, not only the high production rates and high quality but also the least cost of the process should be the primary targets. As the cost of consumables in CMP is now estimated to be about 70 percent of the total CMP unit process cost and as the cost of the polishing pads is the biggest among the consumables, improving the pad life should also be considered for pad optimization. As the pad continuously wears out during the polishing and diamond conditioning processes, while maintaining the optimized pad topography, the pad wear should also be minimized.

Effect of chemistry on pad and layer surface properties – In Chapters 2 to 4, mechanical properties of pad and layer surfaces are assumed to be independent of slurry chemicals. In addition, though the formation of thin reaction film on the surface layer was considered and taken into account in the material removal rate models in chapter 5, the effects of chemical parameters, such as oxidant concentrations and pH level in the slurry, are still empirical and unclear. Therefore, research on the role of chemicals on surface properties may strengthen the developed models, particularly the material removal rate model.

Mitigation of pad scratching by reducing interfacial friction – The pad scratching models, developed in Chapter 2, suggest that the proportion of scratching asperities between the rough pad and the smooth, flat surface can be reduced by decreasing the scratching index, either by reducing the pad hardness or by reducing the interfacial friction between the pad asperities and the surface layer. Reducing the pad hardness, however, as discussed in Chapter 5, may diminish the polishing rate since softer asperities transfers smaller normal loads on the hard particles than do harder asperities. For both scratch mitigation and polishing rate improvement, therefore, reducing the friction seems to be another approach that should be explored.

Probability of scratching by pad asperities with abrasive particles – In Chapter 2, the probability of pad scratching was theoretically and experimentally investigated without considering the abrasive particles between the pad-wafer contact. The work clearly shows that scratching can occur due to the pad asperities themselves and further provides the solutions for mitigating the pad scratching. Once the particles are involved within the pad-wafer contact, however, less number of asperities will be in direct contact, and thus fewer scratches will be generated by the pad asperities. In order for a quantitative analysis of scratching by pad asperities in general CMP conditions, the model can be further advanced considering the interactions among the pad asperities, particles and the surface layers.

APPENDIX A

SURFACE TOPOGRAPHY OF CMP PADS

The characterized topographical data of two different CMP pads used in the scratching and polishing experiments in this thesis is listed. Topographical parameters, asperity height, radius, and spacing of a standard polishing pad, IC1000 manufactured by Dow Chemical Co., and a commercial Pad A, were determined by a stylus proflometer; a Tencor P16 profilometer, Figure A.1. The experimental conditions for the measurement are listed in Table A.1.

Figure A.2 shows the surface profiles of new, broken-in, and used pad A. The pad was "broken-in" in the industrial CMP equipment. To "break-in" the pad, about fifty wafers with monolithic Cu layers on the surface were polished for 1 min per wafer. A diamond conditioner was used to simultaneously regenerate the pad asperities during the "break-in" process. The used pad was selected when a "broken-in" pad polished wafers for 20 hours. The roughness parameters of each profile are calculated and listed in Table A.2. In addition, all determined heights, spacings and radii of the asperities within the scan length of 5 mm are listed in Table A.3.

Similarly, the surface profiles of new, broken-in, and used IC1000 pads are shown in Figure A.3. The roughness parameters are listed in Table A.4, and the determined heights, spacings and radii of the asperities within the scan length of 5 mm are listed in Table A.5.

The surface topographies of asperity-flattened pads used in the scratching and polishing experiments in Chapters 4 and 5 are also determined by a Tencor P16 profilometer. The experimental conditions are the same as listed in Table A.1. The roughness parameters are listed in Table A.6, and the determined heights, spacings and radii of the asperities within the scan length of 5 mm are listed in Table A.7.

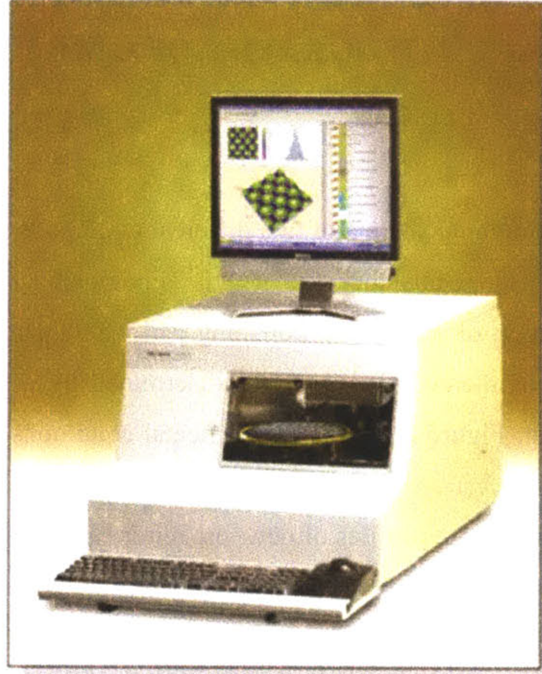

Figure A.1. Tencor P16 Profilometer.

Table A.1. Experimental conditions for pad topography characterization.

Parameter	Value
Tip diameter	2 μm
Normal load	20 μN
Scanning speed	50 μm/s
Sampling rate	200 Hz
Scan length	5,000 μm

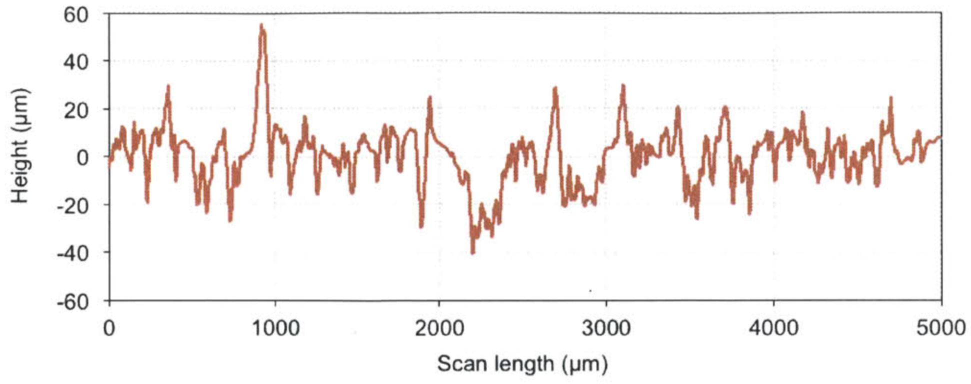

(a) New pad

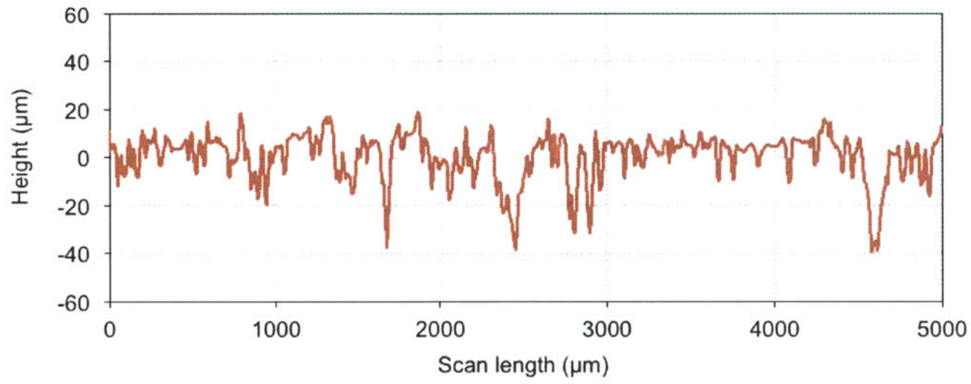

(b) Broken-in pad

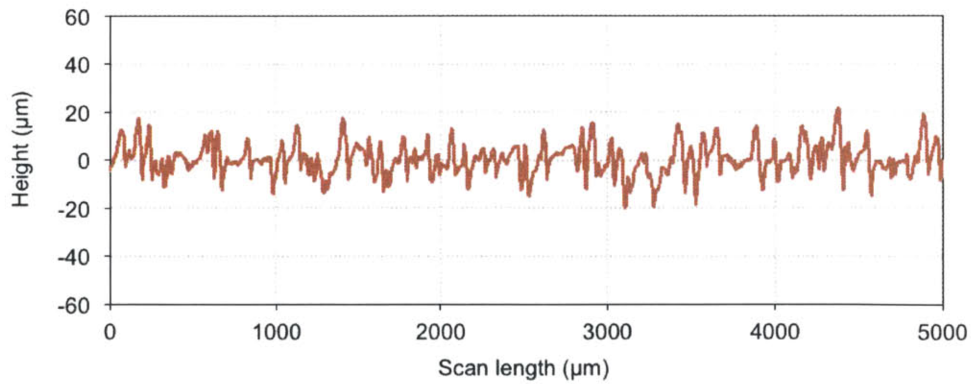

(c) Used pad

Figure A.2. Surface profiles of Pad A.

Table A.2. Roughness parameters of new, broken-in and used Pad A. All measurements are in μm.

Parameter	New	Broken-in	Used
r_a (average roughness)	8.73	7.24	4.85
$r_{a,max}$ (max Ra)	11.68	9.59	6.23
r_q (rms)	11.88	9.73	6.42
r_p (peak)	55.90	18.23	21.14
r_v (valley)	40.65	39.25	21.11
r_t (peak/valley)	96.55	57.48	42.25
r_z (10pt height)	78.35	54.97	37.57

Table A.3. Asperity height, radius and spacing of new, broken-in, and used Pad A.

#	New			Broken-in			Used		
	z_a (μm)	R_a (μm)	λ_a (μm)	z_a (μm)	R_a (μm)	λ_a (μm)	z_a (μm)	R_a (μm)	λ_a (μm)
1	12.5	39.1	64.4	2.2	17.3	52.0	12.2	42.0	101.8
2	13.9	13.0	201.2	6.2	21.5	27.2	16.9	83.3	64.7
3	11.4	14.3	89.4	4.9	13.7	45.7	14.4	79.9	70.9
4	29.6	25.6	250.8	10.4	58.5	139.0	0.6	22.6	39.7
5	5.7	40.0	232.1	9.9	40.4	151.5	1.3	27.9	46.2
6	1.8	23.3	95.6	7.4	79.6	51.7	3.0	40.8	208.2
7	11.1	35.3	170.2	9.3	31.9	45.2	10.3	44.2	34.0
8	55.0	22.3	107.8	5.5	28.4	200.4	11.6	19.2	46.4
9	13.5	21.9	120.6	14.1	48.4	38.9	11.0	39.7	121.1
10	17.0	27.5	33.2	18.1	79.6	94.6	1.0	30.6	95.9
11	3.9	25.3	95.6	3.3	91.5	51.3	9.1	61.9	89.6
12	0.2	21.8	126.5	4.6	31.1	70.2	0.6	24.1	22.1
13	5.4	21.0	39.7	1.6	30.1	163.5	7.9	48.9	15.5
14	2.7	19.6	108.1	4.1	26.0	45.4	14.7	16.4	72.6
15	7.9	21.8	120.6	10.4	17.0	76.4	0.7	32.7	88.4
16	12.9	43.6	493.7	8.8	142.6	88.9	0.2	14.2	46.2
17	12.6	19.7	58.2	15.9	161.6	94.9	2.2	15.5	39.9
18	10.8	22.5	51.9	1.7	35.1	33.0	16.6	32.5	36.9
19	24.0	17.0	145.3	6.8	26.0	57.7	6.1	20.2	156.7
20	1.5	14.8	394.1	6.9	92.9	294.0	9.4	15.2	83.6
21	4.0	42.5	76.9	18.6	61.9	39.2	7.0	25.4	74.6
22	7.5	17.7	33.2	6.3	43.3	64.2	9.7	19.7	68.4
23	5.4	46.5	33.5	2.5	14.8	126.3	2.6	20.9	91.9
24	28.2	40.7	170.3	11.9	110.9	63.9	10.0	34.6	46.9
25	32.1	26.4	164.1	12.2	161.6	157.2	0.7	55.2	45.2
26	4.6	24.3	108.1	15.9	36.8	213.2	12.0	18.2	32.7
27	6.0	22.6	76.9	8.4	85.7	126.0	5.7	17.2	28.5
28	5.1	35.5	89.4	9.0	63.9	194.2	4.3	24.4	50.7
29	4.1	19.7	83.1	4.6	166.9	82.1	4.2	21.4	54.7
30	11.1	17.1	108.1	10.4	21.0	100.8	1.7	18.0	88.1
31	20.0	40.4	95.4	5.9	24.7	119.3	5.0	39.5	73.1
32	8.1	15.6	51.9	7.0	20.6	44.9	5.5	80.7	65.9
33	20.7	34.4	89.4	2.6	11.5	69.9	12.5	77.3	48.2
34	4.1	38.6	64.4	8.9	137.2	200.4	5.0	20.0	63.4
35	10.2	24.3	27.2	9.6	156.2	113.3	13.5	25.4	55.7
36	9.9	26.4	58.2	10.1	29.6	132.0	14.7	38.2	93.1
37	10.2	24.6	51.9	7.3	20.5	88.1	8.5	41.6	45.4
38	17.5	37.6	52.9	4.9	87.5	268.6	4.1	16.6	89.4
39	1.6	31.8	114.1	7.9	48.6	69.7	2.5	37.1	24.5
40	10.4	19.1	157.7	8.0	20.2	181.5	15.0	28.1	172.1
41				15.9	116.2	138.5	3.5	59.4	59.4
42				8.2	167.0	138.0	10.0	21.5	64.7
43				7.9	42.1	75.6	12.2	46.4	108.8
44				4.0	91.0	237.1	1.2	13.9	45.4
45				6.4	69.2	50.7	12.5	30.1	135.1
46				5.2	172.3	63.2	8.2	11.6	19.5
47				2.8	26.3	44.4	1.3	12.9	155.5
48							11.4	30.0	37.2
49							4.9	17.6	73.1
50							4.2	12.6	72.6
51							0.1	22.8	82.4
52							6.9	46.7	66.6
53							2.2	21.8	173.1
54							0.7	42.3	102.3
55							1.2	33.2	84.6

56							0.5	64.5	76.9
57							1.8	26.6	82.6
58							13.2	51.5	35.7
59							4.9	19.0	100.6
60							7.0	35.3	47.7
61							21.6	16.7	18.0
62							6.9	18.1	110.3
63							11.9	35.1	137.8
64							0.7	22.7	21.7
65							1.6	17.8	80.6
66							0.5	27.9	55.2
67							17.9	22.3	47.7
68							9.4	23.5	67.1
Mean	11.8	26.1	117.6	8.0	61.3	106.9	6.9	32.2	72.9
Max.	55.0	46.5	493.7	18.6	166.9	294.0	21.6	83.2	208.2
Min.	0.2	13.0	27.2	1.6	13.7	27.2	0.1	14.2	15.5
Std. Dev.	10.5	9.6	93.4	4.3	46.8	66.0	5.4	18.3	40.0
C.V.	0.89	0.37	0.79	0.53	0.76	0.62	0.78	0.57	0.55

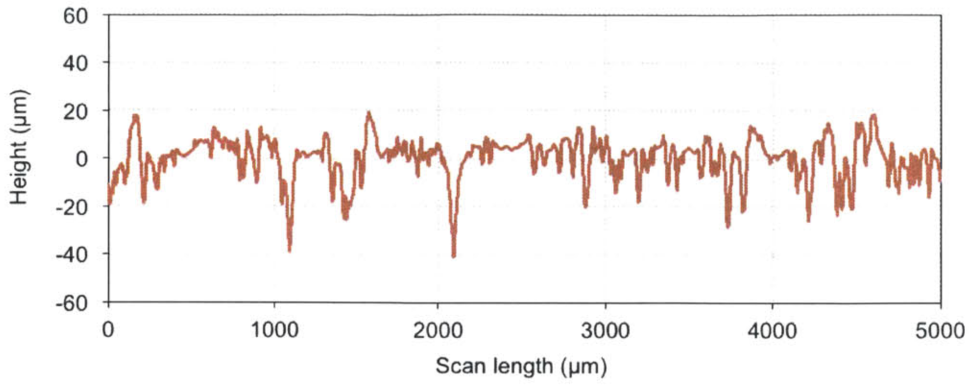

(a) New pad

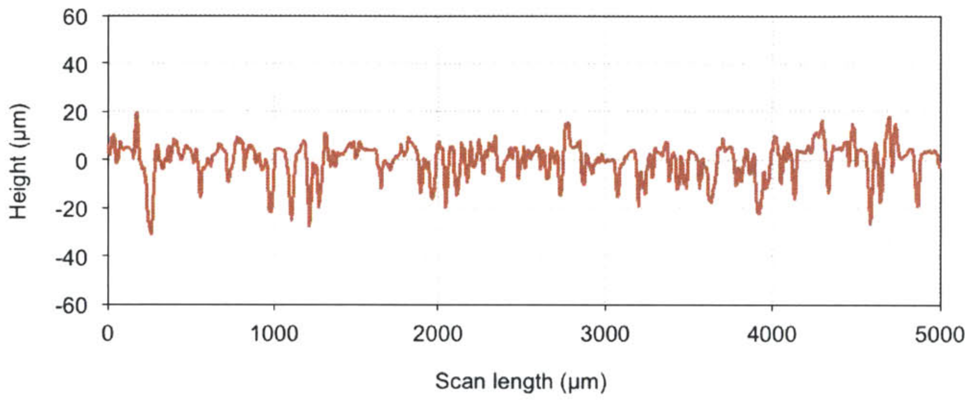

(b) Broken-in pad

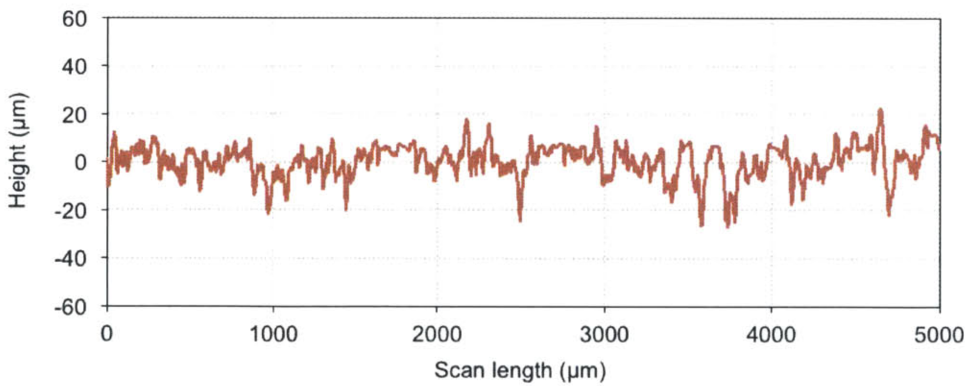

(c) Used pad

Figure A.3. Surface profiles of IC1000 pads.

Table A.4. Roughness parameters of new, broken-in and used IC1000 pads. All measurements are in μm.

Parameter	New	Broken-in	Used
r_a (average roughness)	6.18	5.57	5.42
$r_{a,max}$ (max Ra)	8.71	6.69	7.62
r_q (rms)	8.24	7.39	7.04
r_p (peak)	22.72	22.18	22.13
r_v (valley)	31.05	34.96	27.57
r_t (peak/valley)	53.78	57.14	49.69
r_z (10pt height)	45.17	48.03	43.39

Table A.5. Asperity height, radius, and spacing of new, broken-in, and used IC1000 pads.

#	New			Broken-in			Used		
	z_a (μm)	R_a (μm)	λ_a (μm)	z_a (μm)	R_a (μm)	λ_a (μm)	z_a (μm)	R_a (μm)	λ_a (μm)
1	18.0	26.6	80.9	10.7	11.6	43.4	12.4	39.1	42.4
2	2.0	14.8	93.1	8.0	26.4	105.6	2.8	29.8	37.0
3	1.2	13.5	55.9	19.9	71.6	124.1	4.2	13.6	80.9
4	2.1	50.0	261.1	5.0	187.0	74.1	8.2	30.5	80.6
5	7.5	26.4	205.2	3.6	87.0	49.4	3.6	57.2	49.4
6	12.9	36.9	86.6	8.9	25.0	86.6	10.3	21.8	55.9
7	1.9	29.5	391.6	5.6	25.7	62.2	4.0	22.9	99.4
8	11.1	17.5	192.4	4.5	57.0	74.4	2.8	40.6	99.7
9	12.8	42.0	80.4	1.3	50.3	80.6	5.5	182.0	62.2
10	3.2	41.9	186.2	7.1	33.6	99.1	4.5	91.6	25.0
11	9.7	13.2	99.3	9.2	17.4	74.4	3.3	112.1	49.7
12	0.5	17.6	55.7	6.5	54.8	62.2	6.1	29.2	43.2
13	3.1	28.3	93.1	1.9	10.0	49.7	8.1	129.3	80.3
14	19.5	13.5	223.6	0.3	33.6	74.6	9.1	51.3	317.2
15	3.8	20.6	80.6	4.8	19.4	149.3	2.4	14.1	93.1
16	3.2	10.2	260.8	7.7	56.6	136.8	7.3	35.2	55.9
17	5.1	45.0	74.4	11.0	59.6	49.7	0.7	139.3	31.0
18	7.7	15.2	86.9	3.6	39.9	124.6	5.5	180.2	62.2
19	7.5	9.2	74.4	7.4	98.7	342.2	0.3	84.8	87.1
20	7.2	23.0	80.6	7.2	78.5	87.4	8.2	106.0	37.7
21	7.1	19.0	43.5	9.5	27.5	93.4	0.3	129.9	44.2
22	6.5	23.4	43.9	1.0	22.4	74.5	4.9	100.5	31.5
23	0.3	16.7	93.1	6.7	175.1	62.4	3.7	54.7	44.2
24	9.1	12.2	80.6	5.9	21.7	56.2	7.3	82.4	56.7
25	9.9	16.1	161.5	7.4	20.1	49.9	5.7	27.2	224.6
26	6.1	19.6	61.9	7.3	23.1	99.8	4.2	27.0	50.7
27	5.3	23.3	55.7	8.6	59.9	112.4	0.4	128.0	81.4
28	8.2	24.2	68.1	10.6	29.0	50.1	6.4	143.5	43.9
29	12.3	25.8	62.2	5.4	141.1	87.1	3.1	35.2	25.2
30	13.1	29.3	86.9	5.6	50.1	30.9	17.0	177.5	93.9
31	8.0	17.0	105.8	4.0	173.4	55.9	3.6	35.3	38.0
32	9.3	24.1	80.9	3.9	73.4	31.2	4.3	26.0	31.5
33	2.6	13.8	87.1	5.4	11.4	69.0	14.5	9.7	50.2
34	4.0	48.5	93.4	15.9	12.1	118.3	0.1	26.6	37.9
35	3.7	18.7	149.5	2.7	43.5	68.4	10.4	53.4	100.1
36	4.4	14.5	56.4	2.1	36.7	31.0	3.0	17.9	87.6
37	10.0	28.3	50.2	4.4	20.1	180.5	6.5	19.0	25.7
38	5.6	21.3	50.2	2.7	3.9	105.8	3.7	36.7	25.5
39	4.3	28.7	75.1	7.4	41.2	93.4	4.6	178.2	143.8
40	9.4	22.0	56.4	2.7	3.5	49.9	13.3	87.7	75.4
41	5.5	17.5	93.9	1.8	20.1	37.4	7.8	108.3	81.6
42	3.3	21.4	87.4	4.4	5.8	55.9	1.2	25.3	112.8
43	13.8	25.0	74.6	1.6	43.0	74.6	2.9	125.5	50.7
44	1.3	28.6	99.9	9.5	53.4	118.2	4.3	47.4	38.4
45	3.3	27.8	56.2	4.8	112.2	142.8	8.4	10.2	69.4
46	3.3	29.3	49.9	2.7	92.0	49.5	6.3	39.0	94.1
47	7.0	32.9	25.2	10.4	41.0	124.1	3.1	143.2	113.1
48				5.0	35.9	80.9	1.3	184.1	181.2
49				7.1	188.7	192.7	10.6	88.6	175.2
50				16.4	35.2	143.1	1.9	109.9	75.6
51				7.4	33.6	43.5	11.2	133.7	25.7
52				15.4	36.6	61.9	3.7	104.3	137.8
53				4.7	73.4	99.3	12.4	58.6	57.2
54				7.1	42.6	86.9	10.6	86.3	106.6
55				17.1	154.7	43.2	22.1	31.0	119.1
56				14.8	63.6	204.9	5.1	30.8	106.8

57							2.6	131.8	156.3
58							14.5	147.4	94.1
59							0.2	39.0	94.4
60							0.4	181.4	63.2
Mean	6.7	23.9	102.4	6.9	53.8	89.8	5.9	77.2	79.2
Max.	19.5	50.0	391.6	19.9	187.0	342.2	22.1	182.0	317.2
Min.	0.3	9.2	25.2	0.3	10.0	30.9	0.1	13.6	25.0
Std. Dev.	4.4	9.8	70.1	4.3	45.2	52.8	4.6	54.0	52.5
C.V.	0.66	0.41	0.68	0.63	0.84	0.59	0.77	0.70	0.66

Table A.6. Roughness parameters of IC1000 pads before and after asperity-flattening. All measurements are in μm.

Parameter	New	Flattened		Roll-flattened		Slide-flattened
	(as-received)	300 kPa 25 °C	300 kPa 185 °C	2,300 kPa 25 °C	2,300 kPa 185 °C	2,300 kPa 25 °C
r_a (average roughness)	6.18	5.85	5.87	5.41	5.90	5.52
r_a, max (max Ra)	8.71	9.93	8.98	7.33	7.66	7.74
r_q (rms)	8.24	7.64	7.89	7.33	7.82	7.24
r_p (peak)	22.72	14.97	8.58	15.83	15.52	15.50
r_v (valley)	31.05	29.64	35.63	31.40	36.01	30.81
r_t (peak/valley)	53.78	44.61	44.22	47.23	51.52	46.30

Table A.7. Asperity height, radius, and spacing of IC1000 pads after flattened by compression by a flat plate and after rolling/sliding using a smooth roller.

#	Flattened				Roll-flattened				Slid-flattened	
	300 kPa, 25 °C		300 kPa, 185 °C		2,300 kPa, 25 °C		2,300 kPa, 185 °C		2,300 kPa, 25 °C	
	z_a (μm)	R_a (μm)	z_a (μm)	R_a (μm)	z_a (μm)	R_a (μm)	z_a (μm)	R_a (μm)	z_a (μm)	R_a (μm)
1	15.5	21.9	6.0	368.1	15.5	38.3	8.3	82.8	2.9	247.85
2	3.7	53.4	4.1	67.7	4.1	11.8	11.4	143.6	2.3	51.91
3	3.0	27.2	4.9	181.5	2.9	54.5	7.7	106.1	11.0	77.95
4	5.1	33.0	5.3	53.2	4.6	16.3	4.2	103.9	1.3	38.39
5	8.9	46.8	4.9	483.3	9.1	44.4	2.7	175.1	7.5	17.95
6	3.6	31.5	3.5	114.4	2.9	138.8	5.1	37.1	2.8	30.92
7	1.7	99.9	3.5	159.2	4.2	14.5	5.1	216.7	12.1	178.61
8	0.4	40.5	3.9	38.0	2.3	109.6	2.7	47.7	11.1	92.69
9	9.9	34.4	4.7	60.0	0.2	68.6	6.1	51.0	2.1	185.28
10	5.2	29.4	3.8	105.4	5.0	47.2	1.0	41.7	4.2	29.46
11	4.7	45.4	4.0	10.8	9.5	37.8	2.1	127.9	5.1	92.95
12	7.6	13.0	5.9	262.7	5.2	68.3	4.4	148.7	7.3	22.878
13	4.6	23.5	3.1	388.5	4.8	96.1	7.2	18.2	6.7	26.19
14	2.3	83.8	5.9	187.0	1.3	108.1	9.3	84.6	7.3	184.46
15	12.4	46.9	7.1	43.5	7.5	47.3	9.5	30.4	4.7	29.75
16	3.4	22.4	2.8	126.6	4.5	81.1	5.9	55.0	5.1	33.4
17	7.0	18.4	6.7	44.3	2.2	136.1	4.9	366.2	3.3	41.28
18	4.2	25.7	6.6	84.2	12.4	78.0	1.6	71.8	2.1	17.69
19	9.2	57.2	7.3	78.3	3.2	38.7	7.7	96.9	6.4	20
20	7.1	31.0	5.9	365.0	7.2	12.1	3.2	112.8	8.9	26.93
21	10.0	36.8	5.9	121.5	4.2	31.5	5.8	126.6	10.4	237.65
22	4.4	50.6	6.6	154.2	9.1	18.2	3.5	72.4	9.8	62.11
23	7.2	35.3	5.3	558.0	6.9	69.9	6.8	133.2	8.7	88.15
24	9.9	103.7	6.3	101.8	10.3	16.1	1.1	95.7	12.2	48.59
25	4.8	44.3	1.0	35.5	4.4	22.0	5.1	93.5	9.3	28.15
26	6.0	38.2	5.3	224.0	7.2	68.2	5.6	164.7	9.0	41.12
27	5.8	33.2	5.0	52.0	10	109.5	15.3	26.7	9.2	188.81
28	2.9	49.2	5.7	195.4	5.3	33.5	6.9	206.3	5.52	102.89
29	16.8	16.8	2.1	365.0	4.8	60.8	5.2	37.3	1.7	175.08
30	5.2	27.3	2.5	347.7	5.7	49.0	12.2	40.6	6.5	19.26
31	5.6	87.6	6.0	47.3	6.0	22.5	8.9	31.3	8.4	82.75
32	0.5	50.7	7.2	161.1	2.9	65.2	6.9	117.5	1.6	12.678
33	6.5	13.1	6.7	32.8	16.7	27.0	9.2	138.3	4.2	15.99
34	17.1	44.6	5.3	462.9	5.6	55.1	2.2	100.8	9.5	174.26
35	4.6	18.4	4.7	94.0	5.3	149.5	3.9	116.3	9.0	19.55
36	10.6	24.2	6.9	138.8	0.7	25.2	5.2	114.1	9.5	23.2
37	2.1	38.0	6.2	17.6	6.4	120.3	6.7	185.3	1.8	31.08
38	2.6	22.7	8.1	63.9	17.1	79.3	11.1	47.3	6.8	7.49
39	7.2	91.1	5.4	147.0	4.5	57.9	1.2	226.9	11.3	59.8
40	4.4	31.7	6.7	64.7	1.5	67.3	2.0	57.9	6.5	16.73
41	4.2	25.6	7.7	104.6	10.7	28.0	5.1	61.2	3.1	194.66
42	3.8	20.6	7.3	98.7	2.1	50.4	4.4	51.9	0.5	49.95
43	5.3	36.6	5.9	385.4	2.9	20.8	5.9	138.1	7.4	53.6
44	4.7	4.2	8.1	141.9	6.9	7.5	6.1	158.9	3.4	61.48
45	11.3	14.7	2.1	174.6	4.4	59.2	1.4	121.4	6.6	37.89
46	5.3	75.0	7.0	578.4	4.4	25.4	2.5	136.9	7.1	90.2
47	0.3	38.1	5.4	122.2	11.4	111.3	2.0	134.7	10.1	47.13
Mean	6.1	39.5	5.4	174.7	6.1	57.4	5.8	106.2	6.5	72.7
Max.	17.1	103.7	8.1	578.4	17.1	149.5	15.3	366.2	12.2	336.2
Min.	0.3	4.2	1.0	10.8	0.2	7.5	1.0	18.2	0.5	18.2
Std. Dev.	3.9	23.1	1.7	149.5	3.7	37.2	3.4	67.0	3.3	66.2
C.V.	0.6	0.6	0.3	0.9	0.6	0.6	0.6	0.6	0.5	0.9

APPENDIX B

MECHANICAL PROPERTIES OF CMP PADS, SURFACE LAYERS, AND POLYMER PINS

Mechanical properties, Young's modulus and hardness, for two CMP pads (Pad A and an IC1000 pad), eight thin film layers (Al, Cu, SiO_2, Si_3N_4, TiN and three low-*k* dielectrics), and seven solid polymer pins (LDPE, PP, PTFE, HDPE, PS, PC, and PMMA), were determined by a nanoindenter: the Hysitron Triboindenter TI900, Figure B.1. The experimental conditions for the characterization are listed in Table B.1. Over 100 indentations on each pad, 49 indentations on each monolithic surface layer, and 25 indentations on each polymer pin were made. In all cases, a Berkovich indenter was used and the depth of indentation was 90 nm. Table B.2 and B.3 contains all of the experimental data of new, broken-in, and used pads A and IC1000 pads, respectively, from the nano-indentation tests. Table B.4, B.5, and B.6 lists the data of thin film layers, and Table B.7 and B.8 provides the data of solid polymer pins.

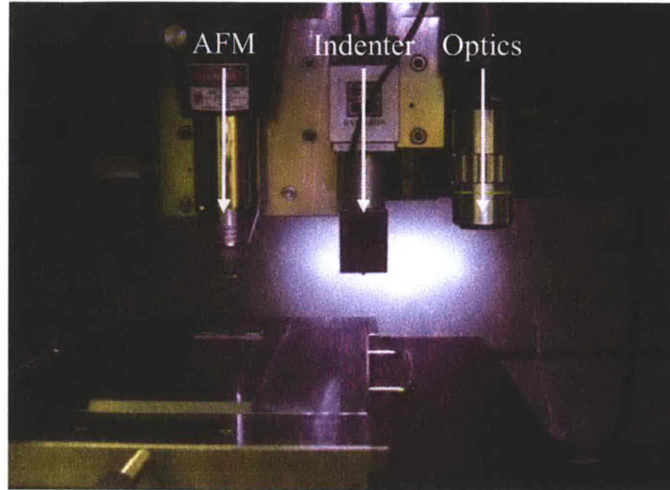

Figure B.1. Hysitron Triboindenter TI 900.

Table B.1. Experimental conditions for Young's modulus and hardness determination.

Parameter	Value
Indenter type	Berkovich
Depth of indentation	90 nm
Number of indentations (Pads)	100 (10×10 grid)
Number of indentations (Thin film layers)	49 (7×7 grid)
Number of indentations (Polymer pins)	25 (5×5 grid)
Distance between each indentation	20 μm

Table B.2. Young's modulus and hardness of new, broken-in, and used Pad A.

#	New		Broken-in		Used	
	E (MPa)	H (MPa)	E (MPa)	H (MPa)	E (MPa)	H (MPa)
1	151	22	109	18	201	51
2	76	32	149	21	175	45
3	119	33	191	21	181	39
4	75	21	125	17	601	55
5	109	21	214	22	214	37
6	136	26	126	19	131	50
7	102	39	243	29	175	33
8	78	19	409	40	346	44
9	90	38	500	42	585	64
10	101	31	123	23	272	36
11	139	21	295	28	282	46
12	77	33	202	20	200	43
13	100	23	343	29	907	112
14	80	34	97	23	1313	278
15	87	34	82	18	194	28
16	151	35	261	23	229	26
17	98	41	222	26	150	55
18	72	24	171	21	153	56
19	104	29	171	19	961	134
20	115	32	278	20	291	42
21	70	30	197	17	245	38
22	257	31	194	25	165	59
23	84	37	339	36	240	44
24	73	22	429	29	189	40
25	96	37	196	28	274	49
26	112	41	669	57	352	35
27	182	20	148	20	164	61
28	251	101	222	19	196	46
29	78	32	133	25	178	42
30	95	24	328	43	277	56
31	269	25	180	22	196	31
32	358	37	159	24	378	62
33	71	27	441	45	243	49
34	66	28	77	17	192	67
35	98	30	327	42	274	59
36	191	28	478	47	294	43
37	337	43	286	38	383	66
38	164	42	130	16	230	50
39	67	29	85	18	186	38
40	98	36	343	31	250	33
41	697	63	243	31	259	42
42	140	44	86	18	182	44
43	76	24	394	31	638	77
44	86	32	186	25	522	69
45	92	30	248	25	392	41
46	156	40	552	52	407	55
47	86	26	128	19	274	46
48	104	38	235	26	287	42
49	105	20	165	22	496	85
50	118	26	163	20	538	81
51	121	24	186	18	306	43
52	333	31	242	25	297	44
53	147	25	355	33	243	44
54	380	83	186	20	425	57
55	89	17	267	24	350	52
56	492	51	137	18	162	46

57	169	18	209	30	232	47
58	251	20	197	24	259	40
59	183	31	84	13	279	58
60	89	30	149	15	444	50
61	85	36	264	24	188	52
62	97	27	227	29	396	63
63	666	162	149	24	187	70
64	222	30	435	37	282	53
65	90	34	91	18	193	44
66	102	29	113	14	156	55
67	117	33	230	24	172	54
68	154	25	155	21	194	29
69	107	38	114	16	157	22
70	76	33	66	20	181	53
71	60	18	357	31	133	41
72	159	47	258	31	177	62
73	421	63	136	18	201	52
74	111	19	230	24	237	26
75	60	20	290	25	179	52
76	101	28	580	49	233	58
77	306	35	143	18	165	44
78	177	35	146	24	214	44
79	100	33	236	23	254	27
80	81	14	207	20	186	48
81	55	15	496	36	1068	126
82	328	85	262	26	208	39
83	103	27	146	19	165	73
84	132	21	191	16	336	60
85	78	24	440	23	685	77
86	58	20	87	26	969	124
87	80	26	151	20	202	54
88	84	35	97	15	165	60
89	123	26	275	22	315	53
90	60	23	395	32	507	52
91	85	35	291	26	937	125
92	73	16	315	24	222	46
93	137	22	273	26	211	59
94	118	25	656	136	325	30
95	82	34	346	29	268	49
96	76	34	172	25	206	38
97	52	16	131	18	224	52
98	138	22	72	16	190	68
99	47	9	672	159	279	62
100	151	22	158	24	236	50
Mean	143	32	242	28	313	56
Max.	697	162	672	159	1313	278
Min.	47	9	66	13	131	22
Std. Dev.	115	19	137	19	218	31
C.V.	0.80	0.46	0.57	0.70	0.69	0.55

Table B.3. Young's modulus and hardness of new, broken-in, and used IC1000 pads.

#	New		Broken-in		Used	
	E (MPa)	H (MPa)	E (MPa)	H (MPa)	E (MPa)	H (MPa)
1	1809	218	598	44	245	26
2	2543	264	1091	78	319	29
3	2626	281	2760	214	942	81
4	1844	117	2528	221	2165	225
5	3257	282	2016	100	1734	114
6	2789	328	2876	215	711	59
7	723	79	599	60	1375	140
8	618	87	922	127	684	84
9	2694	337	1232	152	458	108
10	533	82	858	70	252	54
11	5327	560	1166	83	226	16
12	3203	350	280	35	652	105
13	2702	318	1154	69	1068	108
14	3075	303	1563	139	1667	186
15	3031	383	3486	402	2612	213
16	3688	361	2244	187	1121	113
17	715	161	4737	517	1202	106
18	2710	398	1521	216	756	45
19	2682	475	5759	758	873	82
20	3167	446	2545	281	791	66
21	5140	828	714	91	1076	58
22	3107	456	900	168	815	74
23	2262	231	906	213	1397	100
24	5482	547	793	203	1874	120
25	5879	645	1291	70	139	21
26	2148	216	303	20	808	99
27	2395	321	421	84	718	136
28	344	93	2368	219	1075	84
29	192	35	817	42	1883	197
30	208	29	599	89	1823	233
31	2620	287	365	149	1647	166
32	3129	387	759	188	691	121
33	2986	383	92	23	1017	67
34	5179	641	205	24	3020	212
35	4204	649	214	38	186	43
36	2737	343	204	41	143	19
37	3183	281	2099	231	193	46
38	4990	915	1988	234	673	97
39	307	76	886	62	213	74
40	1242	109	352	59	1879	243
41	2721	334	231	58	603	114
42	5266	884	116	42	628	75
43	2962	372	77	19	779	47
44	4100	526	130	44	1272	164
45	2457	335	160	33	1383	202
46	1608	344	1325	122	413	36
47	1686	180	836	64	118	23
48	750	88	2480	235	182	14
49	362	98	3627	397	3369	326
50	499	135	65	15	1212	106
51	1801	292	107	40	590	61
52	2664	411	197	39	684	137
53	5025	679	209	97	391	66
54	4469	497	177	80	411	92
55	2551	319	2248	183	902	125
56	2584	318	1937	192	1483	201

57	3783	528	3727	381	139	15
58	3691	287	3259	366	94	31
59	561	57	441	64	1656	108
60	539	97	436	51	1786	208
61	1664	262	137	56	1265	86
62	2489	470	176	71	1524	119
63	1680	170	225	95	2406	130
64	4720	694	2753	277	1432	143
65	3825	502	2135	208	645	132
66	1009	161	2177	197	823	131
67	721	65	3229	188	98	13
68	2476	335	2741	230	363	37
69	699	65	207	70	141	32
70	3031	337	1391	54	973	95
71	2506	310	142	38	158	50
72	2976	355	205	95	977	62
73	332	52	1844	207	502	108
74	2600	375	2519	307	1527	176
75	2732	367	2303	242	309	103
76	474	57	2094	245	1923	195
77	1437	256	2639	199	671	44
78	347	72	2160	448	3593	393
79	3257	345	344	84	394	60
80	568	94	844	62	1398	140
81	5477	904	2883	231	1360	145
82	741	99	2711	302	2456	258
83	158	26	2253	281	2130	166
84	245	44	4863	611	873	69
85	195	45	1817	80	1281	125
86	378	96	1839	190	168	71
87	412	131	1206	132	1533	112
88	73	26	129	43	735	71
89	171	35	1364	82	818	58
90	122	23	1355	108	118	41
91	3430	730	320	52	2128	292
92	489	94	130	28	787	28
93	2675	244	113	44	1978	167
94	119	55	175	31	396	49
95	4332	665	210	23	1787	180
96	1703	73	126	28	687	110
97	425	155	134	37	159	26
98	315	45	140	18	861	71
99	399	108	991	83	526	151
100	1885	168	1885	168	99	34
Mean	2212	293	1323	147	1021	109
Max.	5879	915	5759	758	3593	393
Min.	73	23	65	15	94	13
Std. Dev.	1591	220	1230	133	753	72
C.V.	0.72	0.75	0.93	0.91	0.74	0.66

Table B.4. Young's modulus and hardness of Al and Cu layers.

#	Al		Cu	
	E (MPa)	H (MPa)	E (MPa)	H (MPa)
1	98.9	1.12	137.4	1.44
2	84.6	1.01	143.3	1.98
3	99.4	1.16	141.9	1.62
4	96.5	1.08	130.6	1.43
5	76.1	1.03	136.1	1.94
6	69.4	0.69	121.6	1.45
7	75.6	0.81	123.7	1.71
8	92.8	0.90	108.6	1.74
9	106.7	0.73	138.6	1.81
10	70.2	0.84	154.5	1.54
11	87.1	0.89	146.6	1.80
12	99.2	1.11	128.8	1.71
13	95.6	1.21	122.4	1.62
14	80.4	0.83	143.0	1.52
15	101.7	1.12	127.6	1.77
16	99.1	1.28	114.7	0.93
17	87.0	1.01	130.9	1.50
18	92.1	1.24	126.0	1.98
19	101.9	1.11	115.9	1.37
20	102.9	1.05	128.7	1.86
21	105.2	1.09	105.4	1.35
22	94.3	0.93	114.0	1.50
23	100.0	1.11	128.4	1.76
24	94.7	1.01	112.7	1.48
25	103.0	0.87	137.4	1.28
26	94.3	0.92	128.0	1.55
27	89.7	0.92	128.3	1.55
28	91.3	1.04	110.3	0.97
29	96.3	1.01	116.6	1.32
30	65.2	0.70	135.7	2.09
31	85.2	0.96	145.3	1.71
32	101.6	1.17	133.5	1.32
33	79.8	0.99	137.5	1.62
34	104.5	1.18	136.0	1.34
35	101.2	0.79	141.2	1.69
36	97.5	0.92	147.4	1.89
37	81.6	0.95	132.3	1.69
38	84.1	0.86	109.2	1.54
39	101.3	1.10	132.2	1.76
40	79.6	0.84	129.2	1.67
41	95.0	1.08	115.6	1.30
42	44.8	0.72	115.5	1.82
43	72.3	0.83	106.9	1.29
44	75.9	0.83	134.2	1.73
45	57.5	0.64	138.4	1.59
46	90.0	0.71	109.5	1.31
47	67.9	0.82	121.7	1.47
48	79.2	0.95	106.3	0.99
49	95.1	1.18	116.0	1.13
Mean	88.7	0.97	127.5	1.56
Max.	106.7	1.28	154.5	2.09
Min.	44.8	0.64	105.4	0.93
Std. Dev.	13.6	0.16	12.6	0.26
C.V.	0.15	0.17	0.10	0.17

Table B.5. Young's modulus and hardness of low-*k* A, B, and C layers.

#	Low-*k* A E (GPa)	Low-*k* A H (GPa)	Low-*k* B E (GPa)	Low-*k* B H (GPa)	Low-*k* C E (GPa)	Low-*k* C H (GPa)
1	7.80	1.35	23.8	1.82	26.1	2.52
2	7.71	1.36	24.9	1.96	26.3	2.53
3	7.71	1.36	24.6	1.96	26.3	2.49
4	7.73	1.35	24.0	1.91	26.2	2.49
5	7.71	1.36	23.6	1.82	25.9	2.45
6	7.81	1.37	22.8	1.77	26.3	2.47
7	7.66	1.33	21.5	1.72	26.0	2.50
8	7.83	1.36	24.7	1.92	25.1	2.57
9	7.82	1.37	24.0	1.92	25.7	2.48
10	7.66	1.36	24.0	1.87	25.6	2.51
11	7.71	1.35	23.2	1.86	26.1	2.43
12	7.69	1.34	23.6	1.83	26.2	2.39
13	7.73	1.38	23.3	1.75	26.1	2.40
14	7.71	1.34	22.8	1.77	26.0	2.41
15	7.69	1.37	24.1	1.89	26.1	2.51
16	7.84	1.36	23.0	1.85	25.6	2.39
17	7.84	1.39	23.7	1.83	25.0	2.47
18	7.81	1.34	23.8	1.84	26.0	2.50
19	7.66	1.36	23.3	1.82	26.5	2.53
20	7.63	1.35	22.2	1.76	24.6	2.48
21	7.67	1.36	22.3	1.76	26.2	2.46
22	7.91	1.40	22.8	1.77	26.3	2.49
23	7.76	1.38	23.3	1.79	26.0	2.46
24	7.69	1.36	23.7	1.86	25.4	2.40
25	7.73	1.35	23.2	1.77	25.8	2.42
26	7.71	1.36	22.2	1.73	26.2	2.50
27	7.73	1.38	21.6	1.65	26.1	2.52
28	7.68	1.36	22.3	1.69	26.1	2.47
29	7.73	1.35	23.7	1.85	25.8	2.46
30	7.82	1.38	23.1	1.80	25.8	2.40
31	7.82	1.36	23.4	1.85	25.7	2.45
32	7.75	1.37	22.9	1.78	25.9	2.46
33	7.67	1.34	23.1	1.77	26.0	2.45
34	7.76	1.38	23.5	1.73	24.9	2.52
35	7.65	1.35	22.5	1.69	25.7	2.41
36	7.71	1.37	23.4	1.86	26.0	2.38
37	7.74	1.37	23.1	1.83	25.6	2.45
38	7.70	1.36	22.9	1.80	25.9	2.40
39	7.78	1.37	23.0	1.78	25.7	2.53
40	7.77	1.34	23.1	1.69	25.2	2.57
41	7.80	1.35	21.9	1.69	26.1	2.54
42	7.68	1.38	22.1	1.70	25.7	2.42
43	7.79	1.37	23.0	1.78	26.1	2.48
44	7.79	1.36	23.7	1.82	26.1	2.50
45	7.79	1.33	22.8	1.78	25.0	2.52
46	7.78	1.35	22.8	1.78	24.8	2.48
47	7.75	1.34	22.2	1.71	26.2	2.49
48	7.75	1.37	22.1	1.70	25.7	2.43
49	7.75	1.39	22.1	1.67	25.9	2.47
Mean	7.74	1.36	23.1	1.80	25.8	2.47
Max.	7.91	1.40	24.9	1.96	26.5	2.57
Min.	7.63	1.33	21.5	1.65	24.6	2.38
Std. Dev.	0.06	0.02	0.8	0.08	0.4	0.05
C.V.	0.01	0.01	0.03	0.04	0.02	0.02

Table B.6. Young's modulus and hardness of SiO_2, Si_3N_4 and TiN layers.

#	SiO_2		Si_3N_4		TiN	
	E (MPa)	H (MPa)	E (MPa)	H (MPa)	E (MPa)	H (MPa)
1	69.7	8.0	123.1	9.9	173.1	15.4
2	69.0	8.1	120.7	9.7	171.0	15.4
3	69.7	7.9	122.7	9.9	172.9	15.4
4	70.9	7.9	128.4	9.8	172.9	15.3
5	70.8	7.8	123.5	9.8	172.5	15.2
6	69.8	8.0	127.9	9.7	171.6	15.4
7	69.3	7.8	125.2	9.7	172.9	15.3
8	69.8	8.1	127.0	9.9	172.4	15.3
9	70.3	7.8	122.1	9.7	173.2	15.4
10	70.8	7.9	124.5	10.0	173.4	15.4
11	70.0	7.9	130.7	10.0	171.9	15.3
12	69.5	7.9	128.3	9.9	172.3	15.3
13	69.2	7.9	125.4	10.0	170.6	15.3
14	68.1	7.7	122.8	9.9	176.0	15.3
15	70.5	8.0	122.4	9.6	172.0	15.2
16	70.2	8.1	123.7	9.8	170.3	15.3
17	69.0	7.9	125.4	9.9	171.3	15.4
18	69.4	8.1	127.4	9.9	172.3	15.4
19	69.0	8.0	124.9	9.9	171.0	15.3
20	69.7	8.1	124.0	9.8	174.6	15.6
21	70.3	8.1	125.3	9.7	173.3	15.6
22	69.4	8.0	122.1	9.8	172.5	15.6
23	72.2	8.2	120.3	9.8	170.9	15.5
24	70.3	8.0	122.8	9.9	170.6	15.5
25	70.1	8.0	122.9	9.7	172.3	15.2
26	70.1	7.8	125.5	9.8	171.6	15.3
27	69.1	8.0	122.0	9.6	173.7	15.2
28	69.3	8.0	124.4	9.8	172.6	15.4
29	70.1	8.1	119.5	9.8	170.0	15.5
30	70.2	8.1	121.3	9.6	172.5	15.5
31	69.8	8.2	122.4	9.6	171.6	15.2
32	68.8	8.2	123.0	9.9	173.1	15.1
33	69.4	7.9	124.1	9.7	172.0	15.1
34	68.8	8.0	125.4	9.8	172.4	15.1
35	69.8	7.9	122.6	10.0	171.2	15.3
36	70.3	8.1	120.5	9.5	172.2	15.6
37	69.6	8.1	117.9	9.6	170.9	15.2
38	70.7	8.0	120.2	9.9	172.5	15.5
39	70.5	8.0	119.9	9.4	172.8	15.3
40	70.4	8.1	120.6	9.5	171.7	15.3
41	69.4	8.1	124.3	10.0	173.3	15.1
42	69.7	8.1	118.3	9.6	177.0	15.3
43	68.7	8.0	118.8	9.5	169.6	15.3
44	70.3	8.1	121.6	9.7	171.3	15.6
45	71.3	8.0	124.4	9.9	168.0	15.3
46	69.3	8.1	120.3	9.6	172.4	15.5
47	69.6	8.1	122.2	9.8	174.3	15.8
48	69.9	7.9	124.1	10.1	174.2	15.4
49	69.6	8.0	119.3	9.8	170.9	15.3
Mean	69.8	8.0	123.2	9.8	172.2	15.4
Max.	72.2	8.2	130.7	10.1	177.0	15.8
Min.	68.1	7.7	117.9	9.4	168.0	15.1
Std. Dev.	0.7	0.1	2.8	0.2	1.5	0.2
C.V.	0.01	0.01	0.02	0.02	0.01	0.01

Table B.7. Young's modulus and hardness of polymer pins (LDPE, PP, PTFE and HDPE).

#	LDPE		PP		PTFE		HDPE	
	E (MPa)	H (MPa)	E (MPa)	H (MPa)	E (MPa)	H (MPa)	E (MPa)	H (MPa)
1	569	121	4233	460	1474	158	5120	470
2	539	96	813	115	2233	310	345	42
3	497	131	2855	254	1756	303	1270	111
4	966	204	2393	154	1041	116	1969	167
5	831	169	3431	346	1130	223	1961	217
6	487	109	1920	165	1369	237	2275	163
7	1040	215	1711	145	1467	256	2451	248
8	475	110	1863	229	1137	175	1090	54
9	883	154	467	79	936	133	1585	180
10	308	46	619	20	1404	232	1508	64
11	997	298	2580	232	829	97	3061	307
12	593	153	3099	260	946	149	821	83
13	717	149	2164	183	1015	123	2558	225
14	885	177	502	62	1255	222	2710	347
15	760	94	2800	235	2308	324	1160	50
16	586	158	1858	173	950	116	750	101
17	1197	369	3000	206	1023	132	2004	265
18	512	104	692	28	906	92	2725	233
19	571	161	2012	229	233	84	166	57
20	1442	256	2475	239	255	69	3752	526
21	763	233	1655	148	1732	257	1402	159
22	551	117	817	54	1643	275	3237	248
23	1100	309	1337	94	1579	275	1730	144
24	569	127	2314	290	960	145	1902	146
25	636	201	1803	169	760	108	1624	128
Mean	739	170	1976	183	1214	184	1967	189
Max.	1442	369	4233	460	2308	324	5120	526
Min.	308	46	467	20	233	69	166	42
Std. Dev.	269	76	983	102	502	80	1103	125
C.V.	0.36	0.45	0.50	0.56	0.41	0.43	0.56	0.66

Table B.8. Young's modulus and hardness of polymer pins (PS, PC, and PMMA).

#	PS		PC		PMMA	
	E (MPa)	H (MPa)	E (MPa)	H (MPa)	E (MPa)	H (MPa)
1	2889	177	4954	419	4569	273
2	3066	226	3823	269	2969	149
3	3894	329	2616	147	5480	440
4	2775	245	5479	417	6608	674
5	2344	191	4616	309	5915	326
6	2792	149	3424	205	7124	483
7	4423	380	4886	351	5971	316
8	6693	595	4499	334	4228	150
9	3405	270	4461	321	5965	533
10	3196	266	5412	358	9187	787
11	2332	173	1757	86	5305	420
12	2725	166	3527	290	7535	680
13	736	72	5492	509	6889	374
14	2800	205	3159	219	4688	294
15	3866	244	4008	315	6998	554
16	3146	292	2173	124	4143	280
17	4307	373	3547	199	4348	269
18	3807	299	5846	377	4126	287
19	1763	116	2203	194	1903	105
20	2732	228	7646	584	6809	810
21	3490	304	1444	70	3434	164
22	5499	508	5148	412	3815	245
23	4570	376	6079	608	5243	449
24	3319	230	6159	607	6313	401
25	3606	240	4969	337	4433	256
Mean	3367	266	4293	323	5234	389
Max.	6693	595	7646	608	9187	810
Min.	736	72	1444	70	1903	105
Std. Dev.	1185	117	1531	151	1614	196
C.V.	0.35	0.44	0.36	0.47	0.31	0.50

APPENDIX C

ANALYTICAL DERIVATION OF MAXIMUM VON MISES STRESS IN AN ELASTIC HALF-SPACE UNDER FRICTIONAL CONTACT

C.1. Stress field in an elastic half-space

Analytical solutions for the stresses produced in an elastic half-space under certain normal and tangential tractions on the surface can be obtained by the Boussinesq approach using the theory of potentials [Love, 1952; Johnson, 1985]. The potential functions, F and H, for the distribution of tangential traction $q_x(\xi, \eta)$ and normal traction $p(\xi, \eta)$ within a surface area S, Figure C.1, are defined as:

$$F = \iint_S q_x(\xi,\eta)\left\{z\ln(\rho+z)-\rho\right\}d\xi d\eta \tag{C.1a}$$

$$H = \iint_S p(\xi,\eta)\left\{z\ln(\rho+z)-\rho\right\}d\xi d\eta \tag{C.1b}$$

where $\rho = \{(\xi - x)^2+(\eta - y)^2 + z^2\}^{1/2}$, and each function satisfies the Laplace's equation

$$\nabla^2 F = \nabla^2 H = 0 \tag{C.2}$$

Then the components of elastic displacements at any point (x, y, z) are given as [Love, 1952; Johnson, 1985]:

$$u_x = \frac{(1+\nu)}{2\pi E}\left[2\frac{\partial^2 F}{\partial z^2} - \frac{\partial^2 H}{\partial x \partial z} + 2\nu\left(\frac{\partial^2 F}{\partial x^2} + \frac{\partial^2 H}{\partial x \partial z}\right) - z\left(\frac{\partial^3 F}{\partial x^2 \partial z} + \frac{\partial^3 H}{\partial x \partial z^2}\right)\right] \tag{C.3a}$$

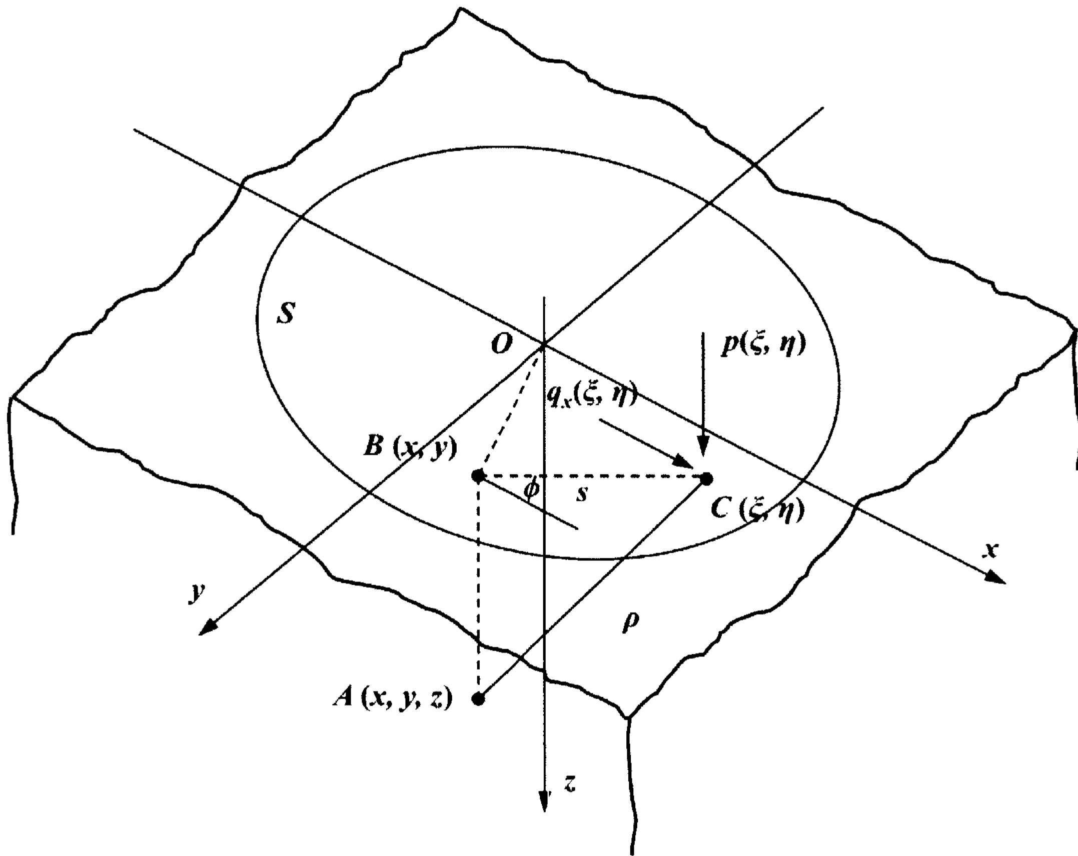

Figure C.1. Elastic half-space under normal and tangential tractions.

$$u_y = \frac{(1+v)}{2\pi E}\left[-\frac{\partial^2 H}{\partial y \partial z} + 2v\left(\frac{\partial^2 F}{\partial x \partial y} + \frac{\partial^2 H}{\partial y \partial z}\right) - z\left(\frac{\partial^3 F}{\partial x \partial y \partial z} + \frac{\partial^3 H}{\partial y \partial z^2}\right)\right] \tag{C.3b}$$

$$u_z = \frac{(1+v)}{2\pi E}\left[\frac{\partial^2 H}{\partial z^2} + (1-2v)\left(\frac{\partial^2 F}{\partial x \partial z} + \frac{\partial^2 H}{\partial z^2}\right) - z\left(\frac{\partial^3 F}{\partial x \partial z^2} + \frac{\partial^3 H}{\partial z^3}\right)\right] \tag{C.3c}$$

where E is the Young's modulus and v is the Poisson's ratio of the elastic half-space.

When the pad asperity deformation is fully-plastic, the pressure distribution is uniform in the contact area [Nagaraj, 1984; Stronge, 2000]. In addition, the tangential traction would be proportional to the normal pressure at every point, and their ratio is the coefficient of friction, μ. As normal pressure, p, and tangential traction in x-direction, μp, are uniformly distributed in the circular region S, on the surface, $z = 0$, the distribution of the tractions are:

$$q_x(\xi,\eta) = \begin{cases} \mu p \;, & \sqrt{\xi^2+\eta^2} < a \\ 0 \;, & \sqrt{\xi^2+\eta^2} > a \end{cases} \tag{C.4a}$$

$$p(\xi,\eta) = \begin{cases} p \;, & \sqrt{\xi^2+\eta^2} < a \\ 0 \;, & \sqrt{\xi^2+\eta^2} > a \end{cases} \tag{C.4b}$$

and the potential functions, F and H, defined by Eq. (C.1), are related as $F = \mu H$. From Eqs. (C.1), (C.2) and (C.3), the components of stresses at any point (x, y, z) can be calculated from the corresponding strains by Hooke's law and are given as [Johnson, 1985]:

$$\frac{\sigma_x}{p}=\frac{1}{2\pi}\iint_S\left\{-\frac{3(\xi-x)^2 z}{\rho^5}+(1-2\nu)\left(-\frac{1}{\rho(\rho+z)}+\frac{z}{\rho^3}+\frac{(\xi-x)^2}{\rho^3(\rho+z)}+\frac{(\xi-x)^2}{\rho^2(\rho+z)^2}\right)\right.$$

$$+\mu\left[\frac{2(\xi-x)}{\rho^3}+2\nu\left(\frac{(\xi-x)}{\rho^3}-\frac{3(\xi-x)}{\rho(\rho+z)^2}+\frac{(\xi-x)^3}{\rho^3(\rho+z)^2}+\frac{2(\xi-x)^3}{\rho^2(\rho+z)^3}\right)\right. \tag{C.5a}$$

$$\left.\left.-z\left(\frac{3(\xi-x)}{\rho^3(\rho+z)}+\frac{3(\xi-x)}{\rho^2(\rho+z)^2}-\frac{3(\xi-x)^3}{\rho^5(\rho+z)}-\frac{3(\xi-x)^3}{\rho^4(\rho+z)^2}-\frac{2(\xi-x)^3}{\rho^3(\rho+z)^3}\right)\right]\right\}d\xi d\eta$$

$$\frac{\sigma_y}{p}=\frac{1}{2\pi}\iint_S\left\{-\frac{3(\eta-y)^2 z}{\rho^5}+(1-2\nu)\left(-\frac{1}{\rho(\rho+z)}+\frac{z}{\rho^3}+\frac{(\eta-y)^2}{\rho^3(\rho+z)}+\frac{(\eta-y)^2}{\rho^2(\rho+z)^2}\right)\right.$$

$$+\mu\left[2\nu\left(\frac{(\xi-x)}{\rho^3}-\frac{(\xi-x)}{\rho(\rho+z)^2}+\frac{(\xi-x)(\eta-y)^2}{\rho^3(\rho+z)^2}+\frac{2(\xi-x)(\eta-y)^2}{\rho^2(\rho+z)^3}\right)\right. \tag{C.5b}$$

$$-z\left(-\frac{3(\xi-x)(\eta-y)}{\rho^3(\rho+z)^2}-\frac{4(\xi-x)(\eta-y)}{\rho^2(\rho+z)^2}+\frac{3(\xi-x)(\eta-y)^3}{\rho^5(\rho+z)^2}\right.$$

$$\left.\left.\left.+\frac{6(\xi-x)(\eta-y)^3}{\rho^4(\rho+z)^3}+\frac{6(\xi-x)(\eta-y)^3}{\rho^4(\rho+z)^3}\right)\right]\right\}d\xi d\eta$$

$$\frac{\sigma_z}{p}=\frac{1}{2\pi}\iint_S\left\{-\frac{3z^3}{\rho^5}+\mu\left[\frac{3(\xi-x)z^2}{\rho^5}\right]\right\}d\xi\,d\eta \tag{C.5c}$$

$$\frac{\sigma_{xy}}{p}=\frac{1}{2\pi}\iint_S\left\{-\frac{3(\xi-x)(\eta-y)z}{\rho^5}+(1-2\nu)\left(\frac{(\xi-x)(\eta-y)}{\rho^3(\rho+z)}+\frac{(\xi-x)(\eta-y)}{\rho^2(\rho+z)^2}\right)\right.$$

$$+\mu\left[\frac{(\eta-y)}{\rho^3}+2\nu\left(-\frac{(\eta-y)}{\rho(\rho+z)^2}+\frac{(\xi-x)^2(\eta-y)}{\rho^3(\rho+z)^2}+\frac{2(\xi-x)^2(\eta-y)}{\rho^2(\rho+z)^3}\right)\right. \tag{C.5d}$$

$$-z\left(-\frac{(\eta-y)}{\rho^3(\rho+z)}+\frac{(\eta-y)}{\rho^2(\rho+z)^2}-\frac{3(\xi-x)^3(\eta-y)}{\rho^5(\rho+z)}-\frac{3(\xi-x)^2(\eta-y)}{\rho^4(\rho+z)^2}\right.$$

$$\left.\left.\left.-\frac{2(\xi-x)^2(\eta-y)}{\rho^3(\rho+z)^3}\right)\right]\right\}d\xi d\eta$$

$$\frac{\sigma_{yz}}{p}=\frac{1}{2\pi}\iint_S\left\{\frac{3(\eta-y)z^2}{\rho^5}+\mu\left[-\frac{3(\xi-x)(\eta-y)z}{\rho^5}\right]\right\}d\xi\,d\eta \tag{C.5e}$$

$$\frac{\sigma_{xz}}{p}=\frac{1}{2\pi}\iint_S\left\{\frac{3(\xi-x)z^2}{\rho^5}+\mu\left[-\frac{3(\xi-x)^2 z}{\rho^5}\right]\right\}d\xi\,d\eta \tag{C.5f}$$

Although the general solutions of all these stress components are difficult to obtain, because of the complicated double integrals, the problem can be simplified if the location of the maximum von Mises stress is known. The analytical solution of elastic half-space under Hertzian normal and tangential traction distributions indicates that the maximum von Mises stress remains near the z-axis below the surface if $\mu < 0.3$ and on the surface at $x = -a$, $y = 0$ if $\mu > 0.3$ [Hamilton and Goodman, 1966; Hamilton, 1983]. Moreover, the results of finite element analysis (FEA) show that the stress field under uniform pressure distribution may develop similarly as in the case of Hertzian pressure distribution. While the von Mises stress is maximized below the surface at low friction, a new region of the maximum von Mises stress develops on the surface as the friction coefficient becomes greater than 0.1 [Eusner, 2010]. Therefore, it is reasonable to assume that the von Mises stress is maximized at the trailing edge of the contacted area, A(x, y, z) = ($-a$, 0, 0) in the case of high-friction contact.

C.2. Estimation of maximum von Mises stress

The stress components at the point A(x, y, z) = ($-a$, 0, 0) can be obtained from Eq. (C.5) by substituting $z = 0$, $(\xi + a) = s\cos\phi$, $\eta = s\sin\phi$, and $d\xi d\eta = sdsd\phi$. However, because of the singularity at $s = 0$, the integration must be carried out in two parts, from $s = 2a\sin\phi$ to ε and from $s = \varepsilon$ to 0, where ε is a vanishingly small distance from the edge and in which the uniform tractions gradually decrease to zero. If $\varepsilon = 0$, the pressure distribution is ideally uniform everywhere inside the contact area and zero outside; i.e., the pressure distribution is discontinuous, Figure C.2a. Practically, however, a finite boundary region may always exist so that the pressure distribution is continuous at the surface boundary, Figure C.2b. Therefore, the ratio of the boundary width to the contact radius, ε / a, indicates the steepness of the pressure decline at the periphery of the contact area. In the case of fully-plastic asperity contact, the boundary width is much smaller than the contact radius.

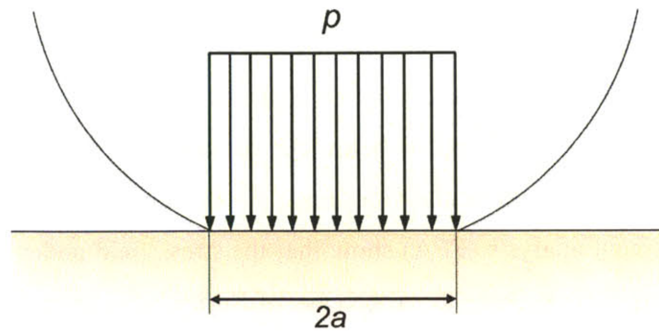

(a) uniform pressure distribution ($\varepsilon = 0$)

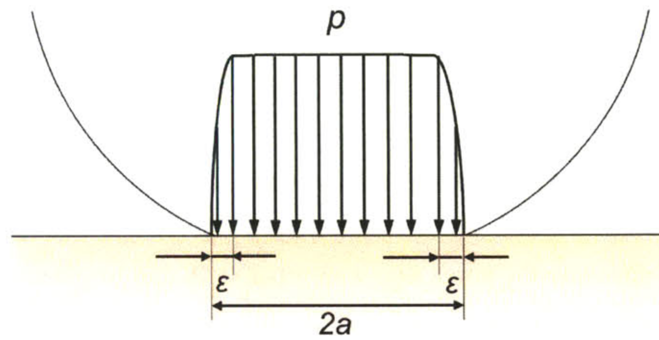

(b) uniform pressure distribution ($\varepsilon > 0$)

Figure C.2. Pressure distribution of fully-plastically deformed pad asperity under frictionless contact: (a) the pressure is uniform inside the contact area (discontinuous pressure distribution) and (b) the pressure is uniform except in an annulus at the edge where the pressure gradually decreases to zero (continuous pressure distribution).

First, the integral from $s = 2a\sin\phi$ to ε can be obtained as:

$$\frac{\sigma_x}{p} = \frac{1}{\pi}\int_0^{\pi/2}\int_\varepsilon^{2a\sin\phi}\left\{(1-2\nu)\frac{\cos 2\phi}{s} + \mu\left[2(1-2\nu)\frac{\cos\phi}{s} + 6\nu\frac{\cos^3\phi}{s}\right]\right\}ds\,d\phi$$
$$= -\frac{(1-2\nu)}{4} - \frac{\mu}{\pi}\left[\left(\frac{22}{3} - 4\nu\right) + (6-4\nu)\ln\frac{\varepsilon}{2a}\right] \quad \text{(C.6a)}$$

$$\frac{\sigma_y}{p} = \frac{1}{\pi}\int_0^{\pi/2}\int_\varepsilon^{2a\sin\phi}\left\{(1-2\nu)\frac{\sin^2\phi - \cos^2\phi}{s} + \mu\left[6\nu\frac{\cos\phi\sin^2\phi}{s}\right]\right\}ds\,d\phi$$
$$= \frac{(1-2\nu)}{4} - \frac{\mu\nu}{\pi}\left[\frac{2}{3} + 2\ln\frac{\varepsilon}{2a}\right] \quad \text{(C.6b)}$$

$$\frac{\sigma_z}{p} = \frac{\sigma_{xy}}{p} = \frac{\sigma_{xz}}{p} = \frac{\sigma_{yz}}{p} = 0 \quad \text{(C.6c)}$$

Second, the integral from $s = \varepsilon$ to 0 can be approximated as:

$$\frac{\sigma_x}{p} = \frac{\sigma_y}{p} = \frac{1}{2}\nu \quad \text{(C.7a)}$$

$$\frac{\sigma_z}{p} = -\frac{1}{2} \quad \text{(C.7b)}$$

$$\frac{\sigma_{xz}}{p} = \frac{1}{2}\mu \quad \text{(C.7c)}$$

$$\frac{\sigma_{xy}}{p} = \frac{\sigma_{yz}}{p} = 0 \quad \text{(C.7d)}$$

Therefore, the stress components at A(x, y, z) = ($-a$, 0, 0) is given from the sum of the respective terms in Eqs. (C.6) and (C.7):

$$\frac{\sigma_x}{p} = -\frac{(1-4\nu)}{4} - \frac{\mu}{\pi}\left[\left(\frac{22}{3} - 4\nu\right) + (6-4\nu)\ln\frac{\varepsilon}{2a}\right] \quad \text{(C.8a)}$$

$$\frac{\sigma_y}{p} = \frac{1}{4} - \frac{\mu\nu}{\pi}\left[\frac{2}{3} + 2\ln\frac{\varepsilon}{2a}\right] \quad \text{(C.8b)}$$

$$\frac{\sigma_z}{p} = -\frac{1}{2} \tag{C.8c}$$

$$\frac{\sigma_{xz}}{p} = \frac{1}{2}\mu \tag{C.8d}$$

$$\frac{\sigma_{xy}}{p} = \frac{\sigma_{yz}}{p} = 0 \tag{C.8e}$$

Thus, the normal stresses are functions of the dimensionless width of the boundary whereas the shear stresses are not. Figure C.3 shows the dimensionless normal stresses, σ_x/p and σ_y/p, at A(x, y, z) = ($-a$, 0, 0) versus ε/a for ν = 0.33. If μ = 0, the von Mises stress at the trailing edge does not depend on the steepness of decrease in pressure at the edge. However, if $\mu \neq 0$, both normalized stresses increase as μ increases, and both increase infinitely as the boundary width approaches zero. It may be noted that the tensile stress in x-direction becomes much greater than that in y-direction or other stress components as the pressure abruptly decrease at the edge.

From Eq. (C.7), the von Mises stress at A(x, y, z) = ($-a$, 0, 0), the point where it is maximum, in the elastic half-space under uniform normal and tangential tractions can be obtained as:

$$\begin{aligned}\frac{\sigma_M}{p} = \Bigg\{ & \frac{1}{\pi^2}\left[4\left(7\nu^2-15\nu+9\right)\left(\ln\frac{\varepsilon}{2a}\right)^2+\frac{8}{3}\left(17\nu^2-47\nu+33\right)\ln\frac{\varepsilon}{2a}\right. \\ & \left.+\frac{2}{9}\left(86\nu^2-286\nu+242\right)+\frac{3}{4}\pi^2\right]\mu^2+\frac{1}{\pi}\left[\frac{1}{2}\left(20\nu^2-31\nu+3\right)\ln\frac{\varepsilon}{2a}\right. \\ & \left.+\frac{1}{6}\left(52\nu^2-99\nu+11\right)\right]\mu+\frac{1}{16}\left(16\nu^2-4\nu+7\right)\Bigg\}^{1/2}\end{aligned} \tag{C.9}$$

The equation indicates that the maximum von Mises stress is a function of the friction coefficient, Poisson's ratio, and the ratio of the boundary width to the contact radius. However, as can be seen in Figure C.4, the maximum von Mises stress is not much sensitive to the value of Poisson's ratio.

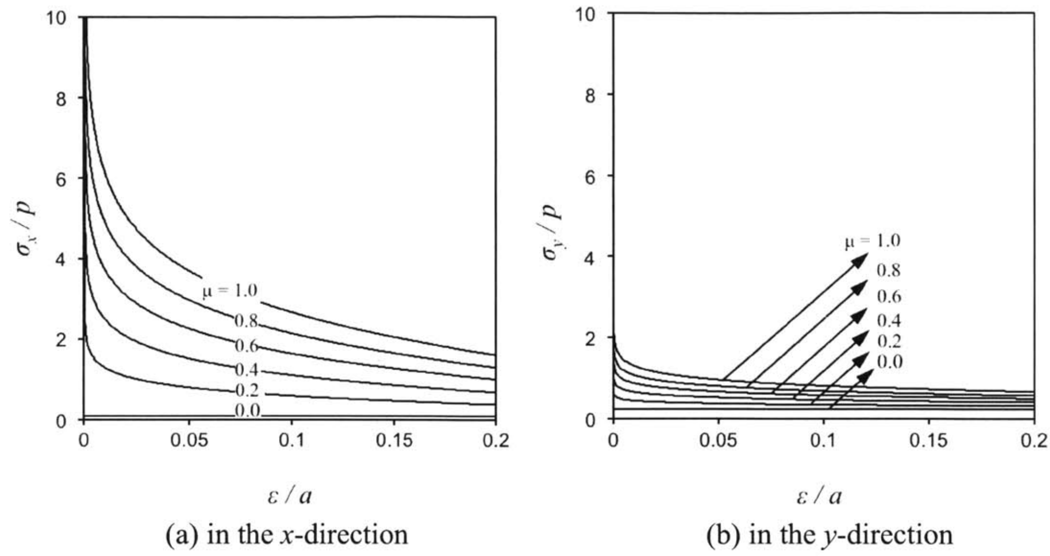

Figure C.3. Normalized normal stresses, σ_x/p and σ_y/p, at the trailing edge as a function of normalized boundary width, where pressure decreases to zero, for different coefficients of friction and $v = 0.33$.

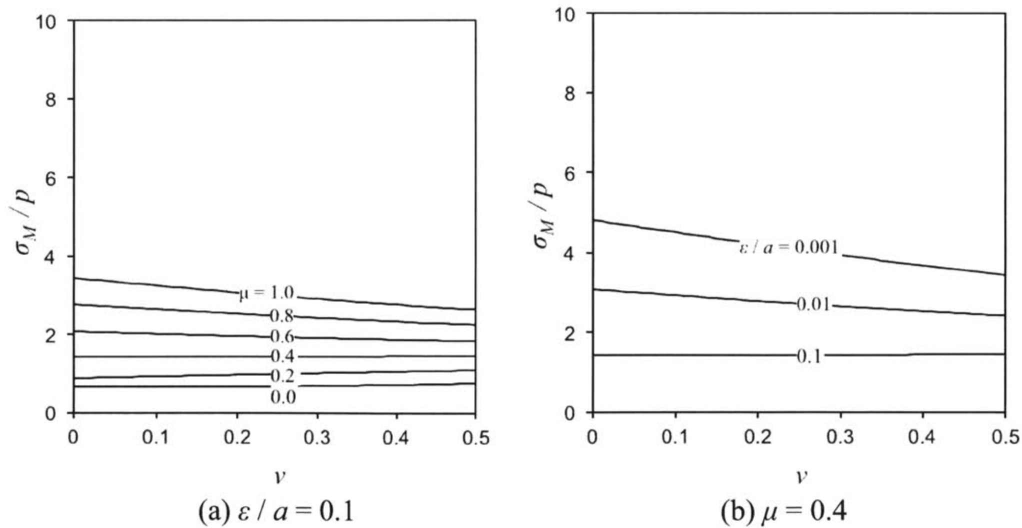

Figure C.4. Normalized maximum von Mises stress, σ_M/p, as a function of Poisson's ratio, v.

Figure C.5 shows the effect of the steepness of the pressure decrease at the edge of the contact area on the maximum von Mises stress for various friction coefficients. The steeper the pressure changes at the edge, the larger the maximum von Mises stress is. This is due to the increase in tensile stresses, σ_x and σ_y. It may also be noted that the normalized maximum von Mises stress is similar to σ_x since it is dominant at the trailing edge, particularly at high friction, compared with the other stress components. Figure C.6 shows the effect of the coefficient of friction on the maximum von Mises stress.

For $\nu = 0.3$ and $\varepsilon / a = 0.1$, the maximum von Mises stress can be given by:

$$\frac{\sigma_M}{p} = \left[6.138\mu^2 + 1.560\mu + 0.464\right]^{1/2} \tag{C.10}$$

As shown in Figure C.6, Eq. (C.10) is in good agreement with the FEA results, which are also listed in Table C.7.

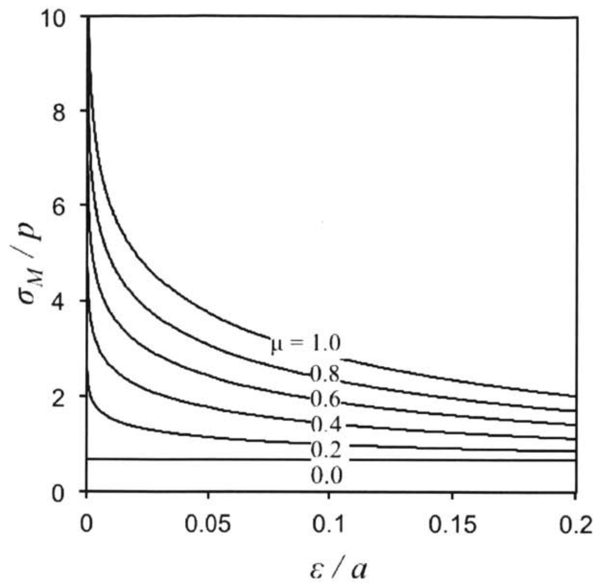

Figure C.5. Normalized maximum von Mises stress, σ_M/p, as a function of normalized boundary width, ε/a, for different coefficients of friction, μ.

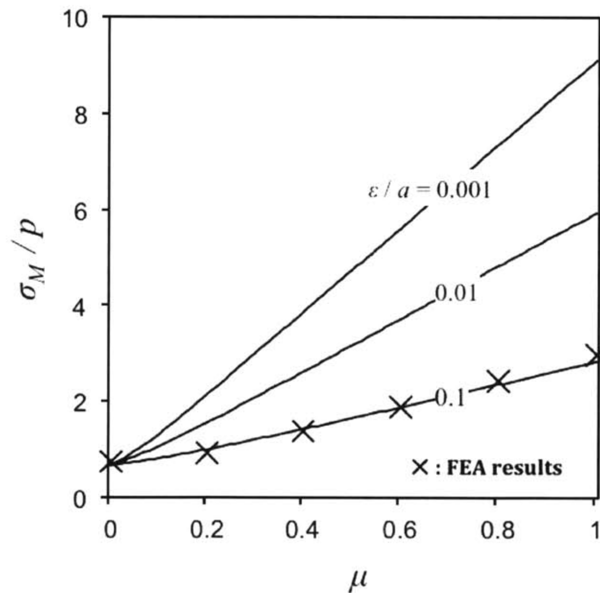

Figure C.6. Normalized maximum von Mises stress, σ_M / p, as a function of the coefficient of friction, μ. The lines show the values for different normalized boundary widths, ε/a, and the × points indicate the results of finite element analysis [Eusner, 2010].

Table C.1. Results of finite element analysis for normalized maximum shear stress, τ_{max} / p, and normalized maximum von Mises stress, σ_M / p [Eusner, 2010].

μ	τ_{max}/p	σ_M/p	$(2\tau_{max} - \sigma_M)/p$
0.0	0.412	0.750	0.10
0.2	0.527	0.931	0.13
0.4	0.784	1.396	0.12
0.6	1.069	1.911	0.12
0.8	1.365	2.445	0.12
1.0	1.666	2.987	0.12

Nomenclature

a	contact radius [m]
E	Young's modulus [N m^{-2}]
F, H	potential functions [N m]
p	pressure [N m^{-2}]
q_x	tangential traction in x-direction [N m^{-2}]
s	$= \{(\xi - x)^2+(\eta - y)^2\}^{1/2}$ [m]
x, y, z	Cartesian coordinates
ε	width of pressure transition region [m]
μ	coefficient of friction
v	Poisson's ratio
ρ	$= \{(\xi - x)^2+(\eta - y)^2 + z^2\}^{1/2}$ [m]
ξ, η	surface coordinates [m]
σ_M	Von Mises stress [N m^{-2}]
$\sigma_x, \sigma_y, \sigma_z$	axial stresses [N m^{-2}]
$\sigma_{xy}, \sigma_{yz}, \sigma_{xz}$	shear stresses [N m^{-2}]
τ_{max}	maximum shear stress [N m^{-2}]

References

Eusner, T., 2010, "Multi-scale scratches in chemical-mechanical polishing," Ph.D. Thesis, Department of Mechanical Engineering, MIT, Cambridge, MA.

Hamilton, G. M. and Goodman, L. E., 1966, "The stress field created by a circular sliding contact," *J. Appl. Mech.*, vol. 88, pp. 371-376.

Hamilton, G. M., 1983, "Explicit equations for the stresses beneath a sliding spherical contact," *Proc. Instn. Mech. Eng.*, vol. 197, pp. 53-59.

Johnson, K. L., 1985, *Contact Mechanics*, Cambridge University Press, Cambridge, UK.

Love, A. E. H., 1952, *A Treatise on the Mathematical Theory of Elasticity*, 4th Edn., Cambridge University Press, Cambridge, UK.

Nagaraj, H. S., 1984, "Elastoplastic contact of bodies with friction under normal and tangential loading," *ASME J. Tribo.*, vol. 106, pp. 519-26.

Stronge, W. J., 2000, *Impact Mechanics*, Cambridge University Press, Cambridge, UK.

APPENDIX D

EFFECTS OF GRIT SIZE AND SHAPE ON PAD TOPOGRAPHY IN DIAMOND CONDITIONING

In general CMP systems, diamond conditioners are used to manipulate the surface topography of the polishing pads. As the pad topography is found to be important on both scratching and material removal in Chapters 4 and 5, the role of conditioners seems to be crucial. IC1000 pads were conditioned without polishing wafers under the conditions listed in Table D.1. Seven diamond conditioners with different diamond grit sizes and shapes are used. Table D.2 contains the determined average roughness, asperity radius and the standard deviation of asperity heights after ten minutes conditioning. In all cases, the average roughness values were not significantly different, between 4 to 7 micrometers. The ratios of asperity radius to standard deviation of asperity heights, R_a / σ_z, were found to be decreasing by diamond conditioners. However, the effects of different grit sizes and shapes of the diamonds on R_a / σ_z were also found to be negligible. To increase the R_a / σ_z of the pad, accordingly, other means, such as asperity-flattening suggested in Chapters 4 and 5, need to be developed.

Table D.1. Process conditions for pad conditioning.

Parameter	Value
Normal load	12 lbf
Diameter of conditioner	4 in
Pressure	1 psi
Center-to-center distance	4 in
Rotational speed of conditioner	60 rpm (CCW)
Rotational speed of pad	150 rpm (CW)
Conditioning time	10 min

- CMP pad : IC1000
- Deionized water was used.

Table D.2. Properties of IC 1000 pads before and after conditioning using conditioners with different diamond shapes and sizes.

Pad Designation	Conditioner		Average roughness	Topography		
	Diamond Shape	Diamond Size (μm)	r_a (μm)	R_a (μm)	σ_z (μm)	R_a / σ_z
O	None	-	6.50	41.44	3.24	12.79
D1	Semi-Blocky	252	5.67	24.23	5.71	4.24
D2	Semi-Blocky	181	4.96	30.26	4.09	7.40
D3	Semi-Blocky	151	5.12	29.35	4.83	6.08
D4	Semi-Sharp	107	4.52	27.69	4.62	5.99
D5	Semi-Blocky	76	4.31	25.81	4.96	5.20
D6	n / a	200	5.87	23.85	5.39	4.42
D7	Semi-Blocky (low concentration)	181	6.27	29.91	4.91	6.09

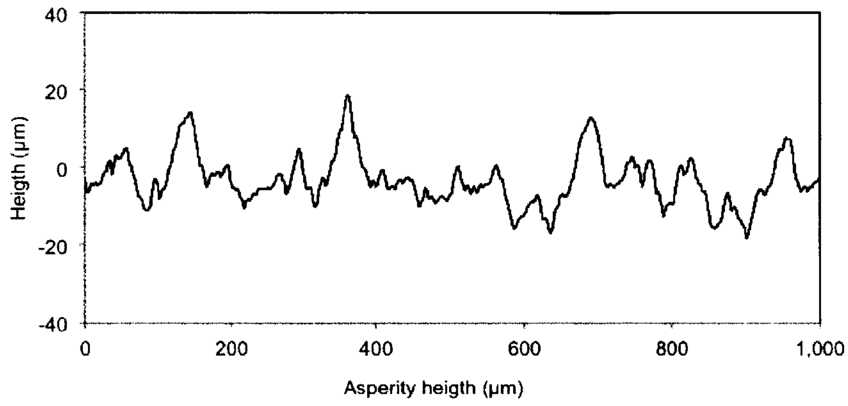

(a) Pad D1

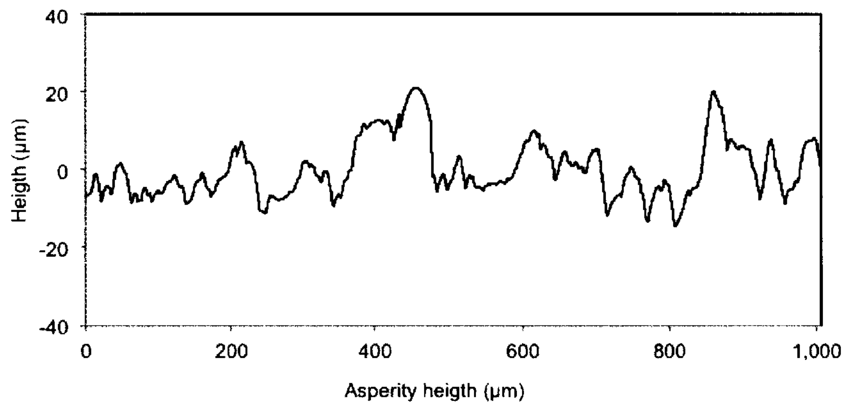

(b) Pad D4

Figure D.1. Surface profiles of the IC1000 pads after diamond conditioning.

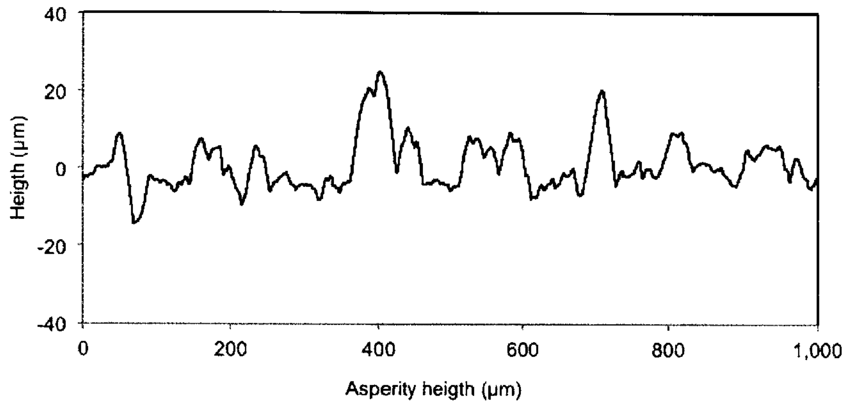

(a) Pad D5

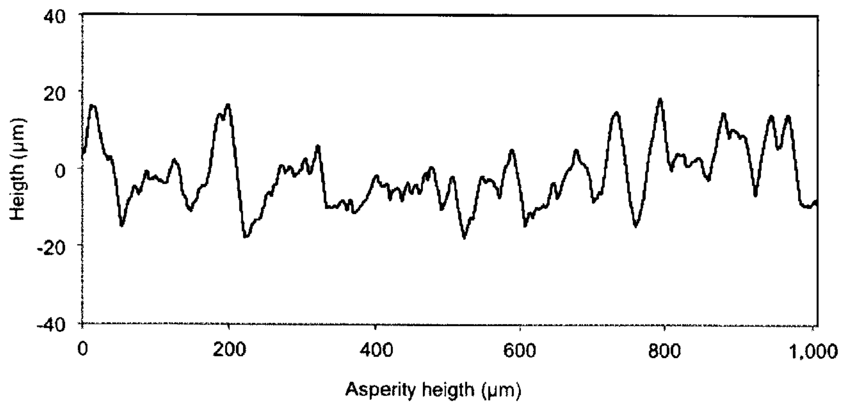

(b) Pad D6

Figure D.2. Surface profiles of the IC1000 pads after diamond conditioning.

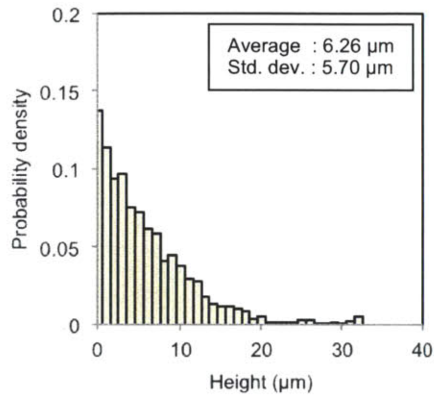

(a) Pad D1

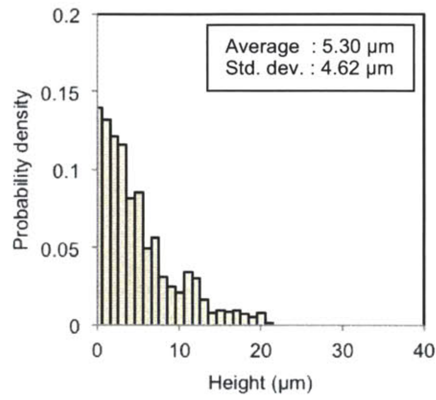

(b) Pad D4

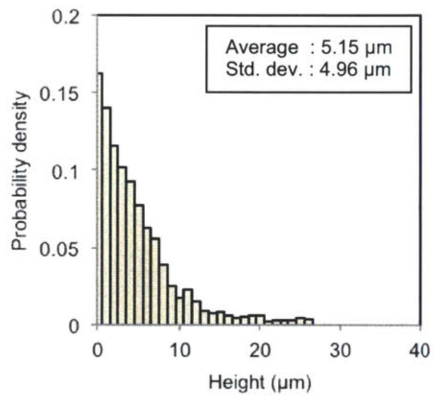

(c) Pad D5

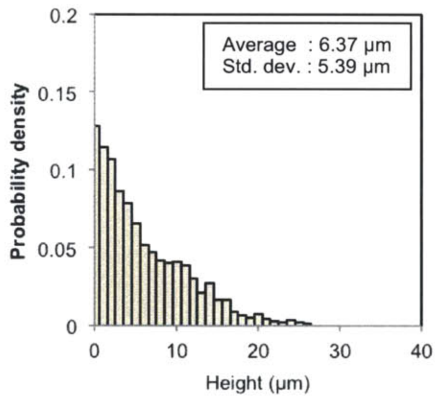

(d) Pad D6

Figure D.3. Height distribution of pad surfaces after diamond conditioning.

APPENDIX E

METHODS OF FLATTENING PAD ASPERITIES

As theoretically and experimentally shown in Chapter 4, increasing the R_a/σ_z value of CMP pads will decrease the proportion of plastically deforming pad asperities while polishing, and therefore less scratching by pad asperities. For pads that have the hardness-to-Young's modulus ratio, H_a/E_a, between 0.1 to 0.5, the R_a/σ_z value should be increased to more than 20 so that less than 10 percent of pad asperities being in contact will deform plastically. Since the new commercial pads typically have R_a/σ_z value of about 5, novel methods of increasing the R_a/σ_z value by controlling the pad topography are required to reduce the scratching. The technologies appear as filed in Saka, N., Chun, J.-H., Kim, S., and Shin, S.-H., "Scratch reduction by pad topography control in chemical-mechanical polishing," *US Provisional Patent*, Application number: 61/758,449, 2013.

E.1. Compression by a smooth, flat metal plate

To increase the R_a/σ_z value of the pad without using dummy wafers or slurries, flattening processes of pad asperities by smooth, rigid surfaces can be suggested. The first suggested method is compression of a new pad using a smooth, flat plate. As shown in Figure D.1, using a rigid metal plate with a given normal load, the asperities can be flattened and the R_a/σ_z value of the pad should increase. That is, the radius of curvature of the compressed asperities will increase and, simultaneously, the standard deviation of asperity heights will decrease. Moreover, the flattening effect will be greater if the temperature of the metal plate is increased. Therefore, the increment of R_a/σ_z will be greater as the applied normal load and the plate temperature are higher. It is also important to note that the surface of the plate should have roughness much smaller than

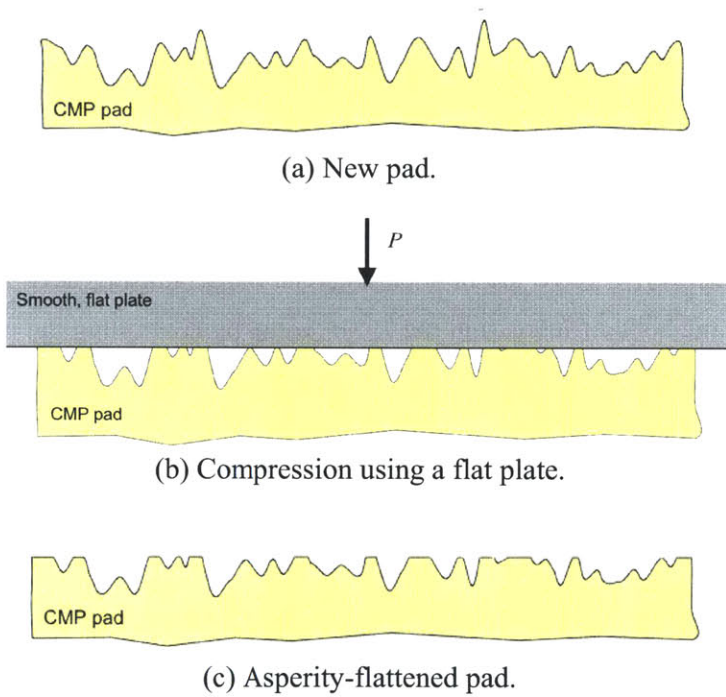

(a) New pad.

(b) Compression using a flat plate.

(c) Asperity-flattened pad.

Figure E.1. Asperity-flattening by compressing with a smooth, flat plate.

that of the pad surface. Since the average roughness of the commercial pads is about 5 μm, roughness of the plate surface should be 100 nm or less. "Asperity-flattening" using a flat plate can be conducted either by compressing a large plate, or by compressing a small plate and sliding it over the pad.

Figure E.2 is a schematic of an "asperity-flattening" equipment using a large flat plate. The system comprises a bottom plate to which the polishing pad is fixed and an upper plate for flattening. Both plates have the same diameter as that of the pad. The upper plate is preferred to be made of a metal with much higher Young's modulus and hardness than those of the pad material. The system includes the means for urging the upper plate and the polishing pad into contact and the means for heating the upper plate.

Figure E.3 is a schematic of an equipment using a flat plate of smaller diameter than that of the pad. Both upper and bottom plates are rotated. In addition, the upper plate should have the availability of translation motion. Asperities can be flattened by rotating the plates with the same rotational speed at the required normal load. The smaller upper plate is preferred to be made of a metal with much higher Young's modulus and hardness than those of the pad material and with high wear resistance. The system also includes the means for urging the upper plate and the polishing pad into contact and means for increasing the temperature of the upper plate.

Figure E.4 is a schematic of a CMP machine with a small flat plate for in-situ "asperity-flattening." The smooth, rigid plate is located between the conditioner and the polishing head. It has the means for compressing the pad surface and also for rotating the plate.

E.2. Rolling/sliding by a smooth metal roller

The second suggested method of the "asperity-flattening" processes is a rolling/sliding system using a roller. As shown in Figure E.5, by rolling or sliding a rigid metal roller over the pad surface with at a given normal load and relative velocity, pad asperities can be flattened. If the radius of the roller is much greater than the asperity radius, R_a, and

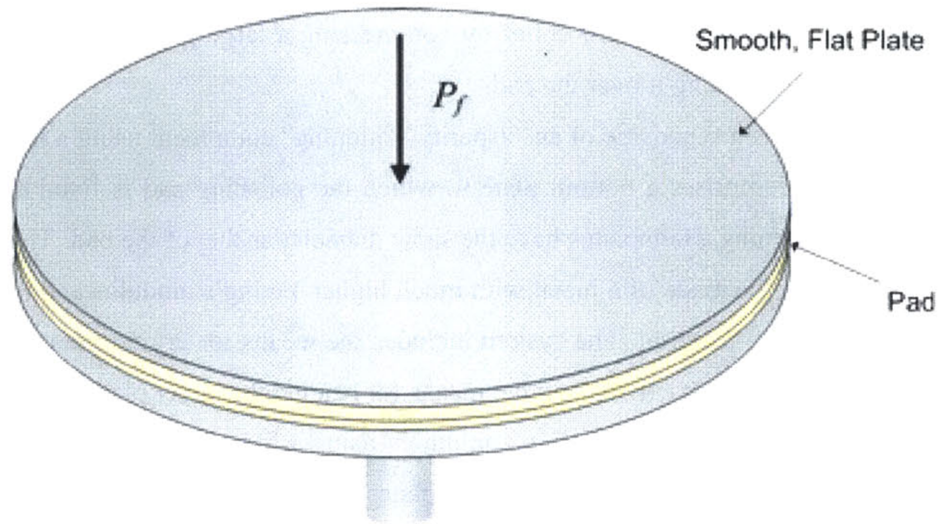

Figure E.2. Schematic of "asperity-flattening" using a smooth, flat plate that has the same radius as that of the pad.

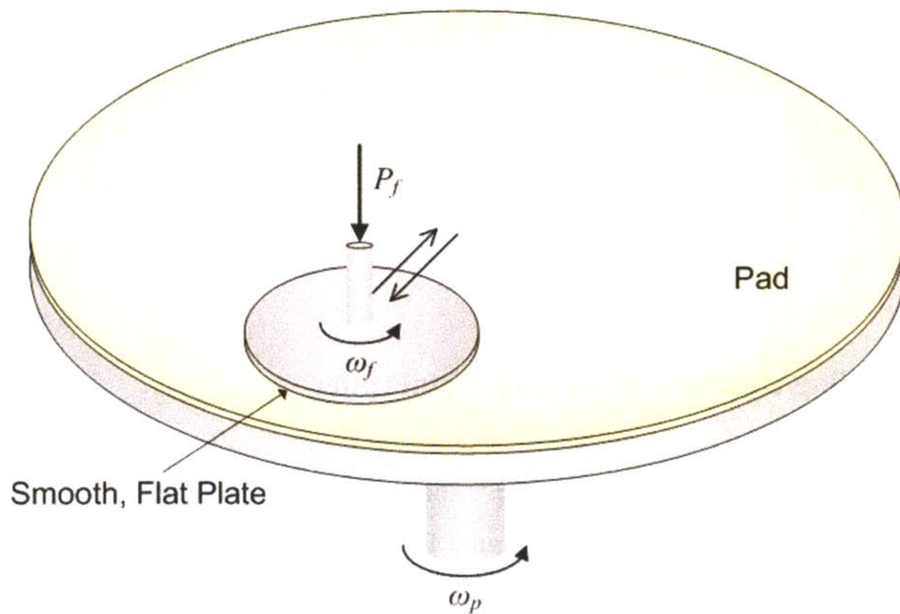

Figure E.3. Schematic of "asperity-flattening" using a smooth, flat plate that has a smaller radius than that of the pad.

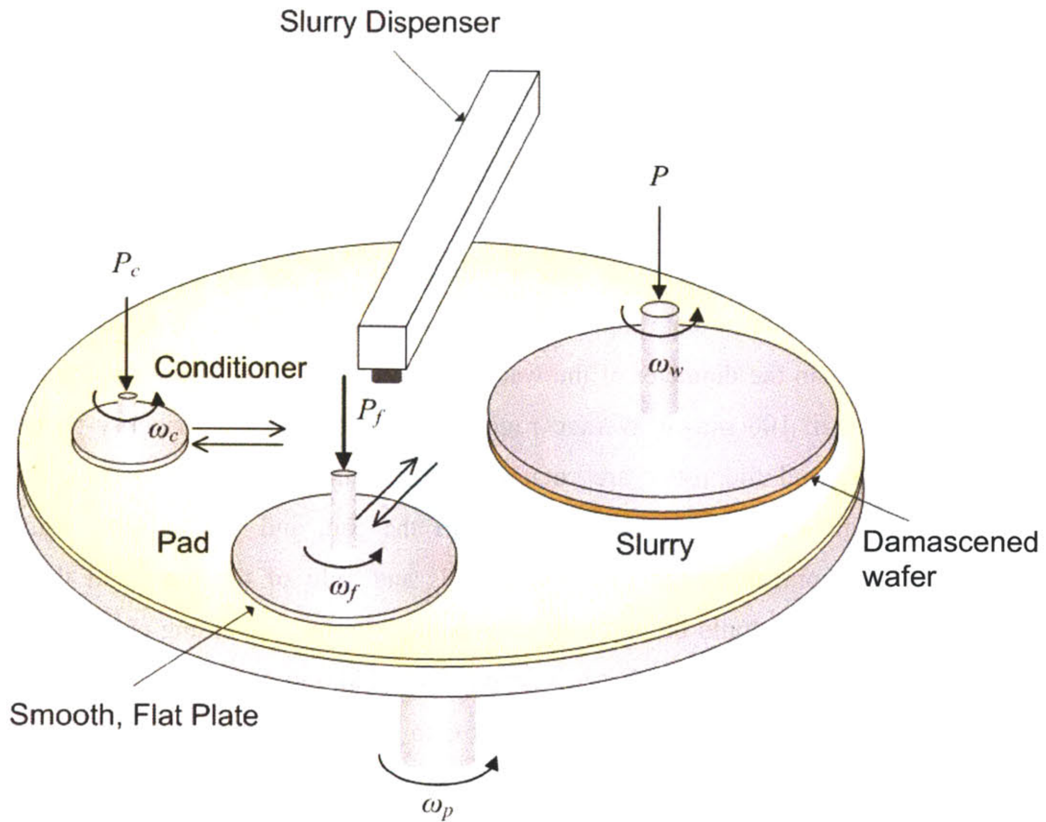

Figure E.4. Schematic of in-situ "asperity-flattening" in CMP using a smooth, flat disk.

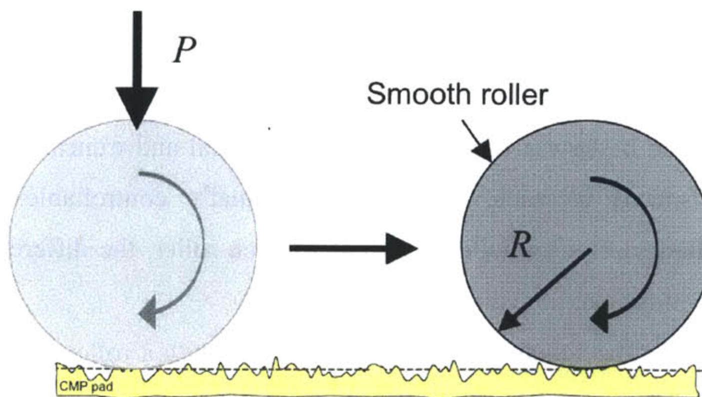

Figure E.5. "Asperity-flattening" process by rolling/sliding using a smooth roller.

asperity spacing, λ_a, of the pad then the deformation of the bulk layer underneath the asperity level of the pad is negligible, and it can be assumed that only the pad asperities will deform while flattening. Typically, the asperity radius and spacing of commercial pads are about 20 μm and 100 μm, respectively. Therefore, more than 2 mm of radius is required for the roller. The advantage of the roller compared to that of the flat plate is that the roller requires much less normal load.

Figure E.6 is a schematic of an "asperity-flattening" equipment using a cylinder. The system contains a bottom plate supporting the polishing pad and a cylinder which has the length greater than the diameter of the wafer to be polished. The surface of the cylinder requires less than 100 nm of average roughness for an effective "asperity-flattening." Both the plate and the roller are rotatable. The cylinder should have much higher Young's modulus and hardness than those of the pad, and should have high wear resistance. By controlling the rotational speeds and radii of the plate and the roller, sliding, if necessary, could be imposed between the interface. If sliding exists during the "asperity-flattening," friction force is applied in addition to the normal force and therefore the increase in R_a/σ_z will be greater than that of the frictionless case. However, sliding induces wear of the pad surface and may decrease the pad lifetime. Therefore, the relative velocity in every contact point is preferred to be zero in order to avoid pad wear during the "asperity-flattening."

In order to minimize sliding between the plate and the roller, different designs of the roller instead of a cylinder, Figure E.7a, can be used. Figure E.7b shows a cone-shaped roller. Since the linear velocity of the pad increases from the center to the edge, the roller radius should designed to increase such that the relative velocities at every contact point are the same or even zero.

Figures E.8a and b show a combination of cylindrical and truncated conical rollers. The rotational speeds of each roller are individually controllable. Therefore, by controlling the diameter and rotational speeds of each roller, the differences in relative velocities can be minimized or enhanced.

Figure E.9 shows the schematic of a CMP machine with a roller for in-situ asperity-flattening CMP. The smooth, rigid roller is located between the conditioner and the polishing head. It has the means for compressing the roller on the pad surface and also

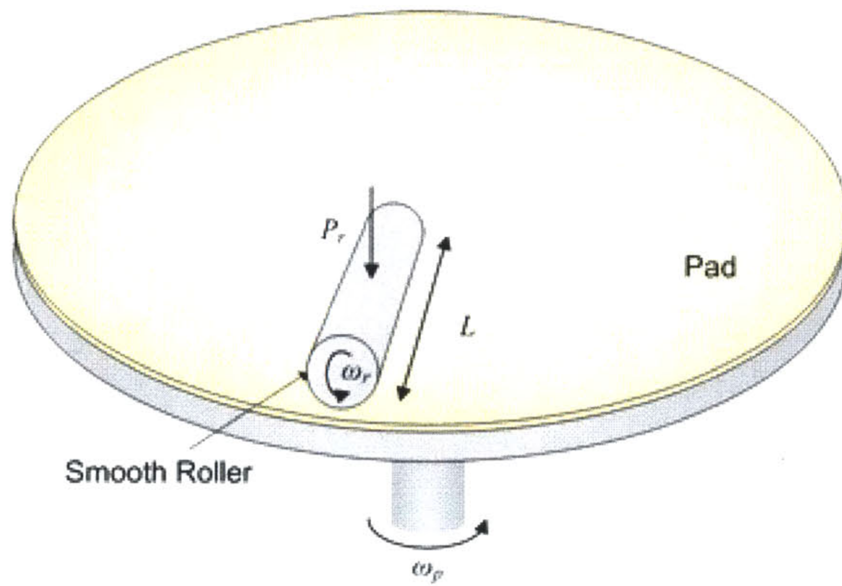

Figure E.6. Schematic of "asperity-flattening" using a smooth roller.

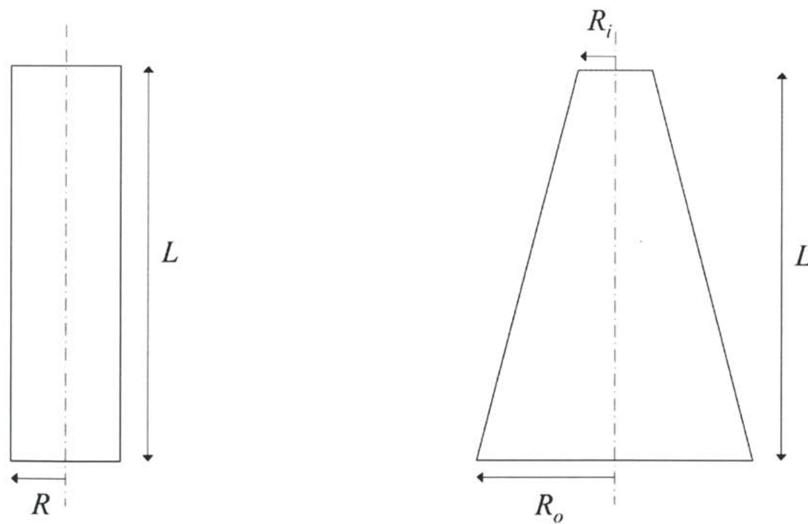

(a) Cylindrical roller (b) Cone-shaped roller

Figure E.7. Top view of the rigid metal rollers.

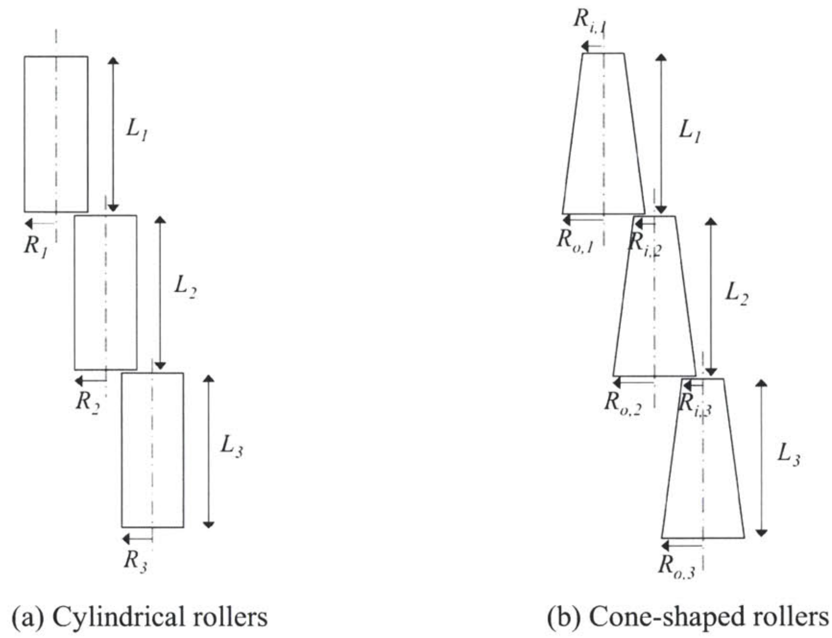

(a) Cylindrical rollers (b) Cone-shaped rollers

Figure E.8. Top view of the combinations of short rollers.

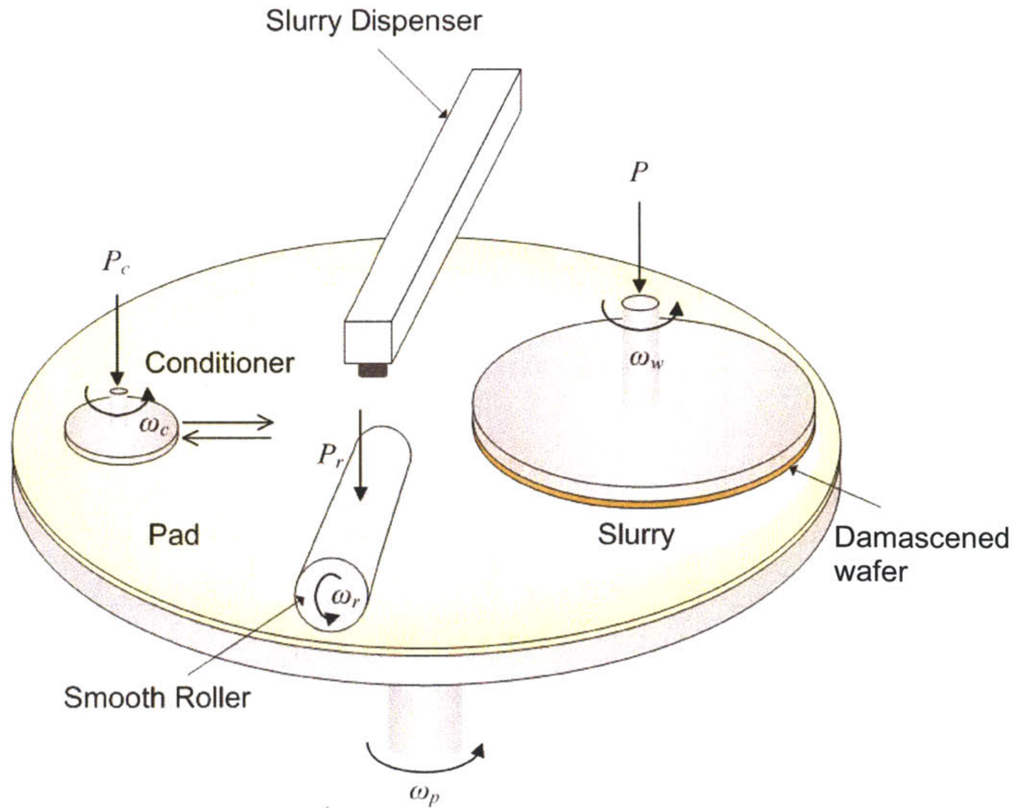

Figure E.9. Schematic of in-situ "asperity-flattening" using a smooth roller.

has those for rotating the roller. Any roller design, represented in Figures E.7 and E.8, can be used.

E.3. Sliding by a smooth metal torus

The third proposed method for asperity-flattening is a sliding system using a torus combined with the diamond conditioner. As shown in Figure E.10, a torus, which has a relatively smooth and rigid surface compared with the pad surface, is integrated with the conditioner. The system urges the hybrid conditioner and the polishing pad into contact and the means for increasing the temperature of the torus material, if necessary. The torus should be made of a metal with high Young's modulus and hardness, and also should have high wear resistance. The height of the torus, h_t, should be greater than that of the height of the conditioner, h_c, in order to apply higher pressure in asperity-flattening and lower pressure in diamond conditioning. This hybrid device could be used for both conditioning (i.e., roughening) and breaking-in a CMP pad, as shown in the Figure E.11. The hybrid conditioner requires slightly more normal load for both asperity-flattening and diamond conditioning than that for typical conditioning.

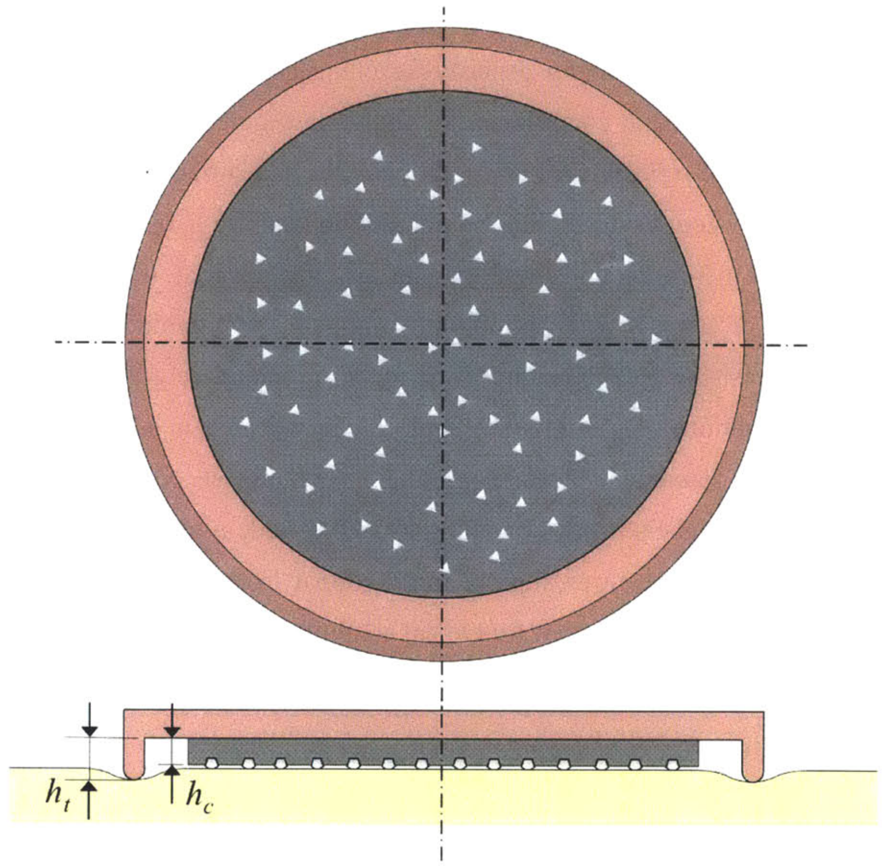

Figure E.10. Schematic of a diamond conditioner with a smooth, rigid torus attached at the circumference for in-situ asperity-flattening.

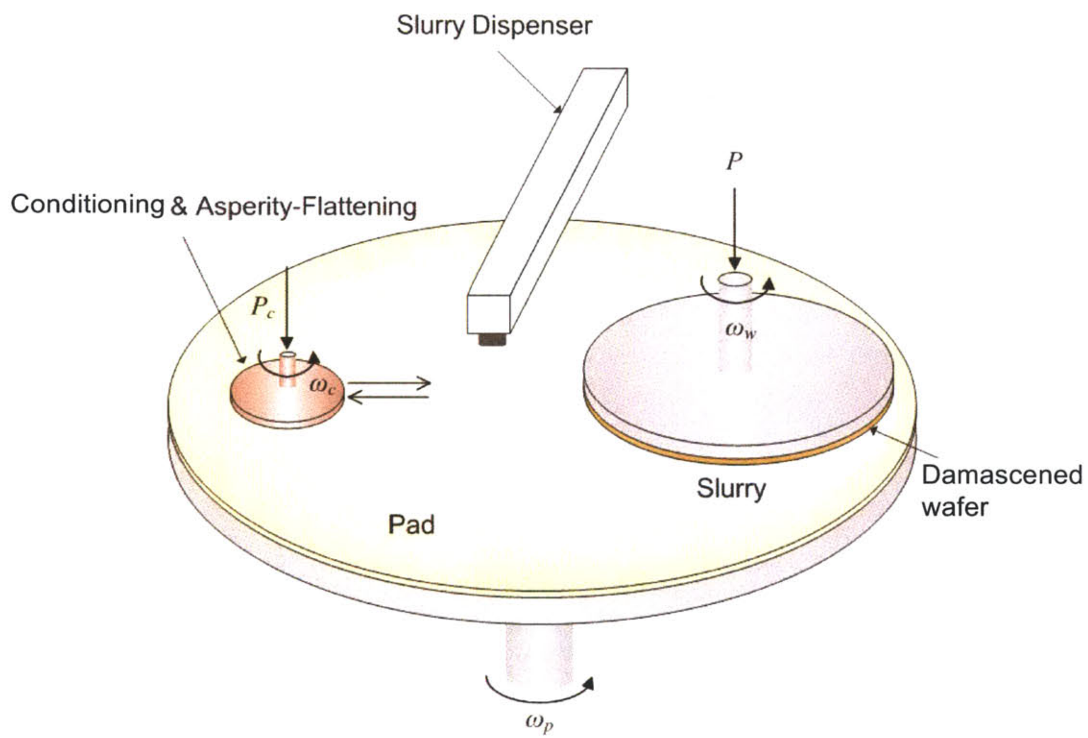

Figure E.11. Schematic of in-situ pad conditioning and asperity-flattening by a hybrid conditioner.

APPENDIX F

PAD SLIDING EXPERIMENTS USING ASPERITY-FLATTENED PADS ON PATTERNED CU/DIELECTRIC LAYERS

In Chapter 4, scratch mitigation by pad topography control was theoretically and experimentally investigated. Pad scratching models showed that the number of scratches can be decreased by reducing the probability of plastically deformed asperities in contact, which is strongly determined by the plasticity index. The experimental results on monolithic Cu layers showed that the asperity-flattened pads generate less scratches than the new pads by increased ratio of asperity radius to standard deviation of asperity heights, R_a / σ_z, i.e., by decreased plasticity index. As scratching on patterned Cu/dielectric layers is also caused primarily by the plastically deformed asperities, as discussed in Chapter 3, asperity-flattened pads are expected to reduce scratching on the patterned surfaces.

Figure F.1. shows the face-up polisher used for the experiments, and Table F.1 lists the experimental conditions. Two different pads, pad A and IC1000, before and after asperity-flattening, were slid over 300 mm wafers with patterned structures on the surface. Each wafer had about 50 dies that have 24 patterned blocks with different Cu and dielectric linewidths, Figure F.2 and Table F.3. The pads were slid over the patterns on about 32 dies, Figure F.3. The scratched pattern blocks after the experiments were examined by optical microscopes, Figure F.4. Table F.3, F.4, F.5, and F.6 contain the number of scratched blocks by the four different pads. Figure F.6 compares the total number of scratches generated by new IC1000 pad, asperity-flattened IC1000 pad, new pad A and asperity-flattened pad A. For both pad A and IC1000, asperity-flattened pads showed less scratches than the new pads. Since pad A is much softer than IC 1000, fewer scratches were found by pad A, and furthermore, surprisingly, no scratches were found by asperity-flattened pad A.

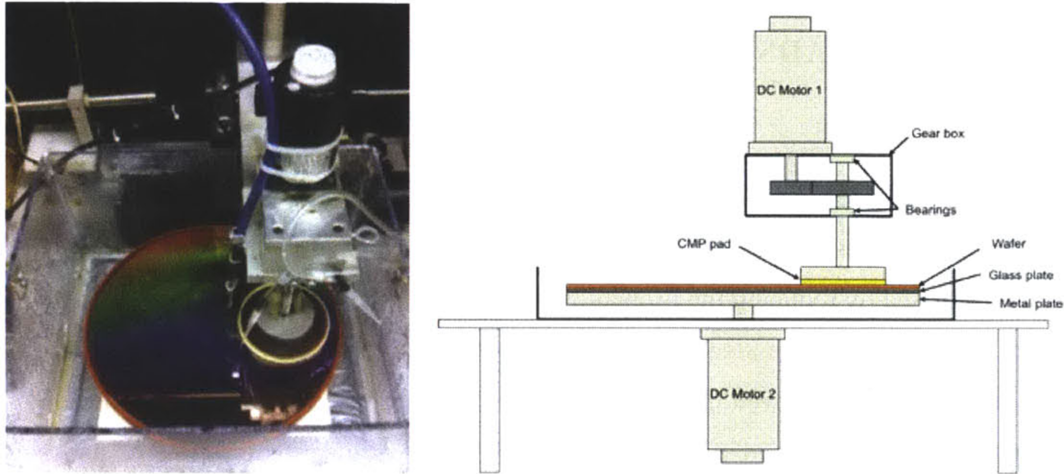

Figure F.1. Photograph and schematic of the face-up polisher.

Table F.1. Experimental conditions

Parameter	Value
Normal load	24 N
Nominal contact area	0.002 m^2
Nominal pressure	7 kPa (1 psi)
Rotational speed	90 rpm
Relative velocity	0.75 m/s
Duration	5 min

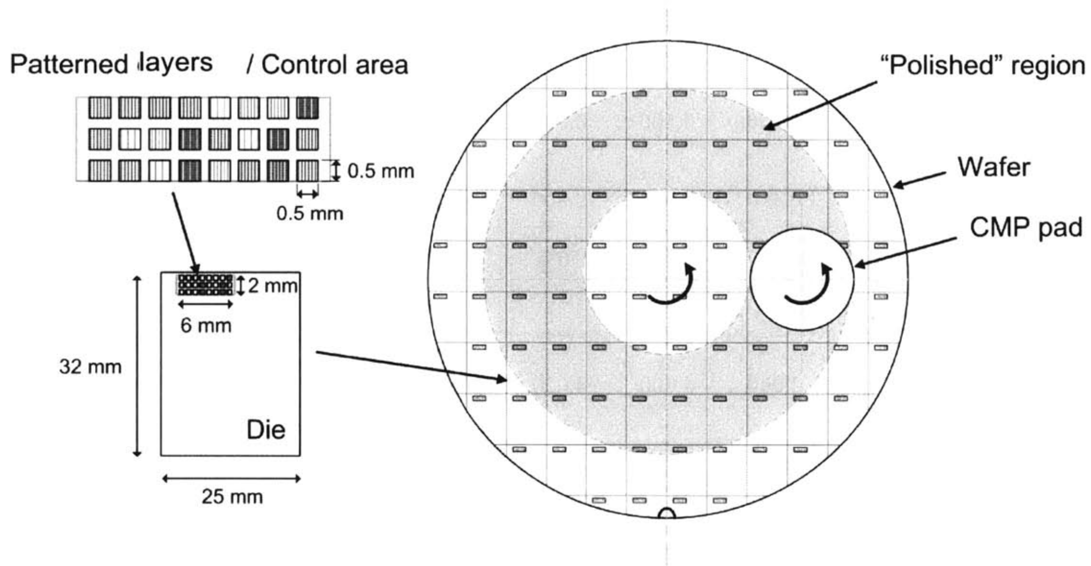

Figure F.2. Patterned layers within the controlled area in each die. The shaded area is the "polished" region on the faced-up polisher.

Table F.2. Linewidthes and pattern density of patterned Cu/low-k layers.

		Block1	Block2	Block3	Block4	Block5	Block6	Block7	Block8
Row 1	Cu Linewidth (μm)	0.350	0.500	0.800	2.000	4.500	2.000	0.700	1.000
	Low-k A Linewidth (μm)	0.350	0.500	0.800	2.000	1.000	1.300	0.300	4.000
	Pattern density	50%	50%	50%	50%	82%	61%	70%	20%
Row 2	Cu Linewidth (μm)	2.000	4.000	4.000	3.000	4.500	1.120	0.100	0.050
	Low-k A Linewidth (μm)	3.000	1.000	2.000	9.000	4.500	0.280	0.400	0.050
	Pattern density	40%	80%	67%	25%	50%	80%	20%	50%
Row 3	Cu Linewidth (μm)	1.000	0.100	0.560	0.150	0.300	0.200	0.050	0.075
	Low-k A Linewidth (μm)	1.000	0.100	0.140	0.650	0.200	0.200	0.100	0.075
	Pattern density	50%	50%	80%	19%	60%	50%	33%	50%

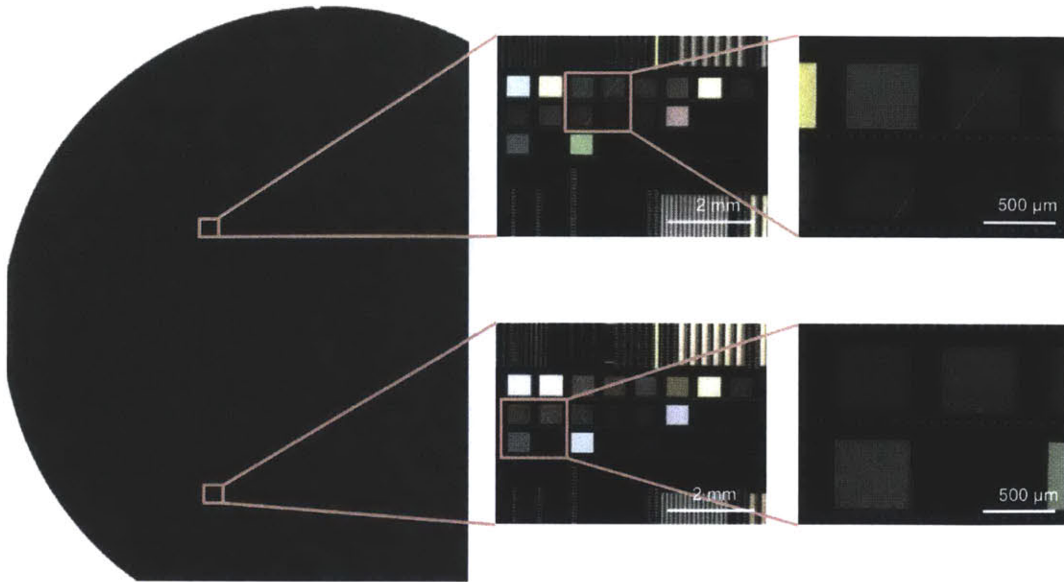

Figure F.3. Images of patterned Cu/low-*k* layers after pad sliding experiments using a new IC1000 pad.

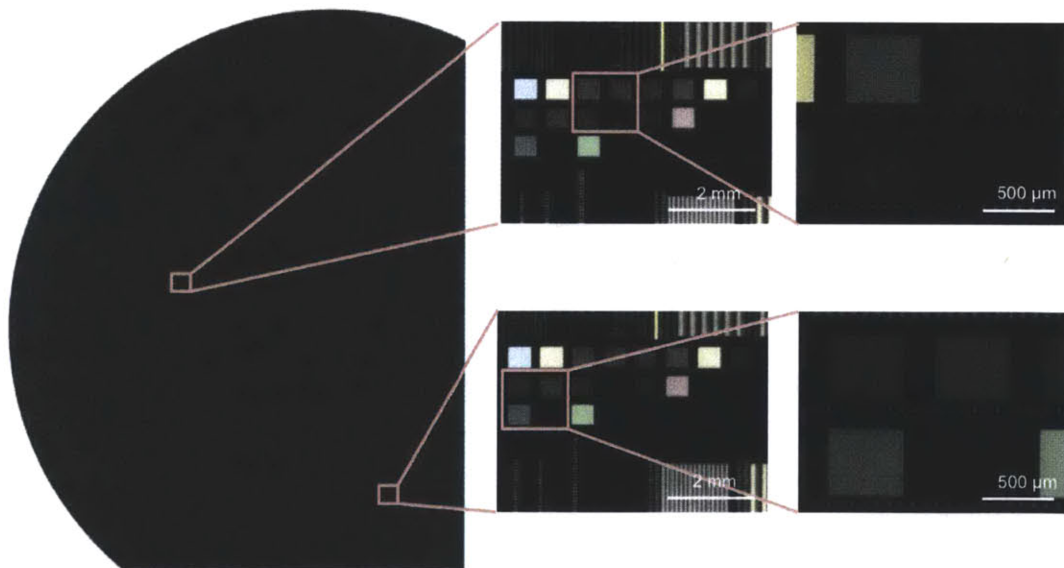

Figure F.4. Images of patterned Cu/low-*k* layers after pad sliding experiments using a new Pad A.

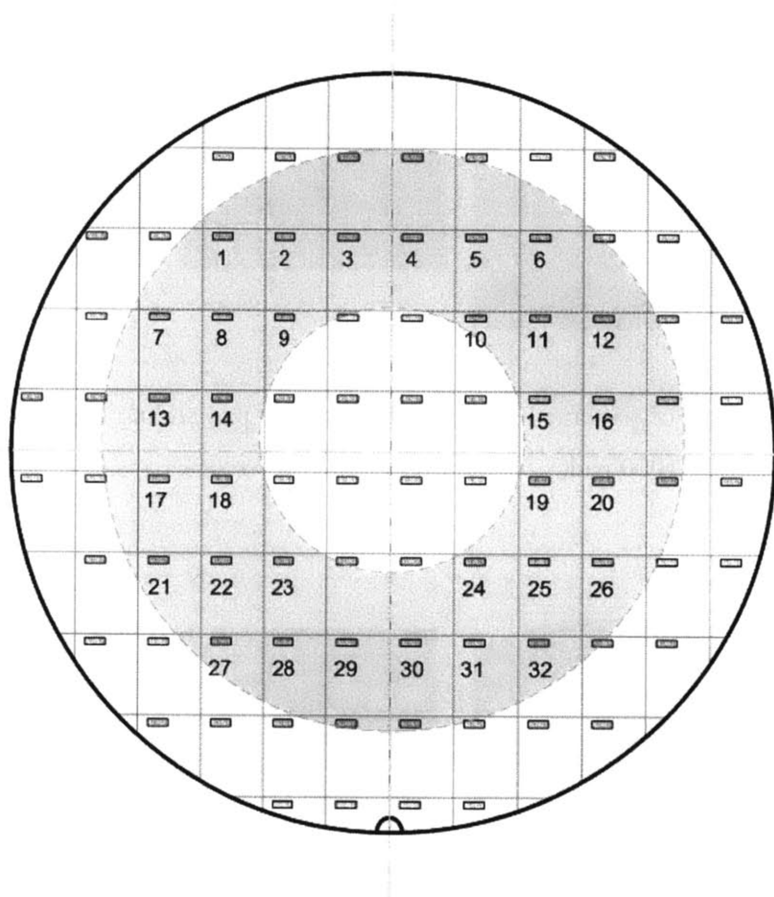

Figure F.5. Thirty-two sets of patterned layers within the "polished" region.

Table F.3. Scratched patterned blocks after the "polishing" experiments using a new IC1000 pad.

Set #	Row 1								Row 2								Row 3							
	B1	B2	B3	B4	B5	B6	B7	B8	B1	B2	B3	B4	B5	B6	B7	B8	B1	B2	B3	B4	B5	B6	B7	B8
1	No	No	No	No	No	No	No	No	No	No	No	No	No	No	No	No	No	No	No	No	No	No	No	No
2	No	Yes	Yes	Yes	Yes	No	No	No	No	Yes	Yes	No	No	Yes	Yes	No	Yes	No	No	Yes	No	Yes	No	No
3	No	No	No	No	Yes	Yes	Yes	Yes	No	No	No	No	Yes	No	Yes	No	No	No	No	No	No	No	No	No
4	No	No	Yes	Yes	Yes	Yes	No	No	No	No	No	No	No	Yes	No	No	No	No	No	No	No	No	No	No
5	No	Yes	Yes	Yes	Yes	Yes	No	No	Yes	Yes	Yes	No	Yes	Yes	Yes	No	Yes	No	No	No	No	No	No	No
6	Yes	Yes	No	No	No	Yes	Yes	Yes	No	No	No	Yes	No	No	No	Yes	No	No	No	No	No	No	No	No
7	No	No	No	No	No	Yes	No	Yes	No	No	No	No	No	Yes	No	Yes	No	No	No	No	No	No	No	No
8	Yes	Yes	Yes	Yes	Yes	Yes	Yes	Yes	No	No	Yes	Yes	No	Yes	No	Yes	Yes	No	Yes	Yes	No	No	No	No
9	No	No	No	Yes	No	No	No	Yes	No	Yes	No	No	No	No	Yes	No	No	Yes	No	No	No	No	No	No
10	No	Yes	Yes	Yes	No	No	No	Yes	No	Yes	No	No	No	No	Yes	No	No	No	No	No	No	No	No	No
11	No	No	Yes	Yes	Yes	No	Yes	Yes	No	No	No	No	Yes	Yes	Yes	Yes	No	No	No	No	No	No	No	No
12	No	No	No	Yes	Yes	Yes	Yes	No	No	Yes	Yes	No	Yes	Yes	No	No	No	No	No	No	No	No	No	Yes
13	Yes	Yes	Yes	Yes	No	No	Yes	Yes	No	Yes	Yes	No	Yes	Yes	Yes	Yes	Yes	Yes	Yes	Yes	Yes	Yes	Yes	Yes
14	Yes	Yes	Yes	Yes	Yes	Yes	Yes	No	Yes	Yes	No	No	No	Yes	No	No	Yes	Yes	Yes	No	Yes	Yes	No	No
15	Yes	Yes	Yes	Yes	Yes	Yes	No	No	Yes	Yes	Yes	No	Yes	Yes	Yes	No	Yes	No	Yes	No	No	No	No	No
16	No	Yes	Yes	Yes	Yes	Yes	Yes	Yes	No	Yes	Yes	Yes	Yes	Yes	Yes	No	Yes	No	Yes	No	Yes	Yes	No	No
17	No	Yes	Yes	Yes	Yes	Yes	Yes	Yes	No	Yes	Yes	Yes	Yes	Yes	Yes	Yes	Yes	No	Yes	Yes	Yes	Yes	No	Yes
18	No	Yes	Yes	No	No	No	Yes	Yes	No	Yes	Yes	No	No	Yes	Yes	Yes	No	No	No	No	Yes	Yes	No	No
19	No	Yes	No	No	Yes	Yes	Yes	No	No	Yes	Yes	No	No	No	Yes	No	No	No	No	No	No	No	No	Yes
20	Yes	Yes	Yes	Yes	Yes	Yes	Yes	Yes	Yes	Yes	Yes	Yes	Yes	Yes	Yes	Yes	Yes	Yes	Yes	Yes	Yes	Yes	Yes	Yes
21	Yes	Yes	Yes	Yes	Yes	Yes	Yes	Yes	No	Yes	Yes	No	Yes	Yes	Yes	No	No	No	No	No	Yes	Yes	No	No
22	Yes	No	No	No	Yes	No	No	No	Yes	Yes	No	No	No	No	Yes	No	No	No	Yes	No	No	No	No	No
23	No	No	No	No	Yes	No	No	No	Yes	Yes	No	No	No	No	Yes	No	No	No	Yes	No	No	No	No	No
24	No	No	No	No	No	Yes	No	Yes	No	No	No	Yes	No	No	No	No	Yes	No	Yes	No	No	No	No	No
25	Yes	Yes	Yes	No	Yes	Yes	Yes	Yes	No	Yes	Yes	No	No	Yes	Yes	No	Yes	No	No	No	Yes	No	No	No
26	No	No	Yes	Yes	Yes	Yes	Yes	No	No	No	Yes	No	No	Yes	Yes	No	No	No	Yes	No	Yes	No	Yes	No
27	Yes	Yes	Yes	Yes	Yes	Yes	Yes	Yes	Yes	Yes	Yes	Yes	Yes	Yes	No	Yes	Yes	Yes	Yes	Yes	Yes	Yes	Yes	No
28	No	Yes	Yes	Yes	No	No	Yes	Yes	No	No	No	No	No	No	No	No	No	No	Yes	No	No	Yes	No	No
29	No	Yes	No	No	No	No	No	No	No	No	No	No	No	No	No	No	No	No	Yes	No	Yes	No	No	No
30	No	Yes	Yes	Yes	No	No	No	No	No	No	No	No	No	Yes	Yes	No	No	No	No	No	No	No	No	No
31	Yes	No	No	No	Yes	Yes	Yes	Yes	No	Yes	Yes	No	No	Yes	Yes	No	No	No	No	No	Yes	No	No	No
32	No	No	Yes	Yes	Yes	Yes	Yes	Yes	Yes	Yes	Yes	No	Yes	No	Yes	No	No	No	Yes	No	No	Yes	No	Yes
Total	11	19	20	20	21	20	19	19	8	20	17	7	12	20	21	9	12	5	15	6	12	11	4	6

Table F.4. Scratched patterned blocks after the "polishing" experiments using an asperity-flattened IC1000 pad.

	Row 1								Row 2								Row 3							
Set #	B1	B2	B3	B4	B5	B6	B7	B8	B1	B2	B3	B4	B5	B6	B7	B8	B1	B2	B3	B4	B5	B6	B7	B8
1	No	No	No	No	No	No	No	No	No	No	No	No	No	No	No	No	No	No	No	No	No	No	No	No
2	No	No	No	No	No	No	No	No	No	No	No	No	No	No	No	No	No	No	No	No	No	No	No	No
3	No	No	No	No	No	No	No	No	No	No	No	No	No	No	No	No	No	No	No	No	No	No	No	No
4	No	No	No	No	No	No	No	No	No	No	No	No	No	No	No	No	No	No	No	No	No	No	No	No
5	No	No	No	No	No	No	No	No	No	No	No	No	No	No	No	No	No	No	No	No	No	No	No	No
6	No	No	No	No	No	No	No	No	No	No	No	No	No	No	No	No	No	No	No	No	No	No	No	No
7	No	No	No	No	No	No	No	No	No	No	No	No	No	No	No	No	No	No	No	No	No	No	No	No
8	No	No	No	No	No	No	No	No	No	No	No	No	No	No	No	No	No	No	No	No	No	No	No	No
9	No	No	No	No	No	No	No	No	No	No	No	No	No	No	No	No	No	No	No	No	No	No	No	No
10	No	No	No	No	No	No	No	No	No	No	No	No	No	No	No	No	No	No	No	No	No	No	No	No
11	No	No	No	No	No	No	No	No	No	No	No	No	No	No	No	No	No	No	No	No	No	No	No	No
12	No	No	No	No	No	No	No	No	No	No	No	No	No	No	No	No	No	No	No	No	No	No	No	No
13	No	No	No	No	No	No	No	No	No	No	No	No	No	No	No	No	No	No	No	No	No	No	No	No
14	No	Yes	No	No	Yes	No	No	No	No	No	No	No	No	No	No	No	No	No	No	Yes	No	No	No	No
15	Yes	Yes	Yes	No	No	No	No	No	No	Yes	No	Yes	No	No	No	No	Yes	No	No	No	No	No	No	No
16	No	No	No	No	No	No	No	No	No	No	No	No	No	No	No	No	No	No	No	No	No	No	No	No
17	No	Yes	No	No	No	No	No	No	No	No	No	No	No	No	No	No	No	Yes	No	No	No	No	No	No
18	No	Yes	No	No	No	No	Yes	No	No	No	No	No	No	No	No	Yes	Yes	No	No	No	No	No	No	Yes
19	No	No	No	Yes	No	No	No	No	No	No	No	Yes	No	No	No	No	No	No	No	Yes	No	No	No	No
20	No	No	No	No	Yes	No	No	No	No	No	No	No	Yes	Yes	No	No	No	No	No	No	Yes	No	No	No
21	No	No	No	No	No	No	No	No	No	No	No	No	No	No	No	No	No	No	No	No	No	No	No	No
22	No	No	No	No	No	No	No	No	No	No	No	No	No	No	No	No	No	No	No	No	No	No	No	No
23	Yes	No	No	No	No	No	No	Yes	No	No	No	No	Yes	No	Yes	No	No	No	No	No	No	No	No	No
24	No	No	No	No	No	No	No	No	Yes	Yes	No	No	No	No	No	No	Yes	No	No	No	No	No	No	No
25	Yes	Yes	No	No	No	Yes	Yes	No	No	No	No	No	No	No	No	No	Yes	No	No	No	No	No	No	No
26	No	No	No	No	No	No	No	No	No	No	No	No	No	No	No	No	No	No	No	No	No	No	No	No
27	No	No	No	No	No	No	No	No	No	No	No	No	No	No	No	No	No	No	No	No	No	No	No	No
28	No	No	No	No	No	No	No	No	No	No	No	No	No	No	No	No	No	No	No	No	No	No	No	No
29	No	No	No	No	No	No	No	No	No	No	No	No	No	No	No	No	No	No	No	No	No	No	No	No
30	Yes	Yes	No	No	No	No	No	No	No	No	No	No	No	No	No	Yes	No	No	No	No	No	No	No	No
31	No	No	No	No	No	No	No	No	No	No	No	No	No	No	No	No	No	No	No	No	No	No	No	No
32	No	No	No	No	No	No	No	No	No	No	No	No	No	No	No	No	No	No	No	No	No	No	No	No
Total	**4**	**6**	**1**	**1**	**2**	**1**	**2**	**1**	**1**	**1**	**0**	**2**	**2**	**1**	**1**	**2**	**4**	**1**	**0**	**2**	**1**	**0**	**0**	**1**

Table F.5. Scratched patterned blocks after the "polishing" experiments using a new Pad A.

	Row 1								Row 2								Row 3							
Set #	B1	B2	B3	B4	B5	B6	B7	B8	B1	B2	B3	B4	B5	B6	B7	B8	B1	B2	B3	B4	B5	B6	B7	B8
1	No	No	No	No	No	No	No	No	No	No	No	No	No	No	No	No	No	No	No	No	No	No	No	No
2	No	No	No	No	No	No	No	No	No	No	No	No	No	No	Yes	No	No	No	No	No	No	No	No	No
3	No	Yes	Yes	No	No	No	No	No	No	No	No	No	No	No	No	No	No	No	No	No	No	No	No	No
4	No	No	No	No	No	No	No	No	No	No	No	No	No	No	No	No	No	No	No	No	No	No	No	No
5	Yes	Yes	No	No	No	No	No	No	No	No	Yes	No	No	Yes	Yes	No	No	No	No	No	No	No	No	No
6	No	No	No	No	No	No	No	No	No	No	No	No	No	No	No	No	No	No	No	No	No	No	No	No
7	No	No	No	No	No	No	No	No	No	No	No	No	No	No	No	No	No	No	No	No	No	No	No	No
8	Yes	Yes	No	No	No	No	No	No	No	No	Yes	No	No	No	No	No	Yes	No	No	No	No	No	No	No
9	No	No	No	Yes	No	Yes	Yes	No	No	Yes	No	No	No	No	No	No	No	No	No	No	No	No	No	No
10	No	No	No	No	No	No	No	No	No	No	No	No	No	No	No	No	No	No	No	No	No	No	No	No
11	No	No	No	No	No	No	No	No	No	No	No	No	No	No	No	No	No	No	No	No	No	No	No	No
12	No	No	No	No	No	No	No	No	No	No	No	No	No	No	No	No	No	No	No	No	No	No	No	No
13	No	No	No	No	No	No	No	No	No	No	No	No	No	No	No	No	Yes	No	No	No	No	No	No	No
14	No	No	No	No	No	No	No	No	No	No	Yes	No	No	No	No	No	No	No	No	No	No	No	No	No
15	No	No	No	No	No	Yes	No	No	No	No	No	No	No	No	No	No	No	No	No	No	No	No	No	No
16	No	No	No	No	No	No	No	No	No	No	No	No	No	No	No	No	No	No	No	No	No	No	No	No
17	No	No	No	No	No	No	No	No	No	No	No	No	No	No	No	No	No	No	No	No	No	No	No	No
18	No	Yes	No	No	No	No	No	No	No	No	Yes	No	No	No	No	No	No	No	Yes	No	No	No	No	No
19	No	No	No	No	No	No	No	No	No	No	No	No	No	No	No	No	No	No	No	No	No	No	No	No
20	No	No	No	No	No	No	No	No	No	No	No	No	No	No	No	No	No	No	No	No	No	No	No	No
21	No	No	No	No	No	No	Yes	No	No	No	No	No	No	No	No	No	No	No	No	No	No	No	No	No
22	No	No	No	No	No	No	No	No	No	No	No	No	No	No	No	No	No	No	No	No	No	No	No	No
23	No	No	Yes	No	No	No	No	No	No	No	No	No	No	No	No	No	No	No	No	No	No	No	No	No
24	No	No	No	No	No	No	No	No	No	No	No	No	No	No	No	No	No	No	No	No	No	No	No	No
25	No	No	No	No	No	No	No	No	No	No	Yes	No	No	No	No	No	No	No	Yes	No	No	No	No	No
26	No	No	No	No	No	No	No	No	No	No	No	No	No	No	No	No	No	No	No	No	No	No	No	No
27	No	No	No	No	No	No	No	No	No	No	No	No	No	No	No	No	No	No	No	No	No	No	No	No
28	No	No	No	No	No	No	No	No	Yes	Yes	No	No	No	Yes	No	No	Yes	No	No	No	No	No	No	No
29	Yes	Yes	Yes	No	No	No	No	No	No	No	No	No	No	No	No	No	No	No	No	No	No	No	No	No
30	No	Yes	Yes	No	No	Yes	No	No	No	No	No	No	No	No	No	No	Yes	No	No	No	No	No	No	No
31	No	No	No	No	Yes	No	No	No	No	No	No	No	No	No	No	No	No	No	No	No	No	No	No	No
32	No	No	No	No	No	No	No	No	No	No	No	No	No	No	No	No	No	No	No	No	No	No	No	No
Total	**3**	**6**	**4**	**1**	**1**	**3**	**2**	**0**	**1**	**2**	**5**	**0**	**0**	**2**	**2**	**0**	**4**	**0**	**2**	**0**	**0**	**0**	**0**	**0**

Table F.6. Scratched patterned blocks after the "polishing" experiments using an asperity-flattened Pad A.

	Row 1								Row 2								Row 3							
Set #	B1	B2	B3	B4	B5	B6	B7	B8	B1	B2	B3	B4	B5	B6	B7	B8	B1	B2	B3	B4	B5	B6	B7	B8
1	No	No	No	No	No	No	No	No	No	No	No	No	No	No	No	No	No	No	No	No	No	No	No	No
2	No	No	No	No	No	No	No	No	No	No	No	No	No	No	No	No	No	No	No	No	No	No	No	No
3	No	No	No	No	No	No	No	No	No	No	No	No	No	No	No	No	No	No	No	No	No	No	No	No
4	No	No	No	No	No	No	No	No	No	No	No	No	No	No	No	No	No	No	No	No	No	No	No	No
5	No	No	No	No	No	No	No	No	No	No	No	No	No	No	No	No	No	No	No	No	No	No	No	No
6	No	No	No	No	No	No	No	No	No	No	No	No	No	No	No	No	No	No	No	No	No	No	No	No
7	No	No	No	No	No	No	No	No	No	No	No	No	No	No	No	No	No	No	No	No	No	No	No	No
8	No	No	No	No	No	No	No	No	No	No	No	No	No	No	No	No	No	No	No	No	No	No	No	No
9	No	No	No	No	No	No	No	No	No	No	No	No	No	No	No	No	No	No	No	No	No	No	No	No
10	No	No	No	No	No	No	No	No	No	No	No	No	No	No	No	No	No	No	No	No	No	No	No	No
11	No	No	No	No	No	No	No	No	No	No	No	No	No	No	No	No	No	No	No	No	No	No	No	No
12	No	No	No	No	No	No	No	No	No	No	No	No	No	No	No	No	No	No	No	No	No	No	No	No
13	No	No	No	No	No	No	No	No	No	No	No	No	No	No	No	No	No	No	No	No	No	No	No	No
14	No	No	No	No	No	No	No	No	No	No	No	No	No	No	No	No	No	No	No	No	No	No	No	No
15	No	No	No	No	No	No	No	No	No	No	No	No	No	No	No	No	No	No	No	No	No	No	No	No
16	No	No	No	No	No	No	No	No	No	No	No	No	No	No	No	No	No	No	No	No	No	No	No	No
17	No	No	No	No	No	No	No	No	No	No	No	No	No	No	No	No	No	No	No	No	No	No	No	No
18	No	No	No	No	No	No	No	No	No	No	No	No	No	No	No	No	No	No	No	No	No	No	No	No
19	No	No	No	No	No	No	No	No	No	No	No	No	No	No	No	No	No	No	No	No	No	No	No	No
20	No	No	No	No	No	No	No	No	No	No	No	No	No	No	No	No	No	No	No	No	No	No	No	No
21	No	No	No	No	No	No	No	No	No	No	No	No	No	No	No	No	No	No	No	No	No	No	No	No
22	No	No	No	No	No	No	No	No	No	No	No	No	No	No	No	No	No	No	No	No	No	No	No	No
23	No	No	No	No	No	No	No	No	No	No	No	No	No	No	No	No	No	No	No	No	No	No	No	No
24	No	No	No	No	No	No	No	No	No	No	No	No	No	No	No	No	No	No	No	No	No	No	No	No
25	No	No	No	No	No	No	No	No	No	No	No	No	No	No	No	No	No	No	No	No	No	No	No	No
26	No	No	No	No	No	No	No	No	No	No	No	No	No	No	No	No	No	No	No	No	No	No	No	No
27	No	No	No	No	No	No	No	No	No	No	No	No	No	No	No	No	No	No	No	No	No	No	No	No
28	No	No	No	No	No	No	No	No	No	No	No	No	No	No	No	No	No	No	No	No	No	No	No	No
29	No	No	No	No	No	No	No	No	No	No	No	No	No	No	No	No	No	No	No	No	No	No	No	No
30	No	No	No	No	No	No	No	No	No	No	No	No	No	No	No	No	No	No	No	No	No	No	No	No
31	No	No	No	No	No	No	No	No	No	No	No	No	No	No	No	No	No	No	No	No	No	No	No	No
32	No	No	No	No	No	No	No	No	No	No	No	No	No	No	No	No	No	No	No	No	No	No	No	No
Total	**0**	**0**	**0**	**0**	**0**	**0**	**0**	**0**	**0**	**0**	**0**	**0**	**0**	**0**	**0**	**0**	**0**	**0**	**0**	**0**	**0**	**0**	**0**	**0**

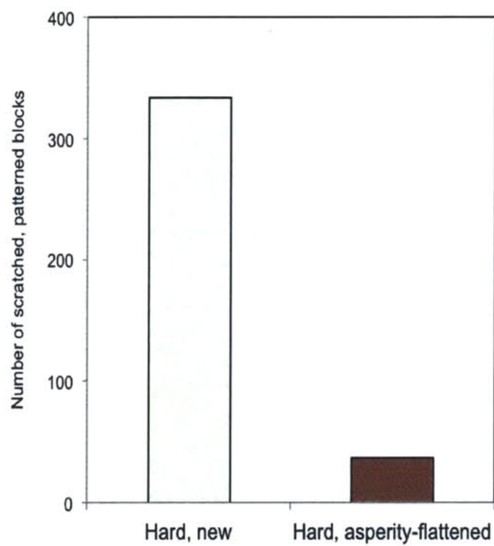

(a) IC1000 pad

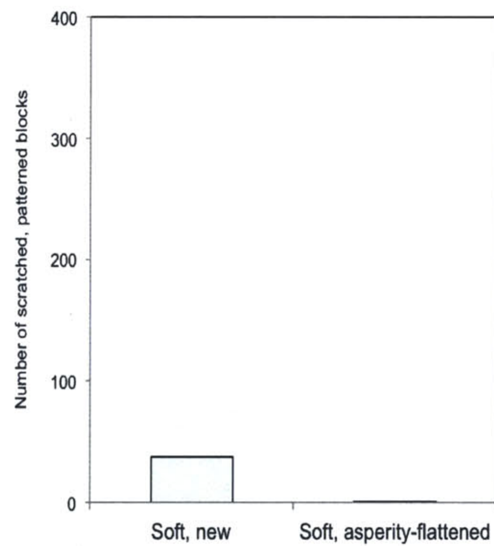

(b) Pad A

Figure F.6. Total number of scratched, patterned blocks after "polishing" experiments using new and asperity-flattened pads.

APPENDIX G

POLISHING EXPERIMENTS USING ASPERITY-FLATTENED PADS ON CU SURFACE LAYERS

The material rates of Cu polishing experiments were calculated from the mass loss measured by Mettler AT-20 Analytical Balance, Figure G.1. The volume removed by two minutes polishing, ΔV_r, can be calculated from the measured mass loss, Δm, as

$$\Delta V_r = \frac{\Delta m}{\rho_{Cu}} \qquad \text{(G.1)}$$

where ρ_{Cu} is the density of the Cu layer (= 9 mg / mm^3). Then, the volumetric material removal rate can be estimated from

$$\frac{dV_r}{dt} \cong \frac{\Delta V_r}{\Delta t} = \frac{1}{\rho_{Cu}} \frac{\Delta m}{\Delta t} \qquad \text{(G.2)}$$

where Δt is the polishing time (= 2 min). The material removal rate, accordingly, can be calculated as

$$\frac{dh_r}{dt} \cong \frac{1}{A_n} \frac{\Delta V_r}{\Delta t} = \frac{1}{A_n} \frac{1}{\rho_{Cu}} \frac{\Delta m}{\Delta t} \qquad \text{(G.3)}$$

where A_n is the nominal contact area (= π(15 mm)^2 = 700 mm^2).

Table G.1. contains all the calculated material removal rates of Cu layers by pads with different plasticity indices.

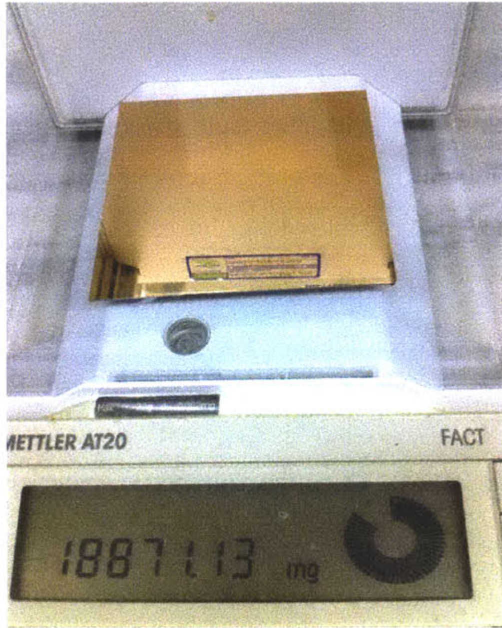

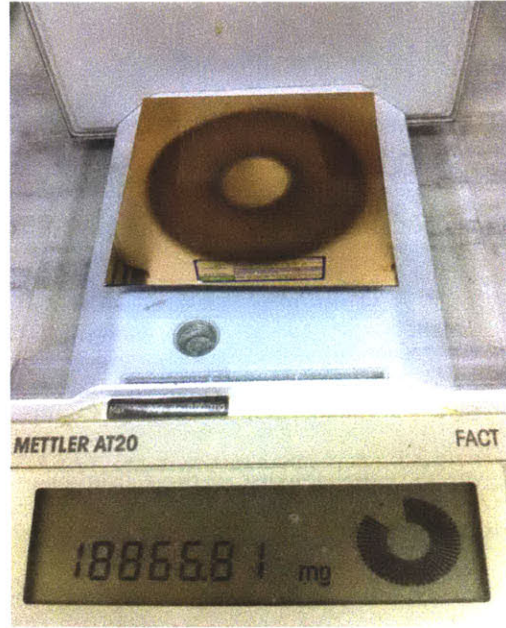

(a) before polishing

(b) after polishing

Figure G.1. Weight of the wafer with Cu surface layer before and after 2 min polishing on a face-up polisher.

Table G.1. Calculated thickness reduction rates of Cu layer, after polishing experiments using pads with different plasticity indices, ψ.

ψ	m_i (mg)	m_f (mg)	Δm (mg)	ΔV_r (mm^3)	$\Delta V_r / \Delta t$ (mm^3 / min)	dh / dt (nm / min)
4.0	18936.27	18932.86	3.41	0.379	0.189	268
	17756.41	17753.35	3.06	0.340	0.170	241
	18925.10	18921.47	3.63	0.403	0.202	285
						Avg.: 264
						Stdev.: 22
3.0	18420.05	18416.51	3.54	0.393	0.197	278
	19014.74	19010.39	4.35	0.483	0.242	342
	18717.48	18713.79	3.92	0.436	0.218	308
						Avg.: 309
						Stdev.: 32
2.4	18831.67	18827.06	4.61	0.512	0.256	362
	18451.29	18447.37	3.92	0.436	0.218	308
	19032.89	19028.88	4.01	0.446	0.223	315
						Avg.: 329
						Stdev.: 29
2.0	18871.13	18866.81	4.32	0.480	0.240	340
	18964.28	18959.27	5.01	0.557	0.278	394
	18859.51	18854.95	4.56	0.507	0.253	358
						Avg.: 364
						Stdev.: 27
1.7	19195.43	19188.34	7.09	0.788	0.394	557
	18857.49	18852.48	4.99	0.554	0.277	392
	18971.10	18966.45	4.65	0.517	0.258	365
						Avg.: 438
						Stdev.: 104
1.0	18911.24	18906.15	5.09	0.566	0.283	400
	19038.61	19034.42	4.19	0.466	0.233	329
	18927.01	18923.13	3.88	0.431	0.216	305
						Avg.: 345
						Stdev.: 49